Rhenium tricarbonyl complexes for the labelling and multimodal imaging of peptides and proteins

Sarah Hostachy

THÈSE DE DOCTORAT DE
l'UNIVERSITÉ PIERRE ET MARIE CURIE

Spécialité

Chimie

École doctorale 406 Chimie Moléculaire de Paris-Centre

Présentée par

Sarah HOSTACHY

Pour obtenir le grade de

DOCTEUR de l'UNIVERSITÉ PIERRE ET MARIE CURIE

Sujet de la thèse :

Rhenium tricarbonyl complexes for the labelling and multimodal imaging of peptides and proteins

soutenue le 12 octobre 2015

devant un jury composé de :

M. Nils METZLER-NOLTE	Rapporteur
M. Anthony ROMIEU	Rapporteur
M^{me} Anna PROUST	Examinatrice
M. Andrew THOMPSON	Examinateur
M. Nicolas DELSUC	Encadrant de thèse
M^{me} Clotilde POLICAR	Directrice de thèse

Remerciements

Une thèse ne s'effectue pas en solitaire, et je souhaiterais remercier ici toutes les personnes qui m'ont accompagnée, aidée et soutenue tout au long de ce projet.

Je tiens tout d'abord à remercier le Pr. Solange Lavielle, le Dr. Sandrine Sagan et le Dr. Jean-Maurice Mallet de m'avoir accueillie au sein de l'équipe Peptides, Glycoconjugués et Métaux en Biologie du Laboratoire des Biomolécules.

Je suis également très reconnaissante au Pr. Nils Metzler-Nolte et au Pr. Anthony Romieu d'avoir accepté d'être les rapporteurs de ce manuscrit, ainsi qu'au Dr. Andrew Thompson et au Pr. Anna Proust, qui ont également accepté de participer au jury qui examine ce travail de thèse.

Je remercie le Dr. Florence Volatron et le Pr. Christophe Thomas, membres de mon comité de suivi, pour leur regard critiques sur ce travail, leurs conseils et leurs encouragements.

Je souhaiterais évidemment remercier ma directrice de thèse, le Pr. Clotilde Policar, dont le dynamisme, l'esprit critique et la capacité à engager des collaborations à l'interface chimie-physique-biologie m'ont accompagnée, déjà bien avant le début de cette thèse. Merci de m'avoir fait confiance, conseillée et soutenue tout au long de ces années.

Un grand, grand merci également au Dr. Nicolas Delsuc, qui a co-encadré ce travail de thèse. Son dynamisme, son optimisme, sa disponibilité, ses conseils et ses encouragements ont été une aide et un soutien précieux pour ce travail, tant scientifiquement qu'humainement. Domo arigato gozaimashita!

J'ai eu la chance de travailler au sein d'un laboratoire interdisciplinaire et en collaboration avec des chimistes, des biologistes et des (bio)physiciens, que je souhaiterais remercier chaleureusement pour tout le temps qu'ils m'ont consacré et l'aide qu'ils m'ont apportée.

Je remercie le Pr. Olivier Lequin pour sa disponibilité, sa gentillesse (et sa patience!) lors des productions et purifications de protéines, ainsi qu'à toute l'équipe "Structure et Dynamique des Biomolécules" (en particulier Ludovic, Bruno, Shahid, Sébastien et Cyril), pour leur accueil et pour leur aide lors de mes passages dans leurs locaux.

Je souhaiterais exprimer ma gratitude à Françoise Illien, Emilie Mathieu et au Dr. Elodie Quevrain pour leur aide, leur gentillesse (et leur patience, encore une fois!) pour la culture cellulaire. Merci également aux équipes "Analyse, Interactions Moléculaires et Cellulaires" et "Micro-organismes et physiopathologie intestinale" de m'avoir accueillie dans leurs locaux.

Je suis reconnaissante au Dr Mayeul Collot de nous avoir fourni le dérivé rhodamine-piperazine qui nous a permis de synthétiser le dérivé rhodamine maléimide pour le marquage de l'homéodomaine.

Je remercie également les membres de la plateforme de spectrométrie de masse et protéomique de Jussieu pour leur accueil souriant.

Ce travail a également bénéficié du regard critique et de discussions fructueuses avec les Prs. Solange Lavielle et Olivier Lequin et les Drs. Fabienne Burlina, Gérard Chassaing, Sandrine Sagan et Jean-Marie Swiecicki, et je souhaiterais les en remercier.

Je remercie très chaleureusement le Dr Zoher Gueroui et son équipe de m'avoir permis d'utiliser leurs microscopes de fluorescence. Je suis également très reconnaissante au Synchrotron Soleil de m'avoir permis l'accès à ses locaux lors de projets avec les lignes SMIS et Nanoscopium. J'adresse tous mes remerciements aux équipes de ces deux lignes pour leur accueil chaleureux. Merci en particulier aux Dr. Christophe Sandt, Andrea Somogyi, Kadda Madjoubi ainsi qu'à Antoine Bergamashi de leur accueil, du temps qu'ils m'ont consacrée et des discussions que nous avons eues.

Je remercie la Japanese Society for the Promotion of Science de m'avoir donné l'opportunité de participer au JSPS Summer Program 2014, ainsi que le Pr. Itaru Hamachi de m'avoir accueillie au sein de son laboratoire à l'université de Kyoto, dans le cadre de ce programme. J'ajoute à ces remerciements l'ensemble de son équipe, qui m'a réservé un accueil chaleureux et dynamique, et en particulier Tatsuyuki Miki, Matsuda Marie et le Dr. Kiyonaka Shigeki qui m'ont aidée au quotidien lors de mon séjour dans leur laboratoire.

Je tiens bien sûr à remercier tous les membres présents et passés du Laboratoire des Biomolécules, sans qui ces années de thèse n'auraient certainement pas été les mêmes... Un grand merci donc à Cécile, Rodrigue, Jean-Marie, Hélène, Paul, Vincent, Héloise, Margherita, Cillian, Guillaume, May Lee, Sylvain, Anne-Sophie, Roba, Julien, Laurent, Alex, Clara, Mehdi, Géraldine, François, Stéphane, Karin et à tous ceux qui ont partagé, de près ou de loin, mon quotidien au laboratoire. Merci pour votre bonne humeur, votre enthousiasme et pour nos discussions, j'ai beaucoup appris - et ri - à vos côtés!

Pour finir, je veux remercier ma famille et mes amis de m'avoir soutenue (et supportée!) tout au long ces années de thèse. Merci en particulier à Madeleine et Daniel pour leur amitié depuis déjà fort fort longtemps, à Mélanie et Natacha pour le stress et les rires partagés. Je remercie mes parents, mes soeurs et mon frère du soutien et de la force qu'ils ont représentés pendant toutes mes études, et qu'ils me donnent encore aujourd'hui. Enfin, je ne remercierai jamais assez Clément pour sa présence et son soutien sans faille.

Contents

Part I

Results and Discussion

Introduction: Re(I) tricarbonyl complexes for the labelling of proteins

Fluorescence microscopy is one of the most widely used techniques for the visualization and study of biological processes. Its good spatial resolution ($\sim 10^2$ nm) makes it well-suited for cell imaging, since typical cell diameters are in the range of a few tens of micrometers. In addition, it is possible to perform fluorescence imaging on live cells. A large set of fluorescent probes with high quantum yields and diverse excitation and emission wavelengths are available, thus enabling sensitive and multi-color imaging. Although highly valuable, fluorescence techniques also suffer from some drawbacks, such as photobleaching and photodamage of cells. Some techniques, like FRAP (Fluorescence Recovery After Photobleaching) or FLIP (Fluorescence Loss in Photobleaching), take advantage of photobleaching to investigate diffusion processes in cell membranes, but generally speaking this effect is undesirable. Moreover, fluorescence intensity of a probe is often very sensitive to its environment, which often makes rigorous quantification difficult.

On the other hand, complementary methods for bio-imaging are emerging. Vibrational techniques such as infrared (IR) and Raman microspectroscopies have raised a particular interest in the past few years. They involve vibrational levels of energy (instead of electronic transitions for fluorescence), thus no photobleaching occurs. In addition, information on the local chemical environment may be collected. However, infrared microspectroscopy generally displays lower spatial resolution than fluorescence microscopy. The spatial resolution of optical microscopy is limited by $\sim \lambda/2$ (Abbe diffraction limit), where λ is the light wavelength. For infrared microscopy, typical spatial resolution is thus in the 1–10 µm range.

Multimodal probes are thus attractive, as they would combine the advantages of the different methods of imaging on a single molecule. To reach that goal, a well-documented strategy consists of combining several modalities by covalently linking a probe for each modality to a template. This leads to high molecular weight compounds which require multi-step synthesis and whose cell penetration can be altered in a large extent. Alternatively, metal complexes may be particularly adapted to obtain multimodality, as some of them display unique spectroscopic properties and can be easily functionalized by ligand modification. In the following chapter, we will particularly focus on luminescent Re(I) tri-

carbonyl complexes, since they display interesting luminescence properties (see Section 1) and intense absorption bands (1800–2200 cm^{-1}) in the IR transparency window of biological samples. Our group has recently been interested in the development of such complexes as *S*ingle *Co*re *M*ultimodal *P*robe for *I*maging (SCoMPI) [1–4]. We will describe examples of utilization of Re(I) tricarbonyl complexes in a biological context, used for their luminescence (Section 1) or for their infrared properties (Section 2). We will finally describe examples of Re(I) tricarbonyl complexes as mutimodal probes. The use of $Re(CO)_3$ complexes for biological applications based either on their luminescence or infrared properties has been extensively reviewed [2, 5–15], and we will attempt here to give an overview of their applications for the labelling and imaging of biomolecules, with a particular interest in peptide and protein labelling.

1 Luminescent $Re(CO)_3$ complexes for bio-imaging

1.1 Spectroscopic properties of luminescent Re(I) tricarbonyl complexes

Re(I) *fac*-tricarbonyl complexes bearing low energy π^* orbitals (e.g. α-diimine or dipicolylamine-derived ligands) display attractive luminescence properties and biocompatibility features. Similarly to other luminescent d^6 complexes (including luminescent Ir(III) and Ru(II) complexes), low-spin, 18 electron Re(I) tricarbonyl complexes are kinetically inert, which limits ligand exchange and the toxicity associated with heavy metal ions [15]. Luminescence properties of $[Re(CO)_3(N\hat{}N)X]$ complexes (L = α-diimine, X = halide, pyridine, ...), e.g. large Stokes shift and long emission lifetimes, are generally associated with ^{3}MLCT excited state (Figure 1): upon irradiation, one electron is promoted from a metal-centered dπ orbital to a ligand-centered π^* orbital (^{1}MLCT excited state); inter-system crossing (ISC) then leads to the emissive ^{3}MLCT excited state. However, halide-to-ligand charge-transfer (^{3}XLCT) or ligand-to-ligand charge-transfer (^{3}LLCT) may also occur, as well as mixing with intraligand ^{3}IL ($\pi \rightarrow \pi^*$) states [8, 16]. Although the nature of their emission is thus phosphorescence, these complexes are widely referred to as luminescent in the literature, and we will use this naming in the following manuscript. Finally, emission properties of Re(I) complexes are often sensitive to the presence of triplet quenchers like $^3O_2$. Although interaction with $^3O_2$ results in emission intensity loss (quenching), this mechanism do not chemically alter the complex, and is thus distinct from photobleaching[1] [15].

Due to their photophysical features, Re(I) tricarbonyl have raised an increasing interest for fluorescence bioimaging applications.[2] Several cellular and biomolecular probes

[1] Photobleaching may be defined as the photochemical destruction of the luminescent probe during the fluorescence microscopy experiment [15].

[2] The term "fluorescence microscopy" is historically used to design this imaging technique, although it may involve fluorescent as well as phosphorescent probes.

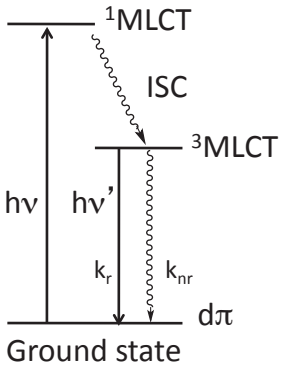

Figure 1: Jablonski diagram for [Re(CO)$_3$(diimine)(X)] complexes (MLCT model) Adapted from reference [16]

based on these complexes have thus been developed. In particular, efforts were - and still are - made to improve the spectroscopic features of these complexes, i.e. to obtain higher quantum yields and excitation at longer wavelength. This is generally done by tuning the structure of the bidentate N^N ligand, since it is involved in the MLCT. Two families of ligand have been particularly explored: (i) polypyridyl ligands, mostly derived from 2,2'-bipyridine and 1,10-phenanthroline (Figure 2) [8–10, 12–15, 17–28] and (ii) bis-quinoline ligand and its derivatives, e.g. bis(phenanthridinylmethyl)amine (bpm) [11, 29–31]. However, other polyazaheterocycles have also been developed, such as 1-R-4-(2-pyridyl)-1,2,3-triazole (pyta, R = linker, functional groups, etc.) and its derivatives [32, 33]. More recently, Re(I) tricarbonyl complexes incorporating 5,5'-disubstituted 3,3'-bisisoxazole have also been described [34]. Modifying the X ligand may also alter the luminescence properties of the complex. For instance, for [Re(CO)$_3$(bpy)(X)] complex, replacing the chloride ligand for a pyridine derivative has an impact on both emission wavelength and quantum yield (Table 1).

Spectroscopic properties of some rhenium complexes are summarized in Table 1. It can be noted that varying the bidentate and ancillary ligands may have a strong influence on quantum yield or emission wavelength. Excitation wavelength, on the other hand, is generally in the 340–360 nm range. Interestingly, though, Re(I) tricarbonyl complexes bearing a bis-quinoline ligand could be imaged in cells by fluorescence microscopy with excitation at 488 nm [35, 36].

1.2 Re(I) tricarbonyl complexes with specific cell localization.

Re(I) tricarbonyl complexes targeting the different cell compartments have been designed. A thiol-reactive chloromethyl group was for instance appended to a Re(I) tricarbonyl complex (**1**, R=Cl) in order to target mitochondria [27]. Indeed, compound **1** (R=Cl) was found to co-localize with TMRE (tetramethylrhodamine ethyl ester), a known marker of mitochondria, in MCF-7 cells (Figure 3). Interestingly, a similar complex bearing a hy-

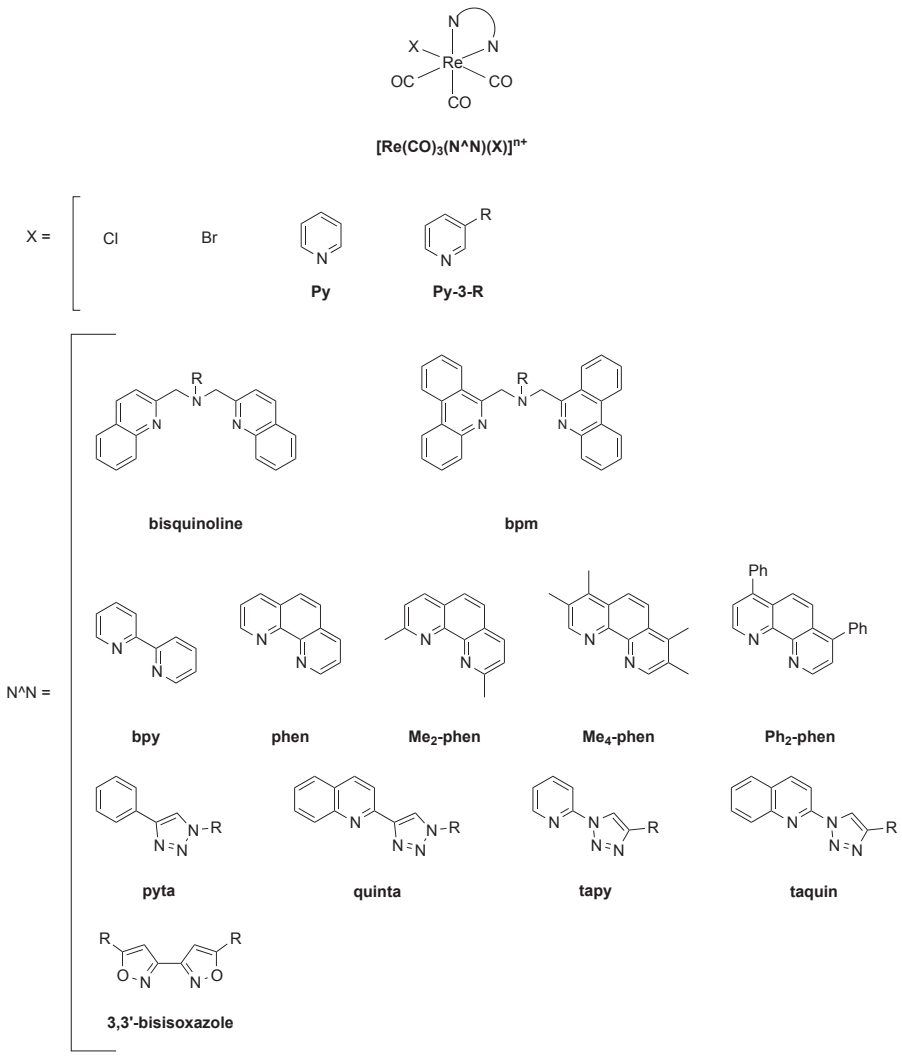

Figure 2: Changing the ligands to tune the spectroscopic properties of Re(I) tricarbonyl complexes [8, 30, 33, 34]

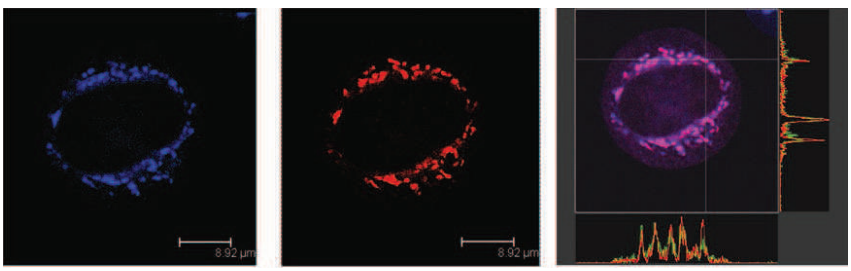

Figure 3: Colocalisation of **1** (R=Cl, left) with TMRE (center) in MCF-7 cell
Reproduced from [27] with permission of The Royal Society of Chemistry, on behalf of the European Society for Photobiology, the European Photochemistry Association and the RSC.

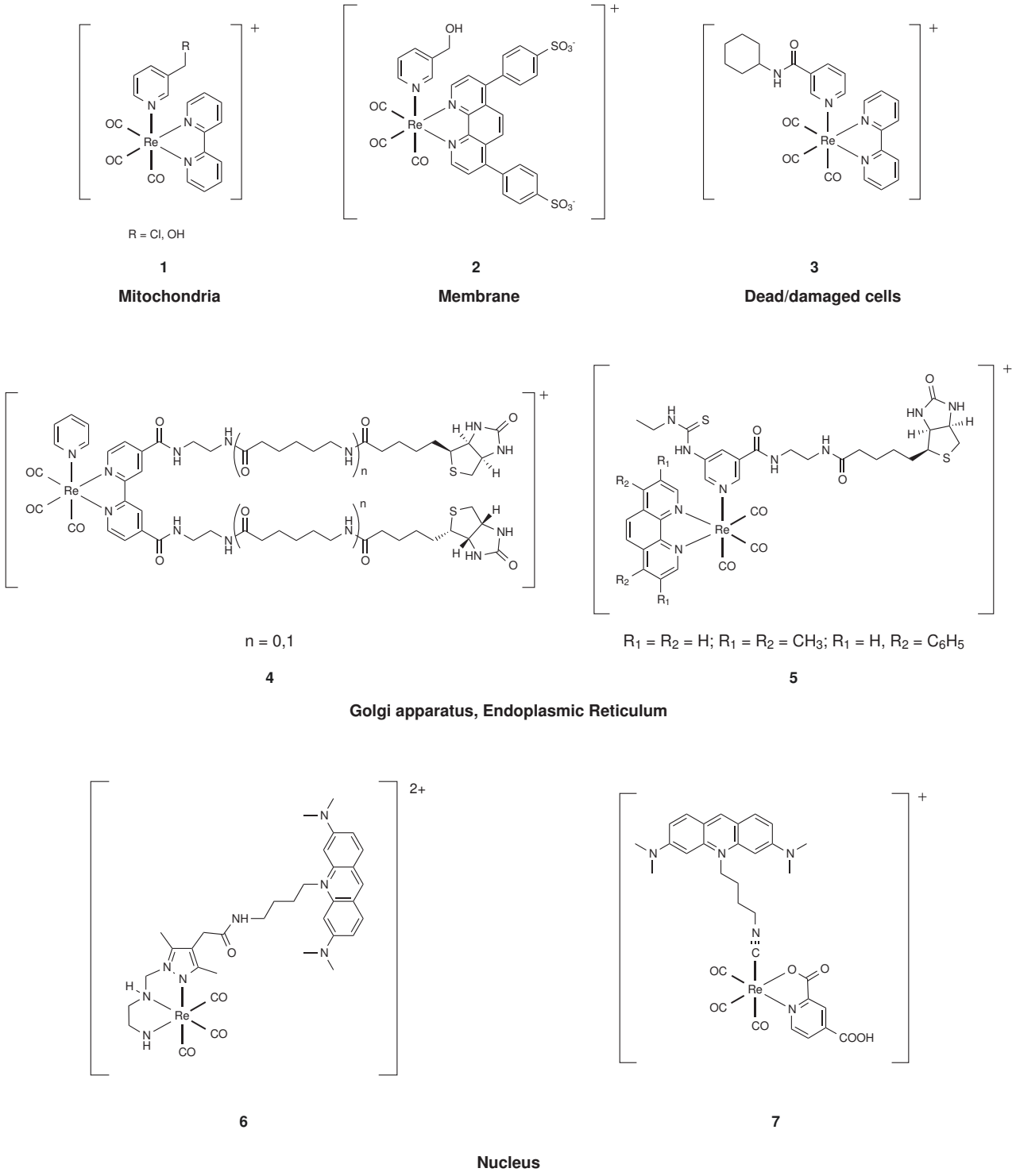

Scheme 1: Examples of luminescent Re(I) tricarbonyl complexes targeting the different cell compartments [27, 28, 38, 39]

Table 1: Examples of photophysical properties of Re(I) tricarbonyl complexes in acetonitrile at 298 K

N^N ligand	X ligand	λ_{exc} (nm)	λ_{em} (nm)	Φ_{em} (%)	Reference
bisquinoline[1]	–	366	425, 580	0.44	[29]
bpm	–	350	570 – 575	N.A.	[30]
bpy	Cl	355	633	0.27	[32]
bpy	Py−3-C(O)NH_2	343	551	15.6	[17]
phen	Py−3-C(O)NH_2	368	546	12.2	[17]
phen	Py-3-C(O)NHEt	355	548	33	[24]
Me_2−phen	Py-3-C(O)NHEt	355	536	30	[24]
Me_4−phen	Py-3-C(O)NHEt	355	515	54	[24]
Ph_2−phen	Py-3-C(O)NHEt	355	560	34	[24]
pyta (R = Bn)	Cl	355	538	0.33	[32]
pyta (R = Alkyl chain)	Cl	332	522	0.1	[33]
quinta[2]	Br	N.E.[2]	N.E.[2]	–	[33]
tapy	Cl	360	569	0.19	[33]
tapy	Br	360	564	0.17	[33]
taquin	Br	380	617	0.06	[33]

[1] Measurements were made in ethylene glycol instead of acetonitrile for this example.
[2] $[Re(CO)_3(Quinta)(Br)]$ complexes are non emissive (N.E.) in acetonitrile [33] but display typical MLCT features in aqueous solution (containing DMSO). Typical photophysical data for those complexes are $\lambda_{ex} \sim 335$–$345\,nm$, $\lambda_{em} \sim 580$–$600\,nm$, and $\Phi \sim 0.2$–$0.6\,\%$ [33, 37].

droxymethyl group (**1**, R = OH) displayed very similar localization pattern in MCF-7 cells, despite the apparent lack of a thiol-reactive group [28]. To explain this mitochondrial localization, it was postulated that phosphorylation of the internalized complex could lead to a thiol-reactive moiety, although no experimental evidence for this hypothesis was obtained. Coogan and co-workers synthesized a range of Re(I) tricarbonyl polypyridyl complexes varying in charge, size and lipophilicity in a first attempt to rationalize the cell localization of such compounds [28]. Although rationalization proved sometimes difficult, they could observe for instance that compound **2** was localized at the plasma membrane of MCF-7 cells, probably interacting with the cationic residues of the glyocoprotein layers (glycocalyx). Additionnally, **3** was found to be internalized only in dead or damaged cells, being thus a potential cell-death marker. Examples of biotinylated $Re(CO)_3$ polypyridyl complexes (**4**, **5**) were found to localize in lipophilic compartments like Golgi apparatus or endoplasmic reticulum [8, 25]. Finally, a few examples of nucleus localization (compounds **6**, **7**) can also be found [38, 39].

On the other hand, targeting specific biomolecules rather than cell compartments is also desirable, and various strategies have been adopted to label (and image) molecules of biological interest (e.g. ions, drugs, sugars, PNA, peptides, proteins,...) with Re(I) tricarbonyl complexes. In the following parts, we will focus on the strategies for the incorporation

of a Re(CO)$_3$ moiety into peptides and proteins.

1.3 Labelling of amino-acids and peptides with luminescent Re(CO)$_3$ complexes

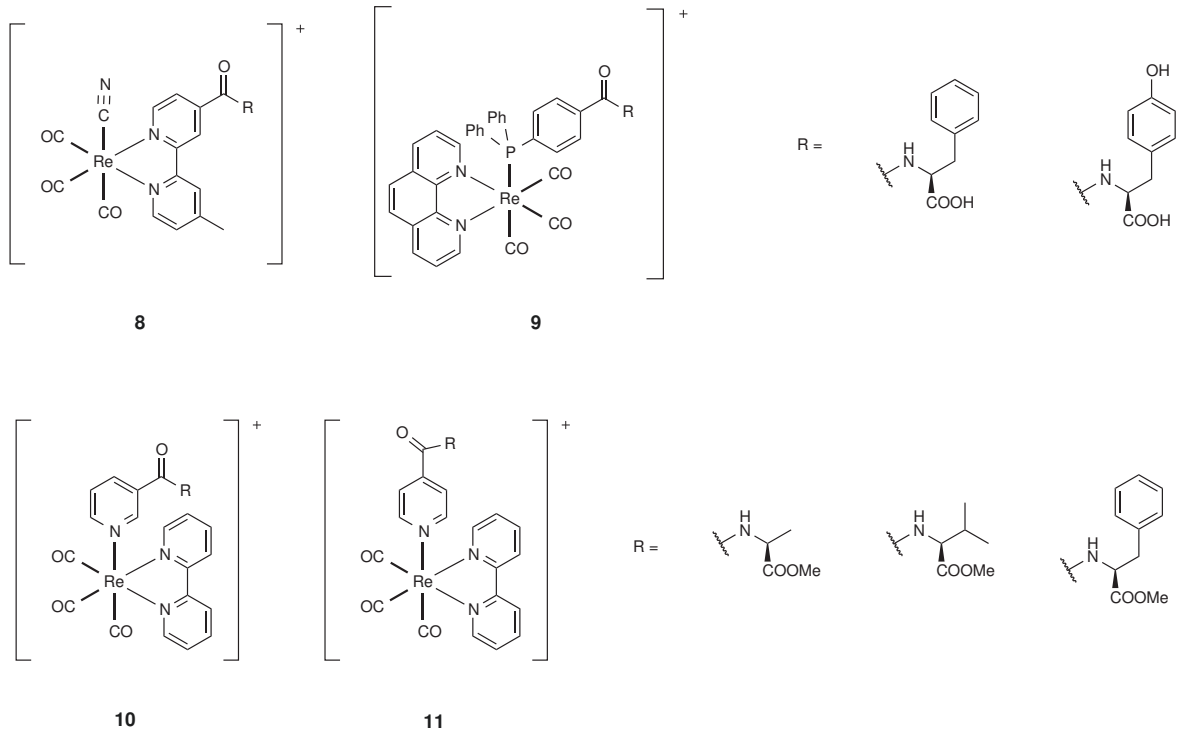

Scheme 2: Examples of Re-appended amino acids. [40, 41]

Single amino-acids have been derivatized with luminescent Re(CO)$_3$ complexes [11, 29–31, 40–43]. Complexes **8** and **9** (Scheme 2), for instance, have been appended with phenylalanine and tyrosine, and their photophysical properties studied [40]. The study particularly focused on the use of the rhenium complex as photo-oxidant to generate tyrosyl radicals. Indeed, MLCT excited states may be used to study redox biological processes, in particular electron transfer (see 1.4).

Gimeno *et al.* synthesized two series of amino-acids appended with $[Re(CO)_3(bpy)(py)]^+$ complexes (compounds **10** and **11**, Scheme 2) [41]. The amino acids were linked to the complex through the pyridine ligand, at either the *meta* (**10**) or *para* (**11**) position of pyridine. They studied the cellular uptake of both series and could observe that this minor change in structure had major consequences on the properties of the complex: the *para* derivatives proved highly cytotoxic and displayed high photobleaching, whereas the cells incubated with the *meta* derivatives remained healthy and displayed localization patterns typical for monocationic, lipophilic Re(I) tricarbonyl complexes (i.e. cytoplasmic staining, with some concentration in mitochondria). Although no explanation could be given as certain, the authors hypothesized that unidirectional electron shuttling from the metal centre to the

amino-acid was easier with the *para* than with the *meta* derivatives, generating an amino-acid radical.

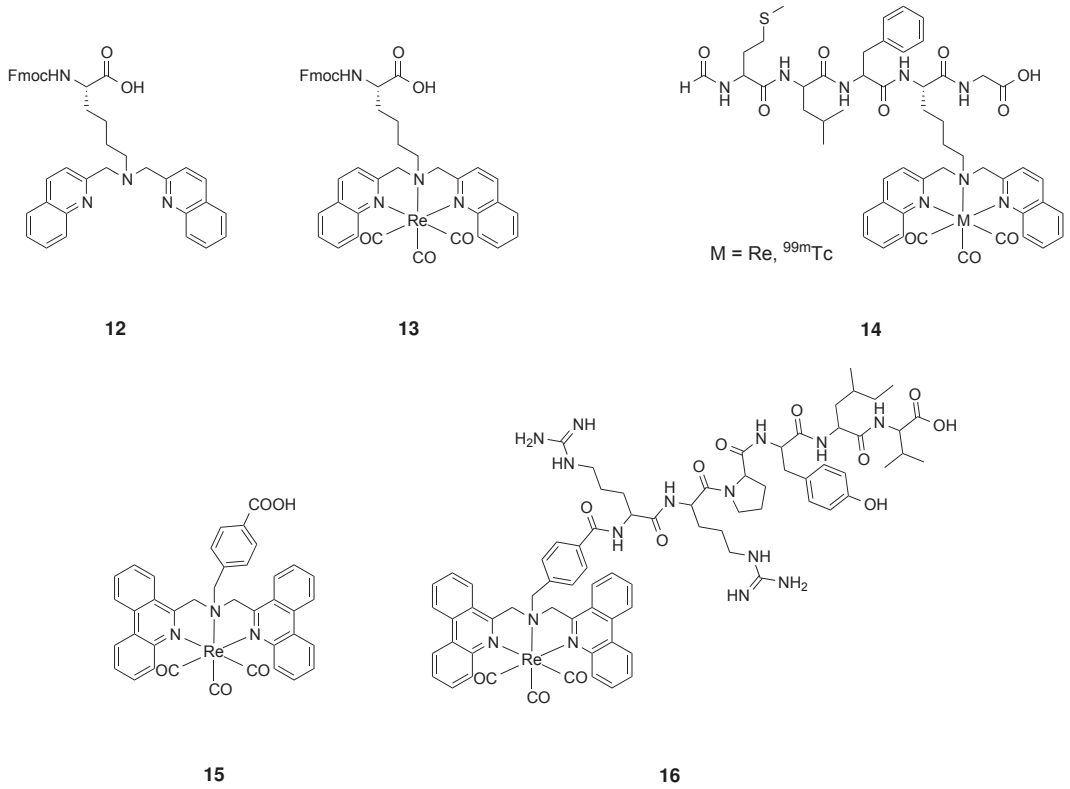

Scheme 3: Re(I) tricarbonyl complexes for the labelling of peptides [29, 30, 43]

The single amino-acid chelate (SAAC) strategy was developed in the early 2000s to incorporate Re/^{99m}Tc complexes into peptides by solid-phase peptide synthesis (using Fmoc strategy). Valliant, Zubieta *et al.* modified a lysine with a bis-quinoline ligand to form the SAAC ligand **12**, which could then be reacted with a $Re(CO)_3$ precursor to form the SAAC-Re complex **13** [29, 43]. Both SAAC and SAAC-Re could be incorporated by automated peptide synthesis into fMLF peptide (fMLF(SAAC-Re)G, **14**), a peptide sequence targeting the formyl peptide receptor (FPR). FPR is expressed on neutrophils and is a target for the (radio)imaging of trafficking of white blood cells. The $Re(CO)_3$-labelled peptide could be observed by fluorescence microscopy in human leukocytes, and its localization was consistent with previous reports on chemotactic peptides. Interestingly, a $^{99m}Tc(CO)_3$ analogue could be easily prepared by reacting the precursor $[^{99m}Tc(CO)_3(H_2O)_3]^+$ with the Re-free peptide fMLF(SAAC)G, thus enabling correlative studies with radioimaging. This strategy was later applied to peptides such as HIV-Tat basic domain or β-breaker peptides[3] [11]. Other biomolecules could also be labelled and imaged, e.g. biotin, folic acid or thymidine derivatives [11].

A Re(I) tricarbonyl complex (**15**), suitable for *N*-terminal labelling of peptides, could

[3] β-breaker peptides are short peptide fragments from the amyloid-β peptide. They can bind to amyloid-β plaques and inhibit fibril formation.

be coupled to neurotensin (8-13) fragment on solid-phase [30]. The complex **15** and the labelled peptide **16** were both internalized in various cell lines, and displayed cytosolic localization. Uptake of the unconjugated complex seemed more efficient than uptake of the labelled peptide. However, more pronounced differences between cell lines could be observed for the peptide, suggesting some selectivity in its uptake mechanism.

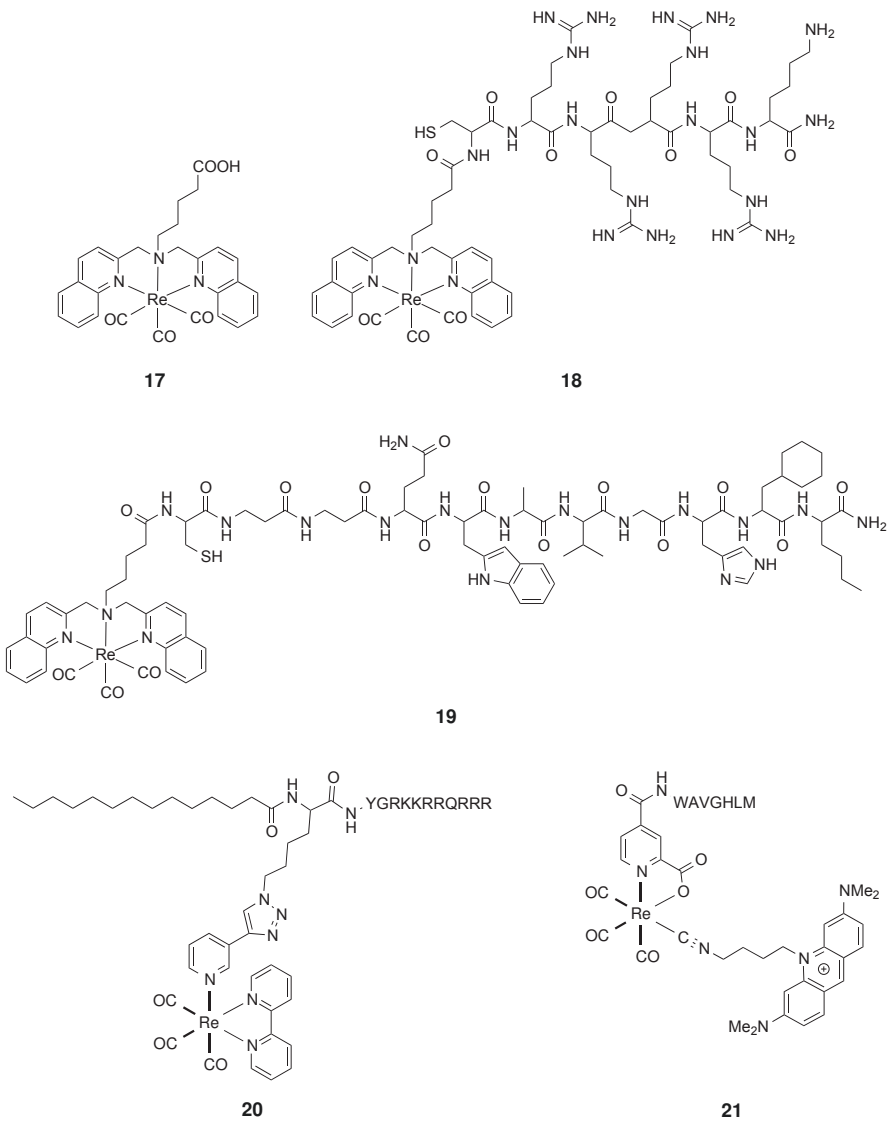

Scheme 4: Examples of Re(I) tricarbonyl complexes conjugated to peptides for specific cell of organelle targeting [39, 44, 45]

On the other hand, peptides may also be conjugated to Re(I) tricarbonyl complexes to target the complex to specific subcellular compartments or to enhance their uptake by (specific) cells, generally for therapeutic purposes. For instance, Gasser *et al.* conjugated Re(I) tricarbonyl bisquinoline compound **17** with a Nuclear Localization Signal (NLS) sequence (**18**) and to a derivative of the Bombesin neuropeptide (**19**) [44]. Bombesin is often used to selectively target cancer cells over healthy cells, since its receptor is overexpressed in some types of cancers. The aim of the study was to evaluate the potential of Re(I) tricarbonyl

complexes as photodynamic therapy (PDT) photosensitizers, namely their ability to generate the reactive singlet oxygen ($^1O_2$) upon light irradiation. Although Ru(II) polypyridyl species have been shown to be efficient photosensitizers for $^1O_2$, there are only scarce examples of use of Re(I) complexes for this application [46–48]. Fluorescence microscopy showed that the NLS-conjugated complex **18** accumulated in nucleoli of HeLa cells, whereas its parent complex was homogeneously distributed in the cells. The Bombesin conjugate (**19**), however, displayed only weak fluorescence in those cells, which was explained by either low uptake of the conjugate or quenching of the luminescence of the complex in the cell. Conjugation to NLS sequence greatly increased the cytotoxicity of the compound **18**, whereas neither the parent complex **17** nor the Bombesin conjugate **19** displayed cytotoxicity in the dark. However, irradiation of the cells incubated with **17** or **19** resulted in increased cytotoxicity (up to 20-fold for Re-Bombesin **19**), which is encouraging for further studies on Re(I) tricarbonyl complexes as photosensitizers. $^1O_2$ production involves non-radiative quenching of the ^{3}MLCT excited state, and thus decreases the effective quantum yield of the complex. However, all derivatives could be detected by fluorescence microscopy in live and fixed cells, with the exception of the Bombesin derivative.

The same group reported the conjugation of a Re(I) tricarbonyl bipyridine complex to a lipopeptide (namely, myristoylated HIV Tat peptide) known for its cell-penetration properties [45]. The conjugate compound **20** displayed enhanced uptake in HeLa cells (Figure 4), as well as increased cytotoxicity. Finally, Alberto *et al.* reported the synthesis of an other Bombesin-conjugated Re(I) tricarbonyl complex, compound **21** [39]. The goal of the study was to design Re/Tc tricarbonyl complexes that could be addressed selectively to the nucleus of cancer cells. The acridine moiety was appended for nucleus targeting, and the bombesin derivative for cancer cell selectivity. Interestingly, compound **21** could be observed by fluorescence microscopy in PC-3 (human prostate adenocarcinoma) cells, which express the GRP receptor (Gastrin releasing peptide receptor) targeted by bombesin, but was not detected in B16-F1 cells (mouse melanoma cell line) which do not express this receptor. As mentioned above, the complex **7** missing the bombesin sequence accumulated in the nucleus. However, the bombesin conjugate displayed homogenous distribution and no nuclear uptake. It was thus hypothesized that the bombesin sequence prevented the nuclear uptake of **21**.

1.4 Labelling of proteins

In vitro covalent labelling of proteins through functionalization of Re(I) tricarbonyl complexes

Luminescent Re(I) tricarbonyl complexes have been functionalized with thiol- or amine-reactive groups in order to label peptides and proteins *in vitro*. For instance, *N*-hydroxysuccinimide ester activated complex **22** was used to label human serum albumin (HSA) and Immunoglob-

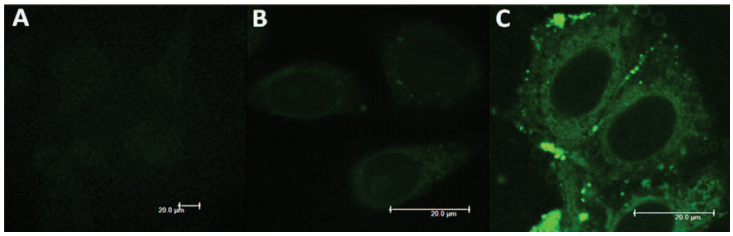

Figure 4: Enhanced cellular uptake of compound **20**
Reprinted with permission from [45]. Copyright 2014 American Chemical Society. Hela cells were fixed after 2h incubation. (A) Control cells; (B) Cells incubated with 100 µM of parent complex; (C) Cells incubated with 20 µM of peptide conjugate **20**.

ulin G (IgG) [49]. The authors later used Re-labelled HSA in a Fluorescence Polarization Immunoassay [50]. The isothiocyanate-functionalized complexes **23**, bearing various bidentate ligands, were coupled to HSA [8]. Similarly, thiol-reactive groups such as iodoacetamide (**24**, Scheme 6) and maleimide (**25**) have been appended to Re(I) tricarbonyl complexes. Compound **24** was successfully used to label HSA, with a final dye:protein ratio of 0.7 [51]. Similarly, compound **25** was used to label HSA and BSA (Bovine Serum Albumin) [23]. Between four and five cystein residues were labelled, over the 35 cystein residues BSA and HSA contain. A luminescent Re(I) complex bearing an epoxide-functionalized bidentate ligand (**26**) was used to label various cystein mutants of cytochrome P450 BM3 heme domain [52]. Interestingly, the 5,6-epoxy-5,6-dihydro-[1,10]phenanthroline bidentate ligand could be coordinated to other metal centres (e.g. Ir^{III}, Ru^{II}, Os^{II}). Very recently, Lo and co-workers published a Re(I) tricarbonyl complex functionalized with a dibenzocyclooctyne (DIBO) (compound **27**) for labelling of azide-modified biomolecules by copper-free azide-alkyne cycloaddition [18]. They could modify BSA and HSA with an azide function at *N*-terminal position, and then label to azide-modified proteins with the DIBO-appended rhenium complex. The same group also designed tetrazine-appended Re(I) tricarbonyl complexes (**28**, **29**) for the labelling of alkyne or alkene-modified protein [53]. They could label efficiently BCN[4]-modified apo-transferrin (aTf) as well as BSA and HSA. Interestingly, the luminescence of the tetrazine-appended Re(I) complexes was quenched due to energy transfer to the tetrazine. Upon reaction with dienophile-labelled proteins, the tetrazine moiety was reacted to a non-quenching moiety and the luminescence was restored. This is thus an interesting example of phosphorogenic Re(I) complexes.

In vitro labelling of proteins by reaction with aqua Re(I) tricarbonyl complexes.

Aqua Re(I) complexes may also react with amino-acids of proteins, in particular with histidines (Scheme 8) [54–57]. A luminescent aqua complex $[Re(CO)_3(phen)(H_2O)]^+$ (phen = 1,10-phenanthroline, compound **30**) and its derivate $[Re(CO)_3(dmp)(H_2O)]^+$ (dmp =

[4]BCN = (*1R,8S,9S*)-bicyclo[6.1.0]non-4-yn-9-ylmethanol

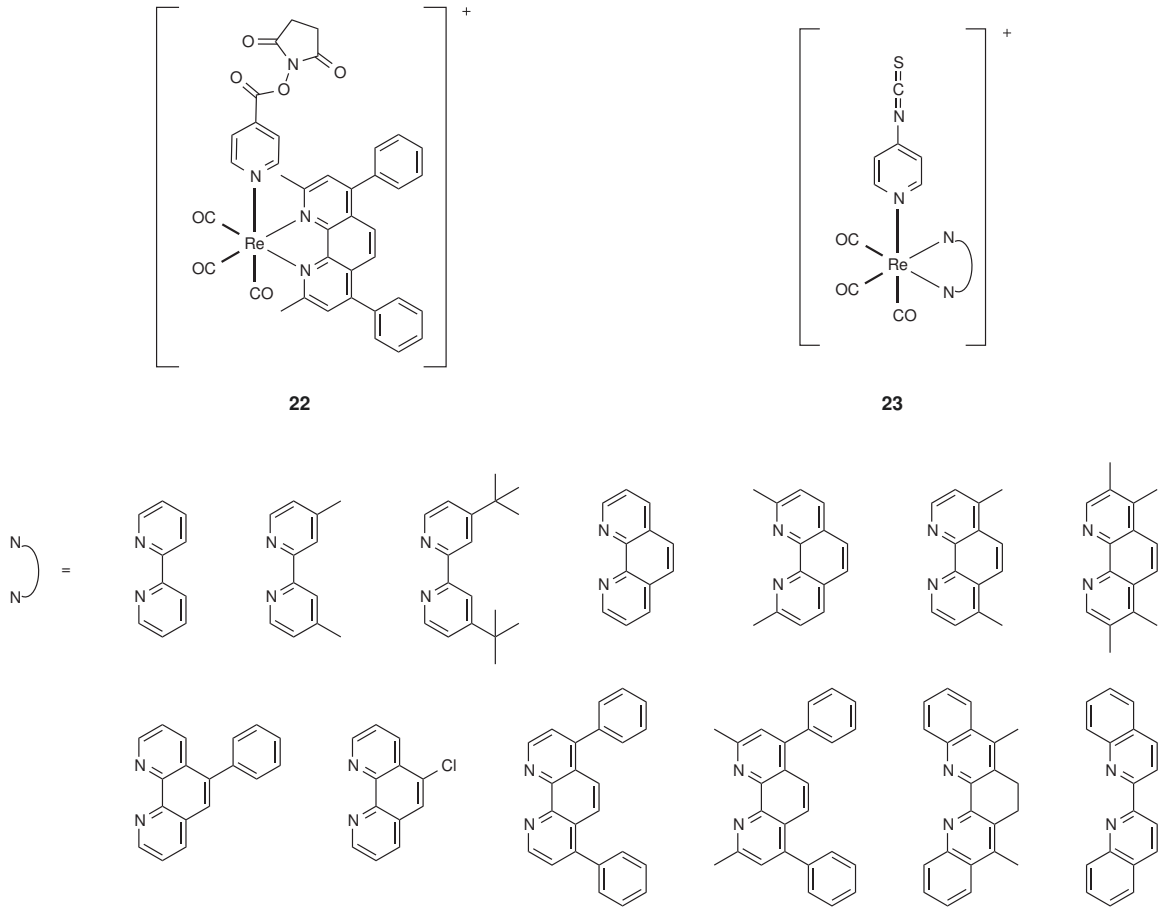

Scheme 5: Examples of luminescent Re(I) tricarbonyl complexes for amine labelling [49, 50] (adapted from [8]).

4,7-dimethyl-1,10-phenanthroline) were shown to label His residues of Azurin from *Pseudomonas aeruginosa* and mutants by substitution of the aqua ligand by the imidazole ring of histidine (see **31**) [54–56]. Photoexcitation of $[Re(CO)_3(N\hat{}N)(His)]$ in the labelled Azurins led to the oxidation of the copper center of the protein. Interestingly, the carbonyl ligands were used in these studies to sense the environment of the complex by Time-Resolved Infrared (TRIR) spectroscopy, thus enabling the author to study structural changes in the structure of the protein, as well as electron transfer processes. It might thus be considered as an example of the use of the multimodality of Re(I) tricarbonyl complexes.

Non covalent labelling of proteins

The protein labelling methods described above, although useful for proof of concept and for *in vitro* studies of purified proteins, are difficult to apply for the selective labelling of proteins in a complex cell environment. To our knowledge, fluorescence cell imaging of proteins with Re(I) tricarbonyl has only been performed using non-covalent methods, i.e. by labelling a specific ligand of the protein of interest with a luminescent Re(I) tricarbonyl complex. For instance, biotinylated complexes **4** and **5** were designed as cross-linkers for

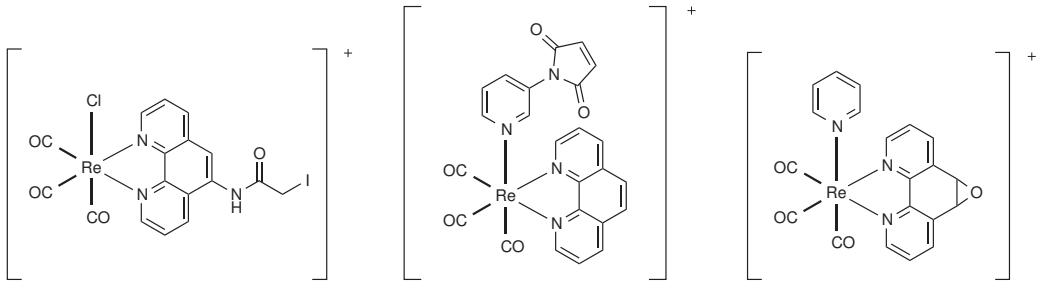

Scheme 6: Examples of luminescent Re(I) tricarbonyl complexes for thiol labelling [51, 52] (adapted from [8])

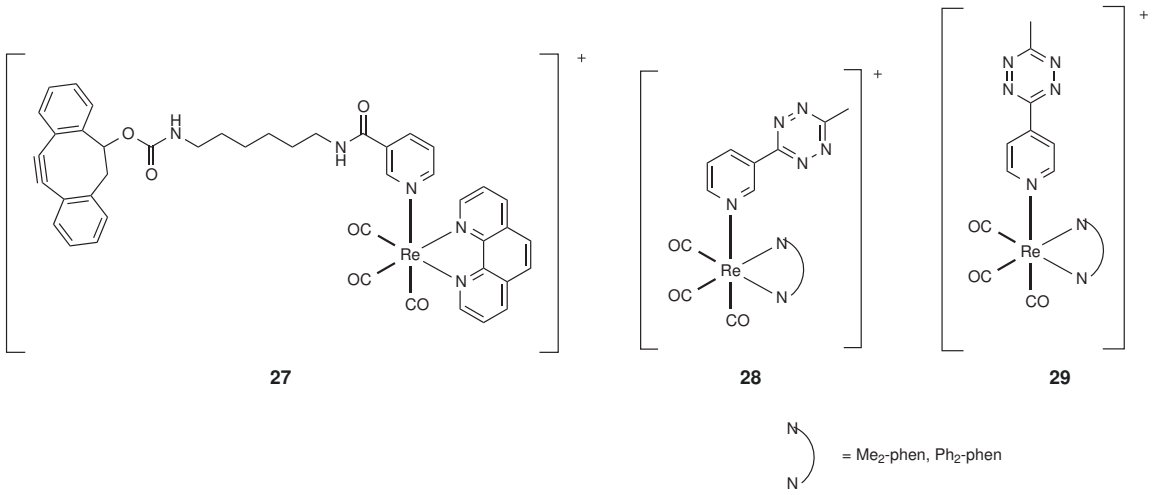

Scheme 7: DIBO and tetrazine-functionalized Re(I) tricarbonyl complexes for bio-orthogonal protein labelling [18, 53]

Scheme 8: An aqua complex for Re(I)-modification of Azurin [54–56]

avidin. Similarly, Re(I) tricarbonyl complexes were appended to estrogen derivatives to target estrogen receptors [3, 9] or to indoles to target indole-binding proteins [9]. Doyle *et al.* conjugated luminescent Re(I) bisquinoline coomplexes to folic acid and to vitamin B_{12} to target folate receptor and cubilin receptor, respectively [35, 42]. We also described above conjugation of Re(I) complexes to bombesin to target GPR receptor.

2 $Re(CO)_3$ complexes for vibrational bio-imaging

2.1 Carbonyl Metallo-ImmunoAssay (CMIA)

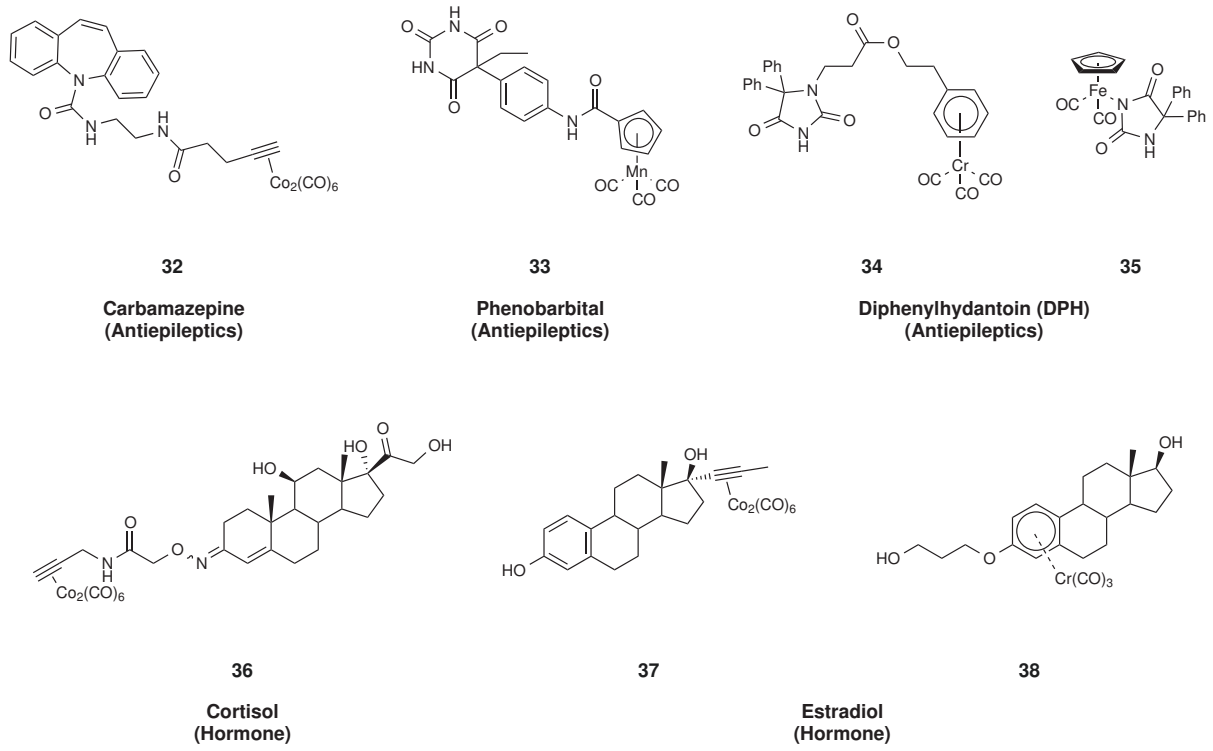

Scheme 9: Examples of molecules labelled with metal-carbonyl complexes for Carbonyl MetalloImmunoAssay (reviewed in [5])

As mentioned in the preamble, metal-carbonyl complexes present attractive infrared properties, with intense absorption bands in the 1800–2200 cm^{-1} range. The first example of utilization of these unique properties in a biological context was a Carbonyl Metallo-ImmunoAssay (CMIA) developed by Jaouen's group. CMIAs are non-isotopic (the tracer is not a radiolabel), competitive (a known quantity of labelled analyte and a known, lesser quantity of the corresponding antibody are introduced in the sample to be analyzed) and heterogenous (a separation step of bound and unbound fractions is required prior to quantification) immuno-assays, where the tracer used for quantifications is a metal-carbonyl moiety. They were able to design mono-immunoassays for various molecules of clinical interest, such as antiepileptics and hormones (Scheme 9), or of environmental interest (pes-

ticides) [5]. Interestingly, when the infrared bands of different M(CO)$_x$ do not overlap (Figure 5), simultaneous immunoassay (multi-CMIA) can be envisioned. Multi-CMIA of compounds **32**, **33** and **34** was reported [58]. Although this principle was applied to *in vitro* assays, it can be envisioned to use it for multi-color infrared imaging.

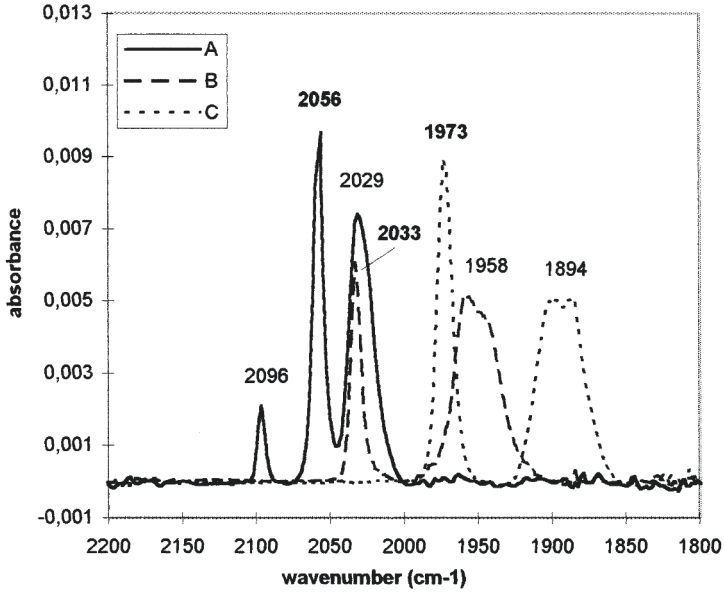

Figure 5: Principle of multi-CMIA: infrared spectra of **32** (A), **33** (B) and **34** (C). Reprinted from reference [58], Copyright (1999), with permission from Elsevier.

2.2 Labelling of proteins with Re(CO)$_3$ moieties for Infrared studies

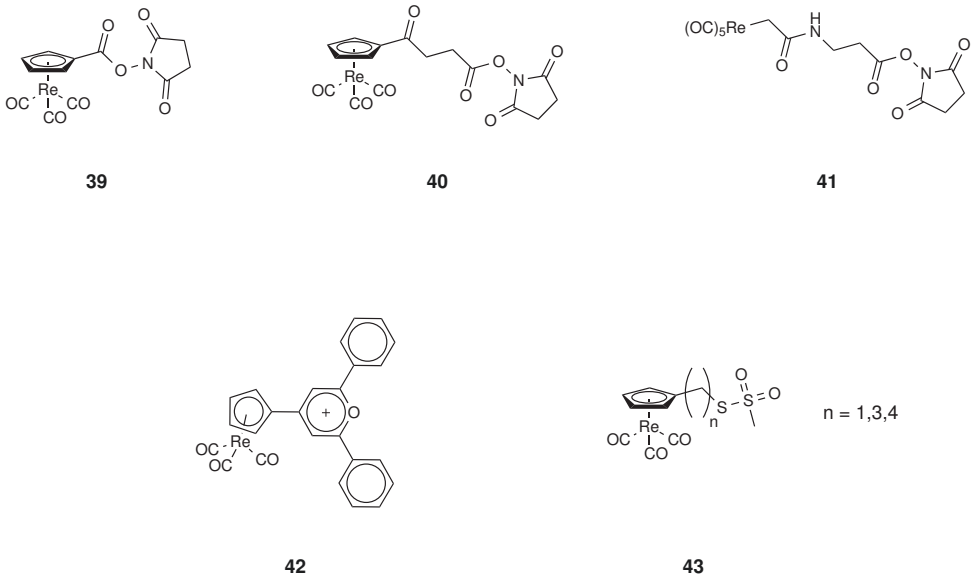

Scheme 10: [Re(CO)$_3$(Cp)] complexes for specific labelling of amines and thiols [59–61]

Due to the sensitivity of vibrational modes to their environment, vibrational spectro-

scopies may be used to probe the structure and dynamics of biomolecules [62]. The position, width, lifetimes of signal of IR probes may for instance give information on the local conformation and dynamics of a protein or on the local electric field near a catalytic site. Although other IR probes (nitrile, azide, etc.) can be used, $Re(CO)_3$ display more intense signals [61], thus allowing a better sensitivity. *In vitro* labelling of proteins with $Re(CO)_3$ complexes may thus be of use not only for further vibrational imaging, but also to study intrinsic properties of the protein. Other metal carbonyl complexes have been used for the labelling of proteins [6], but in this part we will focus on examples with $[Re(CO)_3(Cp)]$.

In addition to the examples described in 1, non-luminescent $Re(CO)_3$ complexes have also been appended to proteins. As for luminescent $Re(CO)_3$, amine-specific (compounds **39**, **40**, **41**, **42**) and thiol-specific (**43**) groups have been appended to the cyclopentadienyl rhenium tricarbonyl complex. NHS-activated esters **39**, **40**, **41** and pyrilium ion **42** were synthesized and used to label BSA, for instance [59, 60]. Compound **43** bears a thiol-reactive group frequently used for nitroxide spin labelling in EPR [61]. Upon reaction with a cystein side chain, the methanethiosulfonate group leaves and a disulfide bond is formed between the label and the protein. This complex was used to label cystein mutants of ubiquitin (K6C and K63C) and α-synuclein (V71C). The authors used 2D IR spectroscopy to measure lifetime and frequency of symetric stretching band in various solvents and when bound to the proteins. They could relate these parameters to solvation and electrostatic field, which can then give insights into the structure and dynamics of the proteins. As mentioned in Section 1, structural changes and electron tunneling of Re-labelled Azurin mutants had also been studied using the carbonyl ligands of the $Re(CO)_3$ moiety.

2.3 Infrared Imaging and Metal Carbonyl complexes

Although examples of infrared bioimaging of proteins do not exist to our knowledge, other biomolecules have been successfully labelled with metal-carbonyl units and image by IR or Raman microscopy. In 2007, Leong and co-workers reported the first example of a biomolecule labelled with a $M(CO)_x$ moiety and imaged in cells by infrared microspectroscopy [63]. They labelled a fatty acid and an analogue of phosphatidylcholine with osmium clusters (compounds **44**, **45**) and were able to detect these compounds in mucosa cells.

Synchrotron sources display much higher brightness[5] than thermal sources ($\sim$ 100-1000 fold) [2, 67], since they focus photons on a smaller area: typical illumination areas are 100 µm for a conventional thermal source, as compared to 10–20 µm for a synchrotron source [67]. A higher flux of photons thus reaches the IR detector, which improves signal-to-noise ratio. As a consequence, with a synchrotron source, it is possible to reduce the aperture size while keeping an acceptable signal-to-noise ratio. It is thus well adapted for

[5]Briefly, brightness is the photon flux per unit area and per unit solid angle at the source, or photon flux density.

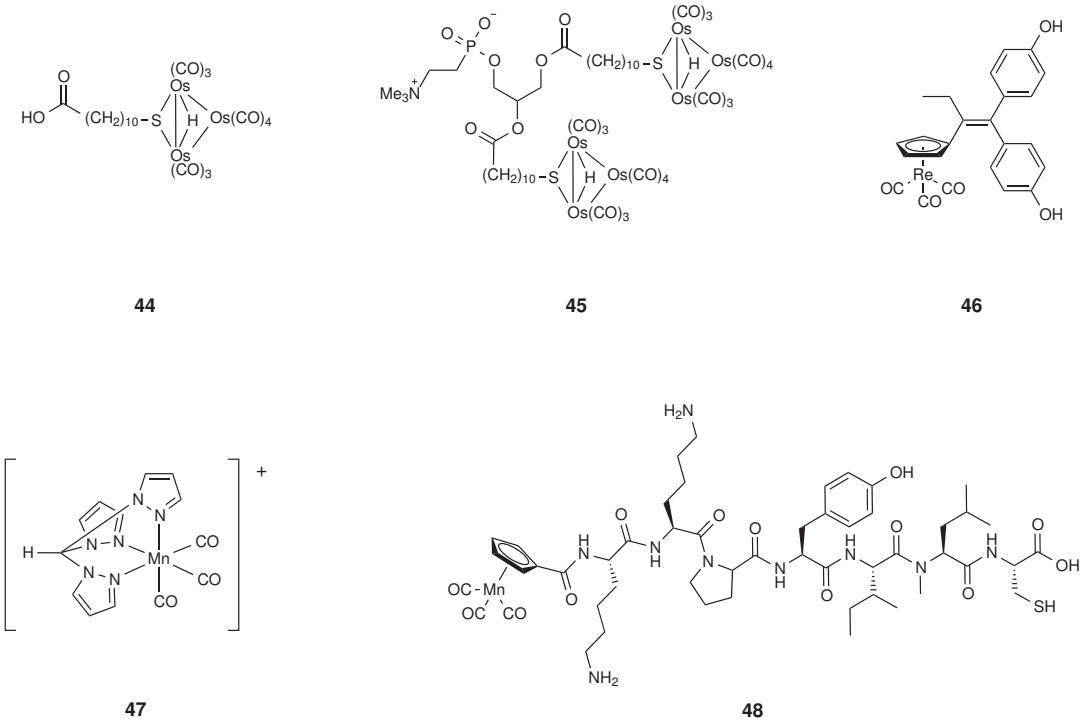

Scheme 11: Metal carbonyl complexes for vibrational imaging [63–66]

sub-cellular imaging of small cells ($< 20\,\mu m$) [68]. A rhenium carbonyl tamoxifen derivative (compound **46**) was imaged in MDA-MB-231 breast cancer cells using this technique [64].

Raman microscopy involves higher energies, but displays a better spatial resolution [2] than IR microscopy. The uptake and distribution of the CO-releasing molecule (CORM) **47** in HT29 cells was investigated using Raman microspectroscopy by Havenith, Metzler-Nolte, Schatzschneider and co-workers [65]. Interestingly, surface-enhanced Raman spectroscopy (SERS) makes use of the local amplification of Raman signals due to surface plasmon resonance of metallic nanostructure, thus enhancing sensitivity of detection. Olivo, Leong *et al.* successfully applied this method to the detection and imaging of an epidermal growth factor receptor (EGFR) in OSCC cells (oral squamous carcinoma cells) overexpressing EGFR: they functionalized PEGylated gold nanoparticles with an anti-EGFR antibody (for selectivity) and with osmium carbonyl clusters for detection (see compounds **44**, **45**) [69]. Coupling of osmium clusters to nanoparticules resulted in better compatibility and enhanced signal. Incubation concentrations were in the picomolar range for nanoparticles, which is equivalent to a $\sim 340\,\mu M$ cluster concentration: this is thus an improvement as compared to the millimolar concentrations often needed for Raman imaging. More recently, they developed an assay for glucose detection based on SERS [70].

Spatial resolution of infrared imaging may also be enhanced by coupling infrared measurement to scanning probe microscopy, e.g. atomic force microscopy (AFM). A cysteine-modified, gold-binding peptide derived from neurotensin was labelled with a cymantrene moiety (compound **48**) for detection by scattering scanning near-field infrared microscopy

(IR s-SNOM) [66]. The $Mn(CO)_3$-labelled peptide was used to map patterned self-assembled monolayer (SAM) gold surfaces, with a good spatial resolution of 90×90 nm^2. Compound **46** was mapped in MDA-MB-231 cells using Photothermal Induced Resonance (PTIR) [71], which couples excitation of a tunable infrared laser with detection of the photothermal response by AFM. In this set-up, also called AFMIR, spatial resolution is the one of the AFM tip, i.e. 20–50 nm.

Finally, development of 3D-IR imaging would provide additional information on subcellular structures and labelled biomolecule localization, and a few examples of tomographic infrared imaging of biological samples are emerging [72, 73].

3 $Re(CO)_3$ as surrogates for $^{99m}Tc(CO)_3$

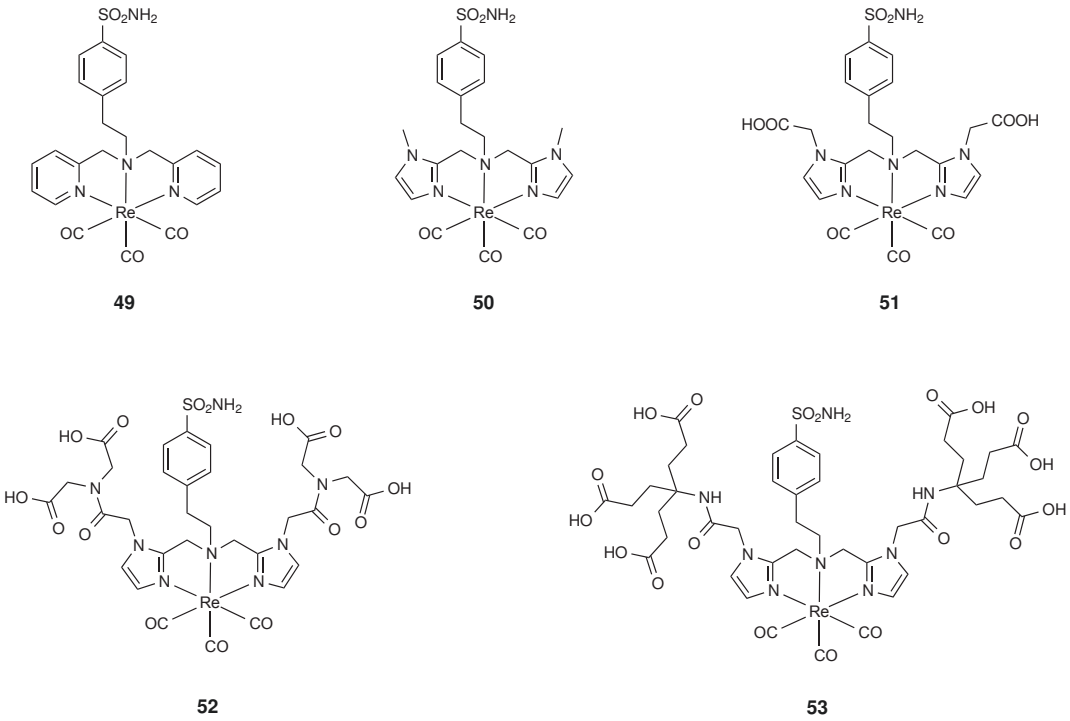

Scheme 12: Examples of $Re(CO)_3$-labelled inhibitors of Carbonic Anhydrase IX [74]

Radiotracers and radiopharmaceuticals are widely used in nuclear medicine for diagnosis and treatment. Among radionuclides, ^{99m}Tc displays attractive features, including availability from commercial generators, and well-suited properties ($t_{1/2}$ = 6 h, 140 keV) [11,74–77]. Moreover, the use of $[^{99m}Tc(H_2O)_3(CO)_3]^+$ reagent, developed by Alberto and Schibli *et al.* , enable efficient preparation of the radiotracer from the ligand [78]. Finally, non radioactive isostructural Re(I) tricarbonyl complexes can be prepared and characterized without handling radioactive materials. As a consequence, a large number of target-specific $Re(CO)_3$ complexes have been developed with the intent to replace Re by its ^{99m}Tc counterpart for the final application. Various proteins have been targeted,

including Translocator Protein TSPO [79], metallothioneins [80], G Protein-Coupled Estrogen Receptor GPER/GPR30 [81] or Carbonic Anhydrase IX [74]. As an example, the synthesis of a series of M(CO)$_3$-based (M = Re, Tc) Carbonic Anhydrase IX inhibitors was developed using Re(CO)$_3$ (Scheme 12), while the affinity for CA-IX was evaluated using the final ^{99m}Tc complexes [74]. Peptides such as bombesin were also labelled with Re/Tc tricarbonyl complexes, generally in order to target specific cell lines or events [57, 82–84]. In most of these examples, the rhenium complex is simply used for its similarity with the technetium. However, as mentioned in Section 1, efforts are made to use the potential of Re(CO)$_3$ complexes as luminescent probes, and to develop isostructural nuclear and optical probes based on ^{99m}Tc and Re, respectively [11, 29, 31, 83, 85]. Nevertheless, these complexes, luminescent or not, may be inspirational for further development of Re(CO)$_3$ complexes as multimodal imaging probes.

4 Use of Re(CO)$_3$ as multimodal probes for correlative imaging: *S*ingle *Co*re Multimodal *P*robes for *I*maging (SCoMPIs)

As described in the preamble and in this chapter, luminescent Re(I) tricarbonyl complexes have a potential for multimodal imaging. A few years ago, Policar *et al.* developed such complexes for the labelling of biomolecules, and their imaging by infrared and luminescence microscopies. This led to the concept of *S*ingle *Co*re Multimodal *P*robes for *I*maging (SCoMPIs) [4], for which a general structure is given in Figure 6. Although most of the examples of luminescent Re(I) complexes presented in this chapter bear polypyridine-derived ligands, other polyazaheterocycle might be used to form luminescent Re(I) tricarbonyl complexes [33, 86–89]. In particular, 4-(2-pyridyl)-1,2,3-triazole (Pyta) ligand is attractive due to its ease of preparation and functionalization, and to the interesting luminescence properties of the related Re(I) tricarbonyl complexes. As a proof of concept, a Re(I) tricar-

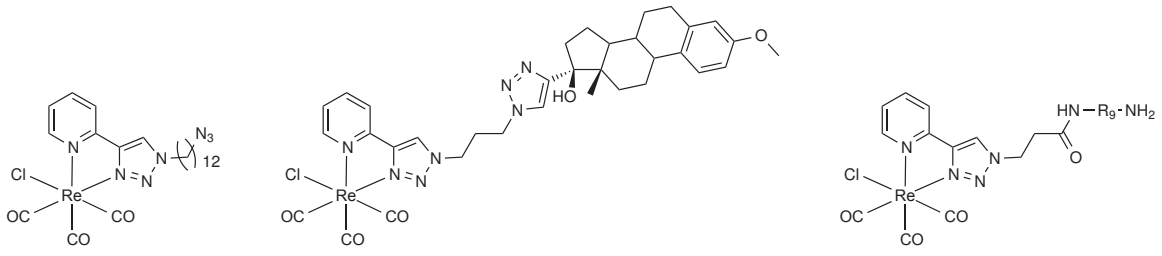

ReC$_{12}$N$_3$ **SCoMPI-R$_9$ (SR$_9$)**

54 **55** **56**

Scheme 13: SCoMPIs used for multimodal imaging in biological samples (cells and skin) [1, 3, 4]

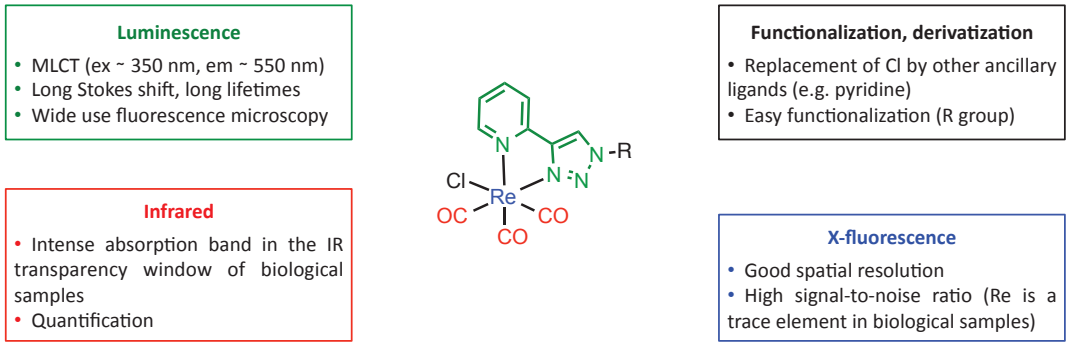

(a) Structure and properties of SCoMPI

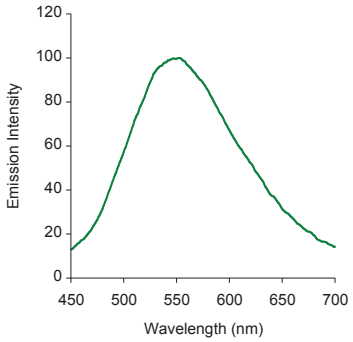

(b) Luminescence signal of SCoMPI ($\lambda_{ex} = 350$ nm)

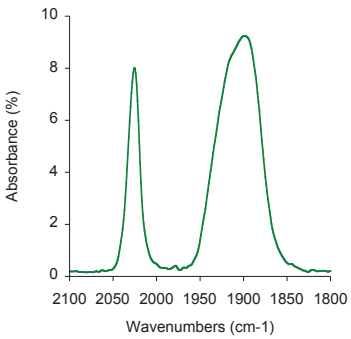

(c) Infrared signal of SCoMPI

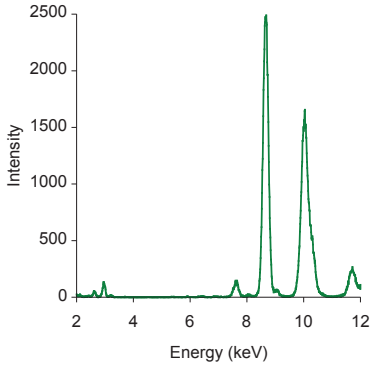

(d) X-Fluorescence of SCoMPI

Figure 6: General structure and features of *S*ingle *Co*re Multimodal *P*robes for *I*maging (SCoMPIs)

bonyl complex bearing a pyta ligand appended with a long alkyl chain (compound **54**) was synthesized, and incubated in MDA-MB-231 cells [4]. The azide moiety was used for comparison of the infrared signals from N_3 and CO groups inside cells. The compound could be detected by both fluorescence and infrared microspectroscopies, with consistent perinuclear location in both microscopies. It was possible to assign the location of the SCoMPI to the Golgi apparatus through colocalization with a fluorescent marker of this organelle. Besides, it was shown on similar compounds that the FTIR signal of the SCoMPI can be used to quantify reliably the cellular uptake of a SCoMPI-labelled compound in a collection of cells [90].

The mestranol derivative **55** could be imaged as well in MDA-MB-231 and MCF-7 breast cancer cell lines [3]. Correlative imaging could be performed using a set of luminescence and vibrational microscopies, including synchrotron radiation UV and FTIR microspectroscopies (SR-UV-MS and SR-FTIR-MS, respectively), wide field and confocal fluorescence microscopies, AFMIR and confocal Raman microscopy.

Recently, the group was also interested in detection of SCoMPIs in skin samples. In collaboration with the group of O. Torres in Barcelona, we used a ReC_{12} SCoMPI (similar to compound **54** without an azide group) to follow the penetration of lipid assemblies into skin by SR-FTIR-MS [91]. A SCoMPI was also conjugated to a nona-arginine peptide (**56**), and its penetration into skin samples was imaged correlatively by SR-FTIR-MS and fluorescence microscopy [1].

All these biomolecules are small, exogenous molecules, and we were interested in the feasibility to label endogenous molecules, in particular proteins, at the cellular level. To reach that goal, we proceeded by steps of increasing difficulty in terms of labelling and detection. We first investigated the cellular uptake of SCoMPI-labelled cell-penetrating peptides (CPP) (Chapter 1). This led us to study the luminescence properties of various SCoMPIs in solution or in presence of lipid membranes (Section 1.2) as well as the evolution of cellular uptake with cell cycle (Section 1.3). We then designed a SCoMPI for *in vitro* thiol-maleimide labelling of cystein-containing proteins. Since the aim of the study was to perform correlative imaging of proteins in cells, labelling a protein that could be internalized in cells was preferable. In collaboration with O. Lequin and S. Sagan, we thus decided to label the homeodomain of *Engrailed-2*, which is known to be internalized into cells (Chapter 2). Finally, we tested the possibility to label and image endogenous proteins with SCoMPI. To do so, we used one of the so-called Traceless Affinity Labelling strategies developed by the group of I. Hamachi for the labelling of endogenous proteins. We targeted Carbonic Anhydrases IX and XII (CA-IX and CA-XII, respectively), two membrane-bound isoforms of Carbonic Anhydrases that are over-expressed in solid tumor cancers.

Notably, the possibility to use SCoMPI as probe for synchrotron-based X-ray fluorescence (SXRF) microspectroscopy (SXRF) was also explored. X-ray absorption or fluorescence methods are valuable for the detection of metal centers and sensing of their chemical

environment, in particular in biological samples [92–95]. SXRF, for instance, enables simultaneous collection of data for multiple elements, provided their edge energy is lower than the incident energy. Information on the chemical environment of the studied metal center is thus immediately available. Moreover, the spatial resolution of this technique is in the nanometer - micrometer range, which is relevant for biological applications. Interestingly, the natural abundance of Re is very low, which would make possible to detect SCoMPI-labelled molecules with a good signal-to-noise ratio. We thus investigated the potential of Re as X-ray fluorescence probe (Figure 6) for the detection and subcellular imaging of proteins. The preliminary results will be discussed in Chapters 2 and 3.

Chapter 1

Labelling of peptides with SCoMPIs

1.1 Introduction: Cell-Penetrating Peptides

1.1.1 Cellular uptake

Cell-penetrating peptides (CPPs) are small peptides (generally 8 to 30 amino acids) that are efficiently internalized into cells. Their ability to deliver various conjugated cargos inside cells makes them potential (drug) delivery or diagnostic agents [96]. Over the past two decades, several cell-penetrating peptides have been discovered or designed [96–101], and numerous examples of intracellular delivery of various cargos (including drugs, nucleic acids or nanoparticles) have been reported [96, 102]. Despite high variability in their sequences, CPPs present physico-chemical similarities. In particular, most CPPs present a high density of positive charges [97, 99]. Actually, the arginine-rich CPPs such as TAT peptides and oligoarginines form an important and extensively studied class of CPPs.

Understanding the mechanism(s) of cellular uptake of CPPs is essential to rationally design new CPPs and to use them efficiently for cargo delivery. Described internalization pathways of CPPs are summarized in Figure 1.1. Cellular uptake may occur through direct translocation or endocytosis (pinocytosis). Energy-dependent endocytotic pathways involve macropinocytosis as well as clathrin-dependent, caveolae/lipid raft-dependent or clathrin/caveolae independent uptake. After endocytosis, the CPP and its cargo must then escape the endosomes to reach cytosol. Direct translocation may also occur, and various model have been suggested: formation of inverted micelles, pore formation, and the carpet model, in which the peptide accumulates at the membrane and induces its disruption above a concentration threshold. Several parameters may impact the efficiency and mechanism of internalization of CPP, among which the nature of the peptide itself (sequence, structure, charge,etc), the nature and size of the cargo, the incubation conditions (concentration, temperature), or the cell type [96, 102, 103]. Due to this variability, determination of the exact mechanism of internalization is sometimes difficult or even controversial, and it is likely that different pathways coexist, even for the same CPP, depending on the experi-

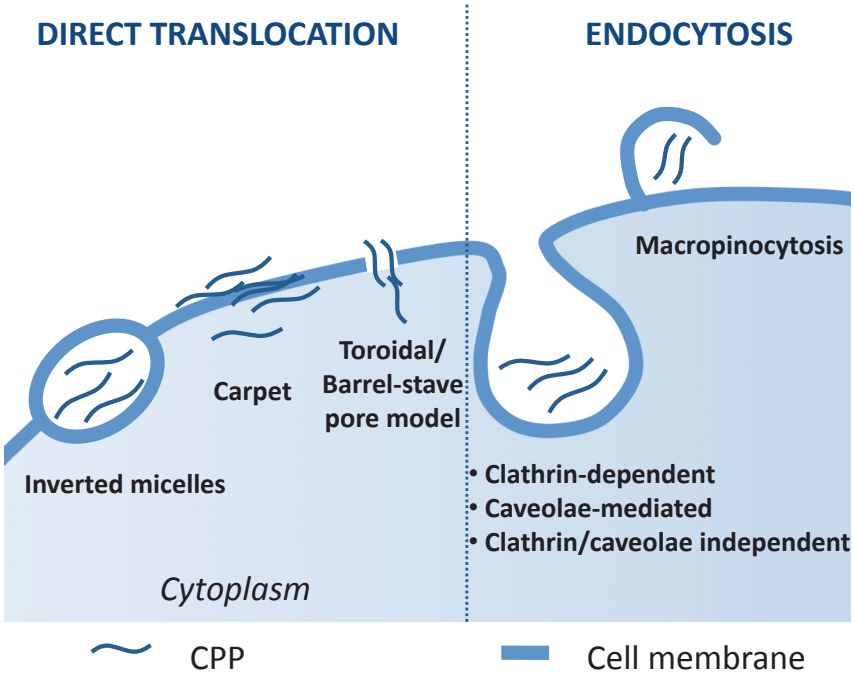

Figure 1.1: Mechanisms for the internalization of Cell-Penetrating Peptides. Inspired by reference [102]

mental conditions. Nevertheless, understanding which parameters are important to favour one pathway or another is potentially important for predicting the uptake and delivery efficiency of a CPP. Biophysical, chemical and biological approaches have thus been developed to address these questions.

1.1.2 Methods for studying the internalization mechanisms

Large and Giant Unilamellar Vesicles (LUVs and GUVs, respectively) are often used as models for cell membrane to study direct translocation of CPP. They enable fine tuning of experimental parameters (lipid composition, temperature, pH, concentration, etc) as well as the use of physico-chemical methods that would be difficult to set up or interpret in living cells (fluorescence spectroscopy, isothermal titration calorimetry, NMR, etc) [104–108]. Such studies showed for instance the importance of membrane fluidity and of the electrostatic interactions of arginine-rich CPPs with anionic lipids for internalization [109].

Mechanisms and efficiency of internalization inside cells have also been intensively investigated for the past decades. One of the most popular techniques to study the CPP distribution is fluorescence microscopy. Although powerful, possible artefacts should be kept in mind when using this tool. For instance, it was shown in the early 2000s that cell fixation could cause redistribution of CPP from endosomes to the cytoplasm and nucleus, thus questioning previous studies [110, 111]. Quantification from fluorescence images is also difficult, as highly cationic CPP tend to adsorb on the plastic or glass slides, and, more importantly, remains bound to cell membrane even after washings. Quantifica-

tion of the internalized peptide thus require to remove the signal of the non-internalized, membrane-bound peptide, for instance using trypsin digestion or chemical methods (e.g. quenching by dithionite of non-internalized CPP labelled with nitrobenzofurazan (NBD) fluorophore) [112]. Finally, fluorescence emission of a given fluorophore may (strongly) depend on its local environment. In fact, a recent study by our laboratory showed that CPPs labelled with common fluorophores (rhodamin and fluorescein) (Lavielle *et al.* , submitted) could remain unseen by fluorescence microscopy in the areas the most concentrated in peptide, because of fluorescence quenching. An elegant dilution protocol of the labelled peptide with "cold" acetylated peptide enabled them to unravel the "hidden" areas where the peptide was the most concentrated. Non-quenching fluorophores such as NBD could be likely to circumvent this problem.

1.1.3 Methods for quantifying the internalization efficiency

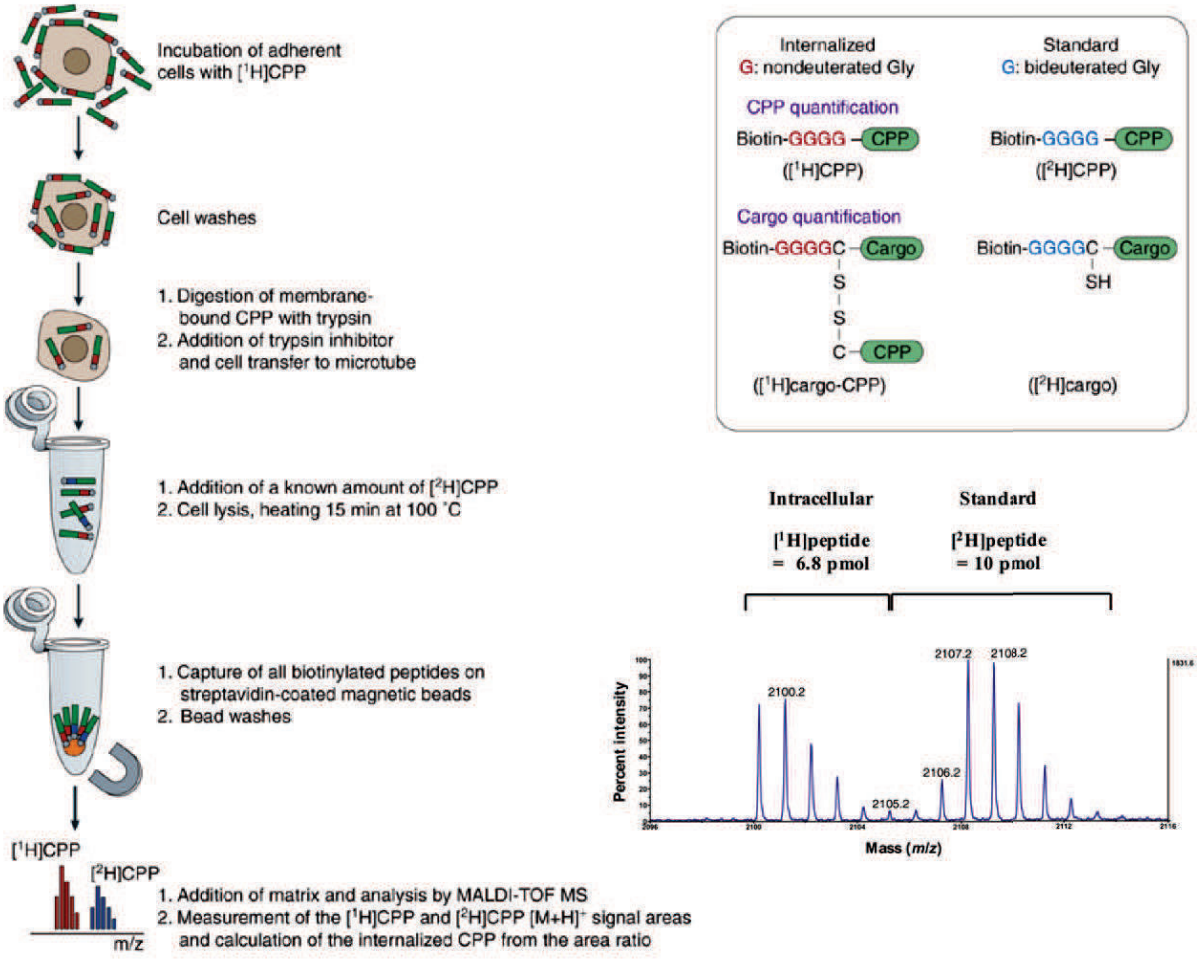

Figure 1.2: Protocol for the quantification of internalization of CPP and CPP-Cargo constructions using MALDI-TOF mass spectrometry. Adapted by permission from Macmillan Publishers Ltd: Nature Protocols (reference [113]), copyright (2006).

A method based on mass spectrometry was previously designed in our laboratory [113]

in order to reliably quantify cell internalization of CPPs (Figure 1.2). Quantification by MALDI-TOF MS relies on the use of an isotope-labelled internal standard having the same sequence as the peptide of interest. To do so, a tag made of either four non-deuterated glycine for the analyte or four bi-deuterated glycines for the internal standard was appended to the peptide sequence. Moreover, both peptides were biotinylated to allow extraction from cell lysate and isolation steps using streptavidin-coated magnetic beads. The internal standard, having the same sequence as the peptide of interest, will be recovered with the same efficiency and give the same intensity response during MALDI-TOF analysis, but with distinguishable spectra ($\delta m/z = 8$). In this protocol, the analyte (non-deuterated [^{1}H]CPP) is incubated on adherent cells, and the excess of peptide is washed after incubation. Membrane-bound peptide was removed by a trypsin digestion step of the membrane-bound peptide (trypsin may be replaced by an other protease, if more appropriate). Cells are then transferred in a microtube, and a known amount of the internal standard ([^{2}H]CPP) is added. After cell lysis, both peptides are captured on streptavidin-coated magnetic beads and undergo several washing steps. Finally, the sample is analyzed by MALDI-TOF MS, the ratio of [M+H] signal areas of both peptides measured, and the quantity of internalized [^{1}H]CPP calculated from this ratio.

Although this method allows to accurately and robustly quantify the global amount of internalized peptide, it does not allow to distinguish between cell compartments. This information on localization can be obtained through fluorescence imaging. However, as described above, self-quenching of some fluorescent probes may lead to misinterpretations on peptide location, and generally speaking, fluorescence dependance on environment results in the impossibility reliably quantify the amount of peptide in a given area. On the other hand, the intensity and area of CO elongation signal from $M(CO)_n$ do not strongly depend on the environment of the molecule. These infrared signals can thus be used for quantification purposes. We wanted to use the bimodality of SCoMPIs in order to detect CPP by fluorescence microscopy (for higher spatial resolution) and by infrared (for quantification).

In this chapter, we will first focus on the effect of environment on the luminescence properties of two SCoMPIs. We designed and synthesized two SCoMPI suitable for *N*-terminal labelling of peptides, and labelled two arginine-rich peptides with them. We studied the spectroscopic properties of the SCoMPI-labelled peptides in solution and in presence of lipid model membranes, to see if self-quenching could occur for these SCoMPIs when locally accumulated.

Besides, our group recently published correlative imaging of SCoMPI-labelled nona-arginine peptide in skin samples [1]. Complementary experiments on keratinocytes highlighted an inhomogeneous fluorescence among cells. Nucleus staining with DAPI then hinted a possible correlation between internalization of the labelled peptide and cell cycle. In a preliminary work, we thus looked at internalization of SCoMPI-labelled CPP depending on the cell division cycle by fluorescence microscopy.

1.2 Luminescence study of SCoMPI-labelled CPPs.

1.2.1 Design and synthesis of Re(I) tricarbonyl derivatives for *N*-terminal labelling of peptides

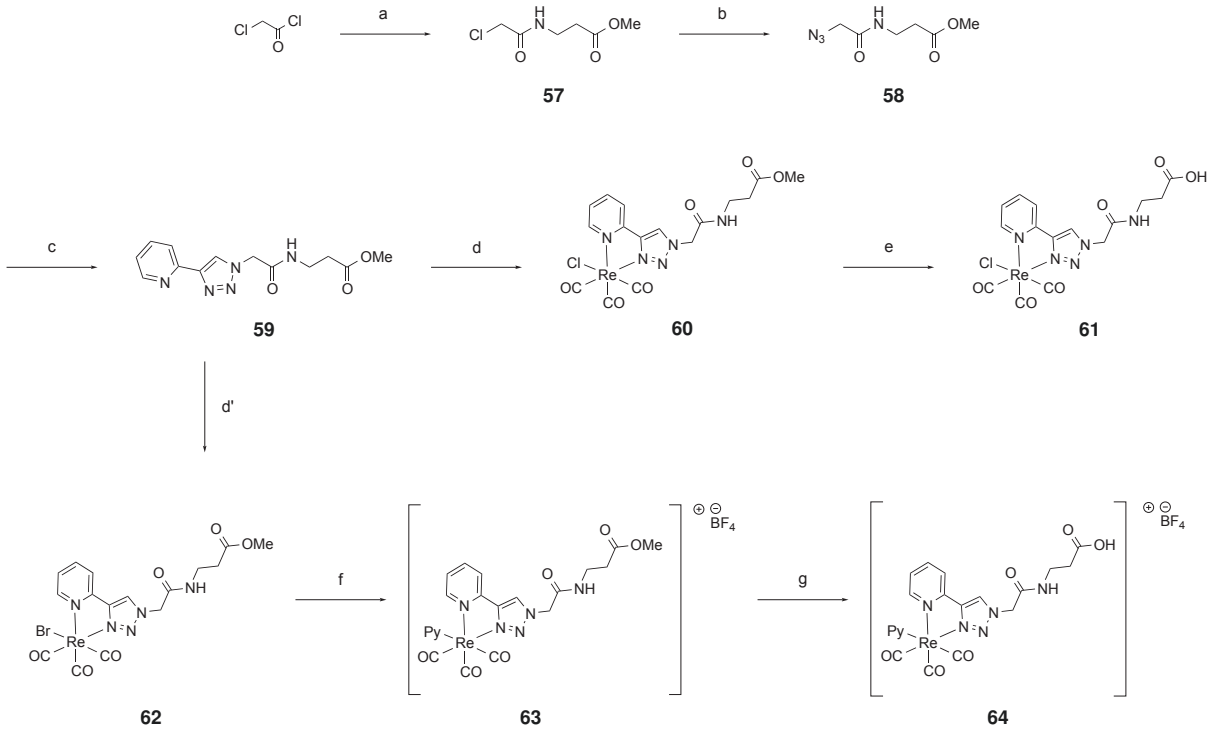

Scheme 1.1: Synthesis of the SCoMPI derivatives for *N*-terminal labelling of peptides. Reaction conditions: (a) β-alanine methyl ester hydrochloride salt, DIEA, dry DCM, 1h, 0 °C to RT, 66%, (b) NaN_3, NaI, acetone:water (3:1 v:v), 16h, 35 °C, 79%, (c) 2-ethynylpyridine, $CuSO_4$, sodium ascorbate, acetone:water (2:1 v:v), 2h, RT, 70%, (d) $Re(CO)_5Cl$, toluene, 6h, reflux, 100%, (d') $Re(CO)_5Br$, toluene, 6h, reflux, 100%, (e) $LiOH \cdot H_2O$, THF:water (2:1 v:v), 45 min, RT, 80%, (f) $AgBF_4$, acetonitrile, 5h, reflux, Ar; pyridine, THF, 20h, reflux, 79%, (g) $LiOH \cdot H_2O$, THF:water (2:1 v:v), 1h, RT, 87 %.

Modifying the rhenium coordination sphere may have an impact on its spectroscopic properties. Our group recently investigated the effects of structural modifications of the bidentate ligand on the luminescence properties of Re(I) tricarbonyl complexes [33]. Here we focused on the effect of the monodentate ancillary ligand (chloride or pyridine) on the spectroscopic and physico-chemical properties of the SCoMPI. Luminescent rhenium tricarbonyl complexes have initially been developed with 2,2'-bipyridine derivatives, and several of these polypyridine complexes, bearing either a halide or a pyridine derivative as monodentate ancillary ligand, have been designed for the labelling of biomolecules and for bioimaging [8]. In addition, luminescent Re(I) complexes presenting other polyaza-heterocyclic ligands have also been developed. 4-(2-pyridyl)-1,2,3-triazole (Pyta) derivatives have raised particular interest due to their ease of synthesis and functionalisation [32, 37, 88, 114–116]. $[Re(CO)_3(Pyta)(L)]^{n+}$ complexes for biomolecule labelling have been widely developed with a halide ligand [1, 32, 37, 88, 114, 115] (L= Cl, Br; n=0), but ex-

amples of such complexes with pyridine (L = Py; n=1) are also described [116]. We thus designed two Re(I) tricarbonyl probes incorporating a Pyta ligand suitable for grafting to the *N*-terminus of peptides, and bearing either a chloride or pyridine as monodentate ligand. The halide ligands are potentially more readily exchanged than the pyridine; besides, it should be noted that the positive charge of the $[Re(CO)_3(Pyta)(Py)]^+$ complex may have an impact on the properties of the probe, including interactions with membranes.

The methyl ester protected 4-(2-pyridyl)-1*H*-1,2,3-triazole ligand (Pyta-COOMe) was easily obtained in three steps and in good yield starting from β-alanine methyl ester (Scheme 1.1). Reaction of chloroacetyl chloride with β-alanine methyl ester hydrochloride salt in dry DCM led to the chloride derivative **57**. The nucleophilic substitution of the chloride by an azido group was then performed with sodium azide in presence of sodium iodide in a acetone:water (2:1 v:v) mixture. The resulting azide derivative (**58**) was finally reacted with 2-ethynylpyridine according to standard CuAAC procedures to lead to the Pyta ligand (**59**). The ligand was then refluxed in toluene in presence of the rhenium precursor $Re(CO)_5X$ (X = Cl, Br), leading to the formation and precipitation of $[Re(CO)_3(X)(PytaCOOMe)]$ complexes (X = Cl, Br).

The chloride derivative (**60**) was then saponified by lithium hydroxide in a mixture of THF and water (2:1 v:v) to obtain **61**. Although exchange of the chloride ligand with carboxylates has been described for rhenium tricarbonyl chloride complexes [117], in our hands this undesired exchange did not occur during saponification. This might be due to different experimental conditions (temperature, base, reaction time).

For the Re(I) bromide complex, on the other hand, ligand exchange was performed using the methyl ester form of the complex (**63**). This bromide derivative of the complex (**62**) was refluxed in acetonitrile in presence of silver tetrafluoroborate, then in THF in presence of an excess of pyridine, to obtain the ester form of the rhenium tricarbonyl pyridine complex (**63**) in good yields. Saponification was then performed on the complex to obtain compound **64**. In both synthetic pathways, the complexes were obtained as a racemic mixture of *fac* isomers.

Due to the harshness of conditions of peptide cleavage from the resin (HF cleavage), labelling of R9 and R6W3 with the rhenium complexes could not be realized on solid support and was rather performed in solution. To do so, the complex was first activated either with EDC or with DCC/NHS, then reacted with the desired peptide. The reaction mixture was then directly purified by HPLC. Particular attention should be paid to the chloride derivative, as we could observe in some cases chloride exchange under HPLC conditions involving 0.1% of trifluoroacetic acid (data not shown). In order to avoid this exchange, the labelled peptide solutions were freeze-dried immediately after purification. Structures of the studied peptides are summarized in Scheme 1.2.

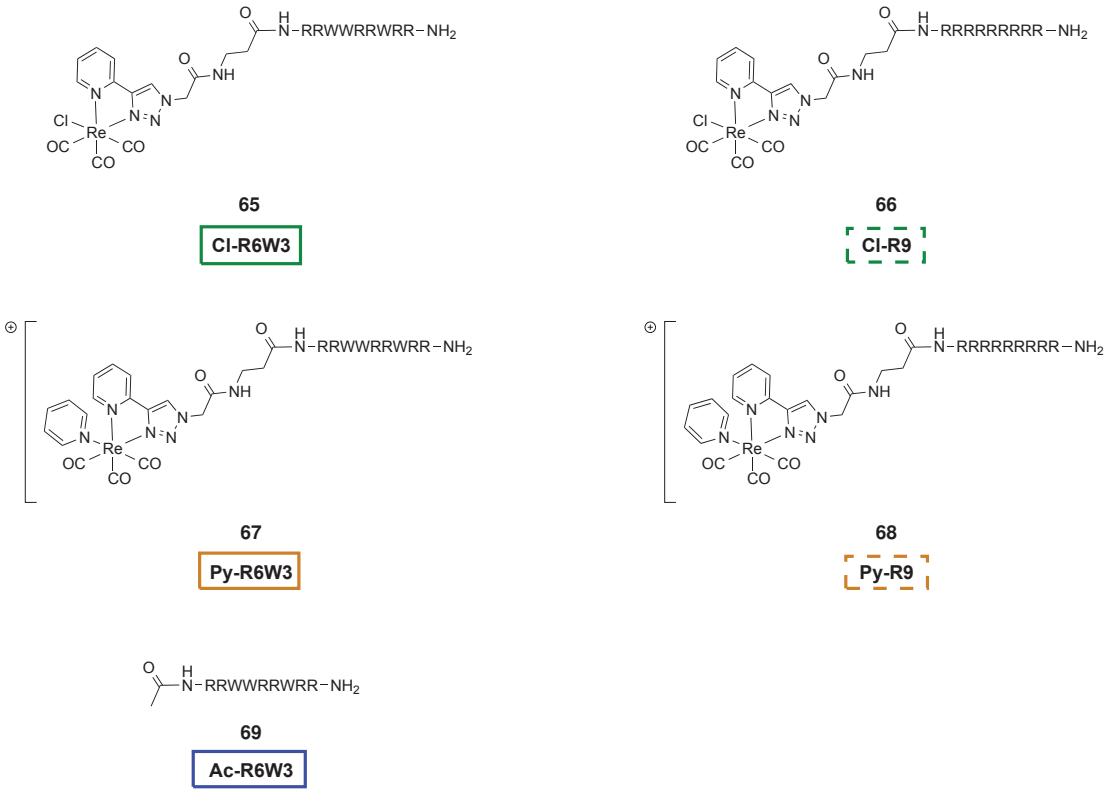

Scheme 1.2: Structure of the SCoMPI-labelled and acetylated CPPs.

1.2.2 Spectroscopic properties of the SCoMPIs in solution

Table 1.1: Spectroscopic properties of $[Re(CO)_3(X)(PytaCOOMe)]$ complexes

	$\epsilon_0^{350}(M^{-1} \cdot cm^{-1})$	$\lambda_{em}^{ex350}(nm)$	$\Phi^a(\%)$
X = Cl (**60**)	1.8×10^3	550	0.044 ± 0.004
X = Py (**63**)	2.0×10^3	495	0.96 ± 0.05

[a] Quantum yields were measured in water containing 2% DMSO by N. Delsuc.

We first focused on the spectroscopic properties of the free Re(I) probes in solution. We recorded the absorption and emission spectra of 10 µM solutions of the methyl ester form of both rhenium complexes in water containing 2% DMSO. Absorption spectra of both complexes showed a shoulder around 335 nm with typical MLCT features. Excitation of the MLCT band at 350 nm led to a broad emission band centered around 550 nm or 495 nm for chloride (**60**) and pyridine (**63**) derivatives, respectively. Moreover, emission intensity was much higher in the case of the pyridine derivative than in the case of the chloride derivative. Indeed, the pyridine derivative presents a higher quantum yield in solution (Table 1.1).

1.2.3 Spectroscopic properties of the labelled peptides in solution

We then studied the properties of the rhenium complexes grafted to peptides R9 and R6W3 (Figure 1.3). Upon excitation at 350 nm, the labelled peptides display trends similar to the cor-

responding probes: the position λ_{max} of maximal intensity is unchanged, and the peptides labelled with the rhenium tricarbonyl pyridine complex display higher emission intensities than those labelled with the chloride derivative. However, the labelled R6W3 peptides exhibited weaker emission intensities than their R9 counterparts. This is particularly true when the probe is the rhenium pyridine complex: emission intensity of Py-R9 is about four times higher than that of Py-R6W3 (Figure 1.3 and Table 1.2). These results may be attributed to luminescence quenching through Photoinduced Electron Transfer (PET) between the SCoMPI and tryptophan(s) of R6W3 peptide [118]. In the literature, intramolecular photooxidation of tryptophan by a rhenium tricarbonyl complex has been reported, and resulted in a decrease of luminescence of the complex [119]. The fact that the rhenium pyridine complex is more sensitive to PET than the rhenium chloride one might be due to various factors, such as oxidation potential of the complex, charge, and aromatic surface.

Table 1.2: Spectroscopic properties of SCoMPI-labelled peptides

	$\epsilon_0^{350}(\mathrm{M}^{-1}\cdot\mathrm{cm}^{-1})$	$\lambda_{em}^{ex350}(\mathrm{nm})$	$\Phi^a(\%)$
Cl-R9 (**66**)	1.8×10^3	550	0.17 ± 0.02
Cl-R6W3 (**65**)	1.8×10^3	550	0.13 ± 0.01
Py-R9 (**68**)	2.0×10^3	495	0.69 ± 0.05
Py-R6W3 (**67**)	2.0×10^3	495	0.14 ± 0.02

[a] Quantum yields were measured in HEPES buffer (100 mM, pH = 7.4) by N. Delsuc.

We also examined the spectroscopic features of the labelled and acetylated R6W3 peptides upon excitation at 280 nm, which is the excitation wavelength of tryptophan. As expected, Ac-R6W3 displays a broad emission band at 355 nm. Both Py-R6W3 and Cl-R6W3 also present this band, but with a much weaker intensity. As emission of tryptophan matches the MLCT band of the rhenium complexes, this decrease might be due to some energy transfer to the rhenium label.

1.2.4 Spectroscopic properties of the labelled peptide in presence of model membranes

Models for fluorescence evolution in presence of lipid vesicles

Fluorescence spectroscopy is widely used to study interactions of cell-penetrating peptides with lipid membranes. When tryptophan is present in the peptide sequence, its fluorescence is often used to characterize the interaction of the peptide with the membrane. For instance, use of membrane-impermeant quenchers (e.g. iodide or acrylamide) or membrane-located quenchers (e.g. lipids brominated at given positions) of tryptophan fluorescence enable the quantification of internalized peptide or the characterization of peptide insertion in the membrane. Shifts of λ_{max} also give information on the environment of tryptophan. Finally, well-established models exist to estimate the apparent partition coefficient K_p of

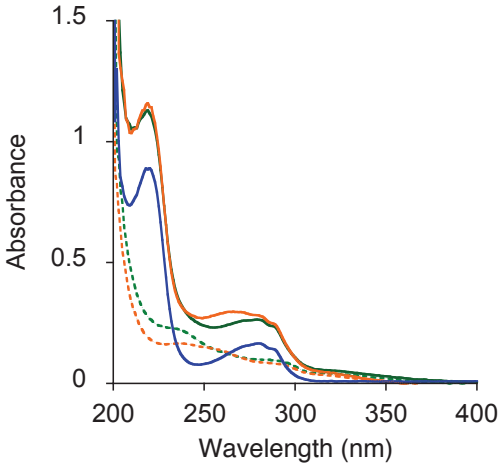

(a) Absorption spectra

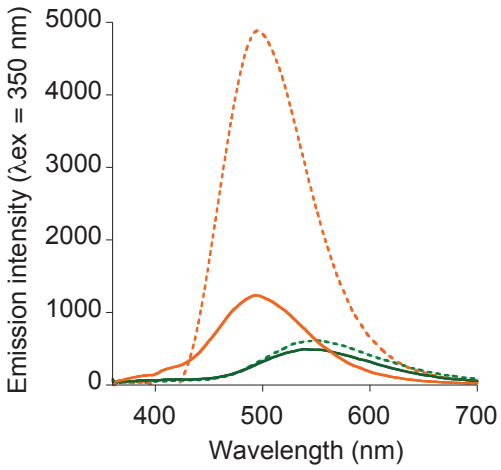

(b) Emission spectra for excitation at 350 nm (emission and excitation slits = 5 nm)

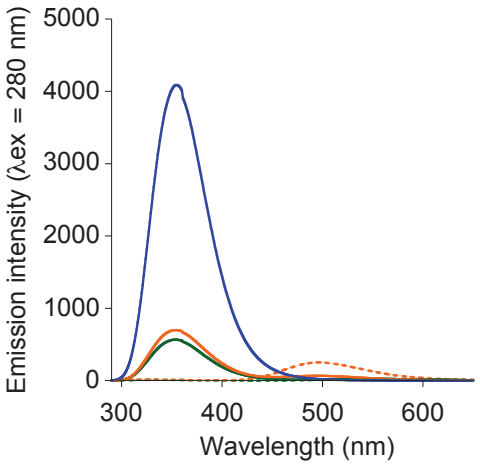

(c) Emission spectra for excitation at 280 nm (emission and excitation slits = 5 nm)

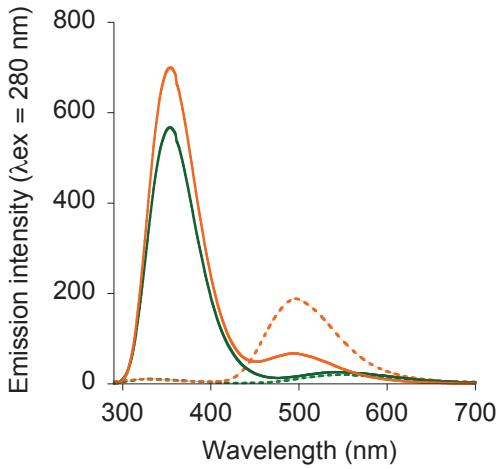

(d) Emission spectra of labelled peptides only for excitation at 280nm (see (c))

Figure 1.3: Spectroscopic properties of the labelled and control peptides
(10 µM peptide solutions in PBS buffer pH = 7.2, 25 °C. Spectra of Ac-R6W3 (plain, blue), Cl-R6W3 (plain, green), Py-R6W3 (plain, orange), Cl-R9 (dashed, green) and Py-R9 (dashed, orange).

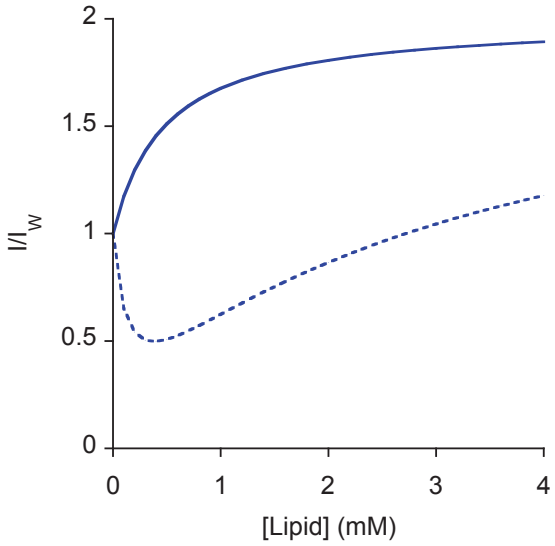

Figure 1.4: Representations of fluorescence evolution with lipid concentration for simple partition model (full) and self-quenching model (dotted).

the peptide between lipid membrane and water from fluorescence titration curves of the peptide with lipid vesicles [106, 120, 121].

Although these models were initially developed for experiments involving tryptophan fluorescence, they can obviously be used for other fluorophores. Indeed, Lavielle *et al.* (submitted) recently used this methodology to study the behaviour of common fluorophores (rhodamin and fluorescein) when accumulated in membranes. They titrated solution of a fluorophore-labelled well-known CPPs (Penetratin, Tat and R9) with increasing amount of lipid vesicles. They showed that at high peptide:lipid ratios, fluorescence dropped dramatically due to interaction between fluorophores.

Stimulated by these results, we investigated the behaviour of SCoMPIs when locally accumulated in membranes. We wanted to determine wether such fluorescence quenching was also observed for our Re-centered complexes grafted onto CPPs. We titrated solutions of these labelled peptides with Large Unilamellar Vesicles (LUV) of DOPG (1,2-Dioleoyl-*sn*-glycero-3-phosho-*rac*-(1-glycerol)), a negatively charged lipid, and studied the evolution of SCoMPI luminescence.

Besides, we were also interested in the impact of the SCoMPI probes (hydrophobicity, charge,...) on the interaction of the peptide with membranes. We thus examined the fluorescence of tryptophans for SCoMPI-labelled R_6W_3 in presence of LUV, and compared it to the unlabelled Ac−R_6W_3. We could estimate partition coefficients for labelled and unlabelled peptides.

In our case, titration curves could be fitted using either simple partition model or self-quenching model (Figure 1.4). In the simple partition model, evolution of emission

intensity can be described by equation (1.1)

$$\frac{I}{I_W} = \frac{1 + K_p \gamma_L \frac{I_L}{I_W}[L]}{1 + K_p \gamma_L [L]} \tag{1.1}$$

where I is the emission intensity, I_W the emission intensity in aqueous solution, I_L the emission intensity of the probe in the lipid phase, γ_L the molar volume of lipid and [L] the concentration of lipids in the sample. In the case of DOPG, we took γ_L=0.7572 L $\cdot$ mol^{-1}, calculated from literature [122].

However, at low lipid/peptide ratios, self-quenching of the fluorophore may occur, resulting in a decrease of emission intensity at low lipid concentrations, followed by increase at higher lipid concentration. In this case, emission intensity is better described by equation (1.2).

$$\frac{I}{I_W} = \frac{1 + K_p \gamma_L \frac{I_L}{I_W}[L]}{1 + K_p \gamma_L [L] + k_2 K_p \gamma_L} + \frac{1}{1 + K_p \gamma_L [L]} \tag{1.2}$$

with

$$k_2 = \frac{k_q}{k_f} \frac{1}{\epsilon l}$$

(k_q being the kinetic constant of quenching and k_f the radiative fluorescence constant).

Results

Tryptophan fluorescence is often used to sense the local environment of peptides and proteins and to study their interaction with model membranes [106]. To evaluate the effect of the probe on peptide interaction with membranes, we examined the evolution of tryptophan emission for three peptides (Cl-R6W3, Py-R6W3 and Ac-R6W3 as a control) in presence of various concentrations of DOPG vesicles. (Figure 1.5a)

The tryptophan emission maxima were blue-shifted for all peptides as the lipid concentration increased (from 355 to 335 nm). Insertion of tryptophan in a hydrophobic environment often results in such a blue shift [106, 121, 123]. At low lipid concentrations ($<$ 10 µM), the maximum emission intensity of Ac-R6W3 showed little (if any) decrease, and it increased at higher lipid concentrations (10–200 µM). On the contrary, for both Cl-R6W3 and Py-R6W3, typical self-quenching profiles could be observed: the tryptophan maximum emission intensity (at $\sim$ 350 nm) first decreased, then increased as the lipid/peptide ratio increased.

Fitting of the data with equation 1.2 allowed us to estimate the partition coefficient of the labelled and control peptides between the aqueous solution and the lipid membrane of the vesicles. The values obtained for Py-R6W3 ($K_P = 6.0 \pm 1.7 \times 10^4$) and Cl-R6W3 ($K_P = 4.4 \pm 1.1 \times 10^4$) were in the same order of magnitude as for Ac-R6W3 ($K_P = 4.0 \pm 1.2 \times 10^4$). The slight increase in K_P for peptides labelled with rhenium complexes may be attributed to the hydrophobicity of the rhenium complex. The additional positive

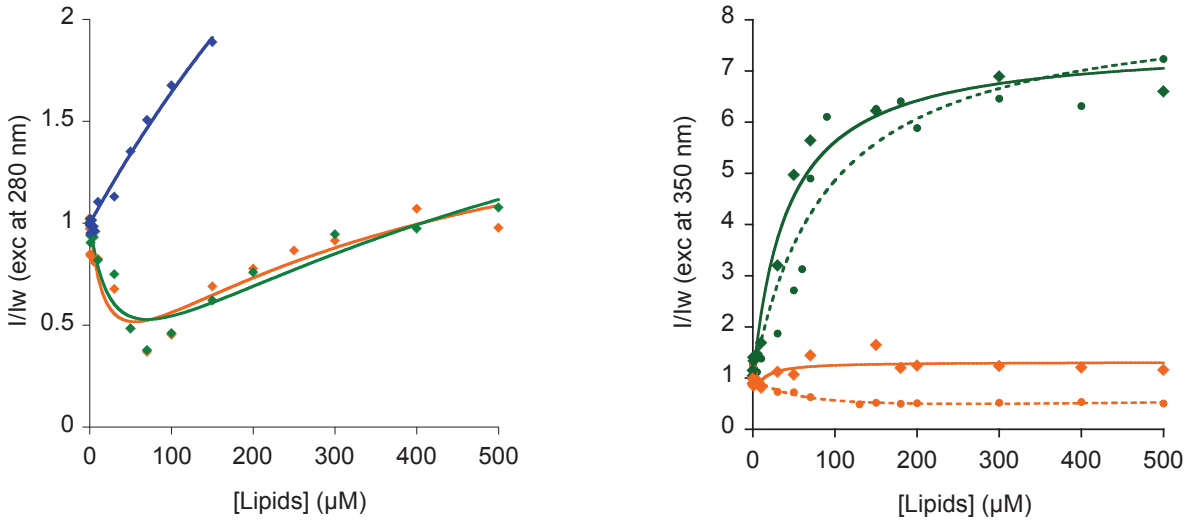

(a) Tryptophan fluorescence ($\lambda_{ex} = 280$ nm; $\lambda_{ex} \sim 350$ nm)

(b) SCoMPI luminescence ($\lambda_{ex} = 350$ nm; $\lambda_{em} \sim 550$ nm (Cl-R9 and Cl-R6W3) or $\lambda_{em} \sim 495$ nm (Py-R9 andPy-R6W3))

Figure 1.5: Evolution of maximum emission intensity of tryptophan and SCoMPIs with lipid concentration.
Titration curves of 1 µM peptide solutions by DOPG vesicles: Cl-R9 (green, circles, dotted line), Py-R9 (orange, circles, dotted line), Cl-R6W3 (green, diamonds, solid line), Py-R6W3 (orange, diamonds, solid line) and Ac-R6W3 (blue, diamonds, solid line)

charge of Py-R6W3 may also play a role, as DOPG is negatively charged. Qualitatively, the presence of the probe does not affect dramatically the interaction of the peptide with the membrane.

We also investigated the evolution of luminescence of the rhenium complexes ($\lambda_{exc} = 350$ nm; $\lambda_{em} \sim 550$ nm for $[Re(CO)_3(Pyta)(Cl)]$; $\lambda_{exc} \sim 495$ nm for $[Re(CO)_3(Pyta)(Py)]^+$) in presence of DOPG vesicles (Figure 1.5b). For both peptides labelled with the probe $[Re(CO)_3(Pyta)(Py)]^+$, maximum emission intensity showed only little or moderate variation and reached a plateau at high lipid/peptide ratios. On the other hand, the peptides labelled with $[Re(CO)_3(Pyta)(Cl)]$ derivative presented important luminescence enhancement at high lipid/peptide ratios (i.e. when most peptides are bound to the membrane). In both cases, emission intensity in lipid environment was more than five times higher than in aqueous solution, and even reached the intensity of luminescence of $[Re(CO)_3(Pyta)(Py)]^+$ observed in aqueous solution. Despite its lower quantum yield in aqueous solution, the chloride derivative is thus more likely to be detected in lipid environments like cell membrane, unlike what has been observed for most fluorophores. Moreover, estimation of K_p in the case of Cl-R6W3 ($K_P = 3.8 \pm 1.1 \times 10^4$) was consistent with the value obtained for tryptophan fluorescence, which validates the consistency of the model.

In model membranes, depending on the nature of the ancillary ligand, the behaviours of the probes are thus totally different. When the ligand is a pyridine, a very small vari-

ation in emission intensity was observed when bound to membranes. Contrarily, emission intensity of the rhenium tricarbonyl chloride derivatives increased remarkably (at least 5 times) when bound to membranes. Moreover, this increase was similar for both labelled peptides (R9 and R6W3).

1.2.5 Luminescence modulations in cells

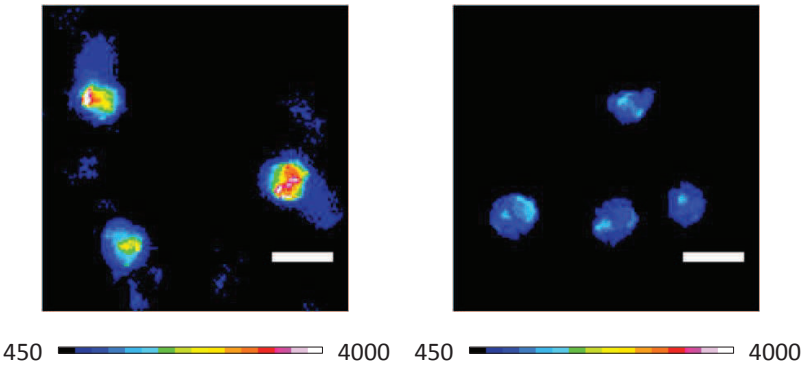

(a) CHO cells incubated with Cl-R9

(b) CHO cells incubated with Py-R9

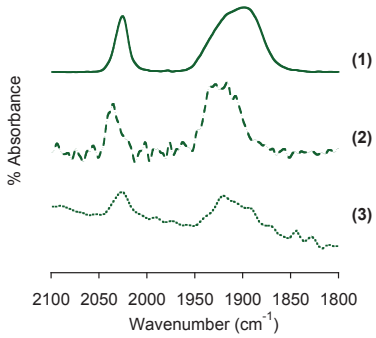

(c) Infrared signal of Cl-R9 in CHO cells

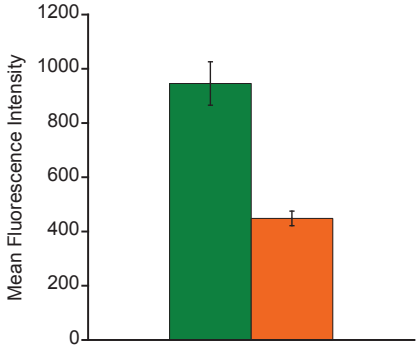

(d) Mean Fluorescence Intensity

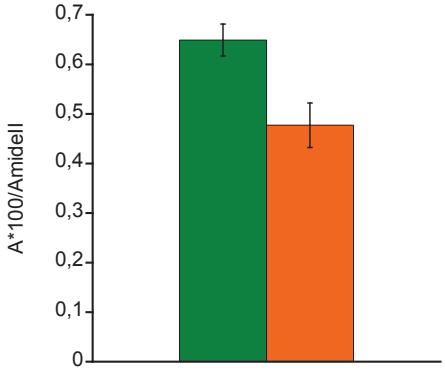

(e) Mean Infrared signal

Figure 1.6: Comparison of Fluorescence and Infrared Signals of CHO cells incubated with SCoMPI-labelled R9.

(a,b) CHO cells incubated for 1h at 37 °C with 10 µM Cl-R9 (a) or Py-R9 (b). Intensity scales were set identical for both images, and vary from black/blue (low intensity) to red/white (high intensity). Scale bars = 20 µm. (c) Infrared absorbance signal of SCoMPI: (1,2) FTIR spectrum of pure $[Re(CO)_3(Cl)(PytaCOOMe)]$ (**60**) (1, full line) and pure Cl-R9 (2, dashed); (3) FTIR-MS of CHO cells incubated with Cl-R9 (3, dots). A_1-band (2025 cm^{-1}) and E-band (1940 cm^{-1}).(d) Mean fluorescence intensities measured on regions of interest (ROI) for CHO cells incubated with Cl-R9 (green, n=47 ROI) or Py-R9 (orange, n=41 ROI). Error bars represent standard error of the mean. (e) Mean Area of A_1-band of SCoMPI for CHO cells incubated with Cl-R9 (green, n=33 spectra) or Py-R9 (orange, n=13 spectra). Error bars represent standard error of the mean.

We wanted to further confirm these results in the much more complex environment of cells. We thus incubated Chinese Hamster Ovarian (CHO) cells with SCoMPI-labelled

nona-arginine peptides Py-R9 or Cl-R9, and compared the fluorescence intensities displayed in both samples. We could observe heterogenous labelling of CHO cells in both cases. However, as can be seen from Figures 1.6a and 1.6b, luminescence observed for cells incubated with Py-R9 was much weaker than the one displayed by cells incubated with Cl-R9. Indeed, mean fluorescence intensity of Cl-R9 was approximately twice that of Py-R9 in cells (Figure 1.6d).

In order to verify that this difference was not due to differences in concentration, we then performed infrared measurements on the same samples. Unlike fluorescence intensity, infrared signals intensities of $Re(CO)_3$ are poorly sensitive to the environment [90]: position of a given infrared band may vary with different environments, but not its area. Infrared signals can thus be reliably used for quantification [90]: the mean area of a specific peak is proportional to the amount of the corresponding chemical function in the sample. The A_1-band was already used in previous studies for quantification purposes [71, 90], and we thus chose to integrate this band in order to compare the amounts of SCoMPI-labelled peptides in cells (Figure 1.6c). We recorded infrared spectra on each sample with a $50 \times 50\,\mu m^2$ resolution on the Nicolet In10 infrared microscope of SMIS beamline at SOLEIL synchrotron. Given this relatively low resolution, we could not record infrared spectra at the single cell level but integrated the signals of a given area comprising several cells. We thus normalized the measured areas of A_1-band by the area of Amide II: Amide II infrared band is due to proteins in cells, and its area is thus proportional to the amount of proteins, and thus to the number of cells.

We could observe that both the mean fluorescence and IR signals of SCoMPI were lower in the cells incubated with Py-R9 than in those incubated with Cl-R9 (Figure 1.6d,1.6e). The mean IR-signal of R9-Py was found to be approximately 75% of the IR-signal of Cl-R9. Amounts of the SCoMPI-labelled peptides are proportional to these signals, the amount of Py-R9 in cells will thus be $\sim 75\%$ of the amount of Cl-R9. However, the difference in fluorescence signals between both samples was more important than for IR signals: luminescence signal in cells incubated with Py-R9 was slightly lower than 50% of the signal for cells incubated with Cl-R9. This is consistent with the results obtained with vesicles: when locally accumulated, the luminescence of Py-R9 is moderately quenched whereas the luminescence of Cl-R9 is enhanced. The behaviour of both SCoMPIs highlighted by experiments on model membranes was thus confirmed in cells.

Although the SCoMPI bearing a chloride ligand was found to have a lower quantum yield in solution, it appeared to be a better choice than its pyridine counterpart for detection of peptides or other biomolecules in a membrane environment. However, the SCoMPI bearing a pyridine ligand can be of use for detection of biomolecules in cytosol, for instance.

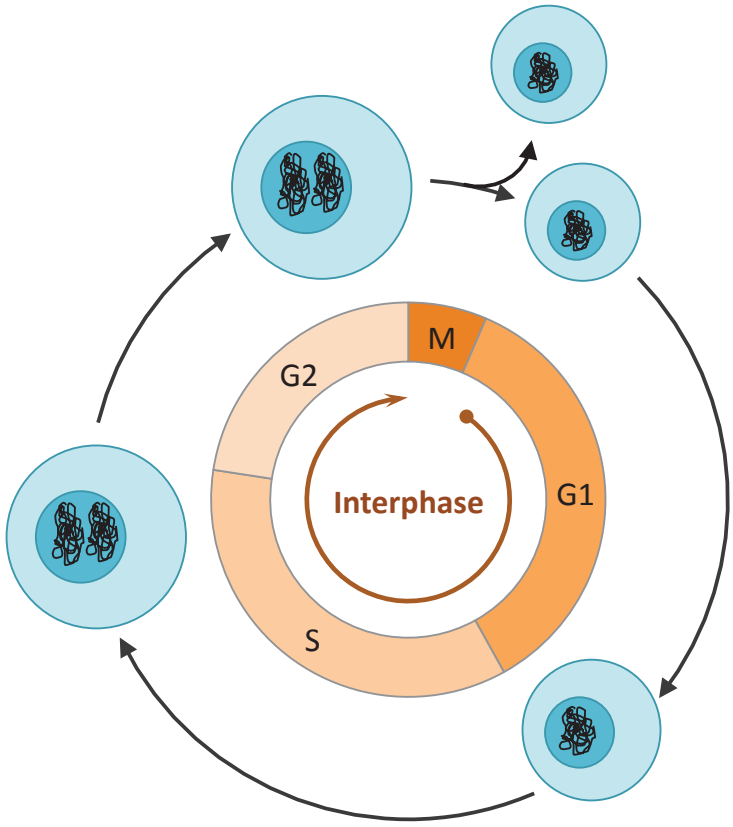

Figure 1.7: The phases of cell cycle.
Inspired by [124]. The cell cycle comprises four main phases: M (mitosis), G_1 (gap 1), S (synthesis) and G_2 (gap 2). DNA replication is performed during S phase, and cell division occrs during M phase. Cells grow during the interphase, which is the time between two cell division (i.e. between two M phases). The interphase thus includes G_1, S and G_2 phases.

1.3 CPP internalization and cell cycle

Our group recently studied the penetration of a Cl-R9 derivative in skin samples by fluorescence and infrared microscopies [1]. During complementary experiments on keratinocytes (HaCaT cells), the main cellular constituent of epidermis, it was observed that internalization was not homogenous among cells, and that this inhomogeneity might be related to cell-division cycle (S.Clède, unpublished data) (Figure 1.7). In order to test this hypothesis, we thus synchronized HaCaT cells by Fetal Bovine Serum (FBS) deprivation [125, 126], and investigated their ability to internalize the SCoMPI-labelled R9 at given times of the cell cycle. Serum deprivation was shown to arrest mammalian cells in a quiescent (G_0) phase. Re-implementing the medium in FBS induces the cells to re-enter synchronously the cell cycle. According to literature protocols, we thus deprived HaCaT cells from serum for three days, before allowing them to re-enter cell cycle at t = 0 h by re-implementing the culture medium with 10% FBS. At given timepoints (every two hours from t = 24 h to t = 32 h), cells were incubated at 37 °C for 1 h with a 10 µM solution of Cl-R9. For each timepoint, a control experiment with unsynchronized cells (FBS+) was performed. After washings and fixation, cells were then observed by fluorescence microscopy.

We could observe that in synchronized samples, only a few cells displayed luminescence due to Cl-R9, except at t = 28h. At this time, synchronized HaCaT displayed relatively homogenous and intense luminescence (Figure 1.9). On the contrary, unsynchronized (FBS+) samples displayed heterogenous luminescence at all times. For each sample, the mean fluorescence intensity on *all* observed cells was thus calculated (Figure 1.8a). For some reason, the unsynchronized control cells also displayed higher luminescence intensity at t = 28 h. In order to compare the mean fluorescence intensity of synchronized samples with their unsynchronized controls, we calculated the ratio of intensities of synchronized cells over unsynchronized cells at each time (Figure 1.8b). This confirmed the first observations: at 24h, luminescence of SCoMPI on synchronized cell population was lower than the one observed in the control population. The ratio increased until t = 28h, were it reached a maximum, and then decreased. No dramatical change could be seen in nuclei morphology by Hoechst staining. However, for samples from t = 26h to t = 30h, nuclei looked smaller, more concentrated and had non circular shapes. This might be a hint for mitosis, although further experiments are needed to confirm this assumption. Nevertheless, this experiment shows a clear time-dependence of internalization efficiency for synchronized cells, and thus a dependence of internalization with cell cycle. Besides, we used fluorescence microscopy to follow the internalization of Cl-R9 on synchronized HaCaT cells. As discussed in 1.2, fluorescence-based methods are not the most reliable for quantification, and further experiments taking advantage of infrared modality of SCoMPI would help consolidate these preliminary results.

In conclusion, we developed two SCoMPI suitable for N-terminal labelling and multi-

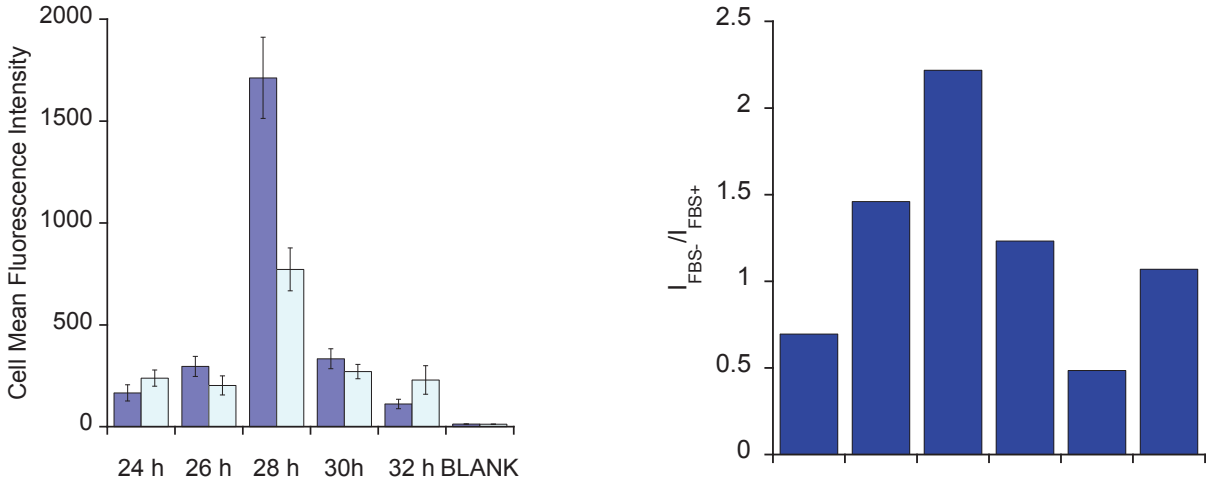

(a) Mean Fluorescence Intensity on HaCaT cells

(b) Fluorescence Intensity Ratio (FBS-/FBS+)

Figure 1.8: Internalization of Cl-R9 on synchronized or unsynchronized HaCaT cells. Mean fluorescence intensity on all cells was determined at given time points (a) for synchronized (dark blue) and unsynchronized (light blue cells). The ratio of intensity of synchronized sample (FBS-) over intensity of unsynchronized (FBS+) sample was then calculated (b).

modal imaging of peptides. We grafted them on two CPPs and studied the spectroscopic properties of the labelled peptides in solution as well as in model membranes and cells. Titration by DOPG vesicles revealed that despite encouraging spectroscopic properties in solution, the SCoMPI-Py derivative could be quenched in membranes. On the contrary, its SCoMPI-Cl counterpart displayed luminescence enhancement in presence of membranes. The same behaviour was found in cell experiments. The multimodality of the probe proved useful in this study, as comparison of SCoMPI quantities in cells was enabled by infrared imaging: this confirmed that the difference in fluorescence intensity between SCoMPI-Py and SCoMPI-Cl in cells could not be only attributed to differences in peptide concentrations, but was mainly due to fluorescence dependence on probe environment.

We could also perform preliminary experiments that confirmed a correlation between cell cycle of HaCaT cells and internalization of SCoMPI-labelled peptides. These encouraging results should be confirmed by further fluorescence and infrared imaging experiments. Moreover, it could be seen in 1.2 that inhomogenous internalization of SCoMPI-R9 could also be observed in CHO cells. Similar synchronization experiments can thus be envisioned for CHO cells.

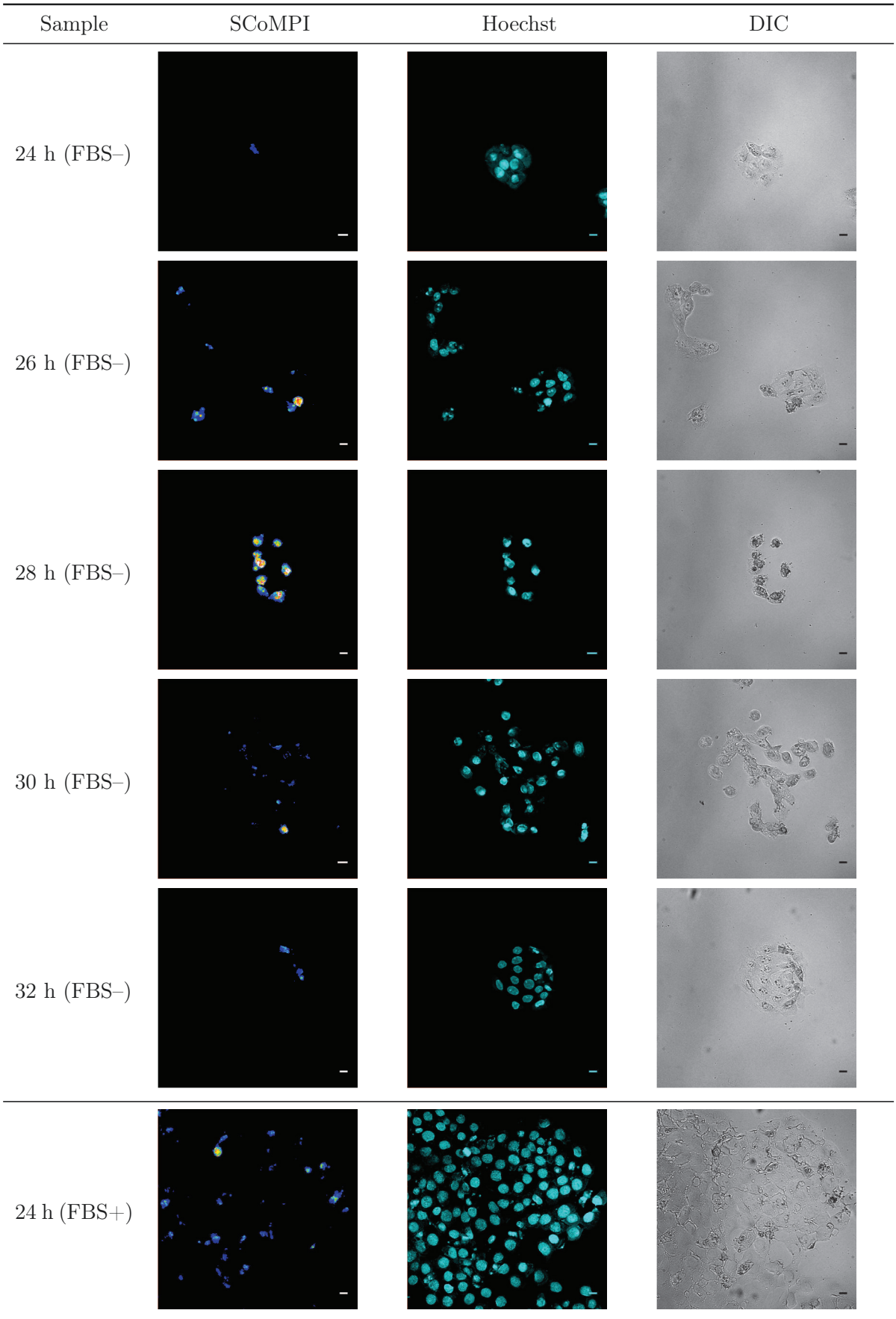

Figure 1.9: Fluorescence Imaging of Cl-R9 internalization in synchronized (FBS–) and unsynchronized (FBS+) HaCaT cells

Chapter 2

In vitro labelling of *Engrailed-2* Homeodomain

Having labelled and imaged peptides by infrared and fluorescence microscopies, we wanted to go further and we thus investigated the possibility to label proteins with SCoMPIs, and to image them inside cells. This is challenging, since proteins are usually found at low concentrations inside cells. A simple way to selectively modify a protein is to perform the labelling *in vitro* on the purified protein. Various reactive groups are available to modify amines (e.g. NHS esters), carboxylic acids (e.g. carbodiimide followed by addition of amine) or sulfhydryl groups (e.g. maleimide or iodoacetamide derivatives) that are present at the protein surface. Easy determination of the labelling efficiency is possible with *in vitro* labelling, as well as isolation of the labelled protein for physico-chemical studies. For a first attempt to label protein with SCoMPIs, we wanted to control the efficiency of labelling, as well as the photophysical properties of the labelled protein. We thus chose to use *in vitro* labelling strategy.

On the other hand, we also wanted to test the possibility to detect the SCoMPI-labelled protein in a cellular environment. We thus chose a protein that could be chemically labelled *in vitro*, and then internalized inside cells. Homeodomains were thus good candidates, as they can be produced and purified, labelled *in vitro*, and are internalized inside cells.

2.1 Homeoproteins and homeodomains

Homeoproteins (HP) form a family of transcription factors involved in several developmental processes, including tissue patterning, axon guidance and cell migration [129, 130]. They are widespread in eukaryotic organisms, and share a highly conserved sequence of 60 amino acids, called homeodomain. This homeodomain structures into three α-helices, among which the third one is essential for the DNA-binding properties of the homeoprotein (Figure 2.1).

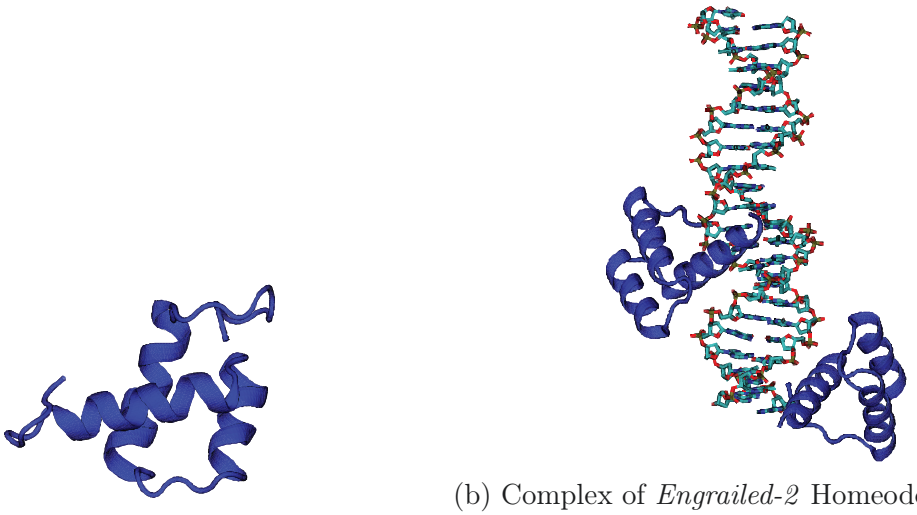

(a) *Engrailed-2* Homeodomain

(b) Complex of *Engrailed-2* Homeodomain with DNA

Figure 2.1: Structure of *Engrailed* Homeodomain on its own (3ZOB in PDB [127]) or in complex with DNA (3HDD in PDB [128])

It was observed in the early 1990s that the homeodomain of *Antennapedia* (a *Drosophilia* transcription factor) was able to cross membranes and to be internalized in various cell types through a non-endocytotic mechanism [131]. This finding came a few years after Frankel and Pabo observed that an other transcription factor, HIV protein Tat, could cross the plasma membrane and be internalized by cells [132]. Investigating the mechanisms of this unexpected internalization enabled the development of the Tat-derived (arginine-rich) and homeodomain-derived (amphipathic) families of Cell-Penetrating Peptides.

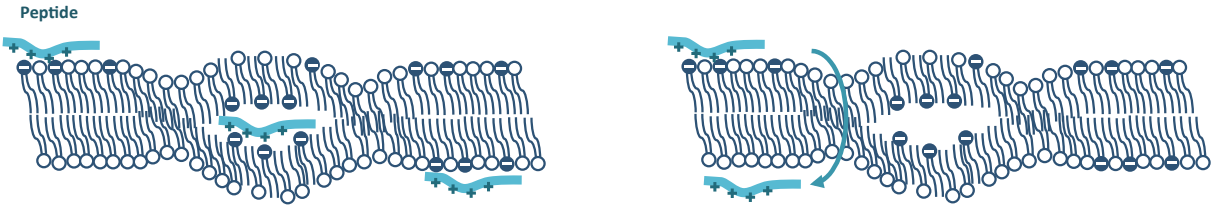

(a) (b)

Figure 2.2: Possible mechanisms for the translocation of Penetratin and Homeodomains. Inspired from references [104, 133].The positively-charged peptide interacts with negative charges on the membrane (sugars, lipids). W48 then induces the formation of inverted micelles [123, 134]. The peptide could then be internalized either inside inverted micelles (2.2a) or directly through the perturbed membrane (2.2b). A recent study seems to make model (a) more likely [104].

In the case of *Antennapedia*, site-directed mutagenesis experiments identified the third helix as essential for the homeodomain internalization [131, 135]. In particular, a 16-amino acids peptide, Penetratin, was shown to keep the translocating properties of its parent protein and was even able to deliver molecular cargos inside cell [100, 136–138]. Several physico-chemical and biophysical studies have been carried on this peptide and its mutants in order to better understand the translocation mechanism. It was shown that internalization depended neither on the presence of specific chiral receptor, nor on the α-helical

structure of the peptide [139, 140]. An internalization mechanism in two steps, based on various cell and model vesicle experiments, has been proposed for penetratin [129]. First, electrostatic interactions drive the binding of the positively charged peptide to the negative charges of the lipids and carbohydrates of the membrane [123,141,142]. Secondly, insertion of the highly conserved tryptophan W48 (also essential for internalization [139]) induces a transient destabilization of the membrane and, in some cases, the formation of inverted micelles [123,134], enabling the peptide to cross the membrane [104,129,133] (Figure 2.2). Although such extensive studies have not been made on full-length homeodomains, it can be assumed that at least part of the internalization model for penetratin is still relevant for homeodomains.

Besides, it was also shown that homeoproteins could travel from one cell to another. In a study by Joliot *et al.* [143], *Engrailed-2*, a homeoprotein involved in mid- and hindbrain patterning phenotype of mouse and chicken, was used as a model homeoprotein. It was expressed in COS7 cells co-cultured with E15 rat embryonic neurons. After incubation, fixation and immunostaining, *Engrailed-2* was found not only in COS-7 cells, but also in the cytoplasm and nucleus of surrounding neurons. The sequences responsible for nuclear addressing (Nuclear Localization Signal, NLS), nuclear export (Nuclear Export Signal, NES) and secretion (Secretion Signal, $\Delta 1$) were then identified on *Engrailed* by site-directed mutagenesis [129,133,143,144]. Interestingly, this sequence is also found within the homeodomain, spanning parts of its second and third helices as well as the β-turn between them. It can also be noted that this sequence is very similar to the leucine-rich nuclear export sequences of several transcription factors, and its removal also blocks nuclear export. In fact, a slightly larger sequence including the secretion signal was found to be a nuclear export sequence. Parallel studies on Knotted-1 (KN1), a plant homeoprotein, highlighted the importance of nuclear localization for secretion: removal of the NLS sequence of KN1 HD redistributed the protein to the cytoplasm, but blocked its secretion. Altogether, this suggests that homeoproteins are made fit for secretion within the nuclear compartment. Furthermore, secretion is sensitive to temperature, suggesting an energy-dependent mechanism: it was shown for instance that SecPen (a contruct including Penetratin sequence and the secretion sequence identified for *Engrailed*) is internalized at 4 °C and 37 °C, but that its secretion is blocked at 4 °C [145]. In addition, cell fractionation experiments showed that within COS7 cells, some *Engrailed-2* was associated with caveolae-like vesicles, rich in cholesterol and glycosphingolipids [146]. Homeoproteins thus seem to follow different mechanisms for entering and exiting cell. A general model for homeoprotein intercellular transport could be elaborated from these studies (Figure 2.3) [129, 133]. However, the exact mechanisms by which homeoproteins are secreted and internalized, as well as the role of homeoproteins in signal transduction, are still under investigation [129].

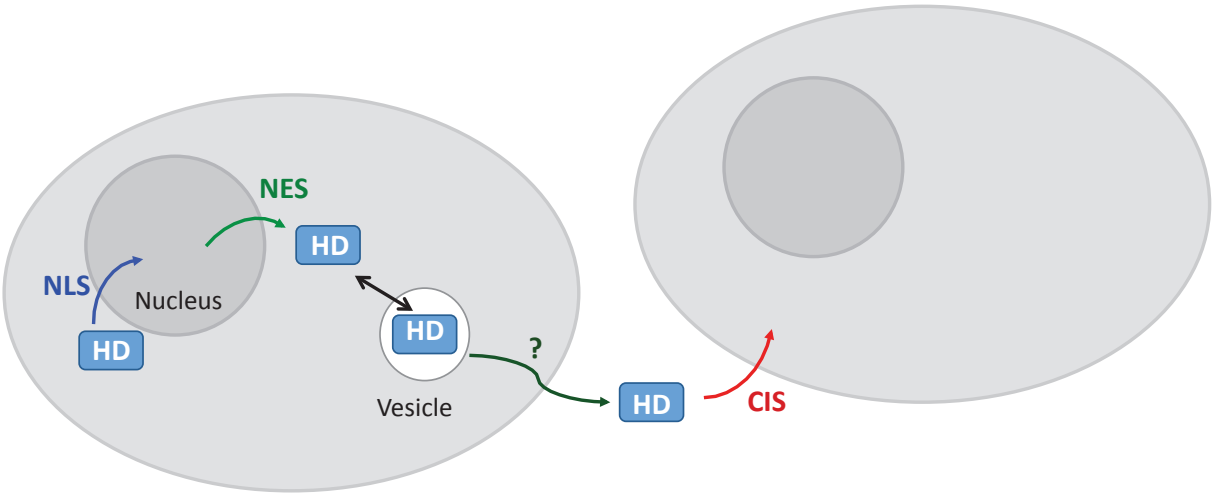

Figure 2.3: A model for the nuclear import, secretion and internalization of homeoproteins.

Adapted from [133].

2.2 Homeodomain production

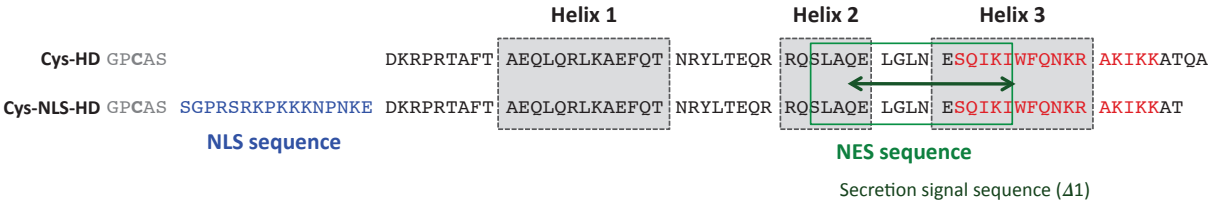

Figure 2.4: Sequences of *Engrailed-2* Cys-HD (top) and Cys-NLS-HD (bottom).
Five amino-acids (GPCAS, grey) do not belong to the sequence of the native HD. They include amino-acids that are part of the recognition site of PreScission enzyme (GP), and the non-native cystein (bold). The Nuclear Localization Signal (NLS) is represented in blue, the Cell Internalization Signal (CIS) in red. Nuclear Export Signal (NES) is framed in green. Grey frames represent the three helical domains of *Engrailed-2* HD. Domains were attributed according to PDB sequence analysis [127] and [129, 133]

As mentioned in the previous section, *Engrailed* homeodomain has been used as a model to study the secretion mechanism of homeodomains and homeoproteins. Indeed, some groups in our laboratory (in particular the groups of O. Lequin and S. Sagan) are investigating the uptake mechanism of *Engrailed* using biological, biophysical and structural approaches. Correlative imaging approaches using SCoMPIs could represent a new tool to address such questions. In the present study, two *Engrailed* homeodomain constructions were produced in collaboration with O. Lequin: the first one consisted of the homeodomain, the second presented an extended sequence comprising a suspected nuclear localization signal (NLS). *Engrailed* homeodomain sequence do not contain cystein. A single cystein was thus introduced at the *N*-terminus of both proteins in order to allow diverse protein labelling through thiol-maleimide coupling. Both constructions were designed and gracefully provided by the group of A. Joliot.

2.2.1 Plasmid construction

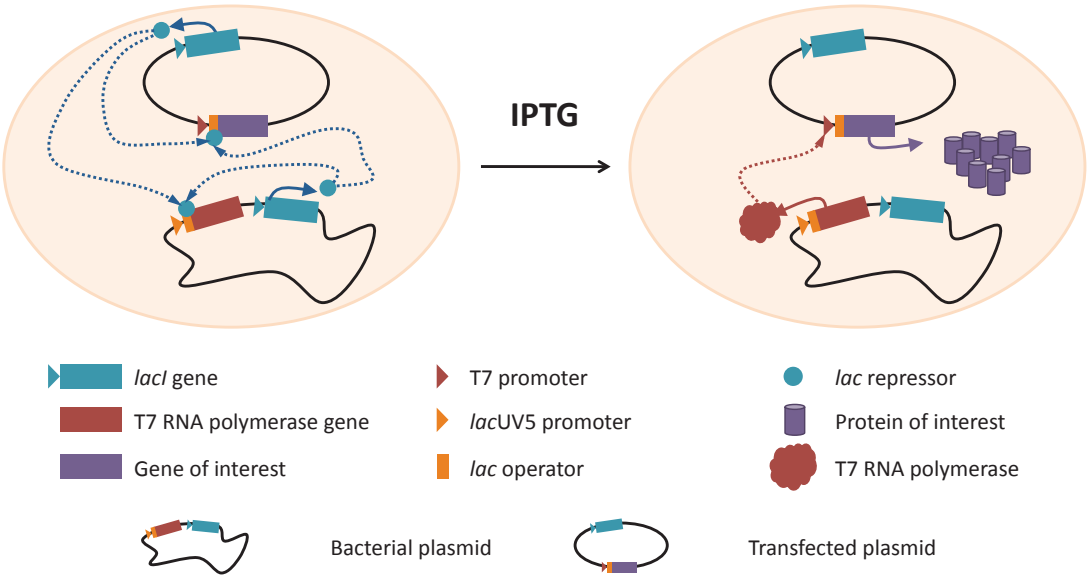

(a) Principle of expression system

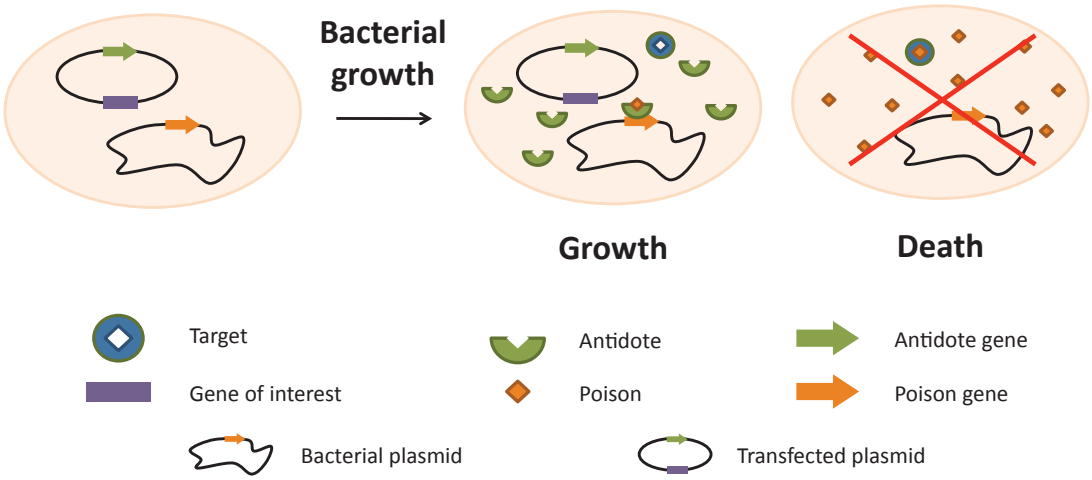

(b) Principle of stabilization system

Figure 2.5: Principle of the Cherry expression and stabilization systems (adapted from Cherry^{TM} Express kit manual).

The protein sequence was inserted in the pStaby2.1 plasmid of Cherry^{TM} Express kit. A hexahistidine tag and aCherry tag (heme binding part of a cytochrome) were fused at the *N*-terminus of the protein of interest (POI). The small, red Cherry tag allows direct visualization of the protein, especially during purification, and may enhance protein solubility.

Production of the protein is based on the very efficient T7 expression system, i.e. on T7 bacteriophage promoter/RNA polymerase pair (Figure 2.5b). T7 promoter is included in plasmid and controls expression of the protein sequence, whereas the gene of T7 RNA polymerase is inserted in the chromosome of the expressing bacteria, under the control

of *lacUV5* promoter, a variant of *lac* promoter. Under normal conditions, expression of T7 RNA polymerase is repressed by the binding of the *lac* repressor to the bacterial *lacO* operator sequence. *lac* repressor is encoded by the *lacI* gene, and two copies of this gene are present in the expression system to ensure maximal repression: one on the plasmid, and one on the bacteria chromosome. As T7 promoter is not recognized by *E. coli* RNA polymerase, expression of the POI is also repressed under normal conditions. After growth phase, adding isopropyl-β-D-thiogalactoside (IPTG) to the medium will thus induce the expression of T7 RNA polymerase and of the POI.

Finally, stabilization of the plasmid was achieved using a bacterial antidote/poison system based on *ccdA*/*ccdB* genes. The poison gene *ccdB* is introduced in the chromosome of the bacteria, whereas antidote gene*ccdA* is introduced in the plasmid (Figure 2.5a). In presence of the plasmid, the promoter for the poison gene is strongly repressed and the bacteria survives. If the bacteria loses the plasmid, the antidote protein is degraded, the promoter for *ccdB* is no longer repressed, and a toxin is produced and causes cell death. This improves the efficiency of the system, as only bacteria carrying the plasmid will be able to grow in the medium.

2.2.2 Protein expression and purification

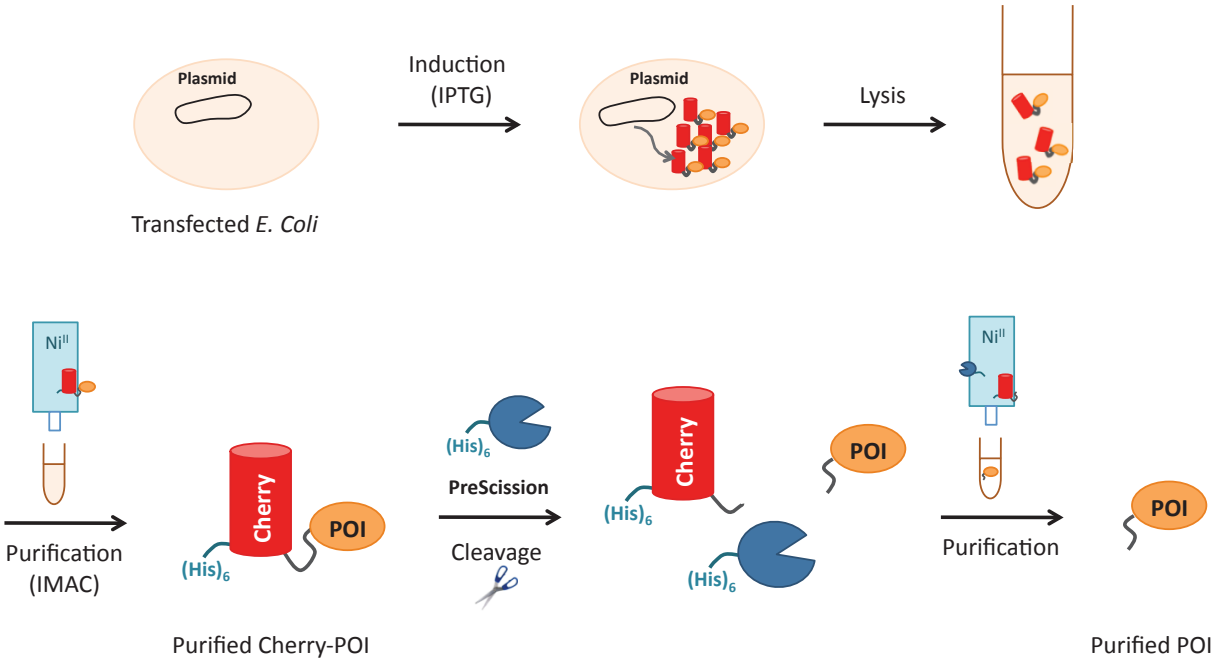

Figure 2.6: Principle of the production and purification of *Engrailed 2* HD and NLS-HD

His_6-Cherry-Cys-NLS-HD and His_6-Cherry-Cys-HD were expressed in BL21DE3 strain following standard procedures: after a growth phase, protein expression was induced by adding IPTG to the medium. Cells were then centrifuged and the pellet lysed. In both cases, the His_6-tagged fusion protein was purified by Immobilized Metal ion Affinity Chro-

matography (IMAC) using the affinity of the polyhistidine tag for Ni complex immobilized on Sepharose^{TM} beads. The resulting purified fusion protein was then cleaved by the enzyme PreScission Protease at a site introduced between His_6-Cherry and the homeodomain. As both PreScission Protease and Cherry bear an hexahistidine tag, elution of the mixture through the IMAC column retains PreScission, cleaved His_6-Cherry and the remaining uncleaved His_6-Cherry-Cys-HD or His_6-Cherry-Cys-NLS-HD, whereas the desired pure protein Cys-HD or Cys-NLS-HD is unretained. Further purification may be achieved by affinity purification on Heparin column. As mentioned earlier, the homeodomains possess a single cystein that will be used for their labelling with a SCoMPI.

2.3 Synthesis of SCoMPIs for thiol-maleimide labelling

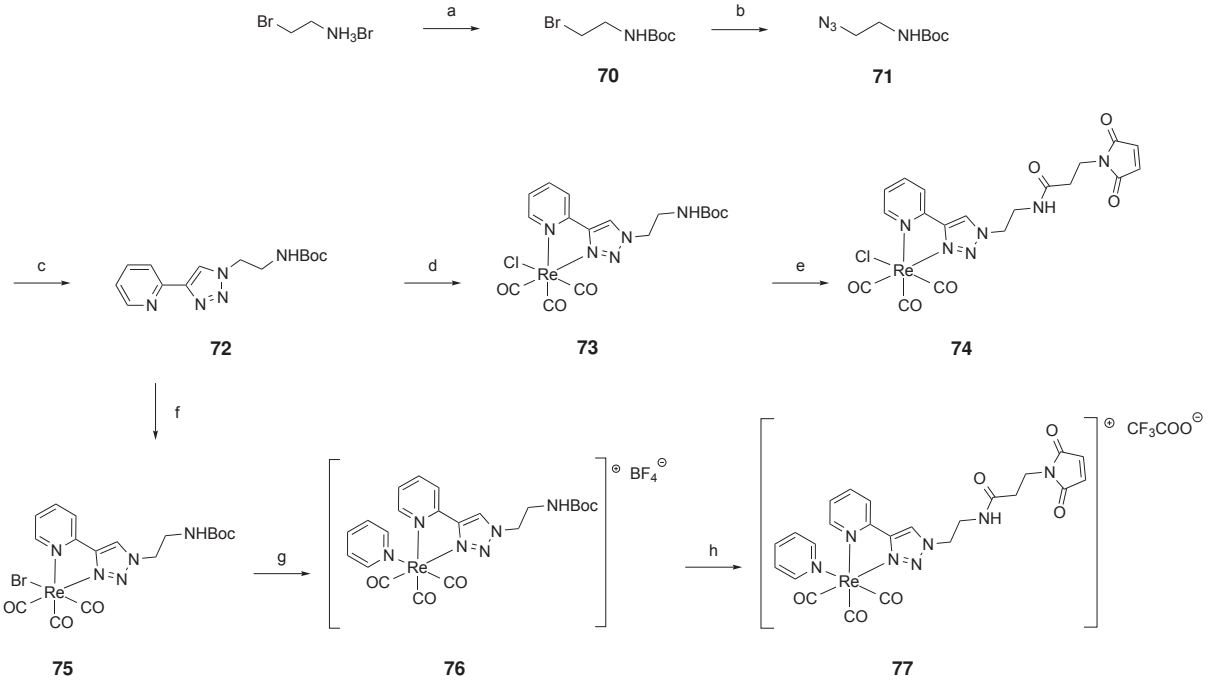

Scheme 2.1: Synthesis of SCoMPIs for thio-maleimide labelling of *Engrailed 2* Homeodomain.

Reaction conditions: (a) Boc_2O, DIEA, THF, 1 h, 0 °C to RT, 99%; (b) NaN_3, NaI, acetone:water (3:1 v:v), 48h, RT, 77%; (c) 2-ethynylpyridine, $CuSO_4$, sodium ascorbate, acetone:water (2:1 v:v), 2h, RT, 78%; (d) $Re(CO)_5Cl$, toluene, 6h, 80 °C, 99%; (e) *i.* TFA:DCM (1:1 v:v), 1 h, RT, *ii.* 3-maleimidopropionic acid *N*-hydroxysuccinimide ester, DIEA, dry DMF, overnight, RT; (f) $Re(CO)_5Br$, toluene, 6h, 80 °C, 94%; (g) $AgBF_4$, acetonitrile, 3 days, 65 °C, Ar; pyridine, THF, 36h, 60 °C, 68%, (h) *i.* TFA:DCM (1:1 v:v), 1 h, RT, *ii.* 3-maleimidopropionic acid *N*-hydroxysuccinimide ester, DIEA, dry DMF, overnight, RT, 34%.

Depending on their sequence, the Cys-HD and Cys-NLS-HD homeodomains are expected to be either distributed in the cytoplasm (Cys-HD) or localized principally (but not exclusively) in the nucleus (Cys-NLS-HD). We thus synthesized two SCoMPIs suitable for thiol-maleimide coupling and bearing either a chloride or a pyridine ligand: as discussed in Chapter 1, the complex bearing a chloride displays a luminescence enhancement when

accumulated in membranes, whereas the pyridine complex has a better quantum yield in solution. We thus wanted to compare the luminescence properties of both SCoMPIs in different cellular localization.

The SCoMPIs were synthesized following a strategy similar to the one described in Chapter 1. Due to the presence of the Boc protecting group, reaction temperatures were lowered when needed in order to be kept below 80 °C. Boc-protection of 2-bromoethylamine (hydrobromide salt) was followed by nucleophilic substitution of the bromide of **70** by an azido group in presence of sodium azide and sodium iodide, to obtain **71**. The Boc-protected ligand (PytaNHBoc, **72**) was easily obtained by the so-called CuAAC "click" reaction of the azide derivative with 2-ethynylpyridine, in good yields. Complexation of the rhenium tricarbonyl core from $Re(CO)_5X$ precursor (X=Cl, Br) in toluene resulted in the precipitation of the rhenium tricarbonyl complex as a pale yellow powder (**73**, X=Cl; **75**, X=Br). Boc-deprotection of the rhenium tricarbonyl chloride complex (**73**) was then performed, and the maleimide moiety was appended to the complex through reaction with NHS-activated 3-maleimidopropionic acid. To generate the pyridinium complex, the bromide ligand of complex **75** was exchanged with pyridine in two steps, first by reaction with $AgBF_4$ in acetonitrile and then with pyridine in non-distilled THF. Boc-deprotection of the complex, followed by introduction of the maleimide moiety, were performed in conditions similar to that of the chloride complex. Both complexes were purified by HPLC prior to protein labelling. As in Chapter 1, particular care was taken for the purification of the chloride complex, since slow exchange of the chloride may occur under HPLC conditions (solvents containing 0.1% TFA): the collected fraction were thus frozen in liquid nitrogen immediately after purification, then freeze-dried.

2.4 Labelling of Homeodomain

The coupling must be carried out under reductive conditions in order to prevent the formation of disulfide bridges between cysteins of proteins and thus under inert atmosphere. Moreover, the protein solution obtained after purification contains a significant amount of DTT (1 mM) that should be removed prior to reaction: DTT being a dithiol, undesired reaction with the maleimide reagent could occur, thus limiting the efficiency of labelling. For these two reasons, the protein solution buffer was exchanged for freshly degased reaction buffer (50 mM phosphate buffer, 150 mM NaCl, 10 mM EDTA, pH 6.7) by ultrafiltration prior to perform the reaction.

The resulting protein solution (100 µM in reaction buffer) was carefully put under inert atmosphere (3 vacuum/Ar cycles, avoiding "bubbling" as much as possible). One equivalent of tris(2-carboxyethyl)phosphine hydrochloride ($TCEP \cdot HCl$) was added in order to reduce any remaining disulfide bridge, and the mixture was stirred at room temperature for thirty minutes to one hour. Although TCEP is generally considered as non-reactive towards

maleimides, it has been reported to react with them under certain conditions [147,148]. We thus limited the amount of TCEP to one equivalent per equivalent of protein. Moreover, TCEP is not very stable in phosphate buffer, and was thus added to the protein solution no more than one hour before reaction.

Five equivalents of the desired probe were then added to the protein solution, and the mixture was stirred overnight under inert atmosphere. The labelling reaction was efficient at room temperature, but also when performed at 7 °C overnight. This second condition should preferentially be used as it limits the risks of protein degradation. The chloride complex **74** was not fully soluble at the desired concentration of 500 µM, even in presence of DMSO ($< 1\%$), and partially precipitated upon addition to the protein solution.

Thiol-maleimide coupling are generally performed at pH between 6.5 and 7.5, as a compromise between reactivity of thiolate group and selectivity of the reaction for cysteins rather than lysines. Various pH were tried, and we found that the reaction was more efficient at pH 7.5 but led to non specific labelling, whereas below pH 7.0 it was more selective. Attempts at pH lower than 6.5 led to partial labelling of the POI. We thus adjusted pH of the reaction buffer between 6.5 and 7.0 (typically, pH = 6.7) to perform the reaction. Under these conditions, labelling was completed overnight. Excess of reagent was then removed by iterated ultrafiltration steps (buffer: 10 mM phosphate buffer, 150 mM NaCl, pH 7.0).

Reaction buffers for thiol-maleimide labelling generally contain EDTA (10 mM) in order to chelate divalent metals that could otherwise promote oxidation of sulhydryls. Such a concentration of chelating agent could have an impact on the integrity of the Re(I) complex by chelating its metal center, thus impairing the spectroscopic properties of the SCoMPI. However, MALDI-TOF MS of the isolated protein showed a peak corresponding to the protein labelled with the intact SCoMPI (except for the Cl or Py ligand that are usually decoordinated during MALDI analysis). Moreover, spectroscopic properties of the labelled proteins were similar or identical to those of the corresponding complexes (Figure 2.7): (i) absorption spectra displayed the MLCT band expected for Re(I) tricarbonyl complexes around 320 nm (Figure 2.7b), (ii) excitation at 350 nm led to an emission either at 500 nm (Re(Py)-HD and Re(Py)-HD) or 525 nm (Re(Cl)-NLS-HD and Re(Cl)-HD) (Figure 2.7c), and (iii) the A_1 and E bands of labelled Re(X)-NLS-HD (X=Cl,Py) match those of the corresponding pure SCoMPI (Figure 2.7d). Altogether, these data confirm that the spectroscopic properties of the SCoMPIs are not impaired during the protein labelling step.

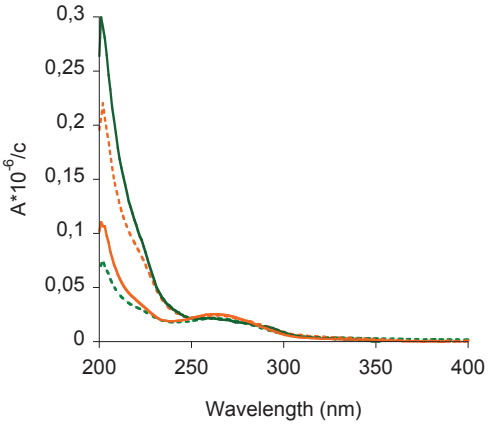

(a) Absorption spectra

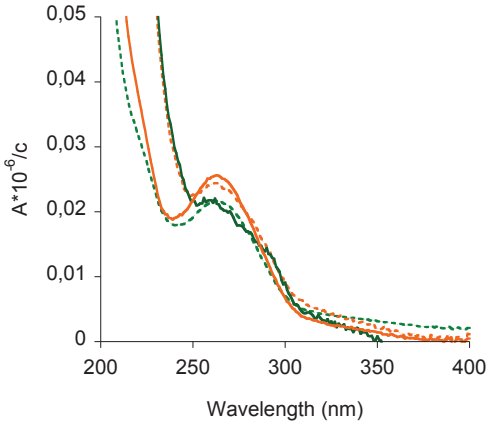

(b) Absorption spectra:
Zoom on Trp and MLCT bands

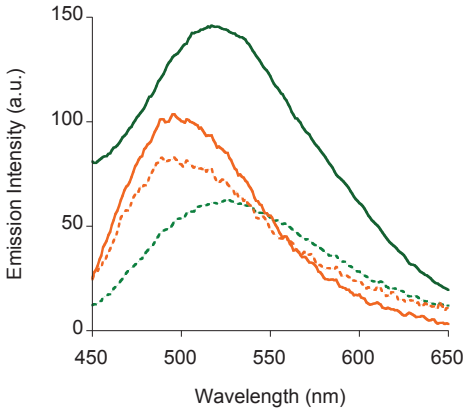

(c) Emission spectra ($\lambda_e x = 350$ nm)

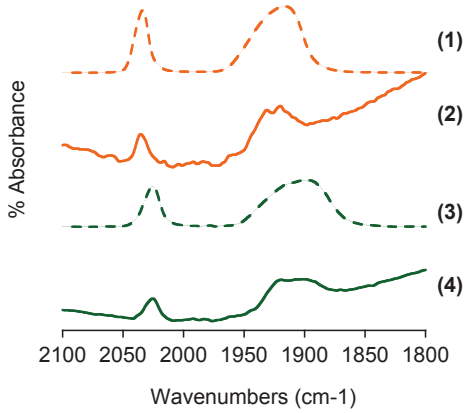

(d) FTIR spectra

Figure 2.7: Spectroscopic properties of SCoMPI-labelled Homeodomains Cys-HD and Cys-NLS-HD.

(a-c) Absorption and emission spectra of Re(Cl)-HD (green, dot line), Re(Py)-HD (orange, dot line), Re(Cl)-NLS-HD (green, full line) and Re(Py)-NLS-HD (orange, full line). Spectra are normalized by concentration of the solution. Emission spectra were recorded for excitation at 350 nm with 5 nm excitation and emission slits. (d) FTIR spectra of $[Re(CO)_3(Py)(PytaCOOMe)]^+$ (**60**) (spectrum (1), orange dashed line); Re(Py)-NLS-HD (spectrum (2), orange, full line), $[Re(CO)_3(Cl)(PytaCOOMe)]$ (**60**) (spectrum (3), green, dashed line) and Re(Cl)-NLS-HD (spectrum (4), green, full line).

2.5 Imaging of Homeodomain

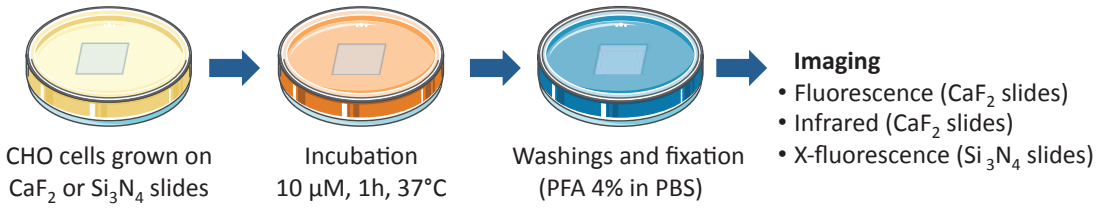

Figure 2.8: Principle of the incubation protocol for multimodal imaging.

Finally, we investigated the possibility to image the SCoMPI-labelled homeodomains by fluorescence, infrared and X-fluorescence microscopies. CHO cells were grown on CaF_2 slides (suitable for infrared microscopy and compatible with fluorescence microscopy) or Si_3N_4 slides (suitable for X-fluorescence) and incubated with 10 µM solutions of labelled proteins for 1 h at 37 °C (Figure 2.8).

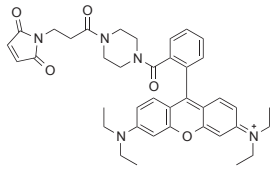

(a) Structure of the rhodamine-maleimide label

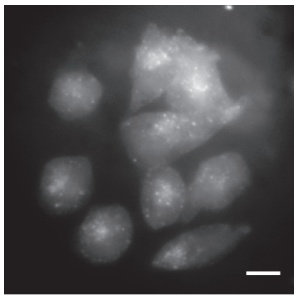

(b) CHO cells incubated with 10 µM Cys-HD-Rhodamine

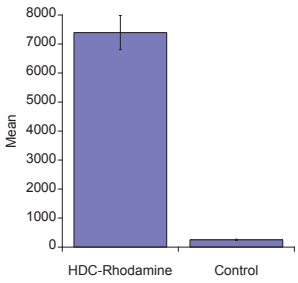

(c) Mean fluorescence intensities of cells

Figure 2.9: Fluorescence imaging of HDC-Rhodamine in CHO cells.
(a) Structure of the rhodamine-maleimide reagent used for the labelling of Cys-HD. Note that the piperazine moiety prevents the cyclization of the rhodamine amide to non-fluorescent rhodamine lactam [149]. (b) CHO cells incubated with HDC-Rhodamine. Scale bar = 10 µM. (c) Comparison of mean fluorescence intensities displayed by cells incubated with HDC-Rhodamine and control cells.

After washing and fixation, cells were first observed by fluorescence microscopy. Unfortunately, none of the SCoMPI-labelled proteins could be detected in cells by this microscopy. For comparison purposes, we also incubated CHO cells with a rhodamine-labelled homeodomain HD (Figure 2.9a). Contrarily to what had been observed for SCoMPI-labelled proteins, Rhodamine-HD could be easily detected in CHO cells (Figure 2.9c), and fluorescence signal of incubated cells was significantly different from control cells (Figure 2.9c). The fact that the SCoMPI-labelled proteins could not be detected by fluorescence microscopy is thus probably due to the modest quantum yield of the SCoMPI. Infrared microspectroscopy was then performed in order to detect the proteins in cells. However, again, no signal corresponding to the carbonyl ligands of the probes could be clearly identified. IR microspectroscopy appeared to be not sensitive enough in this context.

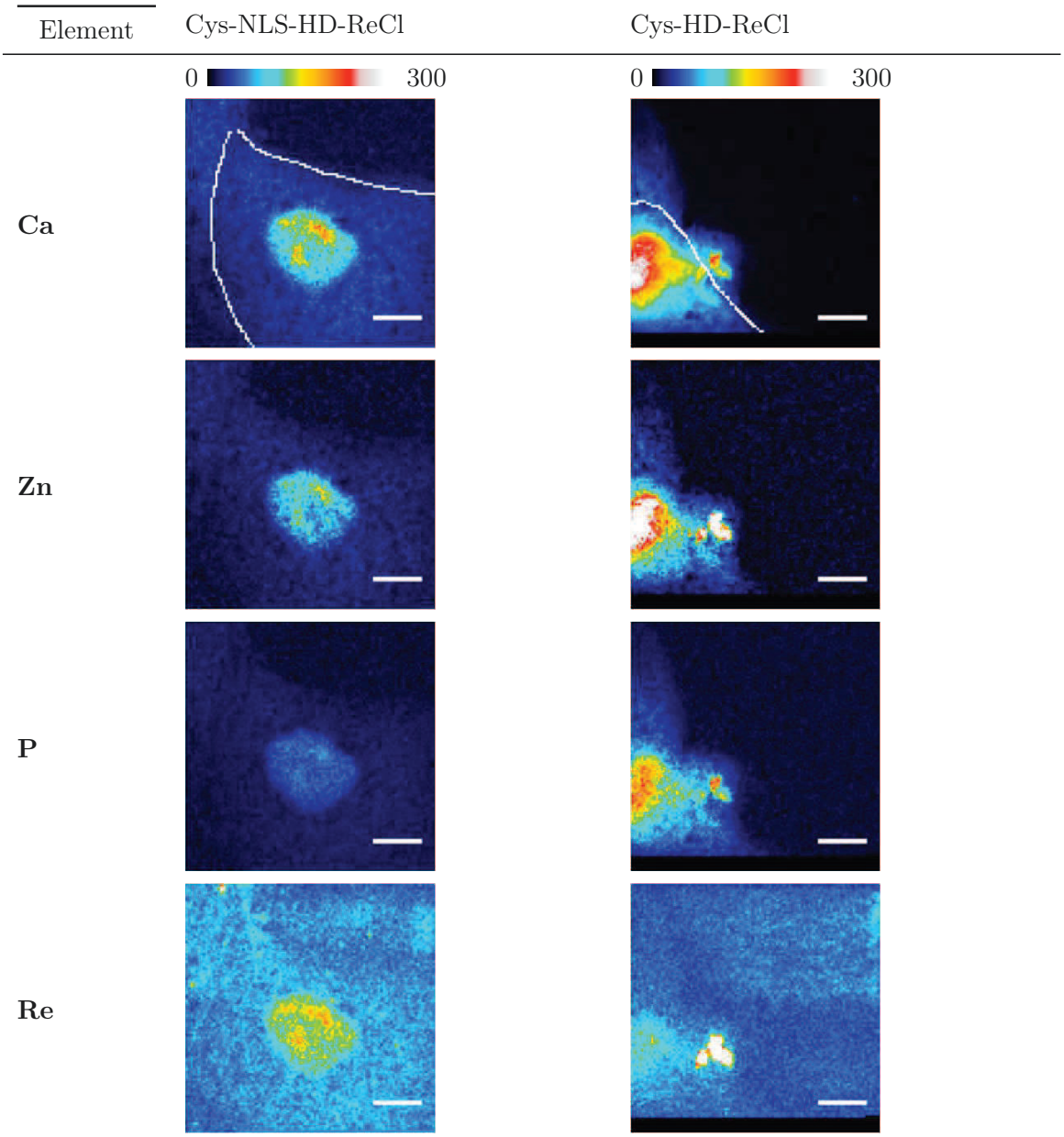

Figure 2.10: X-fluorescence microscopy of CHO cells incubated with Re(Cl)-NLS-HD and Re(Cl)-HD.

Finally, we performed preliminary observations of the cells by synchrotron X-fluorescence microscopy at the synchrotron Soleil, on a new beamline called Nanoscopium. These experiments led to the successful detection of the Re signal and to map the Re distribution in cells incubated with Re(Cl)-HD and Re(Cl)-NLS-HD (Figure 2.10).

Some cells incubated with Re(Cl)-NLS-HD displayed a very localized area where various elements concentrated, including Zn and P (Figure 2.10). Ca signal, although more diffuse and present in the whole cell, was also stronger in this area. Interestingly, Re signal mostly concentrated in this area. According to the literature, P and Zn are accumulated in the nucleus and are often used to identify it [92]. This would thus suggest that the labelled homeodomain is mainly localized in the nucleus. This is consistent with the presence of the NLS sequence in the sequence of the protein. On the other hand, cells incubated with Re(Cl)-HD, missing the NLS sequence, displayed weaker signals which seemed distributed all over the cells. It should be noted that the resulting maps give a 2D-projection of the signal of the cell. If an element is homogeneously distributed in the volume of the cell, its signal will thus be stronger in the thicker areas. This seem to be the case for Re(Cl)HDC. Although the number of observed cells is too small to give statistically significant conclusions, it is encouraging that the observed localizations are consistent with the sequences of the homeodomains. Finally, some Re signal could be detected in some places of the background. This can be easily explained by the fact that homeoproteins, like their derived CPPs, bear several positive charges and tend to adsorb on surfaces.

2.6 Conclusion

We designed and synthesized two SCoMPIs suitable for the labelling of cystein-appended proteins through *in vitro* thiol-maleimide coupling. Conditions allowing complete labelling of both homeodomains (Cys-HD and Cys-NLS-HD) were determined. The SCoMPIs kept their integrity and their spectroscopic properties during the labelling step, and the labelled homeodomains display similar features to their parent complex.

The labelled homeodomains were then incubated on CHO in order to detect them by fluorescence, infrared and X-fluorescence microscopies. Although detection of the SCoMPI in cells by fluorescence and infrared imaging proved unsuccessful, it was possible to detect Re and to map its distribution in cells by X-fluorescence microscopy. These preliminary results illustrate the high sensitivity of X-fluorescence for the detection of Re, and are encouraging for the development of such probes for X fluorescence microscopy. In order to obtain additional maps, application for beamtime on a X fluorescence beamline at the synchrotron APS (Argonne, Chicago) has been submitted.

On the other hand, although it was not possible to detect the SCoMPI-labelled proteins at the single cell level by fluorescence and infrared microscopies, these modalities might still be useful for other applications. For instance, quantification of internalized

homeodomain on a cell population by infrared can be envisioned. In addition, luminescence properties of the SCoMPI could be enhanced by changing the pyridine-triazole ligand [33], thus allowing a better sensitivity by fluorescence.

Chapter 3

Labelling of endogenous Carbonic Anhydrases in cells

Figure 3.1: Structure of Carbonic Anhydrase I hCA-I (2CAB in PDB).

Finally, we investigated the possibility to label endogenous proteins with SCoMPI and to detect them by fluorescence, infrared and X-fluorescence microscopies. To reach that goal, we chose Carbonic Anhydrase (CA) as target. Carbonic anhydrases are widely studied proteins [150], which catalyze *in vivo* hydration of CO_2 and dehydration of bicarbonate. They are involved in several biological processes, including respiration, regulation of acid/base equilibria, metabolism, and many others. They were identified as interesting targets for anti-cancer drug development: hypoxic solid tumours were shown to overexpress some isoforms of CA, in particular hCA-IX and CA-XII; in addition, CA inhibitors may also inhibit tumour growth [151, 152]. Much efforts have been made to develop CA inhibitors for hCA-IX and CA-XII, as well as imaging agents targeting CA to image solid tumours [74, 153–156]. As mentioned in the introduction, some of these imaging agents are based on the $^{99m}Tc(CO)_3$ core for radiolabeling, and could be initially developed with the $Re(CO)_3$ core [153–156]. Membrane-bound hCA-IX and CA-XII are thus biologically relevant targets. In addition, the infrared modality of SCoMPIs is well adapted for tissue imaging, and we envisioned that it could have potential applications for tumor imaging. Endogenous hCA-IX and CA-XII are consequently excellent targets for covalent labelling with SCoMPIs.

3.1 Strategies for the covalent labelling of proteins in living cells

3.1.1 From genetic engineering to synthetic chemistry: strategies to label proteins in living cells

Over the past few decades, significant efforts have been made to develop tools to label and visualize proteins in a complex cellular environment [157–164]. Bio-imaging and studying of numerous types of proteins was made possible by fluorescent protein-fusions (FP-fusions) (3.2a), which are still widely used [160, 165]. However, given the size of such labels (27 kDa for green fluorescent protein GFP), interactions of the fusion protein with its environment, in particular with other proteins, might be altered [166]. Moreover, the labelling is restricted to *N*- or *C*-terminus of the protein of interest (POI), and, so far, the readout to fluorescence imaging techniques.

Labelling strategies based on small chemical probes, that would be less likely to perturb the protein function, have thus been developed (Figure 3.2). Beside their small size, a further advantage of chemical probes compared to FP is their diversity and tunability: common fluorescent probes may of course be used, but also fluorogenic, luminescent, NMR, MRI, infrared probes, etc [167–172]. Many of these labelling methods combine synthetic chemistry and genetic engineering to incorporate non canonical tags or functions into the POI [158, 163, 173]:

- *"Self-labelling protein" (SLP) tags*, often derived from enzymes, can be fused to the POI [158]. The desired chemical probe is generally covalently bound to a specific substrate of the SLP, and the resulting molecule is reactive through an electrophilic group (3.2b). Upon recognition, the SLP reacts with the probe through a nucleophilic side chain, producing a covalent adduct. Well-known examples are HaloTag (derived from haloalcane dehalogenase) and SNAP-tag (derived from human DNA repair protein O^6-alkylguanine-DNA-alkyltransferase (hAGT)). As for FP-fusions, their size may limit some applications, but SLPs offer the advantage of probe diversity [171].

- *Enzyme-mediated labelling* relies on the specific, enzyme-mediated transfer of the probe to a short peptide sequence fused to the POI (3.2c). Examples of labelling enzymes include phosphopantetheinyl transferases (PPTases) (Acyl Carrier Protein (ACP) peptide tag) [174], biotin ligase (biotin ligase acceptor peptide tag) [175], and lipoic acid ligase (lipoic acid ligase acceptor peptide [176, 177]. Although they use small-size tags (less than 20 amino acids) and they are efficient and specific, these labelling systems only accept a few probes due to the enzyme hindering. To extend the range of available probes, further genetic engineering of the labelling enzyme is needed. Moreover, visualization of a POI inside cells requires to overexpress the la-

Approaches based on genetic engineering

(a) Fluorescent Protein (FP) fusion

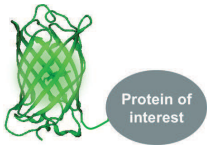

Approaches combining genetic engineering and synthetic chemistry

(b) Self-labelling Protein (SLP) Tag

(c) Enzyme-mediated labelling

(d) Covalent self-labelling Tag

(e) Incorporation of non-canonical functions

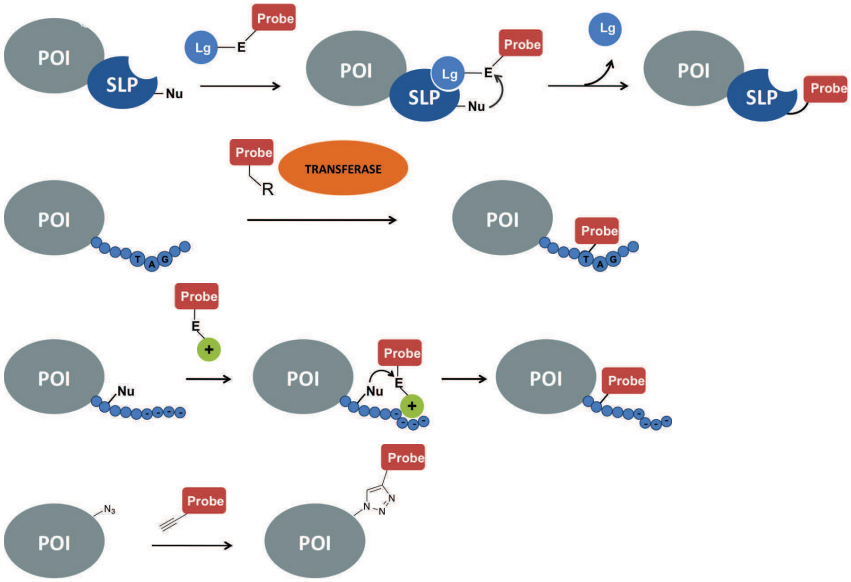

Approaches based on synthetic chemistry for the labelling of endogenous proteins

(f) General Affinity Labelling

(g) Traceless Affinity Labelling

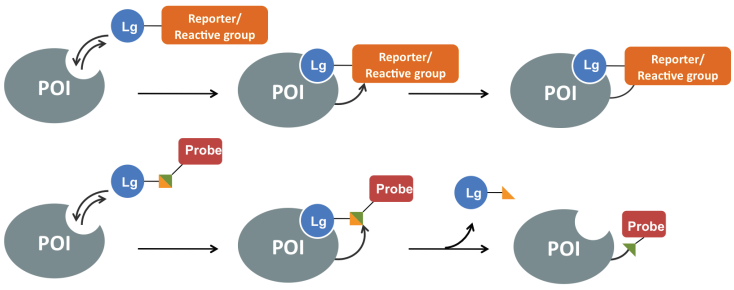

Figure 3.2: Methods for the covalent labelling of proteins in cells. (inspired from ref [157, 158])

belling enzyme in the system.

- *Self-labelling peptide tags* are also short peptide sequences fused to the POI, but they (covalently) bind the probe without need of an enzyme. In many cases, tag/probe binding relies on the affinity of a metal complex for the tag sequence containing nucleophilic amino acids. The first example was developed with a tetracystein tag (CCXXCC) and biarsenical complexes (initially **Fl**uorescein **Ars**enic **H**airpin Binder, FlAsH) by Tsien *et al.* Upon binding of the FlAsH probe to the tetracystein tag, the formed complex exhibited strong luminescence. In following studies, the strong affinity of the tag/probe pair was further improved by optimization of the tetracystein motif (K_d down to 4 pM), and the luminescence properties of the biarsenical probe tuned by changing the fluorescein ligand for other fluorophores, e.g. resorufin (ReAsH probe) [178]. A tetraserine tag, binding a rhodamine-bisboronic acid derivative with $K_d \sim 10^2$ nM, was later developed [179]. Other tag/probe pairs use the proximity induced by metal complexation to promote the formation of a covalent bond between a nucleophilic amino acid of the tag and an electrophilic center of the probe. For instance, His-tags including an additional cystein for covalent labelling were used to label intracellular proteins [161].

- *Unnatural amino acids* bearing bioorthogonal functions may also be incorporated into proteins in living cells by using modified or orthogonal aminoacyl-tRNA synthetase/tRNA pairs [162,163]. Incorporation can be either residue-specific (incorporation of the modified aminoacid in the whole proteome) or site-specific (incorporation of the unnatural amino-acid at a single site in the POI). The non-canonical function can then specifically react with the desired chemical label. Several bioorthogonal reactions have been developed over the past decades, including ketone/aldehyde-hydrazide/hydroxylamine reactions, Staudinger ligation, azide-alkyne cycloaddition (Figure 3.2e), Pd-catalyzed cross-coupling reactions, etc. (see [162, 163] and references therein).

All these methods are highly selective and efficient, and have been used to label and study a large range of proteins. However, direct labelling of endogenously expressed (native) proteins without preliminary genetic modification may sometimes be required. Such labelling should be highly selective and not impair the protein functions. Affinity-guided labelling of proteins could be one strategy to achieve that goal. First introduced in the 1960s [180,181], the method relies on the use of a substrate/inhibitor of the POI, appended with a (photo)chemically reactive group and a reporter group. Upon selective binding of the ligand to the POI, the reactive group reacts with the protein, leading to the covalent labelling of the protein with the probe. Unfortunately, this process usually leads to the inactivation of the POI since the inhibitor is kept inside the active site and blocks it. This is a

strong drawback, which limits the potential application of this strategy for real-time imaging, for instance. Hamachi *et al.* have developed approaches to circumvent this problem by introducing a cleavable reactive group in the probe. Upon reaction of the probe with the protein surface, the ligand part of the probe is released, thus freeing the active site, while the reporter group is covalently bound to the POI. This set of methods, called "Traceless Affinity Labelling" or "Ligand-Directed Labelling", is developed in the next section.

3.1.2 Strategies for traceless affinity-guided labelling of endogenous proteins

Two different strategies exist for the Traceless, Ligand-Directed labelling of endogenous proteins: (i) use of a catalyst appended to the ligand of the POI, that will enhance the transfer of the probe to the surface of the protein (Figures 3.3a, 3.3b, 3.3c) and (ii) use of a single molecular probe containing both the ligand and the label, linked by a cleavable bound.

One of the most studied examples for the first strategy is Affinity-Guided DMAP (AGD) chemistry (Figure 3.3a), designed by Hamachi and co-workers. In this method, a 4-dimethylaminopyridine (DMAP) group is linked to the ligand of the POI. Upon selective binding to the protein, the catalyst will enhance the transfer of the desired probe from an acyl donor (generally a thiophenyl ester) to a nucleophilic amino-acid proximal to the ligand-binding pocket of the protein. It was shown that increasing the number of DMAP catalyst appended to the ligand greatly improved the labelling efficiency [184]. Various membrane proteins were successfully labelled in test tube or in cells using either monovalent or multivalent ligand-directed DMAP catalysts: lectins (Congerin II, Concanavalin A), Src Homology domain 2 (SH2), FK506 Binding Protein 12 (FKBP12) and bradykinin B_2 receptor (B_2R) [182–184, 186]. More recently, endogenous growth factor receptors EGFR and HER2 were labelled using DMAP-appended antibodies instead of affinity ligands [185]. Other examples of such approach have been reported, for instance "Local Single Electron Transfer (SET) Chemistry (LSC)" [188] (Figure 3.3c) and "Modular method for Affinity Labelling" [187] (MoAL method, Figure 3.3b).

To achieve traceless affinity labelling, an alternative approach consists of combining both functionalities (ligand selectivity and label detection) in a single probe, both entities being linked by a cleavable bond. Ligand-Directed Tosyl (LDT) chemistry (Figure 3.3d), for instance, makes use of an electrophilic phenylsulfonate group to connect the ligand of the POI and the label in the LDT reagent. Upon binding to the POI, the chemical label is transferred to the surface of the POI by reaction of a nucleophilic amino acid side chain with the tosylate. This strategy was successfully used to label a large range of proteins (Carbonic Anhydrase [166, 189, 193], FKBP12 [189–191], Congerin II, SH2 domain) in test tube, but also in bacterial lysate, living cells, tissues, and even *in vivo* in mice. Determination of

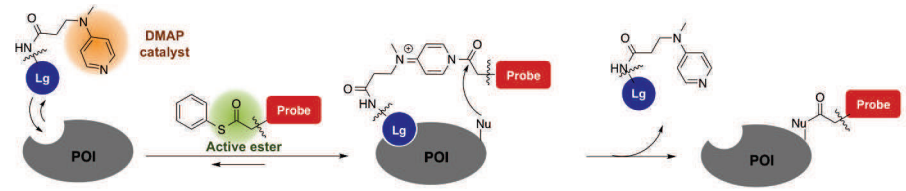

(a) Affinity-Guided DMAP (AGD) Chemistry [182–186]

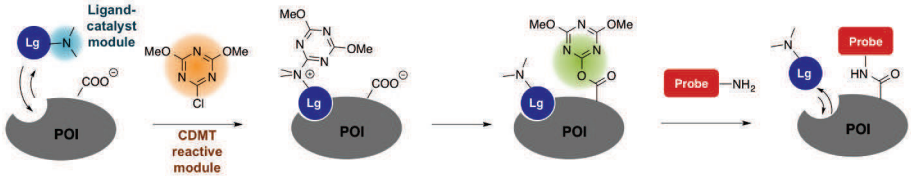

(b) Modular Affinity Labelling [187]

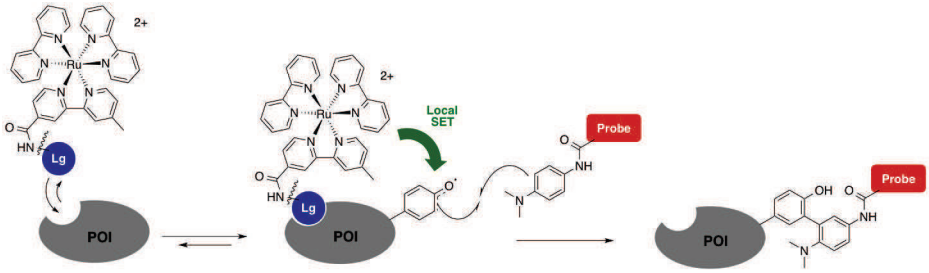

(c) Local Single Electron Transfer (SET) Chemistry (LSC) [188]

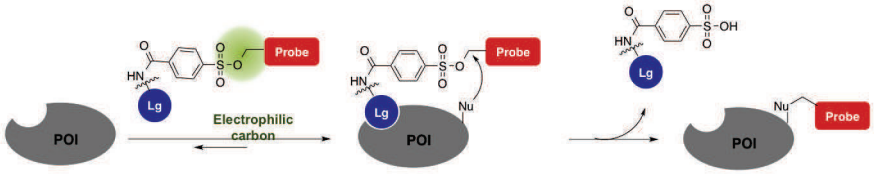

(d) Ligand-Directed Tosyl (LDT) Chemistry [166, 189–194]

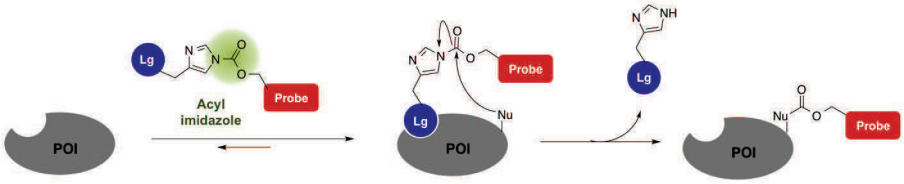

(e) Ligand-Directed Acyl Imidazole (LDAI) Chemistry

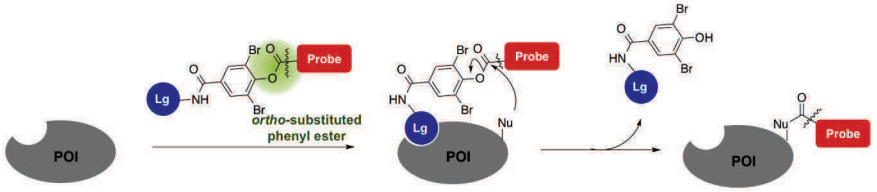

(f) Ligand-Directed diBromophenyl Benzoate (LDBB) Chemistry [195]

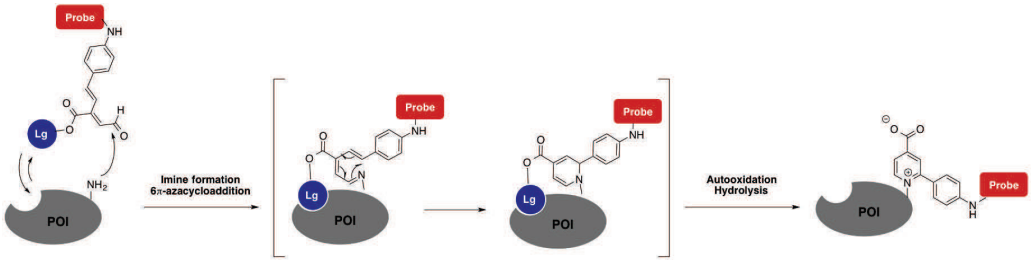

(g) Ligand-Directed Azaelectrocyclization and Autooxidation [196]

Figure 3.3: Examples of strategies for Traceless Affinity labelling

labelling sites for these proteins highlighted that labelled residues were located near the entrance of the enzyme active site, which is one of the features of ligand-directed chemistry. Selectivity towards some amino-acids could also be observed: labelled residues were mostly His, but also Tyr, Glu, Asp and Cys residues. However, no Lys labelling could be observed using this strategy [192].

Table 3.1: Summary of published applications of LDAI labelling system

Target Protein	Ligand/Binding motif	Chemical probe	Labelling conditions	Labelled residue	Ref
Folate Receptor (FR)	Methotrexate	Fluorescein	Test tube	Lys	[197,198]
		Biotin	KB cells		
Carbonic Anhydrase (CA)	Benzenesulfonamide	Coumarin	Test tube	Lys, Ser, Tyr	[198,199]
		Biotin	Red Blood Cell Lysate		
		^{19}F-NMR probe	A549		
		Oregon Green			
Bradykinin B_2 Receptor (B_2R)	Peptide agonist[2]	Biotin	HEK293	N.A.[1]	[198]
NMDA Receptor (NMDAR)	GV150526	Oregon Green	HEK293T	N.A.[1]	[198]

[1] N.A.: Non Available.
[2] {DArg^0[Hyp^3,DPhe^7,Leu^8]BK} B2R peptide agonist appended with a HisGlyGly sequence at *N*-terminus for LDAI formation

A complementary Ligand-Directed strategy was developed by the same laboratory: Ligand-Directed Acyl Imidazole chemistry (Figure 3.3e), in which the acyl is transferred from the imidazole to the surface of the protein. This strategy was shown to have a kinetics different from LDT chemistry, and displayed a different site-selectivity [197]: labelled residues were Lys (forming carbamate bond with the acyl-probe moiety), Ser and Tyr (forming a carbonate bond) [197–199]. Table 3.1 summarizes the applications of this strategy to the labelling of proteins *in vitro* and in cells.

Finally, it should be noted that other examples of LD labelling strategies have emerged recently (Figure 3.3f, 3.3g). In particular, the so-called Ligand-Directed diBromoBenzoate (LDBB) chemistry [195] (Figure 3.3f) was recently published. The Hamachi group built on a ligand-directed strategy independently developed by Fenical *et al.* [200] to elaborate a new LD strategy. The initial strategy used an acyl-dye transfer from a phenyl ester to a lysine of the POI. To elaborate a new LD reagent, Hamachi *et al.* thus screened various *ortho*-substituted phenyl esters and identified *ortho*-dibromobenzoate esters as efficient traceless affinity labelling agents. Labelling of eDHFR in test tube was faster with LDBB reagents than with LDAI reagents. Moreover, they were able to label not only membrane-bound but also intracellular proteins, e.g. hCA XII (membrane-bound) and hCA II (cytosolic) [195].

3.2 Synthesis of the LDAI-SCoMPI reagents

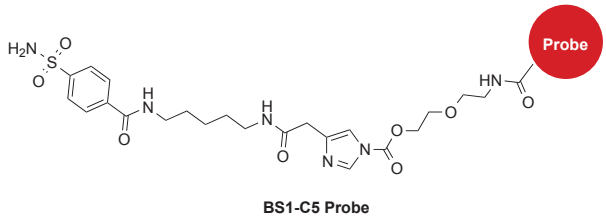

Figure 3.4: Structure of the C5 LDAI reagent for labelling of Carbonic Anhydrases [198, 199]

In a recent study, the Hamachi group designed and optimized a LDAI reagent for the labelling of human Carbonic Anhydrase I (CA-I), a cytosolic isoform of carbonic anhydrase (CA) [199]. They chose 4-carboxy-benzene-sulfonamide (BS1) as ligand for CA, and linked it to the imidazole moiety through alkyl chains of various lengths. They found that the reagent with the C5 linker (see Figure 3.4) was the most efficient for the labelling of CA. They later used this reagent for the labelling of membrane-bound CA-XII (and to a lesser extent hCA-IX) on A549 cells [198]. In collaboration with the Hamachi group, we designed LDAI-SCoMPI reagents for the labelling of Carbonic Anhydrase IX and XII. Since both the choice of the ligand and the flexibility/length of the linker may have an impact on the labelling efficiency of the LDAI reagent, we also designed three LDAI-SCoMPI reagents bearing a slightly different ligand, 4-(2-aminoethyl)sulfonamide (BS2), described to target more specifically hCA-IX, and with various distances between the ligand and the imidazole moiety (Figure 3.4) in order to reach a nucleophilic residue of the protein.

The convergent synthesis of LDAI reagents consisted of the synthesis of the ligand-imidazole moieties on the one hand (Scheme 3.1) and of a NHS-activated carbonate form of the probe on the other hand (Scheme 3.2), followed by the coupling of both entities to form the LDAI reagent in a final step (Scheme 3.3). Synthesis of imidazole moieties proceeded through similar steps. Except for the "C0" compound, the benzenesulfonamide ligand was first coupled in solution to the relevant Boc-protected linker using EDC/HOBt as activators, forming compounds **79**, **80**, **81**. Boc-deprotection was then performed and the resulting amines coupled with 1-trityl-1*H*-imidazole-4-acetic acid in solution. In the case of the C0 compound, 4-(2-aminoethyl)benzenesulfonamide was directly coupled to the Trityl-protected imidazole. Finally, the resulting imidazoles were deprotected in a TFA:DCM mixture (1:4 v:v) in presence of TIS to yield the free imidazoles **85** (C0), **86** (C3), **87** (C6), **88** (C5). It should be noted that a synthesis of the C5 imidazole (**88**) was reported in [199], in which the free 1*H*-imidazole-4-acetic acid was used for coupling to the benzenesulfonamide-linker moiety. However, our attempts to apply this strategy to BS2-linker moieties and use the free form of the imidazole for this coupling were not conclusive: the resulting free imidazoles were difficult to isolate and obtained with an unsatisfactory

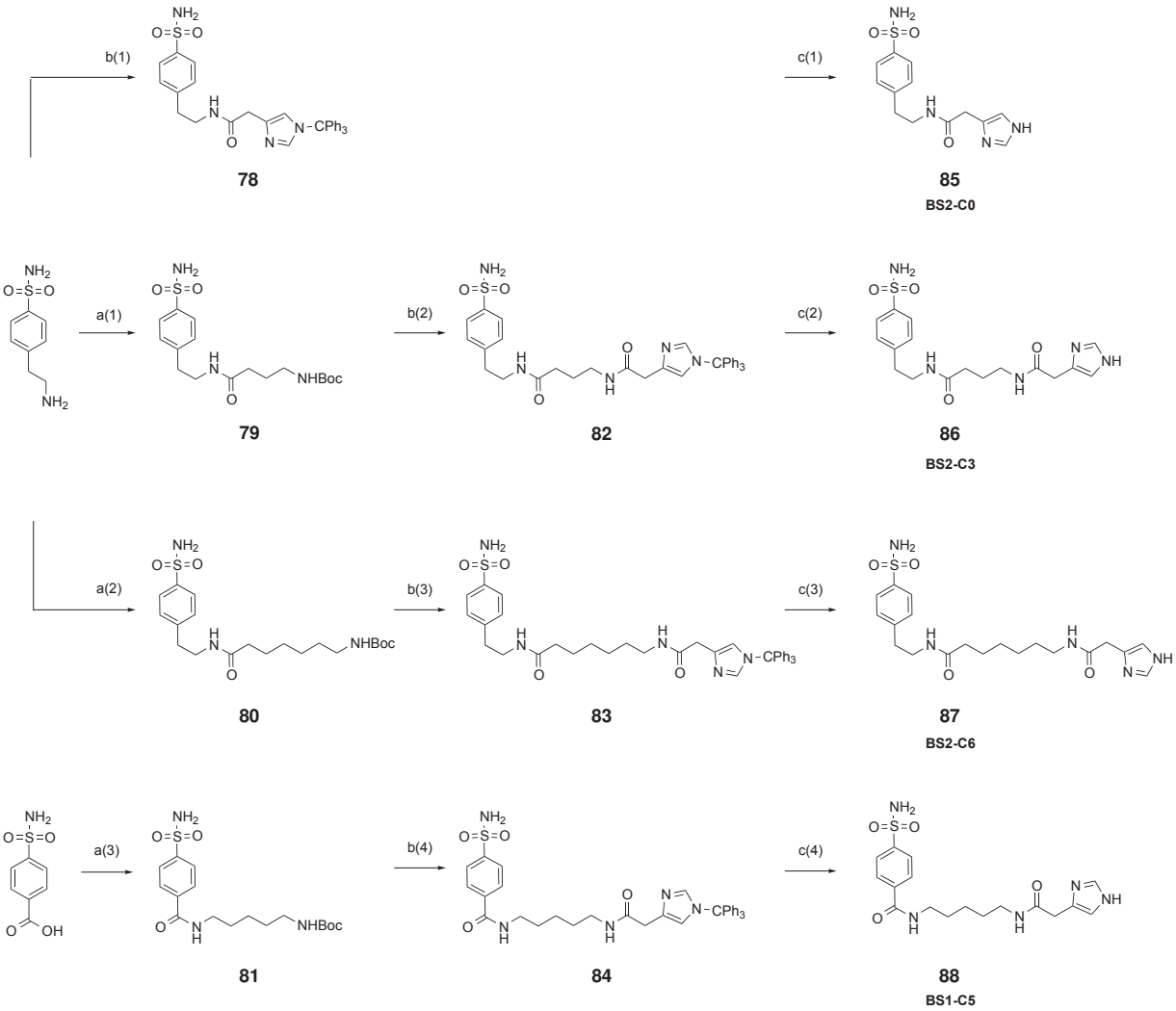

Scheme 3.1: Synthesis of LDAI-SCoMPI reagents: ligand-imidazole moieties
(a1) *N*-Boc-4-aminobutyric acid, EDC, HOBt, DIEA, dry DMF, Ar, overnight, 68%; (a2) *N*-Boc-7-aminoheptanoic acid, EDC, HOBt, DIEA, dry DMF, Ar, overnight, 67%; (a3) *N*-Boc-1,5-diaminopentane, EDC, HOBt, DIEA, dry DMF, Ar, overnight, 74%; (b1) 1-trityl-1*H*-imidazole-4-acetic acid, EDC, HOBt, DIEA, dry DMF, Ar, overnight, 40%; (b2) *i.* TFA:DCM 50:50, 1 h, RT, *ii.* same conditions as (b2), 54%; (b3) same conditions as (b2), 42%; (b4) same conditions as (b2), 34%; (c1) TFA:DCM 20:80, TIS, 1 h, RT, 93%; (c2) same conditions as (c1), 85%; (c3) same conditions as (c1), 88%; (c4) same conditions as (c1), 90%.

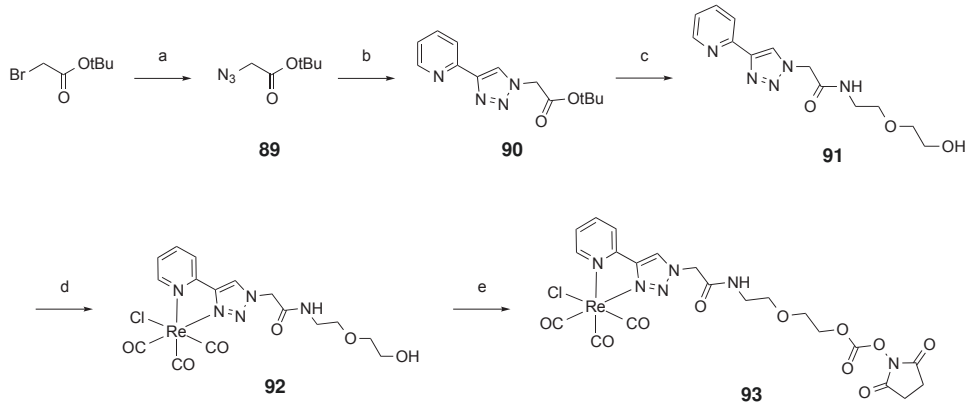

Scheme 3.2: Synthesis of LDAI-SCoMPI reagents: "NHS-activated carbonate" of SCoMPI

(a) NaN_3, acetone:water (3:2 v:v), reflux, 20h, 97%; (b) 2-ethynylpyridine, $Cu(OAc)_2$, sodium ascorbate, *t*-BuOH : H_2O (1:1 v:v), 1 h30, RT, 93%; (c) *i.* TFA:DCM 50:50, 2 h, RT, *ii.* EDC, 2-(2-aminoethoxy)-ethanol, DIEA, 40%; (d) $Re(CO)_5Cl$, MeOH, reflux, overnight, 99%; (e) DSC, triethylamine, dry DMF, 6 h, RT.

purity and/or yield. The use of the tritylated form of the imidazole precursor rather than the free form greatly enhanced the purification and obtention of the desired compound. We thus adopted this strategy for the BS2-C0, BS2-C3 and BS2-C6 imidazoles, and extended it to the BS1-C5 imidazole.

Besides, a SCoMPI derivative suitable for coupling to these imidazoles was designed and synthesized (Scheme 3.2 and Scheme 3.3), inspired by the strategy developed by Hamachi *et al* [199]. The desired Pyta ligand (**91**) was obtained in three steps from *tert*-Butyl bromoacetate. The bromide was first substituted by an azide group following a procedure published by Matsubara *et al.* [201]. A CuAAC "click" reaction was then performed with the resulting azide (**89**) and 2-ethynylpyridine to form 4-(2-pyridinyl)-1*H*-1,2,3-triazole-1-acetic acid *tert*-butyl ester (PytaCOO*t*-Bu, **90**) in very good yield, using conditions slightly adapted from those described by Benoist *et al.* [117]. The *tert*-Butyl ester was then cleaved in presence of TFA, and the resulting free acid was coupled to 2-(2-aminoethoxy)-ethanol using EDC as activator. The resulting ligand was then refluxed in methanol in presence of $Re(CO)_5Cl$ precursor to yield the alcohol complex **92** ($[Re(CO)_3(Cl)(Pyta{-}OH)]$). Finally, reaction of this complex with *N,N'*-disuccinimidylcarbonate in presence of triethylamine [198, 199] allowed the formation of the "NHS-activated" carbonate SCoMPI **93**.

Each imidazole was then reacted with **93** in presence of pyridine to obtain the desired LDAI reagents **94** (C0-SCoMPI), **94** (C0-SCoMPI), **95** (C3-SCoMPI), **96** (C6-SCoMPI), **97** (C5-SCoMPI) (Scheme 3.3). They could be purified by HPLC, using NH_4OAc (pH = 7) buffer and TFA-free acetonitrile and immediately freeze-drying the purified fraction in order to prevent hydrolysis of the acyl imidazole bound. Moreover, under these conditions, no exchange of the chloride ligand of the SCoMPI was observed .

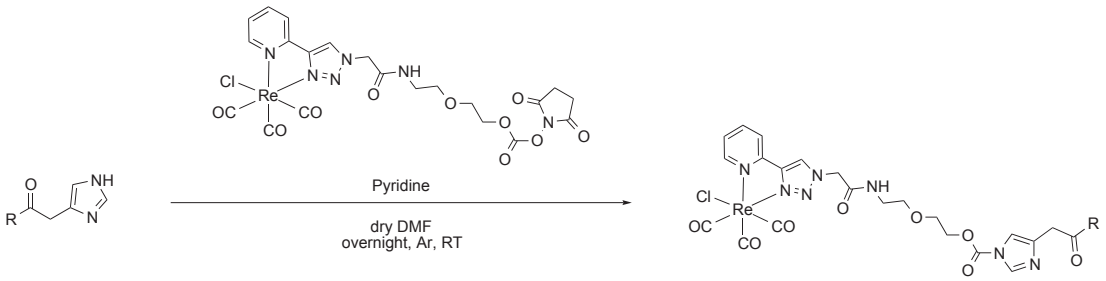

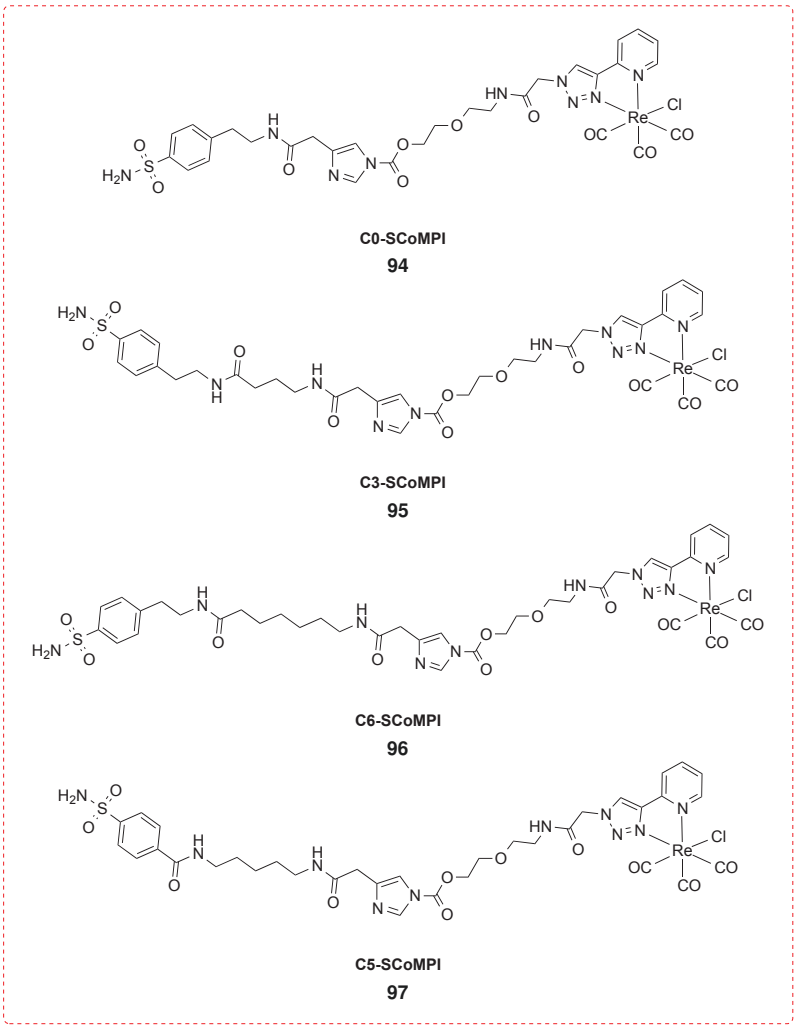

Scheme 3.3: Synthesis of LDAI-SCoMPI reagents: formation of the Acyl-Imidazole reagents

3.3 Determination of *in vitro* labelling efficiency

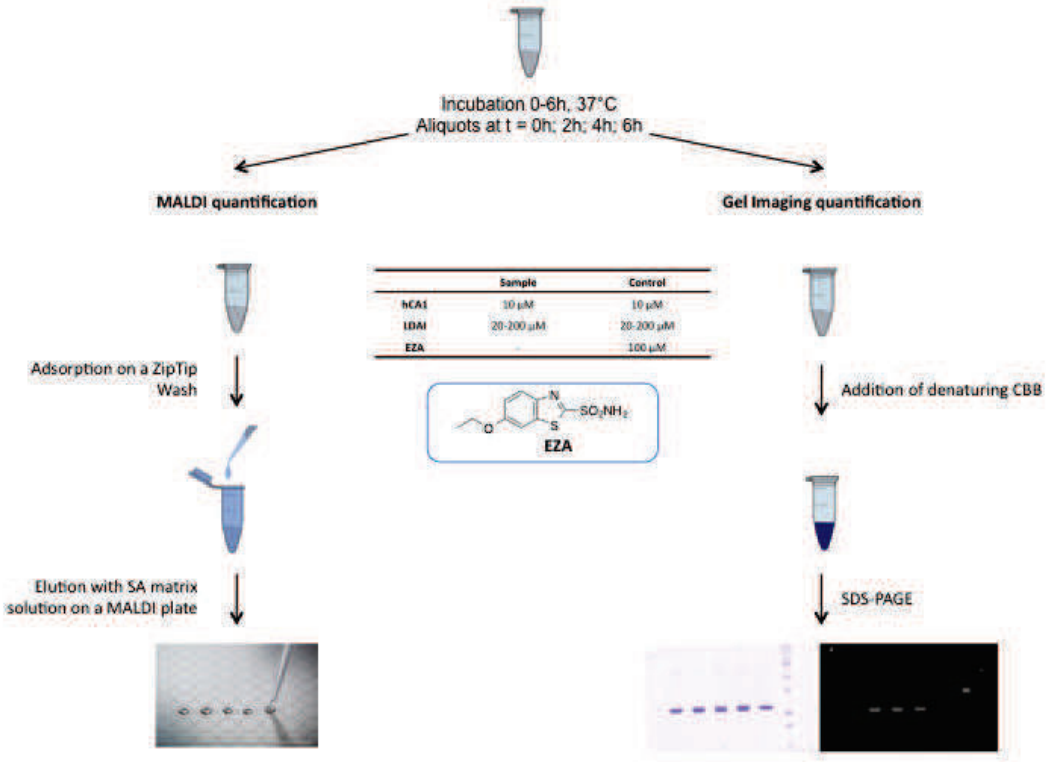

Figure 3.5: Quantification of the labelling of hCA-I by MALDI-TOF MS and fluorescence gel imaging.
For MALDI-TOF MS quantification, 10 µL aliquots of the incubation solution (10 µM hCA-I, 2-20 equiv. LDAI-SCoMPI, 0-10 equiv. EZA; 37 °C) were taken every two hours for 6 h, quenched by adsorption on C18 ZipTip®and washings with 0.1% aqueous TFA, and eluted/spotted on a MALDI plate with the matrix solution. MALDI spectra were then recorded and peak areas of labelled and unlabelled protein measured to determine the labelling percentage. *For fluorescence gel imaging*, 30 µL aliquots of incubation solution were taken at given time points, diluted with 2X denaturing buffer and stored at −30 °C until SDS-Page analysis. After gel migration, fluorescence imaging was performed prior to CBB staining.

Having synthesized four LDAI-SCoMPI reagents, we then examined their *in vitro* labelling efficiency towards human Carbonic Anhydrase I (hCA-I), a soluble isoform of Carbonic Anhydrase. A 10 µM solution hCA-I in HEPES was incubated with 2 or 20 equivalents of the LDAI reagents at 37 °C for 6 h. Aliquots of the solution were taken every two hours for 6 h, treated and analyzed either by MALDI-TOF or fluorescence imaging of SDS-PAGE gel. For each sample, a control containing a competitive inhibitor of hCA-I (namely ethoxzolamide, abbreviated EZA) was prepared and analyzed at the longest incubation time (Figure 3.5). For MALDI-TOF MS analysis, given the small size of the label compared to the protein (29 kDa), it can be assumed that the probe will have negligible influence on ionization properties of the labelled protein compared to the unlabelled one. It was thus possible to measure the areas of the peaks of labelled and unlabelled hCA-I and to use them to determine the labelling percentage.

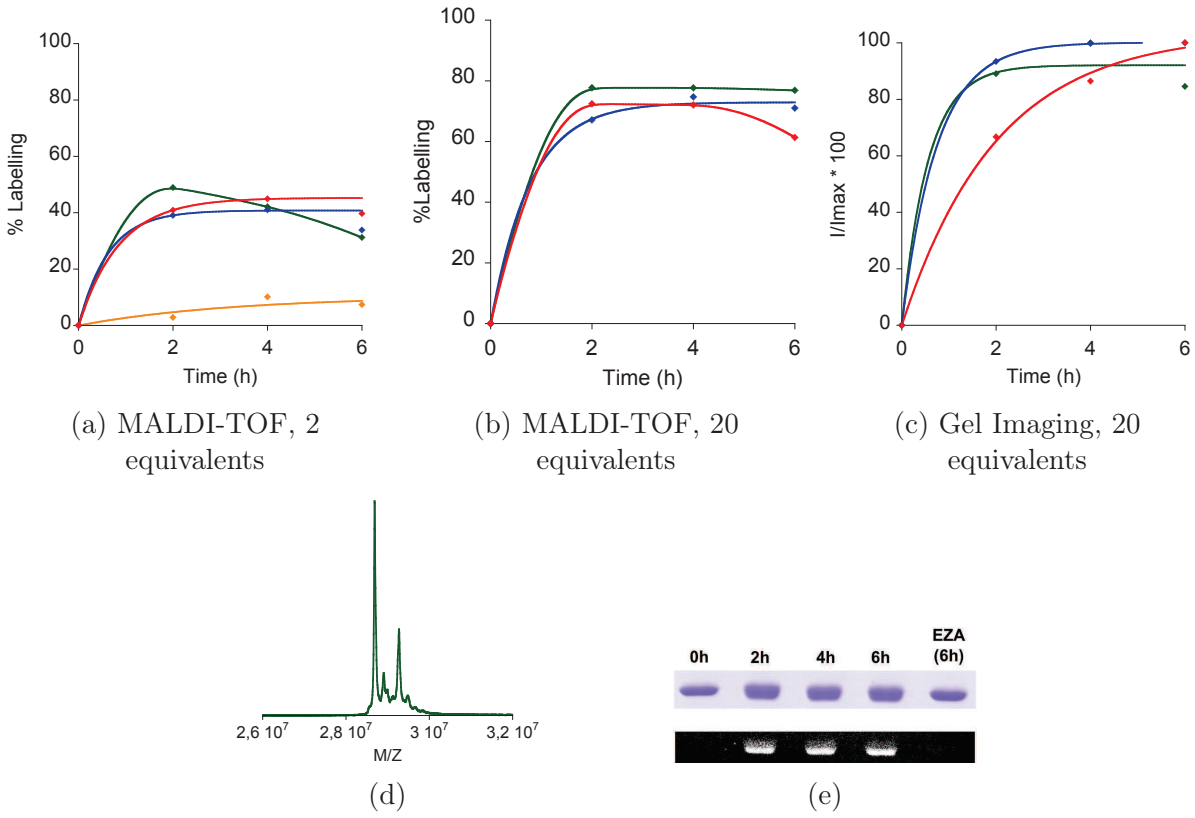

(a) MALDI-TOF, 2 equivalents

(b) MALDI-TOF, 20 equivalents

(c) Gel Imaging, 20 equivalents

(d)

(e)

Figure 3.6: Quantification of *in vitro* labelling of hCA-I by LDAI-SCoMPI reagents. *(a) MALDI-TOF MS:* Time profiles of labelling of hCA-I (10 µM in 50 mM HEPES buffer pH 7.2) for incubation at 37 °C with 2 equivalents of **94** (orange, ReC0), **95** (blue, ReC3), **96** (red, ReC6), **97** (green, ReC5). % Labelling represents the ratio of the area of the labelled protein peak over areas od labelled and unlabelled proteins. *(b) MALDI-TOF MS:* Time profiles of labelling of hCA-I (10 µM in 50 mM HEPES buffer pH 7.2) for incubation at 37 °C with 20 equivalents of **95** (blue, ReC3), **96** (red, ReC6), **97** (green, ReC5); *(c) Fluorescence gel imaging:* Time profiles of labelling of hCA-I (10 µM in 50 mM HEPES buffer pH 7.2) for incubation at 37 °C with 20 equivalents of **95** (blue, ReC3), **96** (red, ReC6), **97** (green, ReC5). Area mean intensities were measured using ImageJ software, and the ratio of the sample intensity over maximal intensity plotted. *(d)* Example of MALDI-TOF spectrum of hCA-I(10 µM) incubated with **97**. The labelled protein peak is starred (*). *(e)* Example of SDS-PAGE analysis for the labelling of hCA-I by 20 equivalents of **97** top: CBB stained, bottom: fluorescence imaging.

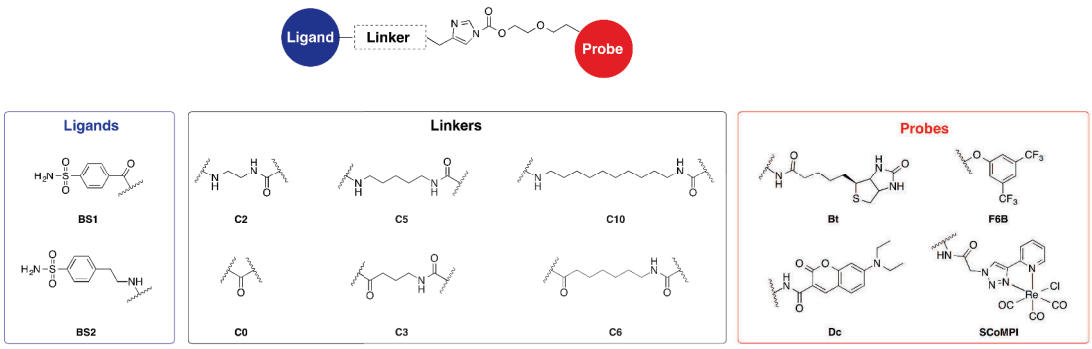

Ligand	Linker	Probe	% Labelled CA1*	Method	Ref
BS1	C2	Dc	43 % (7 h)	Gel imaging	[199]
BS1	C5	Dc	99 % (7 h)	Gel imaging	[199]
BS1	C10	Dc	25 % (7 h)	Gel imaging	[199]
BS1	C5	Dc	65 % (4 h)	MALDI	[199]
BS1	C5	Bt	75 % (4 h)	MALDI	[199]
BS1	C5	F6B	100 % (2 h)	MALDI	[199]
BS1	C5	SCoMPI	40 % (4 h)	MALDI	-
BS2	C0	SCoMPI	10 % (4 h)	MALDI	-
BS2	C3	SCoMPI	40 % (4 h)	MALDI	-
BS2	C6	SCoMPI	45 % (4 h)	MALDI	-

* Experimental conditions: 10 µM hCA-I solution in 50 mM HEPES, incubated with 2 equivalents of LDAI reagent at 37 °C for the indicated time.

Figure 3.7: Comparison of labelling efficiency of LDAI-SCoMPI with published LDAI systems

The labelling efficiency of LDAI-SCoMPI reagents was first evaluated by MALDI-TOF MS. In a first time, we incubated hCA-I (10 µM in 50 mM HEPES buffer pH 7.2) at 37 °C with 2 equivalents of each LDAI-SCoMPI reagent (Figure 3.6a). Compound **94** (ReC0) displayed only poor labelling efficiency, with only about 10% of labelled protein after 6 h. On the contrary, compounds **95** (ReC3), **96** (ReC6) and **97** (ReC5) exhibited comparable labelling yields (around 40%) after 6 h incubation. MALDI spectra of EZA controls were also measured and displayed only the unlabelled protein peak, showing that labelling occurs only upon specific interaction of the LDAI reagent with the protein. Comparison of these results with previously published data is shown in Figure 3.7. First, the effect of the length of the linker on the labelling efficiency is an expected feature of LD strategies: by varying the length of the linker, we vary the area that is "explored" on the protein surface and thus the residues that can be labelled by the acyl-imidazole group. This was already demonstrated in [199] for LDAI reagents bearing C2, C5 and C10 linkers (see table in Figure 3.7, upper rows). "BS1-C2-Probe" and "BS1-C5-Probe" are equivalent to "BS2-C0-Probe" and "BS2-C3-Probe" in terms of number of bonds between the benzenesulfonamide ring and the imidazole ring. The fact that the shorter ReC0 compound is less efficient than ReC3 derivative was thus expected. Secondly, the labelling efficiencies of ReC3, ReC6 and ReC5, although reasonable, are lower than published labelling efficiencies of other probes

(Figure 3.7, table, medium and lower rows). In fact, the probe itself may impact the efficiency of the LDAI reagent, as it interacts with the surface of the protein and influences the conformation of the acyl imidazole near the active site. It was shown, for instance, that the labelling of hCA-I with the small hydrophobic NMR probe F6B occurred very quickly and efficiently compared with other probes such as biotin (Bt) or 7-diaminoethylcoumarin (Dc). The slightly lower efficiency of our reagents may be explained by this interaction of the probe with the protein, and are still reasonable for further studies. Surprisingly, it could be observed that the percentage of labelling decreased for all samples at the longest incubation times. This effect is quite weak for "BS2" LDAI reagents (namely ReC0 (**94**), ReC3 (**95**) and ReC6 (**96**)), but occurs quite early (4 h) for the ReC5 derivative (**97**). This hydrolysis of the bond between the protein and the label might be due to some His labelling: the acyl probe might be transferred to the imidazole side chain of His, resulting in the formation of an acyl imidazole bond more easily hydrolyzed than a carbonate (Ser, Tyr) or carbamate (Lys) bond.

In order to improve the labelling efficiency, we attempted to increase the number of equivalents of LDAI reagents. MALDI-TOF time profiles of the labelling of hCA-I with 20 equivalents of LDAI reagent (ReC3, ReC6 and ReC5) are shown in Figure 3.6b. As expected, increasing the ratio LDAI reagent: hCA-I allowed to efficiently label hCA-I (around 80% for all LDAI-SCoMPI). We also examined the labelling time profile of hCA-I for 20 equivalents of reagent by fluorescence imaging of SDS-PAGE gel. It showed quite similar trends to the MALDI-TOF experiments, as all the reagents had reached their maximal efficiency labelling at 6 h (with a slight delay for ReC6 reagent). Attempts to perform fluorescence gel imaging for 2 equivalents of LDAI reagent were unsuccessful due to the low luminescence signal of the probe.

Taken together, these results showed that: (i) ReC0 reagent is not efficient for the *in vitro* labelling of hCA-I, as expected from formerly published results [199]; (ii) ReC3, ReC6 and ReC5 exhibit lower labelling efficiencies than other LDAI reagents, probably due to interactions of the probe with the protein; these labelling efficiencies are reasonable, though; (iii) increasing the number of equivalents by ten-fold obviously enhanced the labelling efficiency; (iv) the three LDAI reagents (ReC3, ReC6 and ReC6) had similar labelling efficiencies and no clear "winner" could be determined from the MALDI and gel imaging experiments. As a consequence, we chose to test all three compounds for further biological studies. Moreover, we chose to use 10 µM as incubation concentration for cell experiments (instead of the 1 µM generally used for LDAI reagents) in order to improve labelling of endogenous hCA-IX and CA-XII. This concentration is in the typical range of incubation concentrations used for SCoMPIs, and should not impair cell viability.

3.4 Labelling and imaging of Carbonic Anhydrases IX and XII in cells

Finally, we thus investigated the labelling and possible imaging in cells of membrane-bound hCA-IX and CA-XII with three LDAI-SCoMPI reagents, namely ReC5 (**97**), ReC3 (**95**) and ReC6 (**96**). When put under hypoxic conditions, A549 cells overexpress hCA-IX and CA-XII, and can thus be used for the labelling of CA [198]. In their study [198], Hamachi *et al.* showed that CA-XII was labelled with the LDAI reagent up to 3 h of incubation, and that the labelled membrane proteins were then translocated and transferred to lysosomes for degradation. By confocal fluorescence microscopy, membrane labelling was observed at early times, and endosomes were observed at longer times.

Considering these results, we first wanted to examine the fluorescence signal of cells incubated with SCoMPI-LDAI for 3 h, which is the time when membrane labelling is maximum, and for 6 h, when endosomes can be seen. A549 cells were put under hypoxic conditions for 24 h, and incubated for 3 h and 6 h with 10 µM solution of ReC5 reagent. After washings, live cells were observed by fluorescence microscopy. After 3 h, no clear difference could be seen between sample and control experiment. After 6 h, although most of the cells incubated with the reagent did not show obvious difference with control experiment, a few cells seemed to display a faint membrane labelling. However, cell autofluorescence made the interpretation difficult.

We also attempted to detect the labelled CA in fixed cells, both by fluorescence and infrared microscopies. A549 cells were thus grown on CaF_2 slides. Two incubation conditions were tested: after 24 h under hypoxic conditions, A549 cells were fixed either after 6 h incubation in presence of each SCoMPI-LDAI reagent (conditions similar to the previous live cell microscopy experiments), or after 3 h of incubation with SCoMPI-LDAI reagent followed by 3 h of "evolution" of cells, i.e. incubation with DMEM. In this second condition, CAs are expected to be labelled during the first three hours, then internalized in endosomes during the last three hours. Unfortunately, we were unable to detect the signal of SCoMPI neither by fluorescence microscopy nor by infrared microspectroscopy.

Nevertheless, encouraged by the results obtained for *Engrailed* homeodomain by X-fluorescence microscopy, we then attempted to detect SCoMPI in cells using this imaging technique. A549 cells were thus grown on Si_3N_4 slides, put under hypoxic conditions for 24 h, and incubated for 3 hours at 37 °C in presence of ReC5 (10 µM in DMEM), and fixed with PFA (4% in PBS). The cells were first examined using the same conditions as for the homeodomain, but the signal was difficult to detect. Increasing the beam flux and acquisition time (1000 s) enabled us to detect the signal of rhenium. X-fluorescence spectra of cells incubated with ReC5 and of control cells are represented in Figure 3.8. Magnification was made on the 9-11 keV region of the spectra, since the L-band of Re at 10 keV is not mixed with bands of other elements, and can thus be used to detect Re specifically. One

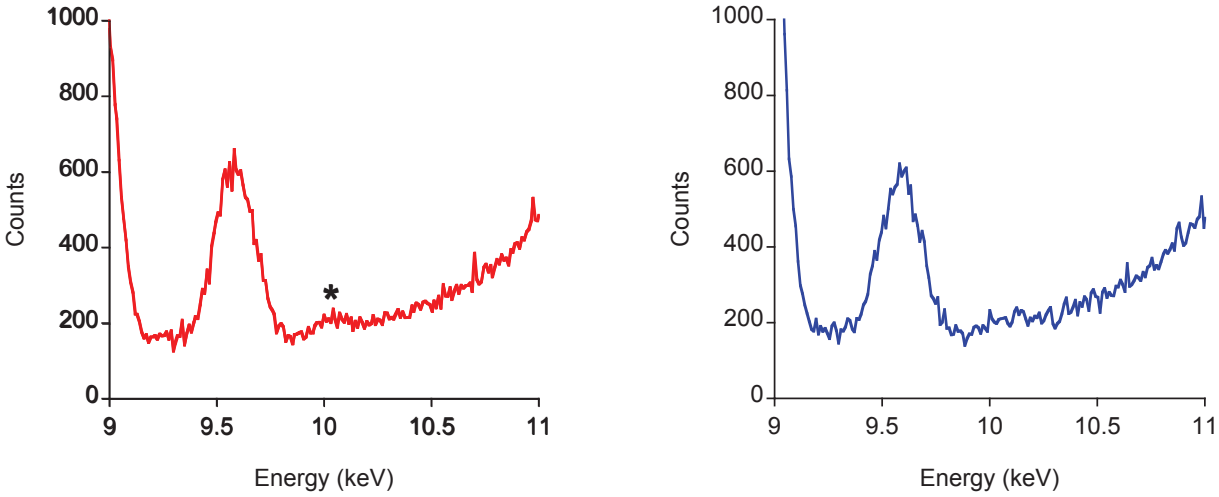

(a) ReC5 (b) Control

Figure 3.8: X fluorescence spectra of A549 cells incubated with 10 µM ReC5 (left) and of control cells (right).

Spectra were recorded for 1000 s. Magnification of the 9-11 keV region of the spectra is represented for both samples. One of the K band of Zinc can be seen in both samples at 9.6 keV with comparable intensities. At 10 keV, one of the L-band of Rhenium can be seen in the sample incubated with ReC5.

of the L-bands of Zinc can be seen at 9.6 keV, with similar intensities for both samples. A small band at 10 keV, assignable to Rhenium, can be seen in the sample incubated with ReC5. Given the long acquisition time needed to record one spectrum, total mapping of a cell could not be performed. However, being able to detect the signal of Re-labelled endogenous CA is very encouraging as regards the sensitivity of X-fluorescence and the potential of Re as X-fluorescence probe. Again, in order to obtain maps, we asked for beamtime at the synchrotron APS (Argonne, Chicago) for the following autumn.

In conclusion, we have synthesized four LDAI-SCoMPI reagents suitable for the "traceless" affinity labelling of CAs. Three of them displayed comparable labelling efficiencies *in vitro* and were used for further studies in cells. Although the signals of SCoMPI could not be detected by fluorescence and infrared microscopies, we were able to detect the signal of Re by X-fluorescence in cells incubated with the ReC5 reagent. This last result, although preliminary, is encouraging, and we are quite confident that mapping of the signal of SCoMPI-labelled CA should be possible in a near future.

Conclusion and perspectives

In the present work, SCoMPIs suitable for labelling of biomolecules *in vitro* and in living cells were developed. Various functional groups could be easily appended to the Re(I) tricarbonyl complexes through the pyta ligand: (i) carboxylic acid for *N*-terminal labelling of peptides; (ii) amine group, used here as an intermediate for the further introduction of a thiol-reactive group; (iii) maleimide group for thiol-specific *in vitro* labelling of a protein; (iv) alcohol function, as a precursor for the formation of a carbonate or carbamate group. It was possible to label *in vitro* cell-penetrating peptides and proteins, as well as endogenous Carbonic Anhydrases. *In vitro*, the SCoMPI-labelled peptides and proteins kept infrared and luminescence properties similar to those of their parent complex.

Table 3.2: Possibility of imaging at the cell level using the modalities of SCoMPIs

	Quantity per cell (mol)	Ref	Fluorescence	Infrared	X fluorescence
CPP (R9, R6W3)					
membrane-bound	$\sim 500 \times 10^{-18}$	[107]	✓	✓	Likely
internalized	$\sim 10 \times 10^{-18}$	[107]			
CysHD *internalized*	$\sim 2 \times 10^{-18}$	*	✗	✗	✓
CA-IX, CA-XII	$\sim 0.3 \times 10^{-18}$	[198]	✗	✗	✓

* Unpublished data

We investigated the possibility to image peptides and proteins at the cell level using the various modalities of SCoMPIs. Cell-penetrating peptides could be easily detected and mapped in cells by both luminescence and infrared modalities of SCoMPI (Table 3.2). Although we did not try to image CPP in cells by X-fluorescence microspectroscopy, it is very likely that they can also be detected using this modality. Rapid screening of the location of the peptides can be performed using the luminescence modality of SCoMPI and fluorescence microscopy. Qualitative estimation of the uptake of the SCoMPI-labelled CPPs is also possible through this modality. However, we showed in Chapter 1 that such complexes could display important luminescence modulations depending on their environment. On the other hand, a more reliable quantification could be done using the infrared modality of the probe.

Although peptides could be easily detected by infrared and fluorescence microscopies, it was not possible to detect neither exogenous (homeodomains) nor endogenous proteins

(carbonic anhydrases) using these two modalities, at least at the cell level. The concentrations involved in these last two cases are lower than those of peptides (Table 3.2), and the quantum yields of SCoMPIs are probably too low to detect such amounts by fluorescence microscopy. On the other hand, it was possible to image homeodomain in cells using X-fluorescence microspectroscopy, and even to detect - although difficultly - endogenous Carbonic Anhydrases in A549 cells. SCoMPIs are thus promising probes for X-fluorescence microspectroscopy, and their application for this kind of imaging is currently being patented.

Considering these results, improving the spectroscopic properties of the SCoMPI (in particular quantum yield) would be desirable in order to obtain higher sensitivity, and thus to be able to detect smaller amounts of labelled biomolecules by fluorescence microscopy. This can be achieved in particular by modifying the diimine ligand of the SCoMPI. Our group recently investigated the luminescence properties of Re(I) tricarbonyl complexes bearing various pyridine triazole analogues. Interestingly, Re(I) tricarbonyl complexes bearing inverse pyridine triazole ligand (1-(2-pyridyl)-1,2,3-triazole, tapy) displayed higher quantum yields than their pyta counterparts, and could be used for the labelling and detection of biomolecules of interest present at low concentrations.

Infrared microspectroscopy gives information on the local environment of the probe: biological processes and SCoMPI concentration can thus be followed simultaneously. In particular, the IR signature of cells changes during cell cycle [202–204]. IR could thus be used to follow the internalization of SCoMPI-labelled CPP at the different steps of the cell cycle, for instance. Although highly valuable, this imaging technique was not sensitive enough to detect low amounts of SCoMPI-labelled proteins at the single cell level. In order to improve the detection by infrared microspectroscopy, labelling with multiple SCoMPI (dimer, trimer, etc.) could be imagined. However, increasing the size of the label may have an impact on the properties of the labelled molecule, including its interactions with environment. Alternatively, it can be envisioned to quantify SCoMPI-labelled biomolecules on cell populations. Infrared imaging is well-suited for thick samples such as tissues or 3D-cell cultures, since infrared light penetrates deeply into samples. In particular, it would be interesting to be able to detect SCoMPI-labelled endogenous CA-IX and CA-XII in tissues, since these proteins are overexpressed in solid tumor cells.

Finally, X-fluorescence microspectroscopy using Re complexes needs to be developed. X-ray fluorescence tomography is an emerging method [205], and three-dimensional imaging of SCoMPI-labelled biomolecules in cell could be performed. As for infrared modality, exchanging Re for an other metal would change the X-ray signature of the complex and thus make possible multi-color X-fluorescence imaging.

SCoMPIs are thus promising tools for the multimodal detection and imaging of biomolecules, and their development will take advantage of the improvements of alternative imaging methods like infrared and X-ray Fluorescence microspectroscopies.

Part II

Experimental section

General considerations

Chemicals and solvents

All chemicals and solvents were purchased from commercial sources (Sigma-Aldrich, Acros, Alfa-Aesar, TCI, Strem, Iris) and were used as received. Dry solvents were purchased from Acros and Sigma and used as received. DOPG was purchased from Avanti Polar Lipids.

Instrumentation and analysis

Purification

Preparative flash chromatography was performed using Normasil 60 (40–60 µm) silica. Analytical HPLC measurements were run on a Dionex Ultimate 3000 instrument using C18 ACE® column (250 × 4.5 mm) packed with spherical 5 µm particles of 300 Å pore size at $1\,mL \cdot min^{-1}$. Preparative HPLC consisted of a dual wavelength UV-Vis absorbance detector (Waters 2487) and a Waters 600 preparative pump. Purification of crude products was achieved with a C18 Nucleodur® preparative column ((250 × 16 mm) packed with spherical 5 µm particles of 300 Å). Experiments were carried out at a flow rate of $14\,mL \cdot min^{-1}$ at room temperature.

Characterization

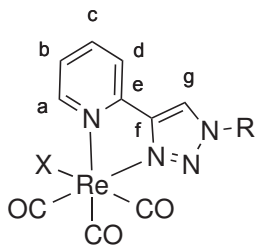

Figure 3.9: Nomenclature used in NMR reports for Re(I) complexes

^{1}H and ^{13}C NMR spectra were recorded on a Bruker DRX300 spectrometer using solvent residual peaks as internal standards [206]. When $CDCl_3$: CD_3OD is indicated as a solvent, a 1:1 ratio of $CDCl_3$: CD_3OD was used as NMR solvent. In this case, the chemical

shifts were calibrated using the residual peak of methanol. For Re(I) complexes and Pyta complexes, the numbering showed in Figure 3.9 is used. J values are given in Hertz.

High resolution mass spectra (HR-MS) were obtained on a Bruker hybride APEX spectrometer (ESI). Peptides were characterized by MALDI-TOF-MS in the positive ion reflector mode on an ABI Voyager DE-Pro MALDI-TOF mass spectrometer (Applied Biosystems) using as matrix a saturated solution of CHCA in ACN/H_2O/TFA (50:50:0.1 v:v:v). UV-visible absorption spectra were recorded on a Varian Cary 300 Bio spectrophotometer, luminescence emission spectra on a Jasco FP-8300 spectrofluorimeter, IR spectra on a Perkin-Elmer Spectrum 100 FT-IR spectrometer.

Imaging

Glass slides were square 18mm×18mm CaF_2 slides were purchased from Crystran (10mm× 10mm × 0.3mm). 1.5mm × 1.5mm × 500nm Si_3N_4 membranes were purchased from Silson Ltd.

Fluorescence imaging was performed using an Olympus X71 microscope equipped with a C9100-02 camera (Hamamatsu Corporation, Sewickley, PA), a X20 objective and a Hg lamp (100W) attenuated by a neutral density filter (ND-1). Luminescence signal of SCoMPIs was detected using the following filter set: excitation D350/50x; beam splitter 400DCLP; emission HQ560/80m; Chroma Technology.

FTIR microspectroscopy was performed on a Nicolet iN10 Infrared Microscope at SOLEIL synchrotron, on SMIS beamline. Aperture was set to 50–50 µm. Spectra were recorded on a 400–4000 cm^{-1} with a 8 cm^{-1} spectral resolution. 256 scans were accumulated for each spectrum. When needed, FTIR interference fringes were removed using the Interference Fringe Removal tool available from http://hines.chem.cornell.edu/FTIR.html and IgorPro.

Chapter 4

N-terminal labelling of peptides with SCoMPIs

4.1 Peptide synthesis

R9 (H-RRRRRRRRR-NH_2), R6W3 (H-RRWWRRWRR-NH_2), Ac-R6W3 (Ac-RRWWRRWRR-NH_2) were synthesized by solid phase peptide synthesis using Boc strategy. Side-chain protected peptides were assembled on MBHA resin (loading $0.54\,\mathrm{mmol}\cdot\mathrm{g}^{-1}$) either manually using HBTU/HOBt as coupling agents in basic conditions or using the peptide synthesizer (Applied Biosystem 433A) with DCC/HOBt as coupling agents. Coupling was achieved using standard coupling conditions: 3 equivalents of Boc-aa-OH, 3 equivalents of HBTU and HOBt and 6 equivalents of DIEA in NMP were shaken with the resin for 1 hour in a reaction vessel (polypropylene syringe with a frit). The side chain of arginine residues was protected by a tosyl group and that of tryptophan residues was protected by a formyl group. Boc group removal was performed using TFA for 1 min (twice) and followed by washing with 10% DIEA in DCM. Deformylation for R6W3 was performed sequentially with 20% piperidine in NMP: once for 1, 3, 5, 7, 15 and 30 min and finally once for 60 min. Cleavage from the resin and tosyl protecting group removal were performed using pure HF in the presence of dimethyl sulfide and anisole for 2 hours at 0 °C. After HF removal, cold diethyl ether was added to precipitate the peptide. The precipitate collected was redissolved using 10% acetic acid in water and freeze-dried. For *N*-terminus acetylated peptides, the acetylation was performed with 10% acetic anhydride in DCM for 1 hour at room temperature. The peptides were synthesized according to standard procedures. When necessary, the peptides were purified by HPLC using a C18 column.

4.2 Synthesis of [Re(CO)$_3$(X)(PytaCOOH)] and labelling of CPP

N-(2-chloroacetyl)-β-alanine methyl ester (57)

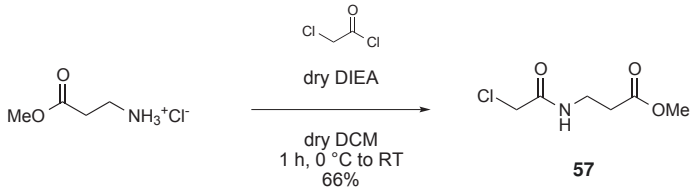

β-alanine methyl ester hydrochloride salt (1.33 g, 9.5 mmol, 1.2 equiv.) was suspended in dry DCM (15 mL) under argon. Dry DIEA (3.5 mL, 20 mmol, 2.5 equiv.) was added, and the suspension was cooled in an ice bath. Chloroacetyl chloride (0.64 mL, 8 mmol, 1 equiv.) was added dropwise, and the reaction mixture was stirred for one hour at room temperature. The organic layer was then diluted with DCM (15 mL), washed once with 0.1N HCl aqueous solution (30 mL), once with 10% $NaHCO_3$ aqueous solution (30 mL) and once with brine (30 mL). It was then dried over anhydrous $MgSO_4$, filtered, and concentrated to yield the expected compound as a colorless oil (0.947 g, 5.3 mmol, 66%).

^{1}H-NMR (300 MHz, $CDCl_3$): δ (ppm) 7.17 (s, 1H, N*H*), 4.03 (s, 2H, ClCH_2), 3.72 (s, 3H, C(O)OCH_3), 3.58 (q, J = 6.0 Hz, 2H, C(O)NHCH_2), 2.58 (t, J = 6.0 Hz, 2H, CH_2COOMe).

^{13}C-NMR (101 MHz, $CDCl_3$): δ (ppm) 172.40 (*C*(O)OCH$_3$), 166.14 (*C*(O)NH), 51.68 (C(O)O*C*H$_3$), 42.40 (Cl*C*H$_2$), 35.14 (NH*C*H$_2$), 33.32 (*C*H$_2$C(O)OCH$_3$).

HR-MS (ESI+): *m/z* calculated for [C$_6$H$_{10}$ClNO$_3$+Na]$^+$: 202.02414, found: 202.02438, error: 1.2 ppm.

N-(2-azidoacetyl)-β-alanine methyl ester (58)

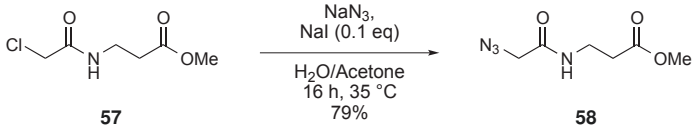

Compound **57** (0.947 g, 5.3 mmol, 1 equiv.) was dissolved in a 3:1 v:v mixture of acetone (15.6 mL) and water (5.2 mL). Sodium azide (0.69 g, 10.6 mmol, 2 equiv.) and sodium iodide (0,079 g, 0.53 mmol, 0.1 equiv.) were then added, and the mixture was stirred at 35 °C (bath temperature) for 16 h. Acetone was removed by rotary evaporation and the solution was diluted with DCM (15 mL) and water (5 mL). The mixture was then decanted, the organic layer dried over $MgSO_4$, filtered and concentrated to compound **58** as a colorless oil (0.78 g, 4.2 mmol, 79%).

^{1}H-NMR (300 MHz, $CDCl_3$): δ (ppm) 6.87 (s, 1H, N*H*), 3.97 (s, 2H,N_3CH_2), 3.72 (s, 3H, C(O)OC*H*$_3$), 3.57 (q, J = 6.0 Hz, 2H, C(O)NHC*H*$_2$), 2.57 (t, J = 6.0 Hz, 2H, C*H*$_2$COOMe).

^{13}C-NMR (101 MHz, $CDCl_3$): δ (ppm) 172.18 (*C*(O)OCH$_3$), 166.94 (*C*(O)NH), 52.00 (C(O)O*C*H$_3$), 51.43 (N_3*C*H$_2$), 34.67 (C(O)NH*C*H$_2$), 33.26 (*C*H$_2$C(O)OCH$_3$). NMR data in agreement with reference [207].

2-(1-[(*N*-3-methoxy-3-oxopropyl)-acetamide]-1*H*-1,2,3-triazol-4-yl)pyridine (59, PytaCOOMe)

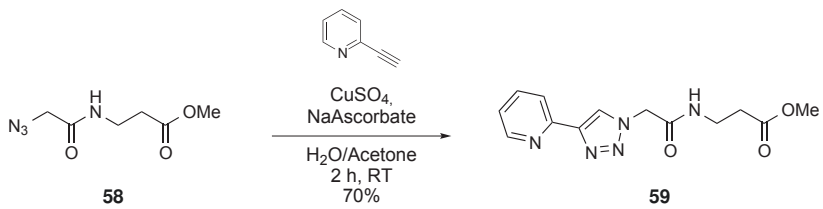

Compound **58** (0.51 g, 2,74 mmol, 1 equiv.) was dissolved in a 2:1 v:v mixture of acetone (36 mL) and water (18 mL). 2-ethynylpyridine (0.28 mL, 2.74 mmol, 1 equiv.), copper sulfate (0.17 g, 0.69 mmol, 0.25 equiv.) and sodium ascorbate (0.14 g, 0.69 mmol, 0.25 equiv.) were then added, and the suspension was sonicated for a few minutes, during which a light brownish precipitate formed. The reaction mixture was then stirred for 2h at room temperature (until the solution turned greenish). The solution was then poured into a 28% ammonia solution and extracted three times with DCM. The organic layers were combined, dried over anhydrous Na_2SO_4, filtered and concentrated. The resulting brown solid was purified by silica gel column chromatography (DCM:EtOAc:MeOH 50:50:0 to 0:98:2 v:v:v) to yield compound **59** (0.56 g, 70%) as a white solid.

^{1}H-NMR (400 MHz, $CDCl_3$): δ (ppm) 8.55 (ddd, J = 4.9, 1.8, 0.9, 1H, H^a pyta), 8.28 (s, 1H, H^g pyta), 8.10 (dt, J = 7.9, 1.0, 1H, H^d pyta), 7.75 (ddd, J = 7.9, 7.6, 1.8, 1H, H^c pyta), 7.21 (ddd, J = 7.5, 4.9, 1.2, 1H, H^b pyta), 6.87 (s, 1H, C(O)N*H*), 5.11 (s, 2H, PytaC*H*$_2$), 3.61 (s, 3H, C(O)OC*H*$_3$), 3.51 (d, J = 6.1, 2H, C(O)NHC*H*$_2$), 2.53 (t, J = 6.2, 2H, C*H*$_2$COOCCH$_3$).

^{13}C-NMR (101 MHz, $CDCl_3$): δ (ppm) 172.5 (*C*(O)OCH$_3$), 165.2 (*C*(O)NH), 149.9 (C^e_{IV} pyta), 149.6 (C^a pyta), 149.0 (C^f_{IV} pyta), 137.0 (C^c pyta), 123.8 (C^g pyta), 123.2 (C^b pyta), 120.4 (C^d pyta), 53.2 (Pyta*C*H$_2$C(O)NH), 52.0 (C(O)O*C*H$_3$), 35.4 (C(O)NH*C*H$_2$), 33.6 (*C*H$_2$C(O)OCH$_3$).

HR-MS (ESI+): *m/z* calculated for $[C_{13}H_{15}N_5O_3+H]^+$: 290.12477, found: 290.11252, error: 1.7 ppm.

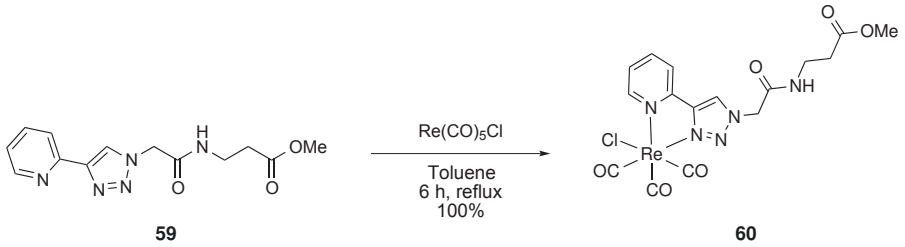

59 **60**

[Re(CO)$_3$(Cl)(PytaCOOMe)] (60)

Compound **59** (36.3 mg, 0.10 mmol, 1 equiv.) was dissolved in hot toluene (1.3 mL). $Re(CO)_5Cl$ (29 mg, 0.1mmol, 1 equiv.) was added, and the suspension was refluxed for 6 h. The resulting yellow precipitate was filtered and washed with cold toluene, to give pure compound **60** (59.5 mg, 0.10 mmol, 100 %).

^{1}H-NMR (400 MHz, $CDCl_3$: CD_3OD): δ (ppm) 8.93 (d, J = 5.4, 1H, H^a pyta), 8.88 (s, 1H, H^g pyta)), 8.09 (m, 2H, H^d + H^c pyta)), 7.49 (q, J = 4.3, 1H, H^b pyta)), 5.33-5.23 (m, 2H, PytaCH_2), 3.68 (s, 3H, C(O)OCH_3), 3.52 (t, J = 6.5, 2H, C(O)NHCH_2), 2.58 (t, J = 6.6, 2H, CH_2COOMe).

^{13}C-NMR (101 MHz, $CDCl_3$: CD_3OD): δ (ppm) 197.6 (Re*C*O), 196.1 (Re*C*O), 189.3 (Re*C*O), 173.1 (*C*(O)OCH$_3$), 165.4 (*C*(O)NH), 153.5 (C^a pyta), 149.9 (C^e_{IV} pyta), 149.5 (C^f_{IV} pyta), 140.7 (C^c pyta), 127.1 (C^g pyta), 126.7 (C^b pyta), 123.2 (C^d pyta), 53.9 (Pyta*C*H$_2$C(O)NH), 52.3 (C(O)O*C*H$_3$), 36.1 (Pyta*C*H$_2$C(O)NH), 34.1 (*C*H$_2$C(O)OCH$_3$).

IR: ν_{ReCO}/cm^{-1} 2025, 1898.

HR-MS (ESI+): *m/z* calculated for $[C_{16}H_{15}ClN_5O_6Re + Na]^+$: 616.01326, found: 616.01333, error: 0.1 ppm.

[Re(CO)$_3$(Cl)(PytaCOOH)] (61)

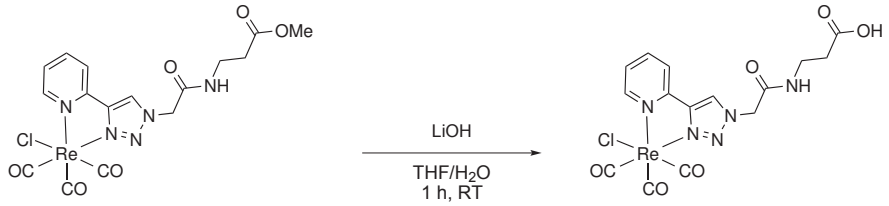

60 **61**

Methyl ester **60** (59.4mg, 0.100 mmol, 1 equiv.) was dissolved in a 2:1 mixture of THF/H_2O (1mL). $LiOH \cdot H_2O$ (5.0 mg, 0.119 mmol, 1 equiv.) was added, and the reaction mixture was stirred at room temperature for 1 hour. THF was removed by rotary evaporation (bath temperature 45 °C). A 1M aqueous solution of HCl was added dropwise to the resulting solution, until pH reached 1 (about 0.5 mL). 1 mL of distilled water was added, and the aqueous solution was extracted with EtOAc (15mL). The organic layer was washed once with brine (2 mL). The aqueous layers were extracted twice more with EtOAc (15mL).

Organic layers were pooled, dried over anhydrous Na_2SO_4, filtered and concentrated to give the desired compound **61** as a yellow powder (46.5 mg, 0.080 mmol, 80%).

^{1}H-NMR (400 MHz, $CDCl_3$: CD_3OD): δ (ppm) 8.95 (d, J = 5.4, 1H, H^a pyta), 8.81 (s, 1H, H^g pyta), 8.10-8.04 (m, 2H, H^d + H^c pyta), 7.49 (td, J = 6.3, 1.4, 1H, H^b pyta), 5.25 (q, J = 19.9, 2H, PytaCH_2), 3.52 (t, J = 6.6, 2H, C(O)NHCH_2), 2.56 (t, J = 6.6, 2H, CH_2COOMe).

^{13}C-NMR (101 MHz, $CDCl_3$: CD_3OD): δ (ppm) 197.5(Re*C*O), 195.9(Re*C*O), 189.3(Re*C*O), 174.5 (*C*(O)OH), 165.3 (*C*(O)NH), 153.6 (C^a pyta), 150.0 (C^e_{IV} pyta), 149.5 (C^f_{IV} pyta), 140.6 (C^c pyta), 126.75 (C^g pyta), 126.60 (C^b pyta), 123.0 (C^d pyta), 53.8 (Pyta*C*H$_2$C(O)NH), 36.2 (Pyta*C*H$_2$C(O)NH), 34.0 (*CH2C(O)OH*).

HR-MS (ESI+): *m/z* calculated for $[C_{15}H_{13}ClN_5O_6Re + Na]^+$: 601.99761, found: 601.99786, error: 0.4 ppm.

[Re(CO)$_3$(Br)(PytaCOOMe)] (62)

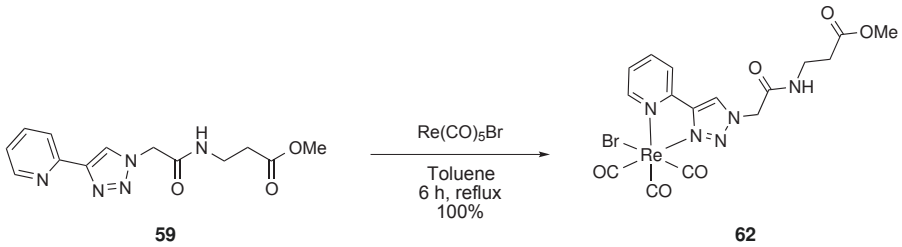

59 62

Compound **59** (146 mg, 0.50 mmol, 1 equiv.) was dissolved in hot toluene (4 mL). Rhenium pentacarbonyl bromide (205 mg, 0.5 mmol, 1 equiv.) was added, and the suspension was refluxed for 6 h. The resulting yellow precipitate was filtered and washed with cold toluene, to give pure compound **62** (323 mg, 0.5 mmol, 100 %).

^{1}H-NMR (300 MHz, $CDCl_3$: CD_3OD): δ (ppm) 8.99 (d, J = 5.5, 1H, H^a pyta), 8.84 (s, 1H, H^g pyta), 8.10-8.08 (m, 2H, H^d + H^c pyta), 7.53-7.48 (m, 1H, H^b pyta), 5.27 (q, J = 17.4 Hz, 2H, PytaCH_2), 3.70 (s, 3H, C(O)OCH_3), 3.54 (t, J = 6.4 Hz, 2H, C(O)NHCH_2), 2.60 (t, J = 6.5, 2H, CH_2COOMe).

^{13}C-NMR (75 MHz, $CDCl_3$: CD_3OD): δ (ppm) 172.10 (*C*(O)OCH$_3$), 164.40 (*C*(O)NH), 152.74 (C^a pyta), 149.02 (C^e_{IV} pyta), 148.53 (C^f_{IV} pyta), 139.35 (C^c pyta), 125.73 (C^g pyta), 125.49 (C^b pyta), 121.95 (C^d pyta), 52.69 (Pyta*C*H$_2$C(O)NH), 51.17 (C(O)O*C*H$_3$), 35.10 (Pyta*C*H$_2$C(O)NH), 32.99 (*CH2C(O)OCH3*).

IR: ν_{ReCO}/cm^{-1} 2025, 1898.

HR-MS (ESI+): *m/z* calculated for $[C_{16}H_{15}BrN_5O_6Re + Na]^+$: 659.96275, found: 659.96321, error: 0.7 ppm.

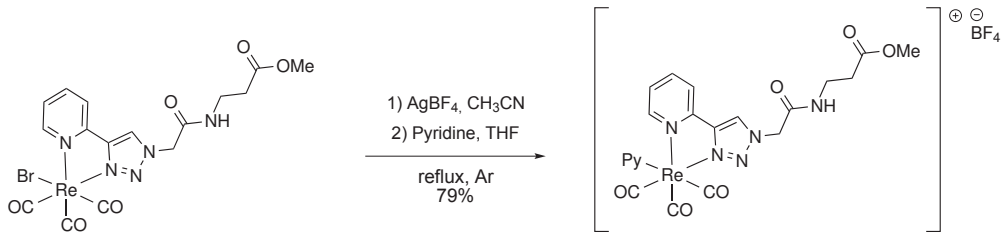

62 **63**

$[Re(CO)_3(Py)(PytaCOOMe)]^+BF_4^-$ (63)

Rhenium tricarbonyl bromide derivative **62** (252.3 mg, 0.394 mmol, 1 equiv.) was dissolved in acetonitrile (49 mL) under argon. Silver tetrafluoroborate (78.9 mg, 0.405 mmol, 1 equiv.) was added and the mixture was refluxed for 5 h, resulting in the formation of a fine dark suspension. Solvent was evaporated to dryness, and the residue was dissolved in THF (58 mL). Pyridine (96 µL, 1.18 mmol, 3 equiv.) was added, and the reaction mixture was refluxed for 20 h. The suspension was filtered over celite and the solvent was removed by rotary evaporation. The crude was co-evaporated three times with toluene, dissolved in the minimal amount of methanol and precipitated in diethyl ether, to give the desired compound **63** as a yellow powder (224.7 mg, 0.310 mmol, 79%).

^{1}H-NMR (400 MHz, CD_3OD : $CDCl_3$): δ (ppm) 9.28 (ddd, J = 5.6, 1.4, 0.8, 1H, H^a pyta), 8.96 (s, 1H, H^g pyta), 8.38 (dt, J = 5.2, 1.4, 2H, $H^{a'}$ pyridine), 8.25 (td, J = 7.8, 1.5, 1H, H^c pyta), 8.15 (ddd, J = 7.9, 1.2, 0.9, 1H, H^d pyta), 7.90 (tt, J = 7.7, 1.5, 1H, $H^{c'}$ pyridine), 7.75 (ddd, J = 7.6, 5.6, 1.4, 1H, H^b pyta), 7.42-7.38 (m, 2H, $H^{b'}$ pyridine), 5.48 (s, 2H, PytaCH_2), 3.69 (s, 3H, C(O)OCH_3), 3.56 (t, J = 6.6, 2H, C(O)NHCH_2), 2.62 (t, J = 6.6, 2H, CH_2COOMe).

^{13}C-NMR (101 MHz, CD_3OD : $CDCl_3$): δ (ppm) 196.60 (Re*C*O), 195.19 (Re*C*O), 192.18 (Re*C*O), 173.60 (*C*(O)OCH$_3$), 166.27 (*C*(O)NH), 154.93 (C^a pyta), 153.31 (2C, $C^{a'}$ pyridine), 150.48 (C^e_{IV} pyta), 150.40 (C^f_{IV} pyta), 142.68 (C^c pyta), 140.96 ($C^{c'}$ pyridine), 128.97 (C^f pyta), 128.65 (C^b pyta), 127.91 ($C^{b'}$ pyridine), 124.26 (C^d pyta), 54.71 (Pyta*C*H$_2$C(O)NH), 52.28 (C(O)O*C*H$_3$), 36.70 (C(O)NH*C*H$_2$CH$_2$), 34.41 (CH$_2$*C*H$_2$C(O)OCH$_3$).

IR: ν_{ReCO}/cm^{-1} 2034, 1917.

HR-MS (ESI+): *m/z* calculated for $[C_{21}H_{20}N_6O_6Re]^+$: 637.09684, found: 637.09735, error: 0.7 ppm.

$[Re(CO)_3(Py)(PytaCOOH)]^+BF_4^-$(64)

Compound **64** was prepared according to the same procedure as compound **61**: compound **63** (148.6 mg, 0.205 mmol, 1 equiv.) was dissolved in a 2:1 v:v mixture of THF (1.3 mL) and water (0.65 mL). Lithium hydroxide monohydrate (8.8 mg, 0.210 mmol, 1 equiv.) was then added, and the reaction mixture was stirred for 1 h at room temperature. THF was removed by rotary evaporation, and the solution was acidified to pH<1 with 1N HCl aque-

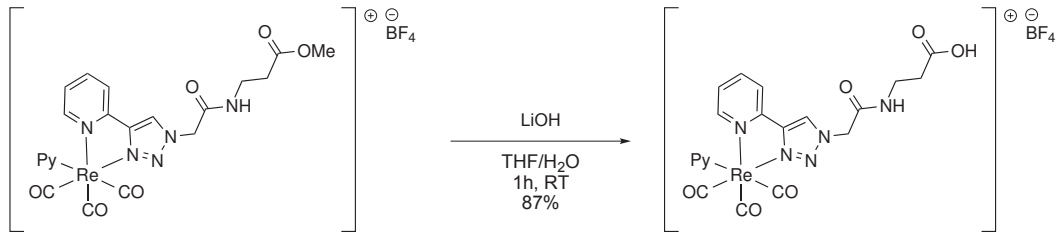

63 **64**

ous solution. The aqueous layer was extracted three times with EtOAc (5mL). The organic layers were combined, dried over anhydrous Na_2SO_4, filtered and concentrated to give compound **64** (127.2 mg, 0.179 mmol, 87%) as a yellow powder.

^{1}H-NMR (400 MHz, CD_3OD): δ (ppm) 9.28 (ddd, J = 5.6, 1.4, 0.8, 1H, H^a pyta), 8.97 (s, 1H, H^g pyta), 8.40-8.37 (m, 2H, $H^{a'}$ pyridine), 8.25 (td, J = 7.8, 1.5, 1H, H^c pyta), 8.15 (ddd, J = 8.0, 1.3, 0.9, 1H, H^d pyta), 7.91 (tt, J = 7.7, 1.5, 1H, $H^{c'}$ pyridine), 7.75 (ddd, J = 7.7, 5.6, 1.4, 1H, H^b pyta), 7.42-7.39 (m, 2H, $H^{b'}$ pyridine), 5.49 (s, 2H, PytaCH_2), 3.55 (t, J = 6.7, 2H, C(O)NHCH_2), 2.60 (t, J = 6.7, 2H, CH_2COOH).

^{13}C-NMR (101 MHz, CD_3OD): δ (ppm) 196.6 (Re*C*O), 195.2 (Re*C*O), 192.1 (Re*C*O), 175.0 (*C*(O)OH), 166.3 (*C*(O)NH), 154.9 (C^a pyta), 153.3 (2C, $C^{a'}$ pyridine), 150.49 (C^e_{IV} pyta), 150.43 (C^f_{IV} pyta), 142.7 (C^c pyta), 141.0 ($C^{c'}$ pyridine), 129.0 (C^f pyta), 128.6 (C^b pyta), 127.9 (2C, $C^{b'}$ pyridine), 124.3 (C^d pyta), 54.7 (Pyta*C*H$_2$C(O)NH), 36.8 (C(O)NH*C*H$_2$CH$_2$), 34.4 (CH$_2$*C*H$_2$C(O)OH).

HR-MS (ESI+): *m/z* calculated for $[C_{20}H_{18}N_6O_6Re]^+$: 623.08119, found: 623.08152, error: 0.5 ppm.

Py-R6W3 (67)

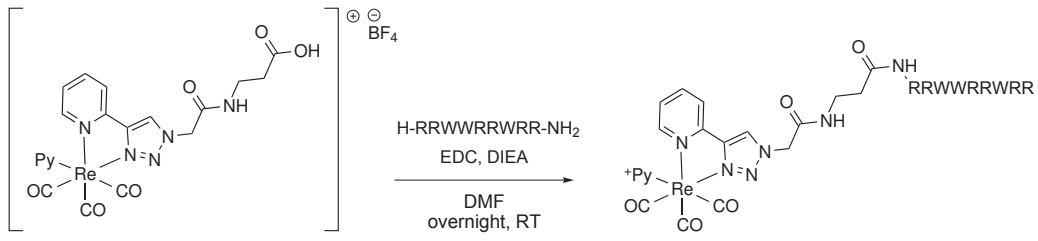

64 **67**

A solution of EDC in DMF (33.3 mg/mL, 187 µL, 32.5 µmol, 1.5 equiv.) were added to compound **64** (15.4 mg, 21.7 µmol, 1 equiv.). The mixture was stirred for 20 min before addition of a solution of R6W3 in DMF (462 mg/mL, 108 µL, 21.6 µmol, 1 equiv.) and of DIEA (7.5 µL, 43.3 µmol, 2 equiv.). The mixture was stirred overnight at room temperature and the crude was purified by HPLC (10 to 70 % ACN 0.1% TFA in 30 min, 14 mL/min, 14 min, purity: 90 %).

MALDI-TOF-MS (CHCA matrix): 2040.48 $[M-Py]^+$

Cl-R6W3 (65)

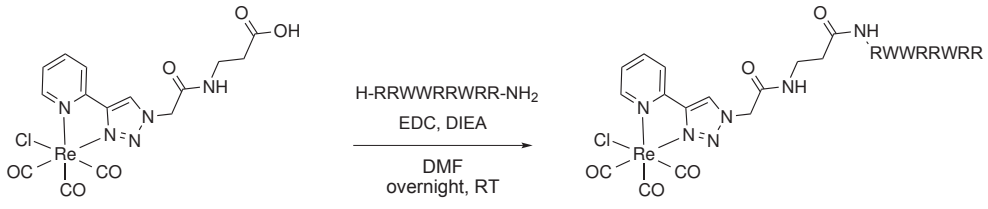

61 65

The procedure is similar to the one used for Py-R6W3 (**67**). A solution of EDC in DMF (33.3 mg/mL, 187 µL, 32.5 µmol, 1.5 equiv.) were added to compound **61** (12.6 mg, 21.7 µmol, 1 equiv.). The mixture was stirred for 20 min before addition of a solution of R6W3 in DMF (462 mg/mL, 108 µL, 21.6 µmol, 1 equiv.) and of DIEA (7.5 µL, 43.3 µmol, 2 equiv.). The mixture was stirred overnight at room temperature and the crude was purified by HPLC (10 to 70 % ACN 0.1% TFA in 30 min, 14 mL/min, 12.8 min, purity: 95 %). The collected pure fraction was frozen and freeze-dried immediately after purification in order to prevent the exchange of the chloride.

MALDI-TOF-MS (CHCA matrix): 2039.8 $[M-Cl]^+$

Py-R9 (68)

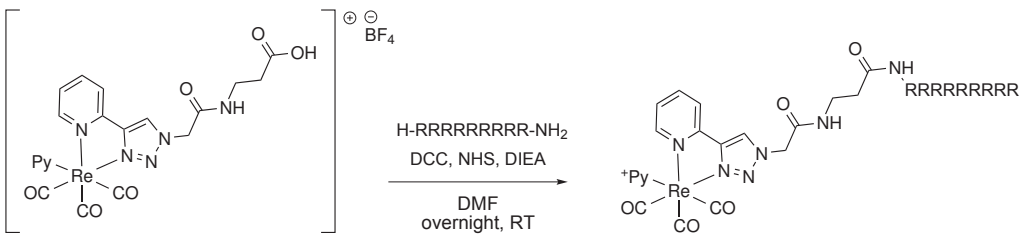

64 68

Compound **64** (17.7 mg, 24.5 µmol, 1.5 equiv.) and N-hydroxysuccinimide (4.8 mg, 42.6 µmol, 2.5 equiv.) were dissolved in a solution of DCC in DMF (4.13 mg/mL, 850 µL, 17.7 µmol, 1.1 equiv.). The mixture was stirred for 20 min, followed by addition of an aqueous solution of R9 (50 mg/mL, 680 µL, 16.8 µmol, 1 equiv.) and DIEA (8.5 µL, 49.1 µmol, 2.9 equiv.). The reaction mixture was stirred overnight at room temperature and then purified by HPLC (10 to 70 % ACN 0.1% TFA in 30 min, 14 mL/min, 10.6 min, purity: > 99 %).

MALDI-TOF-MS (CHCA matrix): 1692.9 $[M-Re(CO)_3Py]^+$

Cl-R9 (66)

Compound **61** (16.1 mg, 27.7 µmol, 1.6 equiv.) and N-hydroxysuccinimide (3.9 mg, 33.8 µmol, 2 equiv.) were dissolved in a solution of DCC in DMF (4.13 mg/mL, 850 µL, 17.7 µmol, 1.1

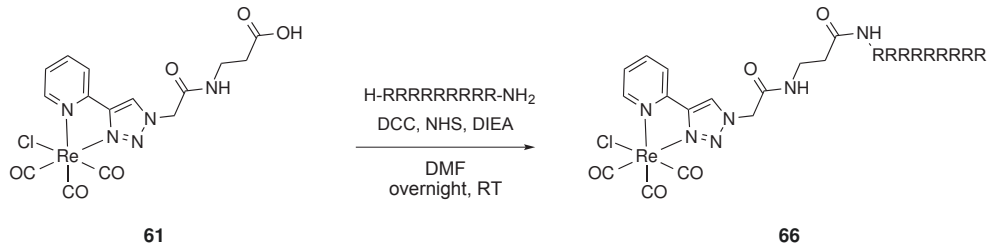

61 66

equiv.). The mixture was stirred for 20 min, followed by addition of an aqueous solution of R9 (50 mg/mL, 680 µL, 16.8 µmol, 1 equiv.) and DIEA (8.5 µL, 49.1 µmol, 2.9 equiv.). The reaction mixture was stirred overnight at room temperature and then purified by HPLC (10 to 70 % ACN 0.1% TFA in 30 min, 14 mL/min, 10.6 min, purity: 92 %). Right after purification, the collected pure fraction was frozen and freeze-dried to prevent the exchange of the chloride.

MALDI-TOF-MS (CHCA matrix): 1692.9 $[M-Re(CO)_3Cl]^+$

IR: ν_{ReCO}/cm^{-1} 2035, 1917.

4.3 Preparation of Large Unilamellar Vesicles (LUV)

319 µL of a DOPG stock solution in chloroform (25 mg/mL, 10 µmol) were diluted in a few mL of chloroform in a 100 mL round-bottomed flask. Chloroform was slowly removed by rotary evaporation and the resulting lipid film was dried under vacuum for at least 1h. It was then hydrated with 10 mL of PBS (pH 7.4). The resulting lipid suspension was then extruded 7 times through 200 nm pores filter and 10 times through 100 nm pores filter. The stock solution was stored at 4 °C and used within 15 days.

4.4 Fluorescence measurement methodology

1 mM stock solutions in PBS were prepared for all peptides. Concentration was controlled by UV-visible. Fluorescence measurements were performed using 3 mL quartz cuvettes. For each measurement, 3 mL of a solution of LUV at the desired concentration were prepared and the blank spectra recorded. 3 µL of stock solution of peptide were then added, and the mixture was incubated 5 min before sample spectra recording.

4.5 Imaging on CHO and HaCaT cells

4.5.1 Internalization of Cl-R9 and Py-R9 in CHO cells

Stock solutions

Stock solutions of peptide were prepared in PBS and stored at 4 °C. Their concentration was checked by measuring UV absorbance at 280 nm.

Incubation conditions

Chinese Hamster Ovarian cells were seeded in 12-well plates containing $10 \sim 10 \sim 0.3\,\mathrm{mm}^3$ CaF_2 slides, and grown for 24 h. Cells were washed once with HBSS buffer and once with fresh DMEM. Cells were then incubated with 10 µM solutions of peptide in DMEM for one hour at 37 °C. Cells were washed twice with PBS, and incubated for 8 min with 500 µL of a 4% PFA solution in PBS at room temperature. Finally, cells were washed once with PBS and twice with milliQ water. CaF_2 slides were left to dry at air prior to examination by microscopy.

Fluorescence imaging of SCoMPI-CPP in CHO cells

Fluorescence imaging of peptides in CHO cells was performed using an Olympus X71 microscope equipped with a C9100-02 camera (Hamamatsu Corporation, Sewickley, PA), a X20 objective and a Hg lamp (100W) attenuated by a neutral density filter (ND-1). Luminescence signal of SCoMPIs was detected using the following filter set: excitation D350/50x; beam splitter 400DCLP; emission HQ560/80m; Chroma Technology.

Data processing. Bright regions of interest (ROI) were automatically detected using ImageJ software Macro functionality. ROI which areas were inferior to 75 pixels^2 were arbitrarily removed from data set, as they were identified as artefactual. Mean intensities were corrected with background and averaged.

IR imaging of SCoMPI-CPP in CHO cells

FTIR microspectroscopy was performed on a Nicolet iN10 Infrared Microscope. Aperture was set to $50\times50\,\mu\mathrm{m}^2$ aperture. Spectra were recorded from 400to4000 cm^{-1} with a $8\,\mathrm{cm}^{-1}$ spectral resolution. 256 scans were accumulated for each spectrum. When needed, FTIR interference fringes were removed using the Interference Fringe Removal tool available from http://hines.chem.cornell.edu/FTIR.html and IgorPro. Peak area of SCoMPI A-band (R9PytaPy: 2055-2017 cm-1; R9PytaCl: 2044-2005 cm-1) and Amide-II band (1573-1493) were integrated using Omnic software. The ratio Area(A-band)/Area(Amide II) was calculated for each spectrum.

4.5.2 Internalization of R9Cl in synchronized HaCaT cells.

Incubation conditions

HaCaT cells were seeded in 6-well plates containing 10 $\sim$ 10 $\sim$ mm^2 glass slides, and grown for 24 h. Cells were then cultured either in serum-containing (FBS+, control) or serum deprived (FBS-, sample) culture medium for three days. After this time, at t = 0h, all cells were supplemented with fresh FBS+ culture medium. Every 2 h from t = 24 h to t = 32h, one well of FBS+ cells and one well of FBS- were incubated with 10 µM solutions of Cl-R9 in DMEM for one hour at 37 °C. Cells were washed twice with PBS, and incubated for 8 min with 500 µL of a 4% PFA solution in PBS at room temperature. Finally, cells were washed once with PBS and twice with milliQ water. Glass slides were left to dry at air prior to examination by fluorescence microscopy.

Fluorescence imaging of Cl-R9 on synchronized HaCaT cells

Experimental setup was the same as described in section 4.5.1. DAPI was detected using the following filter set: excitation D350/50x; beam splitter 400DCLP; emission D460/50m; Chroma Technology.

Data processing. For each picture, *all* cells were manually contoured and set as regions of interest (ROI) using ImageJ software and the DIC channel. The mean intensity of SCoMPI luminescence was collected for each ROI, corrected with background, and averaged. A each time, ratio of mean intensity of synchronized sample over unsychronized control was also calculated.

Chapter 5

In vitro labelling of *Engrailed-2* Homeodomain

5.1 Procedures for the synthesis of Re(I) tricarbonyl complexes for thiol-maleimide labelling

N-(*tert*-Butoxycarbonyl)-2-bromoethylamine (70)

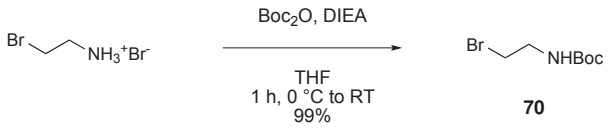

2-bromoethylamine hydrobromide salt (1.02 g, 4.98 mmol, 1 equiv.) was suspended in THF (80 mL). Di-*tert*-butyl dicarbonate (1.23g, 5.64 mmol, 1.1 equiv.) was then added. The white suspension was cooled in an ice bath, and DIEA (1.6 mL, 9.95 mmol, 2 equiv.) was added dropwise. The reaction mixture was stirred for 1 hour, then solvent was removed by rotary evaporation. The resulting crude was dissolved in EtOAc and washed once with 10% aqueous $NaHCO_3$ and once with brine. The organic layer was then dried over anhydrous $MgSO_4$, filtered and concentrated to give the desired compound as a colorless oil (1.107 g, 4.94 mmol, 99%).

^{1}H-NMR (300 MHz, $CDCl_3$): δ (ppm) 4.95 (s, 1H), 3.54-3.51 (m, 2H), 3.47-3.44 (m, 2H), 1.45 (s, 9H); in agreement with reference [208].

N-(2-azidoethyl)-N-(*tert*-Butoxycarbonyl)amine (71)

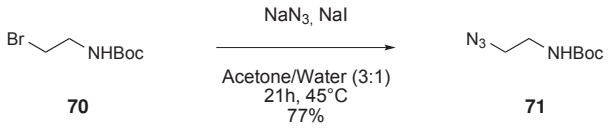

N-(*tert*-Butoxycarbonyl)-2-bromoethylamine (616.8 mg, 2.75 mmol, 1 equiv.) was dissolved in a mixture of acetone and water (10.7 mL, acetone:H_2O 3:1 v:v). The solution was warmed to 45 °C (bath temperature), then sodium azide (359.2 mg, 5.52 mmol, 2 equiv.) and sodium iodide (354.0 mg, 2.36 mmol, 0.85 equiv.) were added. The mixture was stirred overnight, then more sodium azide (187.4 mg, 2.88 mmol, 1 equiv.) was added and the reaction mixture was stirred for 5 more hours. DCM (15 mL) and H_2O (5mL) were added to reaction mixture, and the mixture was decanted. The aqueous layer was extracted once more with DCM (5mL). Organic layers were pooled, dried over anhydrous $MgSO_4$, filtered and concentrated to give *N*-(2-azidoethyl)-*N*-(*tert*-Butoxycarbonyl)amine as a colorless oil (394.0 mg, 2.11 mmol, 77%)

^{1}H-NMR (300 MHz, $CDCl_3$): δ (ppm) 4.84-4.80 (br, 1H, N*H*), 3.41 (t, J = 5.4, 2H, CH_2), 3.30 (t, J = 5.6, 2H, CH_2), 1.44 (s, 9H, C(CH_3)$_3$Boc).

^{13}C-NMR (75 MHz, $CDCl_3$): δ (ppm) 155.83 (O*C*(O)NH), 79.78 (*C*(CH_3)$_3$), 51.25 (N_3*C*H_2), 40.10 (*C*H_2NHBoc), 28.40 (3C, C(*C*H_3)$_3$Boc).

NMR data are in agreement with reference [209].

2-(1-[*N*-*tert*-butoxycarbonyl)ethanamine]-1*H*-1,2,3-triazol-4-yl)pyridine (72)

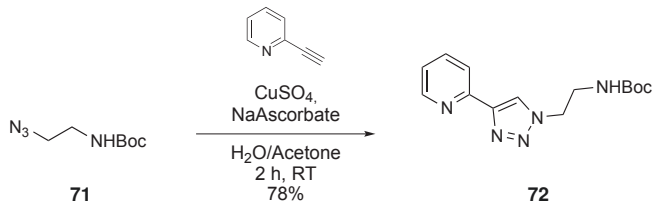

N-(2-azidoethyl)-*N*-(*tert*-Butoxycarbonyl)amine (568 mg, 3.05 mmol, 1 equiv.) was dissolved in a mixture of acetone and water (30 mL acetone:water 2:1 v:v). Anhydrous copper sulfate (131 mg, 0.82 mmol, 0.25 equiv.) and sodium ascorbate (153.8 mg, 0.77 mmol, 0.25 equiv.), followed by 2-ethynylpyridine (310 µL, 3.07 mmol, 1 equiv.), were added. The mixture was sonicated for a few minutes, and reaction mixture was stirred at room temperature for 2 hours. A light brown precipitate formed. Acetone was removed by rotary evaporation, and the aqueous layer was diluted with 28% aqueous ammonia solution. The aqueous layer was extracted once with DCM. The organic layer was then washed once more with 28% ammonia solution, and once with brine. It was then dried over anhydrous Na_2SO_4, filtered and concentrated. The resulting brown solid was purified by automated silica gel flash column chromatography (0-100% EtOAc in cyclohexane) to yield the desired compound as a white solid (692 mg, 2.39 mmol, 78%).

^{1}H-NMR (300 MHz, $CDCl_3$): δ (ppm) 8.33 (d, J = 4.6, 1H, H^a pyta), 8.01 (s, 1H, H^g pyta), 7.90 (d, J = 7.9, 1H, H^d pyta), 7.57 (td, J = 7.7, 1.7, 1H, H^c pyta), 7.03 (ddd, J = 7.5, 4.9, 0.9, 1H, H^b pyta), 5.99 (br, 1H, N*H*), 4.41 (t, J = 5.4, 2H, PytaCH_2), 3.56 (q, J = 5.4, 2H, CH_2NHBoc), 1.30 (s, 9H, C(CH_3)$_3$Boc).

^{13}C-NMR (75 MHz, $CDCl_3$): δ (ppm) 155.91 (O*C*(O)NH), 149.74 (C^e_{IV} pyta), 149.01 (C^a pyta), 147.79 (C^f_{IV} pyta), 136.60 (C^c pyta), 122.74 (C^g pyta), 122.53 (C^b pyta), 119.82 (C^d pyta), 79.41 ($C(CH_3)_3$), 50.11 (Pyta*C*H_2), 40.57 (*C*H_2NHBoc), 28.19 (3C, C(*C*H_3)$_3$Boc).

HR-MS (ESI+): *m/z* calculated for CHCA: [C14H19N5O2 + H]+, found: 290.16115, error: 290.16167 ppm.1.8

[$Re(CO)_3$(Cl)(PytaNHBoc)] (73)

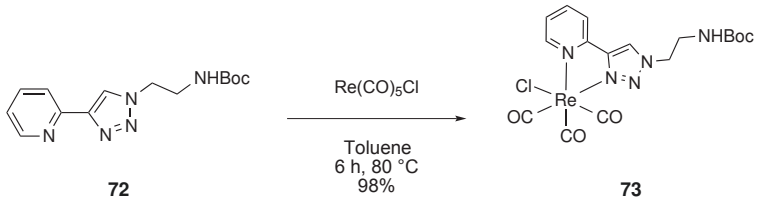

The ligand **72** (49.5 mg, 0.171 mmol, 1 equiv.) was dissolved in warm toluene (5 mL). Rhenium pentacarbonyl chloride (62.9 mg, 0.174 mmol, 1 equiv.) was added, and the mixture was heated at 80 °C (bath temperature) for 6 hours, during which a yellow precipitate formed. The yellow precipitate was filtered and washed with cold toluene to obtain the desired compound (99.7 mg, 0.168 mmol, 98%).

^{1}H-NMR (300 MHz, $CDCl_3$: CD_3OD): δ (ppm) 8.95 (d, J = 5.5, 1H, H^a pyta), 8.77 (s, 1H, H^g pyta), 8.10-8.02 (m, 2H, H^c + H^d pyta), 7.48 (ddd, J = 6.8, 5.6, 2.1, 1H, H^b pyta), 4.64-4.60 (m, 2H, PytaCH_2), 3.62 (t, J = 5.8, 2H, CH_2NHBoc), 1.38 (s, 9H, C(CH_3)$_3$Boc).

^{13}C-NMR (75 MHz, $CDCl_3$: CD_3OD): δ (ppm) 197.3 (Re*C*O), 195.8 (Re*C*O), 188.8 (Re*C*O), 157.4 (O*C*(O)NH), 153.7 (C^a pyta), 150.0 (C^e_{IV} pyta), 149.4 (C^f_{IV} pyta), 140.4 (C^c pyta), 126.5 (C^g pyta), 125.6 (C^b pyta), 122.9 (C^d pyta), 80.5 ($C(CH_3)_3$), 52.4 (Pyta*C*H_2), 40.5 (*C*H_2NHBoc), 28.5 (3C, C(*C*H_3)$_3$Boc).

IR: ν_{ReCO}/cm^{-1} 2025, 1902.

HR-MS (ESI+): *m/z* calculated for $[C_{17}H_{19}ClN_5O_5Re + Na]^+$: 616.04965, found: 616.05007, error: 0.7 ppm.

[$Re(CO)_3$(Cl)(PytaNH−maleimide)] (74, [$Re(CO)_3$(Cl)(PytaNH−mal)])

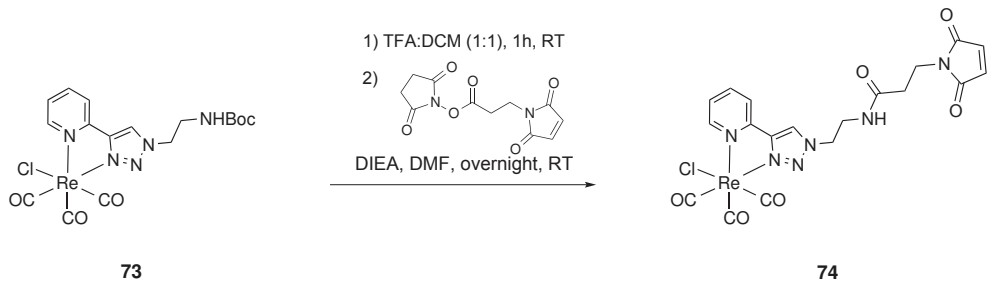

[$Re(CO)_3$(Cl)(PytaNHBoc)] derivative (30.5 mg, 51.3 µmol, 1.3 equiv.) was dissolved in DCM (1 mL) and TFA (1mL) was added drop wise. The reaction mixture was stirred at room temperature for 1 hour, then precipitated in cold Et_2O. The resulting solid was dried under vacuum, put under argon, and dissolved in dry DMF (1.2 mL). 3-maleimidopropionic acid *N*-hydroxysuccinimide ester (10.6 mg, 39.8 µmol, 1 equiv.), then DIEA (27 µL, 156 µmol, 3.9equiv.), were added. Reaction mixture was stirred overnight at room temperature. DMF was removed by rotary evaporation and the resulting crude was directly purified by HPLC (30 to 100 % ACN 0.1% TFA in 30 min, 14 mL/min, 9.3 min, purity: $>98\%$). The collected fraction was frozen in liquid nitrogen immediately after purification to prevent exchange of the chloride ligand.

^{1}H-NMR (400 MHz, $CDCl_3$: CD_3OD): δ (ppm) 8.96 (ddd, J = 5.6, 1.4, 0.9, 1H, H^a pyta), 8.83 (s, 1H, H^g pyta), 8.10-8.08 (m, 1H, H^c pyta), 8.07 (dd, J = 1.7, 0.9, 1H, H^d pyta), 7.51 (ddd, J = 7.3, 5.6, 1.7, 1H, H^b pyta), 6.72 (s, 2H, *H* maleimide), 4.64 (t, J = 5.7, 2H, PytaCH_2), 3.76-3.72 (m, 4H, CH_2NHC(O)CH_2 and CH_2 α to maleimide), 2.42 (td, J = 6.8, 1.0, 2H, CH_2NHC(O)CH_2).

^{13}C-NMR (101 MHz, $CDCl_3$: CD_3OD): δ (ppm) 197.4 (Re*C*O), 195.9 (Re*C*O), 189.3 (Re*C*O), 172.9 (CH_2*C*(O)$NHCH_2$), 171.4 (2C, *C*=O of maleimide ring), 153.7 (C^a pyta), 150.0 (C^e_{IV} pyta), 149.5 (C^f_{IV} pyta), 140.5 (C^c pyta), 134.9 (2C, *C*H of maleimide ring), 126.6 (C^b pyta), 126.0 (C^g pyta), 122.9 (C^d pyta), 51.7 (Pyta*C*H_2), 39.5 (*C*H_2 α to maleimide), 35.17 (*C*H_2NHC(O)CH_2), 34.99 (cH_2NHC(O)*C*H_2).

HR-MS (ESI+): *m/z* calculated for $[C_{19}H_{16}ClN_6O_6Re + Na]^+$: 667.02416, found: 667.02445, error: 0.4 ppm.

[$Re(CO)_3$(Br)(PytaNHBoc)](75)

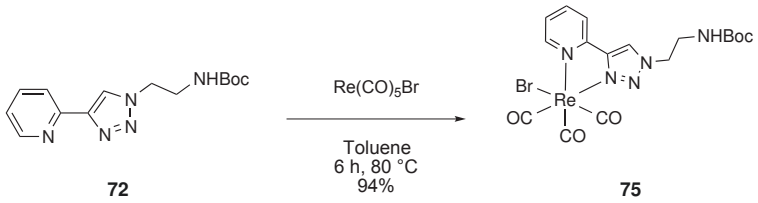

The ligand **72** (206 mg, 0.712 mmol, 1 equiv.) was dissolved in warm toluene (30 mL, 80 °C). Rhenium pentacarbonyl bromide (289 mg, 0.712 mmol, 1 equiv.) was added, and the mixture was heated at 80 °C (bath temperature) for 6 hours, during which a yellow precipitate formed. The yellow precipitate was cooled to room temperature, filtered and washed with cold toluene to obtain the desired compound **75** (428 mg, 0.669 mmol, 94%).

^{1}H-NMR (400 MHz, CD_3OD : $CDCl_3$): δ (ppm) 9.30 (d, J = 5.4, 1H, H^a pyta), 9.09 (s, 1H, H^g pyta), 8.43-8.36 (m, 2H, H^c + H^d pyta), 7.82 (ddd, J = 7.3, 5.6, 1.7, 1H, H^b pyta), 4.96 (t, J = 5.8, 2H, PytaCH_2), 3.96 (t, J = 5.6, 2H, CH_2NHBoc), 1.73 (s, 9H, C(CH_3)$_3$Boc).

^{13}C-NMR (101 MHz, CD_3OD : $CDCl_3$): δ (ppm) 197.25 (Re*C*O), 195.68 (Re*C*O), 188.78 (Re*C*O), 157.44 (O*C*(O)NH), 153.71 (*C*^{a} pyta), 149.98 (*C*$^{e}_{IV}$ pyta), 149.40 (*C*$^{f}_{IV}$ pyta), 140.33 (*C*^{c} pyta), 126.47 (*C*^{g} pyta), 125.57 (*C*^{b} pyta), 122.84 (*C*^{d} pyta), 80.48 (*C*(CH_3)$_3$), 52.37 (Pyta*C*H$_2$), 40.53 (*C*H$_2$NHBoc), 28.53 (3C, C(*C*H$_3$)$_3$Boc).

IR: ν_{ReCO}/cm^{-1} 2025, 1902.

HR-MS (ESI+): *m/z* calculated for [$C_{17}H_{19}BrN_5O_5Re + Na$]$^+$: 659.99913, found: 659.99998, error: 1.0 ppm.

[Re(CO)$_3$(Py)(PytaNHBoc)]$^+$BF$_4^-$ (76)

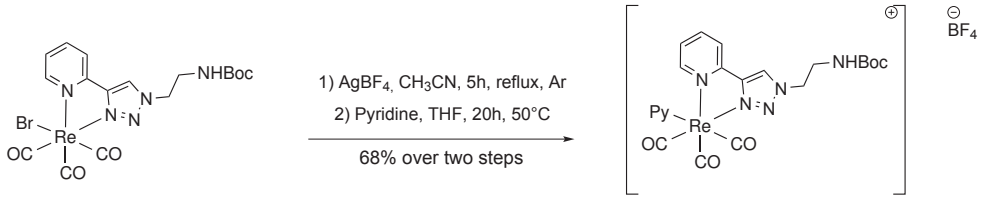

75 **76**

Rhenium tricarbonyl bromide derivative **75** (88.3 mg, 0.138 mmol, 1 equiv.) was dissolved in acetonitrile (25 mL) under argon. Silver tetrafluoroborate (29.5 mg, 0.138 mmol, 1 equiv.) was added, and the reaction mixture was stirred for 3 days at 65 °C (bath temperature), during which a dark precipitate formed. Solvent was then removed by rotary evaporation, and the solid was dried under vacuum. It was then dissolved in *non-distilled* tetrahydrofuran (20 mL), and pyridine (35 µL, 0.434 mmol, 3 equiv.) was added. The reaction mixture was stirred 36h at 60 °C. It was then cooled to room temperature and filtered over celite. The solvent was removed by rotary evaporation, and the resulting yellow oil was co-evaporated three times with toluene. The crude was then dissolved in the minimal amount of methanol and precipitated in cold diethyl ether to give compound **76** (68.3 mg, 0.094 mmol, 68%) as a pale brown solid.

^{1}H-NMR (400 MHz, CD_3OD): δ (ppm) 9.29 (d, J = 5.5, 1H, *H*^{a} pyta), 8.99 (s, 1H, *H*^{g} pyta), 8.45 (d, J = 5.1, 2H, *H*$^{a'}$ pyridine), 8.26 (td, J = 7.8, 1.2, 1H, *H*^{c} pyta), 8.15 (d, J = 7.9, 1H, *H*^{d} pyta), 7.93 (tt, J = 7.7, 1.5, 1H, *H*$^{c'}$ pyridine), 7.75 (ddd, J = 7.4, 5.9, 1.3, 1H, *H*^{b} pyta), 7.42 (t, J = 7.1, 2H, *H*^{b} pyta), 4.74-4.70 (m, 2H, PytaC*H*$_2$), 3.77-3.66 (m, 2H, C*H*$_2$NHBoc), 1.23 (s, 9H, C(C*H*$_3$)$_3$Boc).

^{13}C-NMR (101 MHz, CD_3OD): δ (ppm) 158.0 (NHC(O)O*C*(CH3)3), 155.0 (*C*^{a} pyta), 153.5 (2C, *C*$^{a'}$ pyridine), 150.76 (*C*$^{e}_{IV}$ pyta), 150.58 (*C*$^{f}_{IV}$ pyta), 142.7 (*C*^{c} pyta), 140.9 (*C*$^{c'}$ pyridine), 128.6 (*C*^{g} pyta), 128.03 (*C*^{b} pyta), 127.86 (2C, *C*$^{b'}$ pyta), 124.1 (*C*^{d} pyta), 80.4 (*C*(CH_3)$_3$), 54.1 (Pyta*C*H$_2$), 41.3 (*C*H$_2$NHBoc), 28.5 (3C, C(*C*H$_3$)$_3$Boc).

IR: ν_{ReCO}/cm^{-1} 2034, 1916.

HR-MS (ESI+): *m/z* calculate for [$C_{22}H_{124}N_6O_6Re$]$^+$: 637.13323, found: 637.13369, error: 0.7 ppm.

$[Re(CO)_3(Py)(PytaNH_3)]^{2+}2CF_3COO^-$ (98)

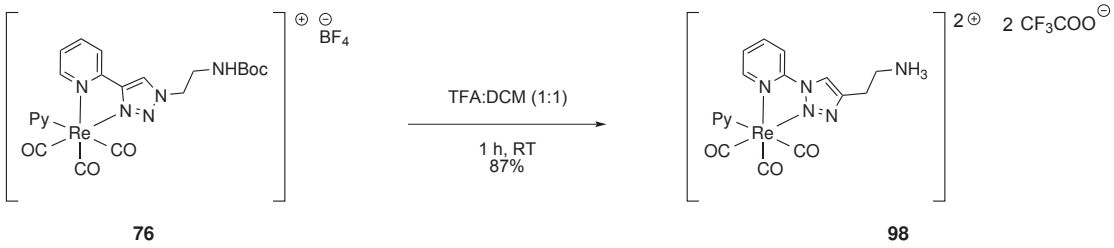

76 98

Boc-protected complex **76** (70 mg, 0.096 mmol, 1 equiv.) was dissolved in DCM, and TFA (0.5 mL) was added carefully to the stirred solution. The reaction mixture was stirred 30 min at room temperature, then solvent was removed under reduced pressure. The resulting crude was dissolved in the minimal amount of methanol and precipitated in diethyl ether to give the desired compound as a solid (64 mg, 83.7 µmol, 87%).

^{1}H-NMR (400 MHz, CD_3OD): δ (ppm) 9.35 (ddd, J = 5.6, 1.5, 0.8, 1H, H^a pyta), 9.11 (s, 1H, H^g pyta)), 8.47-8.45 (m, 2H, $H^{a'}$ pyridine), 8.32 (dd, J = 7.8, 1.5, 1H, H^c pyta), 8.22-8.20 (m, 1H, H^d pyta), 7.97 (dd, J = 8.5, 7.0, 1H, $H^{c'}$ pyridine), 7.81 (ddd, J = 7.7, 5.6, 1.4, 1H, H^b pyta), 7.46-7.43 (m, 2H, $H^{b'}$ pyridine), 5.08-4.97 (m, 2H, PytaCH_2), 3.77-3.67 (m, 2H, CH_2NHBoc).

$[Re(CO)_3(Py)(PytaNH{-}maleimide)]^+CF_3COO^-$ (77)

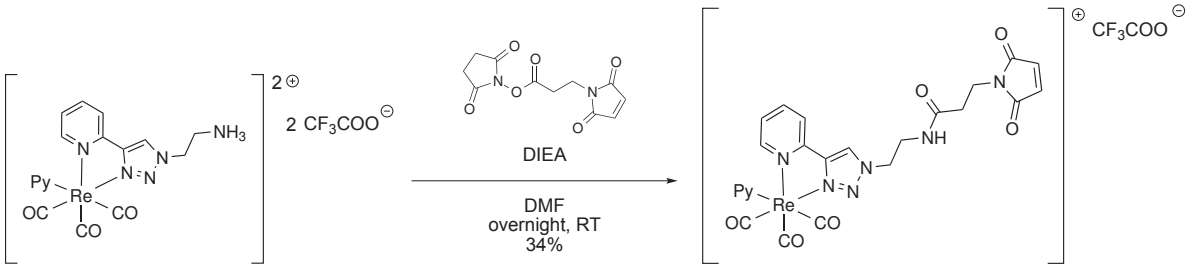

98 77

Compound **98** (61 mg, 79.8 µmol, 1.2 equiv.) was dissolved in dry DMF under argon. 3-maleimidopropionic acid *N*-hydroxysuccinimide ester (17.9 mg, 83.7 µmol, 1 equiv.), then DIEA (33 µL, 191 µmol, 2.8 equiv.), were added. The reaction mixture was stirred overnight at room temperature. The solvent was removed under reduced pressure, and the resulting oil was dilute in DCM and washed twice with aqueous citric acid (5%). The crude was then purified by HPLC (C8, 20 to 80% ACN (0.1% TFA) in 40 min). The product was obtained as a pale yellow powder (18.5 mg, 23.0 µmol, 34%).

^{1}H-NMR (400 MHz, CD_3OD): δ (ppm) 9.29 (d, J = 5.6, 1H), 9.01 (s, 1H), 8.44-8.42 (m, 2H), 8.27 (td, J = 7.8, 1.5, 1H), 8.19-8.15 (m, 1H), 7.94 (tt, J = 7.7, 1.5, 1H), 7.75 (ddd, J = 7.7, 5.6, 1.4, 1H), 7.45-7.41 (m, 2H), 6.77 (s, 2H), 4.78-4.75 (m, 2H), 3.91-3.71 (m, 3H), 3.67 (td, J = 7.0, 2.4, 2H), 2.43 (td, J = 7.0, 0.6, 2H).

^{13}C-NMR (101 MHz, CD_3OD): δ (ppm) 173.53, 172.11, 155.00, 153.51, 150.62, 142.70, 141.08, 135.47, 128.61, 128.01, 124.33, 53.45, 40.02, 35.56, 35.30.

HR-MS (ESI+): m/z calculated for $[C_{24}H_{21}N_7O_6Re]^+$: 688.10774, found: 688.10903, error: 1.9 ppm.

5.2 Production of *Engrailed* Homeodomain Cys-HD and Cys-NLS-HD

Table 5.1: General properties of Cys-HD and Cys-NLS-HD.

Cherry-Cys-NLS-HD	Cherry-Cys-HD Cys-NLS-HD	Cys-HD
MW (Da)	7820.9	9454.8
ϵ_0^{280} ($M^{-1} \cdot cm^{-1}$)	6990	6990
Negatively charged residues (Asp + Glu)	6	7
Positively charged residues (Arg + Lys)	14	21

Cys-HD: `GPCAS DKRPRTAFTA EQLQRLKAEF QTNRYLTEQR RQSLAQELGL NESQIKIWFQ NKRAKIKKAT QA`

Cys-NLS-HD: `GPCAS SGPRSRKPKK KNPNKEDKRP RTAFTAEQLQ RLKAEFQTNR YLTEQRRQSL AQELGLNESQ IKIWFQNKRA KIKKAT`

Table 5.2: Media and buffers used for the purification and production of Cys-HD and Cys-NLS-HD

Medium/Buffer	Concentration
LB medium	$10\,g \cdot L^{-1}$ bactotryptone or casein peptone $5\,g \cdot L^{-1}$ yeast extract $10\,g \cdot L^{-1}$ NaCl
Lysis/Loading buffer	20 mM phosphate buffer pH 7.5 500 mM NaCl 1 mM DTT 30 mM imidazole
Eluting buffer	20 mM phosphate buffer pH 7.5 500 mM NaCl 1 mM DTT 500 mM imidazole
Cleavage buffer	20 mM phosphate buffer pH 7.5 150 mM NaCl 1 mM DTT 1 mM EDTA

E. coli strains transformed with the relevant plasmid were grown in LB medium containing Ampicillin (100 µg) at 37 °C for 3–5 h. IPTG was then added to the medium (final concentration: 1 mM) and the bacteria were incubated 37 °C for 3 h. The culture was centrifuged for 25 minutes at 6000 g at 4 °C. The pellet was taken up in lysis buffer (Table 5.2, 20–40 mL buffer per liter of culture), frozen in liquid nitrogen and kept at −20 °C overnight. The pellet was unfrozen at 42 °C. Lysozyme (final concentration: $1\,\mathrm{mg}\cdot\mathrm{mL}^{-1}$) and protease inhibitor cocktail (PMSF, leupeptine, pepstatine) were added, and the mixture was incubated for 20 min at 4 °C. Sonication cycles were then performed (10 minutes; 1 cycle = 6 s at 70% intensity and 6 s off). The mixture was then centrifuged at 30000 g for 20 min at 4 °C. The supernatant was filtered over 0.45 µm and 0.22 µm filters, and loaded on a HisTrap column (GE Healthcare). The protein was eluted with eluting buffer (Table 5.2). The collected fractions were pooled, and the fusion protein was cleaved overnight at 4 °C in cleavage buffer. Buffer was then exchanged for loading buffer, and the mixture was loaded on a His-Trap column. The non-retained fraction was collected and corresponded to the pure POI.

5.3 Labelling of Cys-HD and Cys-NLS-HD with SCoMPIs

General procedure. A solution of protein in reaction buffer (100–200 µM) was degased and put under argon. 1 equivalent of TCEP was added, and the solution wad incubated for 30 min-1h at room temperature. 5 equivalents of [$Re(CO)_3$(X)(Pyta−maleimide)] (X = Cl, Py) were then added (stock solution in DMSO, final concentration of DMSO < 1% v:v), and the solution was incubated overnight at room temperature under inert atmosphere. Excess of reagent and TCEP were removed by repeated ultrafiltration (cut 3kDa) with EDTA-free phosphate buffer.

Reaction buffer: 50 mM phosphate buffer pH 6.5, 150 mM NaCl, 10 mM EDTA.

EDTA-free phosphate buffer: 50 mM phosphate buffer pH 7.0, 150 mM NaCl.

Cl-HD:

MALDI-TOF-MS (SA matrix): 8117.71 [CysHD + Pyta]

Py-HD:

MALDI-TOF-MS (SA matrix): 8117.45 [CysHD + Pyta]

Cl-NLS-HD:

MALDI-TOF-MS (SA matrix): 10062.16 [Cl−NLS−HD − Cl]

Py-NLS-HD:

MALDI-TOF-MS (SA matrix): 10058.14 [Py−NLS−HD−Py] Due to limited amounts of labelled proteins, UV F/T ratios could not be measured accurately.

5.4 Imaging of SCoMPI-labelled homeodomains on CHO cells

5.4.1 Stock solutions

Stock solutions of labelled homeodomains in EDTA-free phosphate buffer were stored at −20 °C. Their concentration was checked by measuring UV absorbance at 280 nm.

5.4.2 Incubation conditions

Incubation conditions are identical to those used for SCoMPI-labelled CPPs (see section 4.5.1). The only difference is the use of Si_3N_4 slides for X-fluorescence microscopy instead of CaF_2 slides (IR and fluorescence imaging).

5.4.3 Fluorescence and IR imaging

The experimental setups used for fluorescence and IR microscopies were identical to those used for SCoMPI-labelled CPPs (see section 4.5.1).

5.4.4 Synchrotron X-ray Fluorescence microspectroscopy

Samples were examined on the new Nanoscopium beamline at SOLEIL synchrotron. Spectra and maps were collected by two detectors with a $0.5 \times 0.5\,\mu m^2$. For maps, data were collected for 3s/spectrum. Data from both detectors were additioned and processed using PyMCA and ImageJ softwares.

Chapter 6

Labelling of *Carbonic Anhydrases* with SCoMPIs in living cells

6.1 Procedures for the synthesis of LDAI-SCoMPIs for the labelling of Carbonic Anhydrases

2-azidoacetic acid, *tert*-butyl ester (89)

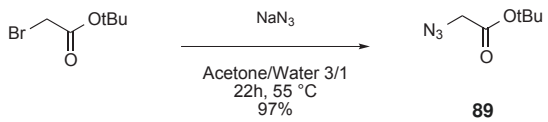

89

2-bromoacetic acid *tert*-butyl ester (1 mL, 6.8 mmol, 1 equiv.) was diluted in a 3:2 (v:v) mixture of acetone (4.1 mL) and water (2.7 mL). Sodium azide (664 mg, 10.2 mmol, 1.5 equiv.) was added, and the mixture was refluxed (sand bath temperature = 78 °C) for 20h. The solution was cooled to room temperature and acetone was removed by rotary evaporation. The solution was diluted with water (6 mL) and extracted three times with Et_2O (3 × 6 mL). The organic layers were pooled, dried over anhydrous $MgSO_4$, filtered and concentrated to the desired compound as a colorless oil (1.034 g, 6.58 mmol, 97%).

^{1}H-NMR (300 MHz, $CDCl_3$): δ (ppm) 3.70 (s, 2H, $N_3CH_2C(O)Ot$-Bu), 1.45 (s, 9H, $(CH_3)_3$, *tert*-Butyl ester).

^{13}C-NMR (75 MHz, $CDCl_3$): δ (ppm) 167.45 ($C(O)Ot$-Bu), 83.06 ($C(CH_3)_3$), 50.97 (N_3CH_2COOt-Bu), 28.07 (3C, $C(CH_3)_3$). NMR data in agreement with reference [117, 201].

2-(1-[acetic acid *tert*-butyl ester]-1*H*-1,2,3-triazol-4-yl)pyridine (PytaCOO*t*Bu, 90)

Compound **90** was synthesiszed by adapting published procedure from Benoist *et al.* [117]. 2-azidoacetic acid *tert*-butyl ester (902.1 mg, 5.74 mmol, 1 equiv.) was dissolved in a

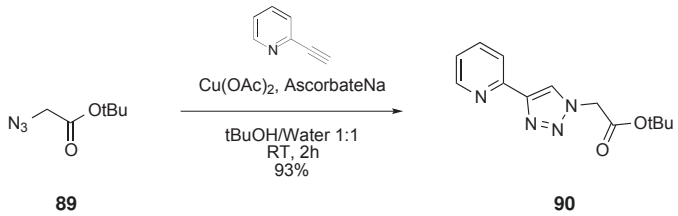

89 **90**

1:1 mixture of *t*BuOH (28 mL) and water (28 mL). Copper acetate (278 mg, 1.40 mmol, 0.25 equiv.), sodium ascorbate (276.8 mg, 1.40 mmol, 0.25 equiv.) and 2-ethynylpyridine (560 µL, 5.54 mmol, 0.96 equiv.) were successively added. The mixture was sonicated for a few tens of seconds, during which a pale brown precipitate formed. The mixture was then stirred at room temperature until the solution turned green (1h30). The solution was diluted with DCM (60 mL) and extracted once. The organic layer was washed twice with aqueous saturated (28%) ammonia solution (2 × 60 mL) and once with brine (60 mL). The aqueous layers were extracted once more with DCM (60 mL), then both organic layers were pooled, dried over anhydrous Na_2SO_4, filtered and concentrated to the desired compound as a white solid (1.3821 g, 5.31 mmol, 93%).

^{1}H-NMR (300 MHz, $CDCl_3$): δ (ppm) 8.42 (d, J = 4.7, 1H, H^a pyta), 8.18 (s, 1H, H^g pyta), 8.00 (d, J = 7.9, 1H, H^d pyta), 7.60 (td, J = 7.7, 1.4, 1H, H^c pyta), 7.06 (dd, J = 6.8, 5.3, 1H, H^b pyta), 5.02 (s, 2H, PytaCH_2C(O)O*t*-Bu), 1.31 (s, 9H, (CH_3)$_3$, *tert*-Butyl ester).

^{13}C-NMR (75 MHz, $CDCl_3$): δ (ppm) 164.99 (C(O)O*t*-Bu), 149.90 (C^e_{IV} pyta), 149.19 (C^a pyta), 148.37(C^f_{IV} pyta), 136.58 (C^c pyta), 123.47 (C^g pyta), 122.63 (C^b pyta), 119.93 (C^d pyta), 83.43 (C(CH$_3$)$_3$), 51.43 (Pyta$C$H$_2$COO*t*-Bu), 27.67 (3C, C(CH$_3$)$_3$).

Pyta-OH (91)

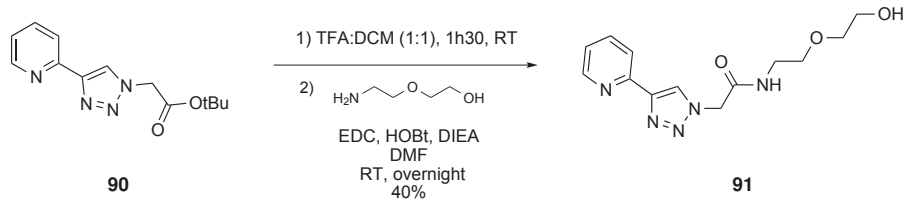

90 **91**

Compound **90** (1.597 g, 6.1 mmol, 1 equiv.) was dissolved in DCM (20 mL), and TFA (20 mL) was added slowly to the solution. The mixture was stirred at room temperature for 2h. Solvents were co-evaporated three times with toluene (3 × 30 mL). EDC · HCl (1.61 g, 8.4 mmol, 1.4 equiv.) was added to the resulting solid, and both solids were dissolved in dry DMF (30 mL) under argon. After 5-10 min stirring, 2-(2-aminoethoxy)ethanol (0.86 mL, 8.6 mmol, 1.4 equiv.) then DIEA (3.2 mL, 18.5 mmol, 3 equiv.) were added. Reaction mixture was stirred overnight at room temperature, and solvent was removed. The resulting crude was purified by flash silica gel column chromatography (0 to 10% MeOH in DCM) to yield the desired compound as a white solid (721 mg, 2.5 mmol, 40%).

^{1}H-NMR (300 MHz, $CDCl_3$: CD_3OD): δ (ppm) 8.29 (ddd, J = 5.0, 1.8, 0.9, 1H, H^a pyta), 8.16 (s, 1H, H^g pyta)), 7.86 (dt, J = 8.0, 1.1, 1H, H^d pyta), 7.61 (td, J = 7.8, 1.8, 1H, H^c pyta), 7.07 (ddd, J = 7.6, 5.0, 1.2, 1H, H^b pyta), 4.93 (s, 2H, PytaCH_2C(O)NH), 3.48-3.45 (m, 2H, OCH_2CH_2OH), 3.34-3.29 (m, 4H, CH_2OCH_2), 3.23-3.20 (m, 2H, C(O)NHCH_2).

^{13}C-NMR (75 MHz, $CDCl_3$: CD_3OD): δ (ppm) 165.46 (CH_2C(O)NH), 149.23 (C^e_{IV} pyta), 148.74 (C^a pyta), 147.28 (C^f_{IV} pyta), 137.39 (C^c pyta), 123.92 (C^g pyta), 123.02 (C^b pyta), 120.31 (C^d pyta), 71.88 (OCH_2CH_2OH), 68.81 (C(O)NHCH$_2$$CH_2OCH_2$), 60.77 ($CH_2CH_2OH$), 52.00 (Pyta$CH_2$C(O)NHCH$_2$), 39.27 ($CH_2$C(O)NH$CH_2$).

HR-MS (ESI+): *m/z* calculated for $[C_{13}H_{17}ClN_5O_3 + Na]^+$: 314.12236, found: 314.12230, error: -0.2 ppm.

[Re(CO)$_3$(Cl)(Pyta-OH)] (92)

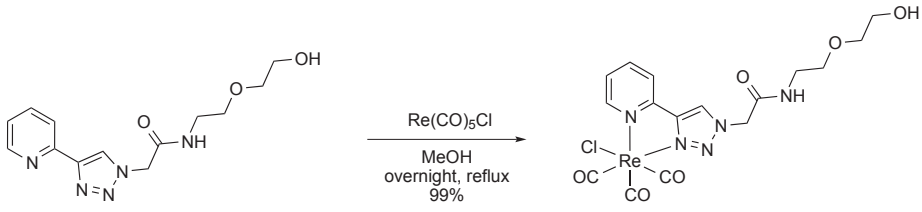

91 **92**

Ligand **91** (105.3 mg, 0.361 mmol, 1 equiv.) was dissolved in warm MeOH (1 mL). $Re(CO)_5Cl$ (133.1 mg, 0.368 mmol, 1 equiv.) was added, and the mixture was refluxed overnight. The yellow precipitate that formed during this time was filtered and dried to give the desired complex **92** (214.2 mg, 0.359 mmol, 99%).

^{1}H-NMR (400 MHz, MeOH : $CDCl_3$): δ (ppm) 8.96 (ddd, J = 5.6, 1.4, 1.0, 1H, H^a pyta), 8.83 (s, 1H, H^g pyta), 8.11-8.05 (m, 2H, H^c + H^d pyta), 7.50 (ddd, J = 7.0, 5.6, 2.0, 1H, H^b pyta), 5.28 (q, J = 20.7, 2H, PytaCH_2C(O)NH), 3.70 (t, J = 4.6, 2H, OCH_2CH_2OH), 3.60-3.56 (m, 4H, CH_2OCH_2), 3.48-3.45 (m, 2H, C(O)NHCH_2).

^{13}C-NMR (101 MHz, MeOH : $CDCl_3$): δ (ppm) 197.5 (ReCO), 195.9 (ReCO), 189.3 (ReCO), 165.3 (C(O)NH), 153.6 (C^a pyta), 150.1 (C^e_{IV} pyta), 149.6 (C^f_{IV} pyta), 140.5 (C^c pyta), 126.76 (C^g pyta), 126.58 (C^b pyridine triazole), 123.0 (C^d pyta), 72.8 (OCH_2CH_2OH), 69.7 ($C(O)NH - CH_2CH_2OCH_2$), 61.7 (CH_2CH_2OH), 53.8 ($PytaCH_2 - C(O)NH - CH_2$), 40.3 ($CH_2C(O)NHCH_2$).

IR: ν_{ReCO}/cm^{-1} 2019, 1891.

HR-MS (ESI+): *m/z* calculated for $[C_{16}H_{17}ClN_5O_6Re + Na]^+$: 618.02918, found: 618.02891, error: 0.4 ppm.

[Re(CO)$_3$(Cl)(Pyta-ONHS)] (93)

Rhenium complex [Re(CO)$_3$(Cl)(Pyta-OH)] **92** (149 mg, 0.25 mmol, 1 equiv.) and *N,N'*-disuccinimidyl carbonate (DSC) (187.4 mg, 0.73 mmol, 2.9 equiv.) were dissolved in dry

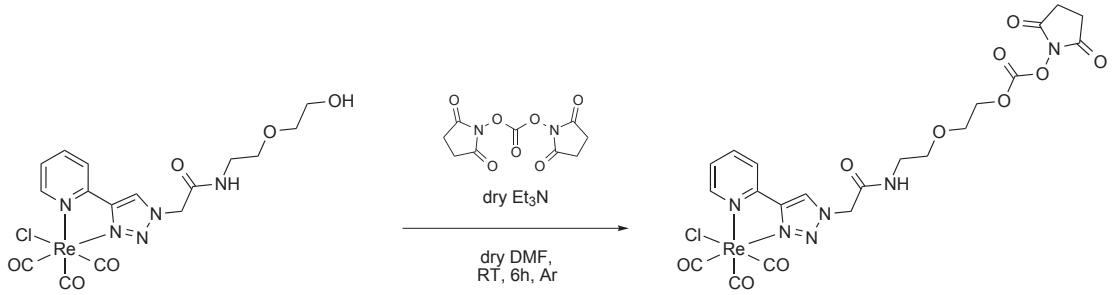

92 **93**

DMF (2.4 mL) under Argon. Dry Et_3N (99.3 µL, 0.71 µmol, 2.9 equiv.) was added and the mixture was stirred at room temperature. After 2h30, more DSC was added (121.8 mg, 0.475 mmol, 1.9 equiv.) and the mixture was stirred at 50 °C (bath temperature) for another 3h30. DMF was removed by rotary evaporation. The resulting crude was dissolved in EtOAc and washed once with a saturated aqueous solution of $NaHCO_3$. The organic layer was dried over anhydrous Na_2SO_4, filtered and concentrated. It was then purified by silica gel column chromatography (0 to 3 to 5 to 10% MeOH in DCM) to yield compound **93** as a yellow solid containing traces of impurities (106 mg).

^{1}H-NMR (300 MHz, $CDCl_3$): δ (ppm) 8.96 (d, J = 5.3, 1H, H^a pyta), 8.60 (s, 1H, H^g pyta), 8.04-7.95 (m, 2H, $H^c + H^d$ pyta), 7.41 (ddd, J = 7.1, 5.6, 1.7, 1H, H^b pyta), 5.14 (q, J = 16.9, 2H, PytaCH_2C(O)NH), 4.48 (tdt, J = 13.0, 8.9, 4.4, 2H, $OCH_2CH_2OC(O)NHS$), 3.73 (t, J = 4.3, 2H, $OCH_2CH_2OC(O)NHS$), 3.58 (t, J = 4.6, 2H, $C(O)NHCH_2CH_2O$), 3.50-3.45 (m, 2H, $C(O)NHCH_2CH_2O$), 2.88 (s, 4H, $(CH_2)_2$ NHS).

^{13}C-NMR (75 MHz, $CDCl_3$): δ (ppm) 197.1 (ReCO), 196.3 (ReCO), 188.9 (ReCO), 169.7 (2C, C=O of NHS ring), 164.2 (C(O)NH), 153.1 (C^a pyta), 151.7 (OC(O)NHS), 149.4 (C^e_{IV} pyta), 148.8 (C^f_{IV} pyta), 139.8 (C^c pyta), 126.05 (C^g pyta), 125.93 (C^b pyta), 122.6 (C^d pyta), 69.9 ($OCH_2CH_2OC(O)NHS$), 69.5 ($C(O)NHCH_2CH_2O$), 68.4 ($OCH_2CH_2OC(O)NHS$), 53.4 (PytaCH_2C(O)NH), 39.9 ($C(O)NHCH_2CH_2O$), 25.76 (2C, CH_2 of NHS).

HR-MS (ESI+): m/z calculated for $[C_{21}H_{20}ClN_6O_{10}Re + Na]^+$: 759.03574, found: 759.03574, error: 0.8 ppm.

C0-Trityl (78)

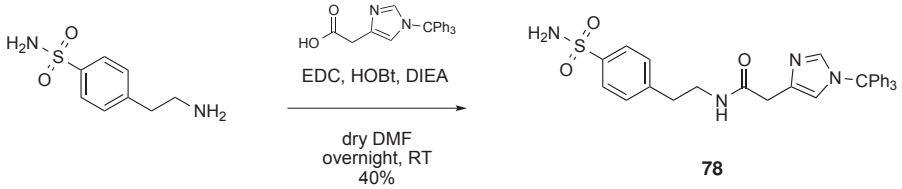

78

1-(triphenylmethyl)-1H-imidazole-4-acetic acid (221.7 mg, 0.60 mmol, 1.2 equiv.), EDC · HCl (146.2 mg, 0.76 mmol, 1.5 equiv.) and HOBt · H_2O (115.8 mg, 0.76 mmol, 1.5 equiv.) were dissolved in dry DMF (2.5 mL) under argon. After 5-10 minutes stirring, 4-(2-aminoethyl)benzene

sulfonamide (100.1 mg, 0.50 mmol, 1 equiv.) and DIEA (260 µL, 1.5 mmol, 3 equiv.) were added and reaction mixture was stirred overnight at room temperature. Solvent was removed by rotary evaporation and the resulting sticky solid was taken up in a 1:1 mixture of EtOAc and saturated aqueous solution of $NaHCO_3$. After decantation, the organic layer was washed with brine, dried over anhydrous Na_2SO_4, filtered and concentrated. The crude was purified by automated silica gel flash column chromatography (5% MeOH in DCM). The resulting oil was co-evaporated with Et_2O until obtention of the desired compound as a white solid, with traces of impurities (109.1 mg, 0.20 mmol, 40%).

^{1}H-NMR (400 MHz, CD_3OD): δ (ppm) 7.79 (d, J = 8.5, 2H,benzenesulfonamide), 7.41-7.33 (m, 9H+2H+1H, 9H trityl+2H benzenesulfonamide + 1H imidazole), 7.16 (ddt, J = 5.1, 2.3, 1.2, 6H, trityl), 6.85 (s, 1H, 1H imidazole), 3.43 (t, J = 7.2, 2H, CH2 benzenesulfonamide), 3.41 (d, J = 1.7, 2H, CH2 alpha imidazole), 2.84 (t, J = 7.3, 2H, CH2 benzenesulfonamide).

^{13}C-NMR (75 MHz, CD_3OD): δ (ppm)

HR-MS (ESI+): *m/z* calculated for $[C_{32}H_{30}N_4O_3S+H]^+$: 551.21114, found: 551.21106, error: -0.1 ppm.

C0NH (85)

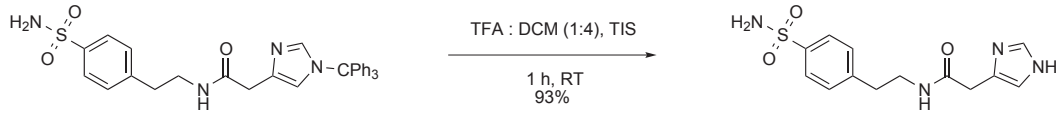

78 85

Trityl imidazole derivative **78** (50.2 mg, 0.091 mmol, 1 equiv.) was dissolved in DCM (0.8 mL). TFA (0.2 mL) was added drop wise, followed by TIS (18.7 µL, 0.091 mmol, 1 equiv.). The mixture was stirred for 1 hour at room temperature, then precipitated in Et_2O to give the desired compound as a white solid/oil containing traces of water (34.6 mg of hydrated compound, 93%).

^{1}H-NMR (300 MHz, CD_3OD): δ (ppm) 8.80 (s, 1H, H^2 of imidazole), 7.80 (d, J = 8.4, 2H, $H^{2,6}$ of benzenesulfonamide), 7.39 (d, J = 8.4, 2H, $H^{3,5}$ of benzenesulfonamide), 7.35 (s, 1H, H^5 of imidazole), 3.67 (s, 2H, CH_2 α to imidazole), 3.49 (t, J = 7.2, 2H, ArCH_2CH_2NHC(O)), 2.90 (t, J = 7.2, 2H, ArC$H_2$$CH_2$NHC(O)).

^{13}C-NMR (75 MHz, CD_3OD): δ (ppm) 169.9 (C(O)NH), 145.2 (C^1 of benzenesulfonamide), 143.1 (C^4 of benzenesulfonamide), 135.0(C^2 of imidazole), 130.4 (2C, $C^{3,5}$ of benzenesulfonamide), 129.2(C^4 of imidazole), 127.3 (2C, $C^{2,6}$ of benzenesulfonamide), 118.5 (C^5 of imidazole), 41.6 (Ar$CH_2$$CH_2$NHC(O)), 36.1 ($CH_2$$CH_2$NHC(O)), 32.0 ($CH_2$ α to imidazole).

HR-MS (ESI+): *m/z* calculated for $[C_{13}H_{16}N_4O_3S+H]^+$: 309.10159, found: 309.10170, error: 0.4 ppm.

C0-SCoMPI (94)

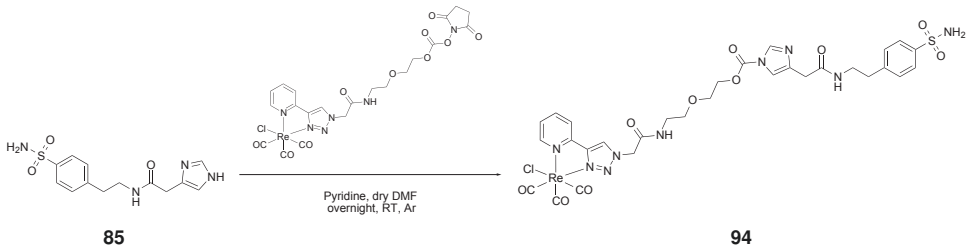

85 **94**

C0-imidazole **85** (8.6 mg, 27.9 µmol, 1.1 equiv.) and the rhenium complex **93** (18.6 mg, 25.2 µmol, 1 equiv.) were dissolved in dry DMF (2 mL) under argon. Dry pyridine (2.2 µL, 27.3 µmol, 1.1 equiv.). Solvent was removed by rotary evaporation and the resulting crude was purified by HPLC (25 to 100 % TFA-free ACN in 10 mM aqueous NH_4OAc pH 7.0 in 30 min, 14 mL/min, 11.4 min, purity: 97%). NH_4OAc was removed by repeated freeze-drying cycles.

^{1}H-NMR (400 MHz, $CDCl_3$: CD_3OD): δ (ppm) 8.96 (d, J = 5.5, 1H, H^a pyta), 8.82 (s, 1H, H^g pyta), 8.14 (s, 1H, H^2 of imidazole), 8.11-8.05 (m, H + H, H^c + H^d pyta), 7.74 (d, J = 8.3, 2H, $H^{2,6}$ of benzenesulfonamide), 7.50 (ddd, J = 7.1, 5.4, 1.8 H^b pyta), 7.36 (s, 1H, H^5 of imidazole), 7.27 (d, J = 8.3, 2H, $H^{3,5}$ of benzenesulfonamide), 5.25 (q, J = 22.2, 2H, CH_2 α to Pyta), 4.55 (m, 2H, $OCH_2CH_2OC(O)$imidazole, under water signal), 3.84-3.82 (m, 2H, $OCH_2CH_2OC(O)$imidazole), 3.64 (t, J = 5.3, 2H, $NHC(O)CH_2CH_2O$), 3.48-3.41 (m + d + s, 2H + 2H + 2H, $NHC(O)CH_2CH_2O$ + CH_2 α to imidazole + $ArCH_2CH_2NHC(O)$), 2.84 (t, J = 7.0, 2H, $ArCH_2CH_2NHC(O)$).

HR-MS (ESI+): *m/z* calculated for $[C_{30}H_{31}ClN_9O_{10}ReS + Na]^+$: 952.10249, found: 952.10229, error: -0.2 ppm.

C3-Boc (79)

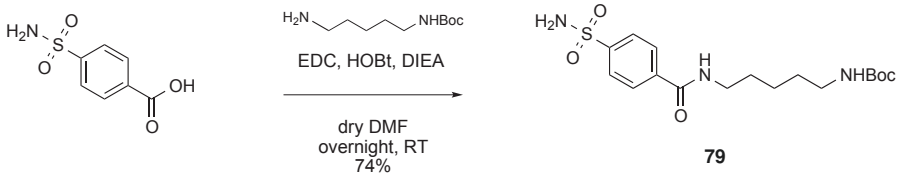

79

Boc-4-aminobutanoic acid (104.6 mg, 0.51 mmol, 1 equiv.), EDC · HCl (143.8 mg, 0.75 mmol, 1.5 equiv.) and HOBt · H_2O (114.6 mg, 0.76 mmol, 1.5 equiv.) were dissolved in dry DMF (2.6 mL) under argon. After 5-10 minutes stirring, 4-(2-aminoethyl)benzene sulfonamide (100.1 mg, 0.50 mmol, 1 equiv.) and DIEA (260 µL, 1.5 mmol, 3 equiv.) were added and reaction mixture was stirred overnight at room temperature. Solvent was removed by rotary evaporation and the resulting sticky solid was taken up in a 1:1 mixture of EtOAc and saturated aqueous solution of $NaHCO_3$. After decantation, the organic layer was washed

with brine, dried over anhydrous Na_2SO_4, filtered and concentrated. The crude was purified by automated silica gel flash column chromatography (5% MeOH in DCM) to give the desired compound as a white solid (133.2 mg, 0.35 mmol, 68%).

^{1}H-NMR (300 MHz, CD_3OD): δ (ppm) 7.83 (d, J = 8.2, 2H, $H^{2,6}$ of benzenesulfonamide), 7.40 (d, J = 8.2, 2H, $H^{3,5}$ of benzenesulfonamide), 3.43 (t, J = 7.1, 2H, $ArCH_2CH_2NHC(O)$), 3.00 (t, J = 6.8, 2H, $CH_2CH_2CH_2NHBoc$), 2.88 (t, J = 7.1, 2H, $ArCH_2CH_2NHC(O)$), 2.16 (t, J = 7.5, 2H, $NHC(O)CH_2CH_2CH_2NHBoc$), 1.70 (quintet, J = 7.2, 2H, $NHC(O)CH_2CH_2CH_2NHBoc$), 1.43 (s, 9H, $(CH_3)_3$).

^{13}C-NMR (75 MHz, CD_3OD): δ (ppm) 175.5 ($CH_2C(O)NHCH_2$), 158.4 ($NHC(O)-Ot$-Bu), 145.3 (C^1 benzenesulfonamide), 142.9 (C^4 benzenesulfonamide), 130.4 (2C, $C^{3,5}$ benzenesulfonamide), 127.2 (2C, $C^{2,6}$ benzenesulfonamide), 79.9 ($C(CH_3)_3$), 41.3 ($ArCH_2CH_2NHC(O)$), 40.7 (CH_2NHBoc), 36.2 ($ArCH_2CH_2NHC(O)$), 34.3 ($NHC(O)CH_2 - CH_2CH_2NHBoc$), 28.8 (3C, $C(CH_3)_3$), 27.2 ($NHC(O)CH_2CH_2CH_2NHBoc$).

HR-MS (ESI+): m/z calculated for $[C_{17}H_{27}N_3O_5S+Na]^+$: 408.15636, found: 408.15718, error: 2.0 ppm.

C3-Trityl (82)

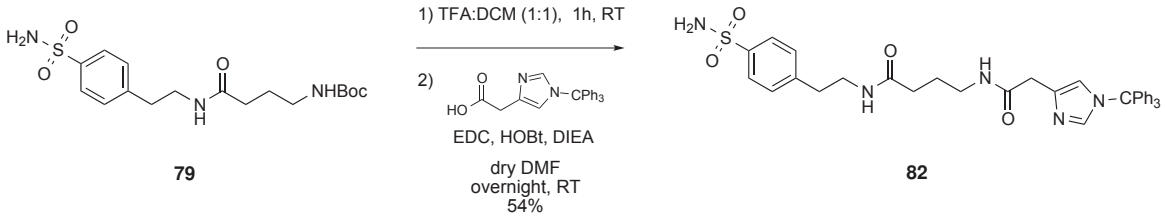

Boc-protected compound **79** (100 mg, 0.26 mmol, 1 equiv.) was dissolved in DCM (1 mL), and TFA (1 mL) was added drop wise. The solution was stirred for 1h at room temperature, then precipitated in cold Et_2O (40 mL) to give a white solid. 1-(triphenylmethyl)-1H-imidazole-4-acetic acid (117.3 mg, 0.32 mmol, 1.2 equiv.), EDC · HCl (75.2 mg, 0.39 mmol, 1.5 equiv.) and HOBt · H_2O (60.5 mg, 0.39 mmol, 1.5 equiv.) were dissolved in dry DMF (1.3 mL) under argon. After 5-10 minutes stirring, the solution was added to the deprotected amine. DIEA (135 µL, 0.78 mmol, 3 equiv.) was added and reaction mixture was stirred overnight at room temperature. Solvent was removed by rotary evaporation and the resulting sticky solid was taken up in a 1:1 mixture of EtOAc and saturated aqueous solution of $NaHCO_3$. After decantation, the organic layer was washed with brine, dried over anhydrous Na_2SO_4, filtered and concentrated. The crude was purified by automated silica gel flash column chromatography (5% MeOH in DCM). The resulting oil was co-evaporated with Et_2O until obtention of the desired compound as a white solid (88.7 mg, 0.14 mmol, 54%).

^{1}H-NMR (400 MHz, CD_3OD): δ (ppm) 7.81 (d, J = 8.4, 2H, $H^{2,6}$ of benzenesulfonamide), 7.43 (s, 1H), 7.36 (ddt, J = 5.9, 2.3, 2.8, 10H), 7.17-7.14 (m, 5H), 6.87 (s, 1H),

3.43 (t, J = 7.1, 4H), 3.11 (dd, J = 8.8, 5.0, 2H), 2.86 (t, J = 7.2, 2H), 2.13 (t, J = 7.4, 2H), 1.70 (t, J = 7.2, 2H).

^{13}C-NMR (75 MHz, CD_3OD): δ (ppm) 175.47, 158.40, 145.31, 142.89, 130.40, 127.24, 79.92, 41.35, 40.72, 36.18, 34.28, 28.76, 27.25.

HR-MS (ESI+): *m/z* calculated for $[C_{36}H_{37}N_5O_4S+H]^+$: 636.26390, found: 636.26423, error: 0.5 ppm.

C3NH (86)

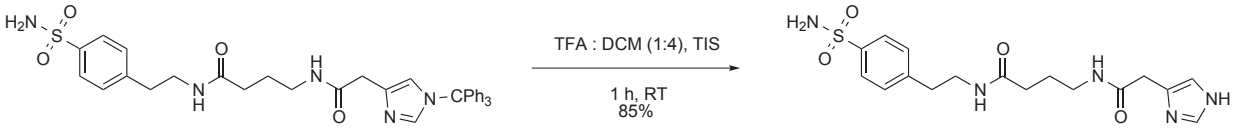

82 **86**

Trityl imidazole derivative **82** (60.6 mg, 0.095 mmol, 1 equiv.) was dissolved in DCM (0.8 mL). TFA (0.2 mL) was added drop wise, followed by TIS (19.5 µL, 0.095 mmol, 1 equiv.). The mixture was stirred for 1 hour at room temperature, then precipitated in Et_2O to give the desired compound as a white solid containing traces of water (39.7 mg of hydrated compound, 85%).

^{1}H-NMR (300 MHz, CD_3OD): δ (ppm) 8.82 (d, J = 1.4, 1H, H^2 imidazole), 7.81 (d, J = 8.5, 2H, $H^{2,6}$ of benzenesulfonamide), 7.39 (d + s, J = 8.5, 2H + 1H, $H^{3,5}$ of benzenesulfonamide + H^5 imidazole), 3.72 (s, 2H, CH_2 α to imidazole), 3.45 (t, J = 7.1, 2H, $ArCH_2CH_2NHC(O)$), 3.13 (t, J = 7.1, 2H, $CH_2CH_2CH_2NHC(O)$), 2.88 (t, J = 7.1, 2H, $ArCH_2CH_2NHC(O)$), 2.17 (t, J = 7.4, 2H, $C(O)CH_2CH_2CH_2NHC(O)$), 1.73 (quintet, J = 7.2, 2H, $CH_2CH_2CH_2NHC(O)$).

^{13}C-NMR (75 MHz, CD_3OD): δ (ppm) 175.3 ($ArCH_2CH_2C(O)NHCH_2$), 169.9 ($CH_2C(O)NHCH_2-$imidazole), 145.4 (C^1 benzenesulfonamide), 142.9 (C^4 benzenesulfonamide), 135.0 (C^2 of imidazole), 130.49 (2C, $C^{3,5}$ benzenesulfonamide), 129.2 (C^4 of imidazole), 127.2 (2C, $C^{2,6}$ benzenesulfonamide), 118.6 (C^5 of imidazole), 41.3 ($ArCH_2CH_2NHC(O)$), 40.1 ($CH_2NHC(O)CH_2-$imidazole), 36.2 ($ArCH_2CH_2NHC(O)$), 34.3 ($Ar(CH_2)_2NHC(O)CH_2$), 32.0 (CH_2 α to imidazole), 26.6 ($NHC(O)CH_2CH_2CH_2NHC(O)$).

HR-MS (ESI+): *m/z* calculated for $[C_{17}H_{23}N_5O_4S+H]^+$: 394.15435, found: 394.15448, error: 0.3 ppm.

C3-SCoMPI (95)

C3-imidazole **86** (11.9 mg, 30.2 µmol, 1.1 equiv.) and the rhenium complex **93** (19.1 mg, 25.9 µmol, 1 equiv.) were dissolved in dry DMF (2 mL) under argon. Dry pyridine (2.2 µL, 27.3 µmol, 1.1 equiv.). Solvent was removed by rotary evaporation and the resulting crude was purified by HPLC (25 to 100 % TFA-free ACN in 10 mM aqueous NH_4OAc pH 7.0 in 30

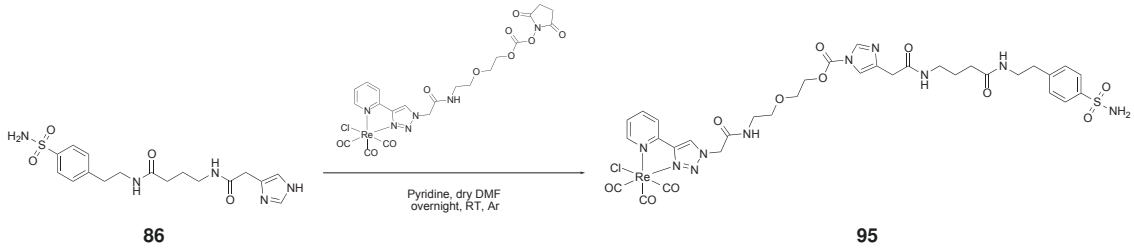

86 **95**

min, 14 mL/min, 10.3 min, purity: 94%). NH_4OAc was removed by repeated freeze-drying cycles.

^{1}H-NMR (400 MHz, $CDCl_3$: CD_3OD): δ (ppm) 8.96 (dt, J = 5.5, 1.1, 1H, H^a pyta), 8.83 (s, 1H, H^g pyta), 8.17 (s, 1H, H^2 of imidazole), 8.13-8.06 (m, 2H, H + H, $H^c + H^d$ pyta), 7.78 (d, J = 8.4, 2H, $H^{2,6}$ of benzenesulfonamide), 7.51 (ddd, J = 6.9, 5.6, 2.1, 1H, H^b pyta), 7.45 (s, 1H, H^5 of imidazole), 7.33 (d, J = 8.5, 2H, $H^{3,5}$ of benzenesulfonamide), 5.26 (q, J = 22.4, 2H, CH_2 α to pyta), 4.58-4.56 (m, 2H, $OCH_2CH_2OC(O)-$imidazole, partly hidden by water signal), 3.83-3.80 (m, 2H, $OCH_2CH_2OC(O)-$imidazole), 3.63 (t, J = 5.2, 2H, $NHC(O)CH_2CH_2O$), 3.47-3.40 (m + d + s, 2H + 2H + 2H, $NHC(O)CH_2CH_2O + CH_2$ α to imidazole + $ArCH_2CH_2NHC(O)$, 3.07 (t, J = 7.0, 2H, $CH_2NHC(O)CH_2-$imidazole), 2.85 (t, J = 7.0, 2H, $ArCH_2CH_2NHC(O)$), 2.10 (t, J = 7.3, 2H, $NHC(O)CH_2CH_2CH_2NH$), 1.73-1.64 (m, 2H, $NHC(O)CH_2CH_2CH_2NH$).

HR-MS (ESI+): *m/z* calculated for $[C_{34}H_{38}ClN_{10}O_{11}ReS+Na]^+$: 1037.15525, found: 1037.15545, error: 0.2 ppm.

C6-Boc (80)

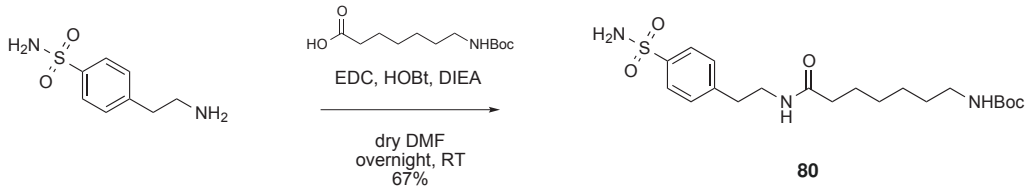

80

Boc-7-aminoheptanoic acid (101.8 mg, 0.51 mmol, 1 equiv.), EDC · HCl (145.7 mg, 0.76 mmol, 1.5 equiv.) and HOBt · H_2O (115.6 mg, 0.76 mmol, 1.5 equiv.) were dissolved in dry DMF (2.6 mL) under argon. After 5-10 minutes stirring, 4-(2-aminoethyl)benzene sulfonamide (249.7 mg, 1.25 mmol, 1 equiv.) and DIEA (260 µL, 1.5 mmol, 3 equiv.) were added and reaction mixture was stirred overnight at room temperature. Solvent was removed by rotary evaporation and the resulting sticky solid was taken up in a 1:1 mixture of EtOAc and saturated aqueous solution of $NaHCO_3$. After decantation, the organic layer was washed with brine, dried over anhydrous Na_2SO_4, filtered and concentrated. The crude was purified by automated silica gel flash column chromatography (5% MeOH in DCM) to give the desired compound as a white solid (146.1 mg, 0.34 mmol, 67%)

^{1}H-NMR (400 MHz, CD_3OD): δ (ppm) 7.84 (d, J = 8.5, 2H, $H^{2,6}$ of benze-

nesulfonamide), 7.41 (d, J = 8.6, 2H, $H^{3,5}$ of benzenesulfonamide), 3.46 (t, J = 7.2, 2H, $ArCH_2CH_2NHC(O)$), 3.02 (t, J = 7.0, 2H, $(CH_2)_5CH_2NHBoc$), 2.90 (t, J = 7.1, 2H, $ArCH_2CH_2NHC(O)$), 2.15 (t, J = 7.5, 2H, $NHC(O)CH_2(CH_2)_5NHBoc$), 1.57 (t, J = 7.1, 2H, $C(O)CH_2CH_2(CH_2)_4NHBoc$), 1.47-1.44 (m, 9H+ 2H, $(CH_3)_3 + C(O)(CH_2)_4CH_2CH_2NHBoc$), 1.30 (dt, J = 6.7, 3.1, 4H, $(CH_2)_2CH_2CH_2(CH_2)_2NHBoc$).

^{13}C-NMR (101 MHz, CD_3OD): δ (ppm) 176.2 ($CH_2C(O)NHCH_2$), 158.5 ($NHC(O)-Ot$-Bu), 145.4 (C^1 benzenesulfonamide), 143.1 (C^4 benzenesulfonamide), 130.4 (2C, $C^{3,5}$ benzenesulfonamide), 127.3 (2C, $C^{2,6}$ benzenesulfonamide), 79.8 ($C(CH_3)_3$), 41.3 (C + C, $ArCH_2CH_2NHC(O)$ + CH_2NHBoc), 37.0 ($NHC(O)CH_2(CH_2)_5NHBoc$), 36.3 ($ArCH_2 - CH_2-NHC(O)$), 30.8 ($CH_2-CH_2-NHBoc$), 29.9 (C(O)(CH2)2CH2), 28.8 (3C, $C(CH_3)_3$), 27.5 ($CH_2 - CH_2 - CH_2 - NHBoc$), 26.9 (C(O)CH2CH2).

HR-MS (ESI+): *m/z* calculated for $[C_{20}H_{33}N_3O_5S+Na]^+$: 450.20331, found: 450.20351, error: 0.4 ppm.

C6-Trityl (83)

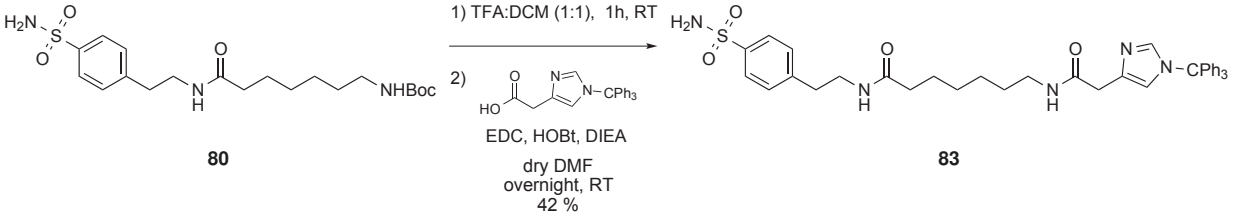

Boc-protected compound **80** (120 mg, 0.28 mmol, 1 equiv.) was dissolved in DCM (1 mL), and TFA (1 mL) was added drop wise. The solution was stirred for 1h at room temperature, then precipitated in cold Et_2O (40 mL) to give the deprotected ammonium salt as a white solid. 1-(triphenylmethyl)-1*H*-imidazole-4-acetic acid (121.2 mg, 0.33 mmol, 1.2 equiv.), $EDC \cdot HCl$ (90.2 mg, 0.47 mmol, 1.5 equiv.) and $HOBt \cdot H_2O$ (65.0 mg, 0.42 mmol, 1.3 equiv.) were dissolved in dry DMF (1.5 mL) under argon. After 5-10 minutes stirring, the solution was added to the deprotected amine. DIEA (146 µL, 0.78 mmol, 3 equiv.) was added and reaction mixture was stirred overnight at room temperature. Solvent was removed by rotary evaporation and the resulting sticky solid was taken up in a 1:1 mixture of EtOAc and saturated aqueous solution of $NaHCO_3$. After decantation, the organic layer was washed with brine, dried over anhydrous Na_2SO_4, filtered and concentrated. The crude was purified by automated silica gel flash column chromatography (5% MeOH in DCM). The resulting oil was co-evaporated with Et_2O until obtention of the desired compound as a white solid (79.8 mg, 0.12 mmol, 42%).

^{1}H-NMR (400 MHz, CD_3OD): δ (ppm) 7.84-7.81 (m, 2H), 7.40-7.34 (m, 12H), 7.16-7.14 (m, 6H), 6.85 (s, 1H), 3.43 (d, J = 7.1, 4H), 3.15 (t, J = 6.9, 2H), 2.87 (t, J = 7.1, 3H), 2.11 (t, J = 7.4, 3H), 1.51 (ddd, J = 30.5, 15.9, 7.1, 5H), 1.30-1.21 (m, 6H).

^{13}C-NMR (101 MHz, CD_3OD): δ (ppm) 176.14, 145.35, 143.61, 143.07, 130.86, 130.41, 129.33, 129.24, 127.28, 41.28, 40.64, 40.45, 36.95, 36.23, 30.15, 29.75, 27.51, 26.84.

HR-MS (ESI+): *m/z* calculated for $[C_{39}H_{43}N_5O_4S+H]^+$: 678.31085, found: 678.31146, error: 0.9 ppm.

C6NH (87)

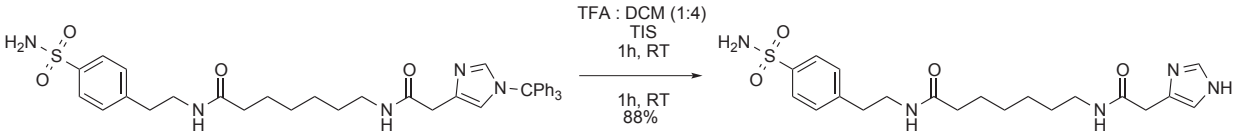

83 **87**

Trityl imidazole derivative **83** (53.6 mg, 0.079 mmol, 1 equiv.) was dissolved in DCM (0.8 mL). TFA (0.2 mL) was added drop wise, followed by TIS (16.2 µL, 0.079 mmol, 1 equiv.). The mixture was stirred for 1 hour at room temperature, then precipitated in Et_2O to give the desired compound as a white solid containing traces of water (35.6 mg of hydrated compound, 0.070 mmol, 88%).

^{1}H-NMR (300 MHz, CD_3OD): δ (ppm) 8.81 (s, 1H, H^2 imidazole), 7.82 (d, J = 8.4, 2H, $H^{2,6}$ of benzenesulfonamide), 7.41-7.38 (d + s, J = 8.3, 2H + 1H, $H^{3,5}$ of benzenesulfonamide + H^5 imidazole), 3.72 (s, 2H, CH_2 α to imidazole), 3.46 (t, J = 7.0, 2H, $ArCH_2CH_2NHC(O)$), 3.18 (t, J = 7.1, 2H, $CH_2NHC(O)CH_2$ − imidazole), 2.89 (t, J = 7.0, 2H, $ArCH_2CH_2NHC(O)$), 2.13 (t, J = 7.4, 2H, $C(O)CH_2(CH_2)_5NHC(O)$), 1.51 (tt, J = 13.7, 6.9, 2H + 2H, $NHC(O)CH_2CH_2(CH_2)_2CH_2CH_2NHC(O)$), 1.33-1.24 (m, 4H, 2H + 2H, $NHC(O)(CH_2)_2CH_2CH_2(CH_2)_2NHC(O)$).

^{13}C-NMR (75 MHz, CD_3OD): δ (ppm) 176.2 ($ArCH_2CH_2C(O)NHCH_2$), 169.8 ($CH_2C(O)NHCH_2$ − imidazole, 145.4 (C^1 benzenesulfonamide), 143.0 (C^4 benzenesulfonamide), 135.0 (C^2 of imidazole), 130.46 (2C, $C^{3,5}$ benzenesulfonamide), 129.4 (C^4 of imidazole), 127.2 (2C, $C^{2,6}$ benzenesulfonamide), 118.5 (C^5 of imidazole), 41.2 ($ArCH_2CH_2NHC(O)$), 40.7 (CH_2−NHC(O)−CH_2−imidazole), 36.9 ($NHC(O)CH_2(CH_2)_5NHBoc$), 36.1 (CH_2CH_2−$NHC(O)CH_2$ − imidazole), 32.0 (CH_2 α to imidazole), 30.1 (CH_2−CH_2−NHC(O)−CH_2 − imidazole), 29.7 (C(O)(CH2)2CH2), 27.6 ($CH_2CH_2CH_2NHBoc$), 26.8 (C(O)CH2CH2).

HR-MS (ESI+): *m/z* calculated for $[C_{20}H_{29}N_5O_4S+H]^+$: 436.20130, found: 436.20148, error: 0.4 ppm.

C6-SCoMPI (96)

C6-imidazole **87** (12.8 mg, 29.4 µmol, 1.1 equiv.) and the rhenium complex **93** (19.4 mg, 26.3 µmol, 1 equiv.) were dissolved in dry DMF (2 mL) under argon. Dry pyridine (2.2 µL, 27.3 µmol, 1.1 equiv.). Solvent was removed by rotary evaporation and the resulting crude was purified by HPLC (25 to 100 % TFA-free ACN in 10 mM aqueous NH_4OAc pH 7.0 in 30

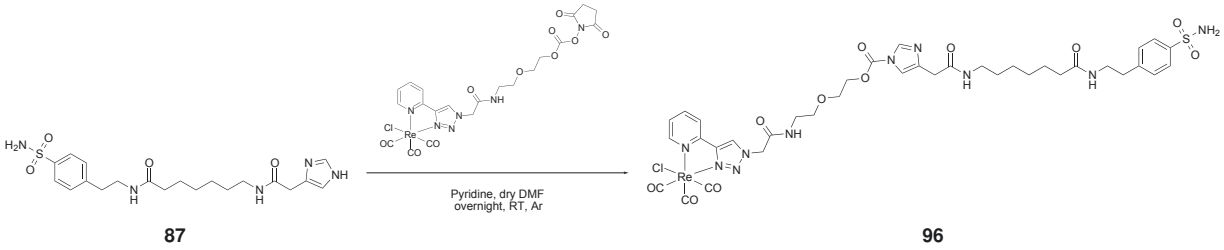

87 **96**

min, 14 mL/min, 11.6 min, purity: 94%). NH_4OAc was removed by repeated freeze-drying cycles.

^{1}H-NMR (400 MHz, CD_3OD : $CDCl_3$): δ (ppm) 8.96 (dd, J = 5.6, 0.5, 1H, H^a pyta), 8.82 (s, 1H, H^g pyta), 8.16 (s, 1H, H^2 of imidazole), 8.10-8.06 (m, 2H, H + H, H^c + H^d pyta), 7.79 (dd, J = 8.5, 1.4, 2H, $H^{2,6}$ of benzenesulfonamide), 7.50 (ddd, J = 7.0, 5.5, 2.0, 1H, H^b pyta), 7.45 (s, 1H, H^5 of imidazole), 7.33 (d, J = 8.5, 2H, $H^{3,5}$ of benzenesulfonamide), 5.25 (q, J = 22.5, 2H, CH_2 α to pyta), 4.56-4.55 (m, 2H, $OCH_2CH_2OC(O)-$imidazole, partly hidden by water signal), 3.82-3.80 (m, 2H, $OCH_2CH_2OC(O)-$imidazole), 3.62 (t, J = 5.3, 2H, $NHC(O)CH_2CH_2O$), 3.44 (dt, J = 12.3, 6.2, m + d + s, 2H + 2H + 2H, $NHC(O)CH_2CH_2O$ + CH_2 α to imidazole + $ArCH_2CH_2NHC(O)$), 3.13 (t, J = 7.1, 2H, $CH_2NHC(O)CH_2-$imidazole), 2.85 (t, J = 7.1, 2H,, $ArCH_2CH_2NHC(O)$), 2.09 (t, J = 7.4, 2H, $NHC(O)CH_2CH_2CH_2NH$), 1.51 (dt, J = 14.4, 7.6, 2H, $NHC(O)CH_2CH_2$), 1.43 (dt, J = 14.6, 7.4, 2H, $CH_2CH_2NHC(O)CH_2-$imidazole), 1.28-1.19 (m, 2H + 2H, $NHC(O)(CH_2)_2CH_2CH_2(CH_2)_2NH$

HR-MS (ESI+): *m/z* calculated for $[C_{36}H_{44}ClN_{10}O_{11}ReS+Na]^+$: 1079.20220, found: 1079.2016, error: -0.6 ppm.

C5-Boc (81)

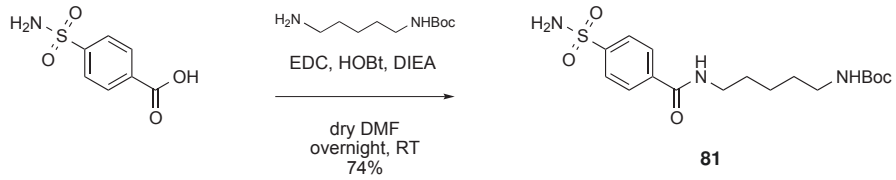

81

4-carboxybenzenesulfonamide (120.8 mg, 0.6 mmol, 1.25 equiv.), EDC · HCl (143.8 mg, 0.75 mmol, 1.6 equiv.) and HOBt · H_2O (114.5 mg, 0.75 mmol, 1.6 equiv.) were dissolved in dry DMF (2.5 mL) under argon. After 5-10 minutes stirring, *N*-Boc-1,5-diaminopentane (0.1 mL, 0.48 mmol, 1 equiv.) and DIEA (260 µL, 1.5 mmol, 3.1 equiv.) were added. Reaction mixture was stirred overnight at room temperature. Solvent was removed by rotary evaporation and the resulting sticky solid was taken up in a 1:1 mixture of EtOAc and saturated aqueous solution of $NaHCO_3$. After decantation, the organic layer was washed with brine, dried over anhydrous Na_2SO_4, filtered and concentrated. The crude was purified by automated silica gel flash column chromatography (5% MeOH in DCM) to give the desired compound as a white solid (173.8 mg, 0.45 mmol, 74%)

^{1}H-NMR (400 MHz, CD_3OD): δ (ppm) 7.98-7.93 (m, 4H, $H^{2,6}$ + $H^{3,5}$ of benzenesulfonamide), 3.39 (t, J = 7.1, 2H, ArC(O)NHCH_2), 3.05 (t, J = 6.9, 2H, CH_2NHBoc), 1.65 (quintet, J = 7.3, 2H, CH_2CH_2NHBoc), 1.56-1.49 (m, 2H, ArC(O)NHCH_2CH_2), 1.42-1.38 (m, 9H + 2H, C(CH_3)$_3$ + (CH_2)$_2$CH_2(CH_2)$_2$).

^{13}C-NMR (101 MHz, CD_3OD): δ (ppm) 168.71 (ArC(O)NH), 158.53 (NHC(O)Ot-Bu), 147.53 (C^1 benzenesulfonamide), 139.16 (C^4 benzenesulfonamide), 128.90 (2C, $C^{3,5}$ benzenesulfonamide), 127.26 (2C, $C^{2,6}$ benzenesulfonamide), 79.80 (C(CH$_3$)$_3$), 41.02 (C + C, CH$_2$NHBoc + ArC(O)NHCH$_2$), 30.03 (C + C, CH$_2$CH$_2$NHBoc + ArC(O)NHCH$_2$$CH_2$), 28.77 (3C, C($CH_3$)$_3$), 25.18 ((CH$_2$)$_2$$CH_2$(CH$_2$)$_2$NHBoc).

C5-Trityl (84)

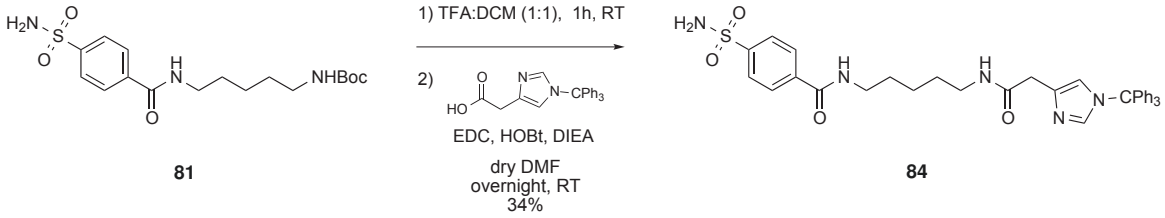

Boc-protected compound **81** (112.7 mg, 0.29 mmol, 1 equiv.) was dissolved in DCM (1.2 mL), and TFA (1.2 mL) was added drop wise. The solution was stirred for 1h at room temperature, then precipitated in cold Et_2O (40 mL) to give the deprotected ammonium salt as a white solid. 1-(triphenylmethyl)-1H-imidazole-4-acetic acid (132.6 mg, 0.36 mmol, 1.2 equiv.), EDC · HCl (88.3 mg, 0.46 mmol, 1.5 equiv.) and HOBt · H_2O (69.3 mg, 0.45 mmol, 1.3 equiv.) were dissolved in dry DMF (1.6 mL) under argon. After 5-10 minutes stirring, the solution was added to the deprotected amine. DIEA (156 µL, 0.9 mmol, 3 equiv.) was added and reaction mixture was stirred overnight at room temperature. Solvent was removed by rotary evaporation and the resulting sticky solid was taken up in a 1:1 mixture of EtOAc and saturated aqueous solution of $NaHCO_3$. After decantation, the organic layer was washed with brine, dried over anhydrous Na_2SO_4, filtered and concentrated. The crude was purified by automated silica gel flash column chromatography (5% MeOH in DCM). The resulting oil was co-evaporated with Et_2O until obtention of the desired compound as a white solid (63.4 mg, 0.10 mmol, 34%).

^{1}H-NMR (400 MHz, CD_3OD): δ (ppm) 7.95 (q, J = 7.1, 4H), 7.41 (s, 1H), 7.37 (dt, J = 4.3, 2.8, 9H), 7.15 (dd, J = 6.8, 3.0, 6H), 6.85 (s, 1H), 3.43 (s, 2H), 3.36 (t, J = 7.1, 2H), 3.19 (t, J = 7.0, 2H), 1.67-1.59 (m, 2H), 1.53 (dt, J = 14.4, 7.2, 2H), 1.38 (dt, J = 15.4, 7.7, 2H).

^{13}C-NMR (101 MHz, CD_3OD): δ (ppm) 172.89, 168.72, 147.61, 143.61, 139.18, 130.87, 129.35, 129.25, 128.93, 127.30, 121.28, 77.00, 41.00, 40.38, 29.99, 29.94, 25.24.

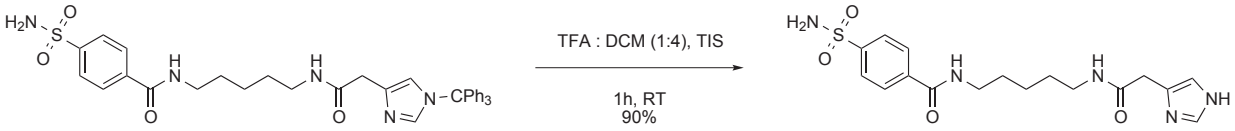

84 88

C5NH (88)

Trityl imidazole derivative **84** (67.4 mg, 0.106 mmol, 1 equiv.) was dissolved in DCM (0.8 mL). TFA (0.2 mL) was added drop wise, followed by TIS (23 µL, 0.112 mmol, 1 equiv.). The mixture was stirred for 1 hour at room temperature, then precipitated in Et_2O to give the desired compound as a white solid containing traces of water (43.2 mg of hydrated compound, 0.095 mmol, 90%).

^{1}H-NMR (300 MHz, CD_3OD): δ (ppm) 8.81 (s, 1H, H^2 imidazole), 7.95 (s, 4H, $H^{2,6}$ + $H^{3,5}$ of benzenesulfonamide), 7.39 (s, 1H, H^5 imidazole), 3.71 (s, 2H, CH_2 α to imidazole), 3.39 (t, J = 6.7, 2H, ArC(O)NHCH_2), 3.22 (t, J = 6.3, 2H, CH_2C(O)NHCH2 - imidazole), 1.61 (td, J = 13.6, 6.7, 2H + 2H, $CH_2CH_2CH_2CH_2CH_2$), 1.41 (t, J = 6.6, 2H, $(CH_2)_2CH_2(CH_2)_2$).

^{13}C-NMR (75 MHz, CD_3OD): δ (ppm) 169.80 (ArC(O)NH), 168.74 (NHC(O)CH_2− imidazole), 147.54 (C^1 benzenesulfonamide), 139.12 (C^4 benzenesulfonamide), 134.96 (C^2 of imidazole), 129.36 (C^4 of imidazole), 128.92 (2C, $C^{3,5}$ benzenesulfonamide), 127.27 (2C, $C^{2,6}$ benzenesulfonamide), 118.49 (C^5 of imidazole), 40.94 (ArC(O)NHCH$_2$), 40.58 (CH$_2$NHC(O)), 31.96 (CH$_2$ α to imidazole), 29.99-29.91 (C + C, ArC(O)NHCH$_2C$H$_2$ + CH$_2$CH$_2$NHC(O)CH_2− imidazole), 25.27 ((CH$_2$)$_2C$H$_2$(CH$_2$)$_2$).

HR-MS (ESI+): m/z calculated for $[C_{17}H_{23}N_5O_4S+H]^+$: 394.15435, found: 394.15443, error: 0.2 ppm.

C5-SCoMPI (97)

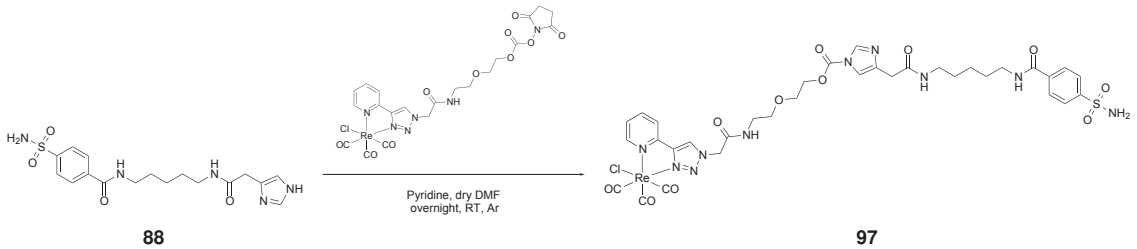

88 97

C5-imidazole **88** (12.4 mg, 31.5 µmol, 1.3 equiv.) and the rhenium complex **93** (18.3 mg, 24.8 µmol, 1 equiv.) were dissolved in dry DMF (2 mL) under argon. Dry pyridine (2.2 µL, 27.3 µmol, 1.1 equiv.). Solvent was removed by rotary evaporation and the resulting crude was purified by HPLC (25 to 100 % TFA-free ACN in 10 mM aqueous NH_4OAc pH 7.0 in 30 min, 14 mL/min, 11.3 min, purity: 96%). NH_4OAc was removed by repeated freeze-drying cycles.

^{1}H-NMR (400 MHz, CD_3OD : $CDCl_3$): δ (ppm)8.96-8.94 (m, 1H, H^a pyta), 8.81 (s, 1H, H^g pyta), 8.13 (s, 1H, H^2 of imidazole), 8.11-8.04 (m, 2H, H + H, H^c + H^d pyta), 7.94-7.89 (m, 4H, $H^{2,6}$ + $H^{3,5}$ of benzenesulfonamide), 7.50 (ddd, J = 7.3, 5.5, 1.8, 1H, H^b pyta), 7.42 (s, 1H, H^5 of imidazole), 5.25 (q, J = 23.0, 2H, CH_2 α to pyta), 4.57-4.55 (m, 2H, OCH$_2$CH_2OC(O)−imidazole, partly hidden by water signal), 3.81 (td, J = 3.1, 2.3, 2H, OCH_2CH$_2$OC(O)−imidazole), 3.62 (t, J = 5.4, 2H, NHC(O)CH$_2$CH_2O), 3.45 (m + s, 2H + 2H, NHC(O)CH_2CH$_2$O + CH_2 α to imidazole), 3.38-3.33 (m, 2H, ArC(O)NHCH_2), 3.18 (t, J = 7.0, 2H, CH_2C(O)NHCH2 - imidazole), 1.61 (dt, J = 14.6, 7.3, 2H, ArC(O)NHCH$_2$CH_2), 1.52 (dd, J = 14.5, 6.9, 2H, CH_2CH2C(O)NHCH2 - imidazole), 1.38 (dd, J = 16.1, 7.6, 2H, (CH$_2$)$_2$CH_2(CH$_2$)$_2$).

HR-MS (ESI+): *m/z* calculated for $[C_{34}H_{38}ClN_{10}O_{11}ReS+Na]^+$: 1037.15525, found: 1037.15464, error: -0.6 ppm.

6.2 Labelling of Carbonic Anhydrases with LDAI-SCoMPI

6.2.1 Stock solutions

Stock solutions of LDAI-SCoMPI reagents were done in DMSO and stored at −20 °C. Concentrations were checked by measuring UV absorption at 280 nm or 335 nm.

6.2.2 *In vitro* labelling of human Carbonic Anhydrase 1 (hCA1)

A solution of hCA1 (10 µM in 50 mM HEPES pH 7.2 was incubated at 37 °C for 6 h with 2 or 20 equivalents of LDAI-SCoMPI reagent. Every two hours, aliquots of the incubation solution were taken, treated and analysed either by MALDI-TOF MS or fluorescence gel imaging. A control experiment consisting in incubation solution + 10 equivalents EZA was performed for each experiment, and analysed at 6h.

Treatment for MALDI-TOF MS analysis: 10 µM of sample solution were quenched and purified using a ZipTip (C18) and 0.1% aqueous TFA, then spotted on a MALDI plate. Peak areas of labelled and unlabelled protein were determined and percentage of labelling calculated.

Treatment for gel imaging analysis: 30 µM of sample solution were diluted with 30 µL 2X denaturing Laemmli buffer and stored at −30 °C prior to gel analysis. Sample were heated at 70 °C for 20 min and loaded on a 12.5% SDS polyacrylamide gel. Fluorescence gel Imaging was performed prior to CBB staining.

6.2.3 Labelling of CA-IX and CA-XII in cells for multimodal imaging

Fluorescence and Infrared Imaging: A549 cells were deposed in 12-wells plates in presence of CaF_2 slides (10^5 cells/well). After 24h, cells were put under hypoxic conditions for 24 h using Oxoid Anaerogen kit. Cells were then incubated at 37 °C with LDAI-SCoMPI reagents under normoxic conditions. Typical incubation conditions are 10 µM reagent for 3–6 h.

X-fluorescence Imaging: A549 cells were deposed in 24-wells plates in presence of Si_3N_4 slides (10^4 cells/well). After 24h, cells were put under hypoxic conditions for 24 h using Oxoid Anaerogen kit. Cells were then incubated with LDAI-SCoMPI reagents (10 µM) under normoxic conditions for 3 h at 37 °C.

6.2.4 Fluorescence and IR imaging

The experimental setups used for fluorescence and IR microscopies were identical to those used for SCoMPI-labelled CPPs (see section 4.5.1).

6.2.5 Synchrotron X-ray Fluorescence microspectroscopy

Samples were examined on the new Nanoscopium beamline at SOLEIL synchrotron. Single spectra were recorded by two detectors for 1000s with a $\sim 1\times1\,\mu m^2$ resolution and an increased flux (~ 2.1 as compared to ~ 0.7 for Homeodomain samples). Spectra from both detectors were additioned and polted using Kaleidagraph software.

Appendix A

Measurements of quantum yields

Measurements were performed by by Dr Nicolas Delsuc. Luminescence quantum yields were measured using a Jasco FP-8300 spectrofluorometer. Emission spectra were recorded upon excitation at 320 nm for both compounds. The quantum yields were calculated according to the following equation [210]:

$$Q_x = Q_r \left(\frac{A_r(\lambda_r)}{A_x(\lambda_x)}\right) \left(\frac{I_r(\lambda_r)}{I_x(\lambda_x)}\right) \left(\frac{n_x^2}{n_r^2}\right) \left(\frac{D_x}{D_r}\right) \tag{A.1}$$

In this equation, Q_r is the quantum yield of the reference, $I(\lambda)$ is the relative intensity of the exciting light at wavelength λ, n is the average refractive index of the solution to the luminescence, D is the integrated area under the emission spectrum, and $A(\lambda)$ is the absorbance of the solution at the exciting wavelength. The subscripts x and r refer to the unknown and reference solutions, respectively. Quinine sulfate in 0.1 N sulfuric acid was used as the standard with a known emission quantum yield of 0.546 (exc 320 nm) [211].

Appendix B

Publication

Colloids and Surfaces B: Biointerfaces 131 (2015) 102–107

Contents lists available at ScienceDirect

Colloids and Surfaces B: Biointerfaces

journal homepage: www.elsevier.com/locate/colsurfb

A rhenium tris carbonyl derivative as a model molecule for incorporation into phospholipid assemblies for skin applications

Estibalitz Fernández[a,*], Gelen Rodríguez[b], Sarah Hostachy[c], Sylvain Clède[c], Mercedes Cócera[b], Christophe Sandt[d], François Lambert[c], Alfonso de la Maza[a], Clotilde Policar[c], Olga López[a]

[a] Institute of Advanced Chemistry of Catalonia (IQAC CSIC), Jordi Girona 18 26, 08034 Barcelona, Spain
[b] Bicosome S.L., Jordi Girona 18 26, 08034 Barcelona, Spain
[c] Ecole Normale Supérieure, Rue Lhomond, 75005 Paris, France
[d] Synchrotron SOLEIL, SMIS Beamline, L'Orme des Merisiers, 91190 Saint Aubin, France

ARTICLE INFO

Article history:
Received 4 March 2015
Received in revised form 7 April 2015
Accepted 20 April 2015
Available online 28 April 2015

Keywords:
Bicosomes
Skin
Fourier transform infrared spectroscopy
Synchrotron radiation
Rhenium tris carbonyl complexes

ABSTRACT

A rhenium tris carbonyl derivative (fac [$Re(CO)_3Cl$(2 (1 dodecyl 1H 1,2,3,triazol 4 yl) pyridine)]) was incorporated into phospholipid assemblies, called bicosomes, and the penetration of this molecule into skin was monitored using Fourier transform infrared microspectroscopy (FTIR). To evaluate the capacity of bicosomes to promote the penetration of this derivative, the skin penetration of the $Re(CO)_3$ derivative dissolved in dimethyl sulfoxide (DMSO), a typical enhancer, was also studied.

Dynamic light scattering results (DLS) showed an increase in the size of the bicosomes with the incorporation of the $Re(CO)_3$ derivative, and the FTIR microspectroscopy showed that the $Re(CO)_3$ derivative incorporated in bicosomes penetrated deeper into the skin than when dissolved in DMSO. When this molecule was applied on the skin using the bicosomes, 60% of the $Re(CO)_3$ derivative was retained in the stratum corneum (SC) and 40% reached the epidermis (Epi). Otherwise, the application of this molecule via DMSO resulted in 95% of the $Re(CO)_3$ derivative being in the SC and only 5% reaching the Epi.

Using a $Re(CO)_3$ derivative with a dodecyl chain as a model molecule, it was possible to determine the distribution of molecules with similar physicochemical characteristics in the skin using bicosomes. This fact makes these nanostructures promising vehicles for the application of lipophilic molecules inside the skin.

1. Introduction

The topical application of different drugs and active compounds has received significant interest in the medical and pharmaceutical fields. However, the incorporation of molecules in the skin is difficult due to the barrier function of the superficial layer of this tissue, the stratum corneum (SC) [1]. The incorporation of lipophilic molecules is facilitated by their dissolution into intercellular lipids around the cells of the SC [2]. Additionally, lipid vehicles are frequently used to facilitate the incorporation of different active compounds in the skin [2,3].

Bicosomes are phospholipid assemblies based on mixtures of spherical vesicles with diameters of approximately 100–200 nm and discoidal structures with sizes of approximately 15–25 nm in diameter and 5.4 nm in thickness (Fig. 1). In this sense, bicosomes combine the advantages of disks and spherical vesicles [4]. Lipid vesicles have been used in dermatological applications for decades as delivery systems with different active compounds in the skin [5], and discoidal lipid structures have recently demonstrated a significant potential as carriers and modifiers of skin permeability [6,7]. The combination of discoidal and vesicular assemblies forming bicosomes could potentiate the effects of both nanostructures on the cutaneous tissue.

Fourier transform infrared spectroscopy (FTIR) has been used to evaluate skin composition as well as penetration of different substances in this tissue [8,9]. This technique is employed to investigate the weak energies involved in vibrational levels. The IR spectrum of the skin shows at least three bands associated with different molecules from polypeptides and proteins, as follows: amide A (NH vibration, approximately 3300 cm^{-1}), amide I (CO vibration, approximately 1650 cm^{-1}), and amide II (CN vibration, approximately 1550 cm^{-1}). The bands associated with the alkyl chains

* Corresponding author. Tel.: +34 934 006 100; fax: +34 932 045 904.
E mail address: efptqt@cid.csic.es (E. Fernández).

http://dx.doi.org/10.1016/j.colsurfb.2015.04.045
0927 7765/

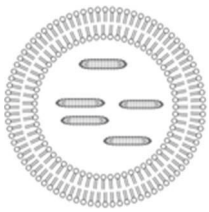

Fig. 1. Bicosome structure.

of skin lipids through the CH_3 and CH_2 stretching vibration are also present (approximately 2920 and 2850 cm^{-1} for asymmetric and symmetric, respectively) [8,9]. Due to the chemical similarity between lipids from different vehicles and skin lipids (both have CH_3 and CH_2 stretching), their characteristic vibrational features cannot be separated. Consequently, in a previous work, the deutera tion of lipids from different vehicles was performed to differentiate the vibrations of endogenous (skin lipids) and exogenous lipids [8,9]. This method allowed for the detection of lipids from vehicles in the skin but not the study of the penetration of other active com pounds in these lipid systems. An IR active probe with vibrational levels that do not interfere with those from the skin and carrier is needed for this evaluation.

In this work, the use of another type of lipid tagging metal–CO probes that are appropriate for IR imaging is proposed [10–12]. Our research group recently showed that $Re(CO)_3$ is a useful probe for IR and luminescent imaging. These compounds can be used for tag ging different molecules, including alkyl chains of various lengths, tamoxifen like derivatives, oestrogen, or peptides, to image them in cells or tissue using both IR microscopy and fluorescence imaging [13–19]. Interestingly, these $Re(CO)_3$ probes, which are very stable in biological environments, show a very intense signal in the region of 1900–2000 cm^{-1}, that does not interfere with the IR signals from the skin and can be easily quantified [13]. For these reasons, they are the probes of choice for detection and quantification in the IR and have been considered for tagging bicosomes and monitoring their penetrations.

A $Re(CO)_3$ derivative can be attached to several different molecules and provides a way to mark and follow these molecules for skin penetration studies. Recently, a nona arginine was con jugated with a $Re(CO)_3$ derivative and imaged in skin after permeation [16]. Moreover, the synthesis, sub cellular imaging and quantification in cells of a $Re(CO)_3$ derivative appended with a $C_{12}N_3$ chain were previously described. In this study, this lipophilic molecule was simultaneously detected using FTIR and fluorescence spectroscopy [13–16,18].

From a spectroscopic point of view, $C_{12}Re(CO)_3$ (Fig. 2) shows a specific vibrational signature with two bands at 1920 cm^{-1} and 2020 cm^{-1}, where no absorption from skin constituents occurs. The first band (E band at 1920 cm^{-1}) corresponds to asymmet ric stretching vibrations, and the second (A_1 band at 2020 cm^{-1}) comes from symmetric stretching vibrations [16,18]. Therefore, this lipophilic molecule can be detected without interference in the skin using FTIR.

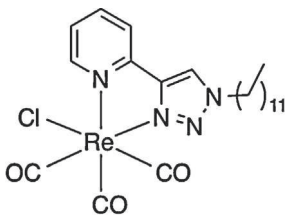

Fig. 2. $C_{12}Re(CO)_3$: (fac [$Re(CO)_3Cl$(2 (1 dodecyl 1H 1,2,3,triazol 4 yl) pyridine)]). See synthesis in [10].

In the present study, the lipophilic $C_{12}Re(CO)_3$, which is com posed of a $Re(CO)_3$ derivative attached to a dodecyl chain, was used. This lipophilic derivative can be inserted into the bicosome membrane. This strategy enables the study of the penetration and location of this molecule inside the skin and, at the same time, the evaluation of bicosome systems as carriers for the incorporation of lipophilic molecules in the skin.

2. Experimental

2.1. Chemicals

Bicosome systems were formed using 1,2 dipalmitoyl *sn* glycero 3 phosphocholine (DPPC) and 1,2 dihexanoyl *sn* glycero 3 phosphocholine (DHPC) purchased from Avanti Polar Lipids (Alabaster, Alabama, USA). Cholesterol (CHO) was obtained from Sigma–Aldrich (St. Louis, MO, USA), and Lipoid S 100, whose main component (>94%) is phosphatidylcholine (PC), was obtained from Lipoid GmbH (Ludwigshafen, Germany). The $C_{12}Re(CO)_3$ was syn thesized and obtained from the Ecole Normale Supérieure (Paris, France) [13,18]. Chloroform and dimethyl sulfoxide 99% (v/v) (DMSO) were purchased from Merck, and purified water was obtained using an ultra pure system, Milli Q plus 185 (Millipore, Bedford, MA, USA).

2.2. Preparation of bicosomes incorporating $C_{12}Re(CO)_3$

Bicosomes incorporating $C_{12}Re(CO)_3$ were prepared by mixing an appropriate amount of DPPC, DHPC and the $Re(CO)_3$ derivative in a chloroform solution to reach a molar ratio of DPPC/DHPC of 3.5. After the components were mixed, the chloroform was evaporated with a rotary evaporator, and the resulting lipid film was hydrated. The resulting solution was subjected to several cycles of sonication and freezing until the sample became transparent.

After that, 80% (w/v) Lipoid S 100 and 20% (w/v) cholesterol in chloroform were mixed and the solvent was removed with a rotary evaporator. The resulting film was hydrated with the previously formed solution [4].

The total lipid concentration in the bicosomes was 15% (w/v) and the concentration of $C_{12}Re(CO)_3$ was 1% (w/v).

The solution in DMSO was prepared by dissolving the appropri ate amount of $C_{12}Re(CO)_3$ in DMSO to reach the same concentration as the bicosomes (1%, w/v).

2.3. Dynamic light scattering (DLS)

The sizes of the bicosomes incorporating $C_{12}Re(CO)_3$ were measured by detecting the hydrodynamic diameter (HD) using a Zetasizer nano ZS90 (Malvern Instruments, Malvern, Worcester shire, UK). For comparative purposes, the size of the bicosomes without any incorporated molecule was also measured.

DLS measures the Brownian motion of the particles and corre lates this to the particle size. The relationship between the size of a particle and its speed due to Brownian motion is defined by the Stokes–Einstein equation:

$$HD = \frac{k_B T}{3\pi\eta D}$$

where HD is the hydrodynamic diameter of a hypothetical hard sphere that diffuses with the same speed as the particle in the experiment, D is the translational diffusion coefficient (m^2/s), k_B is the Boltzmann's constant ($1.3806503 \times 10^{-23}$ $J K^{-1}$), T is the abso lute temperature (K) and η is the viscosity (mPa s) [20].

DLS measurements were performed in triplicate and the mean size and standard deviation (SD) of the different populations in the distribution curves were obtained.

2.4. Preparation of skin samples

Pig skin from the back of a Landrace large white pig weigh ing around 35 kg was obtained at the Autonomous University of Barcelona (Spain). The skin was removed from the back of the pig minutes after the animal was sacrificed. The animal was sac rificed for medical experimentation in the veterinary faculty of Autonomous University of Barcelona (Spain). The protocols used for these medical studies were approved by the Ethical Commis sion of Animal and Human Experimentation (Spanish Government) under the auspices of the Ethical Commission of the Autonomous University of Barcelona.

The removed skin was dermatomed to 500 ± 50 μm thick (Der matome GA630, Aesculap, Tuttlingen, Germany), vacuum packed and stored in a refrigerator. After 18 h, 10 μL of bicosome systems (15%, w/v phospholipids; 85%, w/v water and 1%, w/v $C_{12}Re(CO)_3$) containing $C_{12}Re(CO)_3$ was applied on the skin for 24 h at room temperature (20–25 °C). For comparative purposes and to evaluate the capacity of the bicosomes to promote the penetration capacity of $C_{12}Re(CO)_3$, 10 μL of DMSO solution of this lipophilic molecule was also applied on the skin under the same conditions.

The treatment was performed using three skin pieces for each $C_{12}Re(CO)_3$ solution (bicosomes and DMSO).

The incubation of the skin pieces was performed at room tem perature (20–25 °C) on a Petri plate on wet filter paper. Then, the plate was covered with paraffin. Under these conditions, drying of the skin and evaporation of the solvent (DMSO/bicosomes) were avoided. The relative humidity inside the Petri plate was approxi mately 90%. During the treatment, the hydration and temperature of the skin samples remained constant.

Finally, all skin samples were covered with optimal cutting tem perature compound (OCT) and frozen in liquid N_2 before cutting into transverse 6 μm thick sections. The cuts were performed using a Cryostat CM3050 (Leica Biosystems Nussloch, Germany). The dif ferent skin sections were placed on CaF_2 circular windows (1 cm in diameter).

Considering that a small fraction of the bicosome/DMSO could flow over the edges of the skin, the slices from the edges of the tissue were removed. Only skin slices from the middles of the pieces were used in the FTIR microspectroscopy.

2.5. FTIR experiments

IR microspectroscopy was performed using synchrotron radi ation at the SMIS beamline in synchrotron SOLEIL. Synchrotron radiation was employed because it provides a high spectral quality and produces high contrast chemical imaging. A Thermo Contin uum XL IR microscope coupled to an FTIR Nicolet Nexus 5700 spectrometer (Thermo electron corporation, Madison, WI, USA) was employed in these experiments. The microscope is equipped with a 32X/NA 0.65 Schwarzschild objective and matching con denser, a mercury cadmium telluride (MCT) type A narrow band detector cooled by liquid nitrogen and an X Y Z motorized stage.

Optical micrographs were produced from the microscope in the visible image mode to define the sampling positions. The spec tra were acquired at room temperature in transmission mode, in the 3600–1000 cm^{-1} range, and 128 scans were averaged at 4 cm^{-1} resolution. Spectral maps were recorded with an aperture of 10 μm × 10 μm and steps of 10 μm in X and Y.

2.6. Data treatment

To quantify the amount of $C_{12}Re(CO)_3$ in the skin using the FTIR maps, the ratio between the areas under the curves (AUC) of the $C_{12}Re(CO)_3$ vibrations (A_1 and E) and the Amide II skin vibra tion was calculated. This calculation was performed in all of the maps obtained for skin treated with bicosomes and DMSO solu tion (approximately 7–9). The mean values and SDs of the ratios were calculated and are presented with error bars. Analysis of variance (ANOVA) was used to determine the significant differ ences between the ratios obtained from different treatments of $C_{12}Re(CO)_3$ (bicosomes and DMSO) using the Statgraphics plus 5 programme. A p value below 0.05 was considered significant.

Table 1
Mean value of hydrodynamic diameter (HD) and standard deviation (SD) of different bicosomes and proportion of the particle populations analyzed by intensity of light scattered at 25 °C ($N = 3$).

Lipid system	HD ± SD (nm)	%Int
Bicosomes	185 ± 15	85
Bicosomes + $C_{12}Re(CO)_3$	290 ± 10	85

3. Results

3.1. Characterization of bicosomes using DLS

The HDs obtained using DLS at 25 °C for bicosomes incorpo rating $C_{12}Re(CO)_3$ are shown in Table 1. The HD corresponds to a hypothetical hard sphere that diffuses with the same speed as the particle in the experiment. For comparative purposes, the size of the bicosomes without any incorporated molecules is also shown.

The size of the bicosomes without $C_{12}Re(CO)_3$ was approxi mately 185 nm with a proportion of light scattered approximately 85%. Incorporation of $C_{12}Re(CO)_3$ led to an increase in the particle size with an HD of approximately 290 nm and 85% light scattered.

The size increase of the bicosomes with the incorporation of $C_{12}Re(CO)_3$ could be due to the location of this lipophilic molecule in the bicosome structure. Considering the low solubility in water of $C_{12}Re(CO)_3$, the location of this molecule in the lipophilic region of the bilayer of the bicosomes is expected. Then, the incorporation of this lipophilic molecule inside the lipid bilayer of the bicosomes would promote a slight increase in the sizes of the nanostructures.

3.2. Distribution of $C_{12}Re(CO)_3$ through the skin

3.2.1. Qualitative analysis

IR spectra of skin samples were recorded in transmission mode in the 3600–1000 cm^{-1} range (Fig. 3). The spectrum for skin sam ples treated with $C_{12}Re(CO)_3$ incorporated in bicosomes shows bands that are characteristic of skin amides at approximately 3300 cm^{-1} corresponding to NH vibrations (1); at 1660 cm^{-1}, corresponding to CO vibrations (2); and at 1550 cm^{-1} (3). The characteristic CH_3 and CH_2 stretching vibration of lipids is at approximately 2920 cm^{-1} (4) (Fig. 3) [7]. A_1 and E vibration bands of the lipophilic $C_{12}Re(CO)_3$ are detected in the gap between the amide and the CH_3 and CH_2 stretching, which are at 2020 and 1920 cm^{-1} (5, 6), respectively (Fig. 3) [16,18]. In general, the spec tra obtained for skin samples treated with $C_{12}Re(CO)_3$ in DMSO

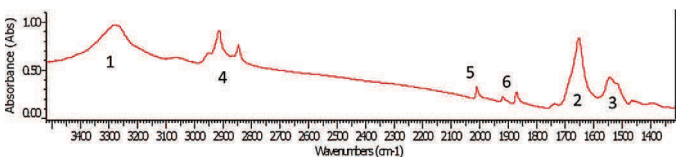

Fig. 3. IR spectra of skin sample treated with bicosomes incorporating $C_{12}Re(CO)_3$ at 1% for 24 h and at room temperature. (1) NH vibration of polypeptides and pro teins of the skin, (2) CO vibration of proteins, (3) CN vibration of proteins, (4) CH_3 and CH_2 stretching vibration of skin and bicosome lipids and (5, 6) symmetric and asymmetric stretching vibrations of $C_{12}Re(CO)_3$ (A_1 and E respectively).

showed similar patterns to the spectra obtained for skin samples treated with bicosomes including the lipophilic molecule. These results demonstrate the possibility of detecting this molecule without any interference when it is applied on the skin.

The maps obtained for skin samples treated with $C_{12}Re(CO)_3$ incorporated in bicosomes or dissolved in DMSO are shown in Fig. 4A–D. The micrograph sections show the skin surface, SC and epidermis (Epi). These figures show the distribution of the lipophilic molecule (A_1 and E bands) among the different regions of the skin. The colour scale from blue to red represents the localization of the molecule. The red areas have the highest concentration of $C_{12}Re(CO)_3$, while the lipophilic molecule is not detected in the blue areas. Yellow and green represent areas with intermediate amounts of $C_{12}Re(CO)_3$.

The maps obtained from skin treated with bicosomes tagged with $C_{12}Re(CO)_3$ (Fig. 4A, B) shows the largest fraction of this lipophilic molecule in the SC. Moreover, $C_{12}Re(CO)_3$ is also observed in the Epi, that is, deeper than the SC. Therefore, the incorporation of this lipophilic molecule in bicosomes leads to deeper penetration into the skin. Considering the enhancing properties of DMSO, a significant penetration of $C_{12}Re(CO)_3$ in the skin would be expected when it was incorporated in this solvent [21]. However, the maps obtained for skin treated with the DMSO solution indicate that the largest fraction of the lipophilic molecule did not penetrate into the skin (Fig. 4C, D). $C_{12}Re(CO)_3$ is often localized outside and on the surface of skin slices, indicating poor penetration of this lipophilic molecule into the tissue. Some $C_{12}Re(CO)_3$ was also detected in the Epi, but the overall amount of $C_{12}Re(CO)_3$ in the skin was less in the case of the DMSO solution than in the case of the penetration using the bicosomes.

3.2.2. Quantitative analysis

To quantify the distribution of $C_{12}Re(CO)_3$ throughout the different layers of the skin and to confirm the qualitative evaluation of the results visualized in the maps, the ratios between the AUC of the $C_{12}Re(CO)_3$ bands (A_1 and E) and the Amide II vibration (skin signal) were calculated and compared. Thus, two parameters were obtained: the $AUC_{C_{12}Re(CO)_3,\ A_1}/AUC_{Amide\ II}$ ratio and the $AUC_{C_{12}Re(CO)_3,\ E}/AUC_{Amide\ II}$ ratio. This quantification was performed for all the maps obtained using FTIR (approximately 7–9, including the skin slices shown in Fig. 4A–D), and the mean values and standard deviations (SD) were calculated for each ratio. The Amide II vibration was used as an internal reference (skin reference). Generally, this vibration is constant at different skin depths. Therefore, the ratio between the $C_{12}Re(CO)_3$ and Amide II vibrations enables the estimation of amounts of $C_{12}Re(CO)_3$ retained in the different skin layers after the application of this molecule incorporated in the bicosomes or DMSO.

Fig. 5 shows the $AUC_{C_{12}Re(CO)_3,\ A_1}/AUC_{Amide\ II}$ (A) and $AUC_{C_{12}Re(CO)_3,\ E}/AUC_{Amide\ II}$ (B) ratios obtained for the skin samples treated with $C_{12}Re(CO)_3$ included in the bicosomes or dissolved in DMSO. The total detected amount of $C_{12}Re(CO)_3$ was smaller in the DMSO experiments. The lipophilic molecule dissolved in DMSO was detected outside of the SC and we did not include these values in the quantitative results. Considering the total values of the ratios (ratio in SC + ratio in Epi) the $C_{12}Re(CO)_3$ incorporated

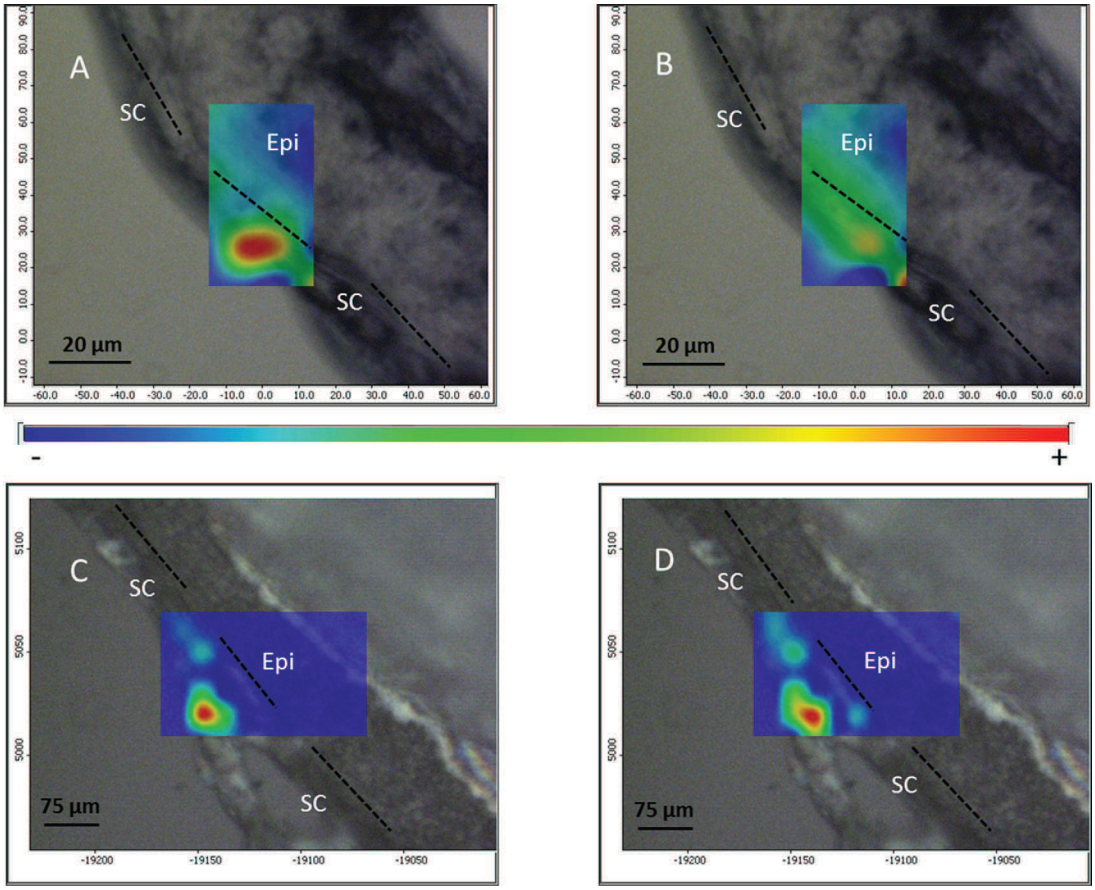

Fig. 4. IR maps obtained from skin samples treated with $C_{12}Re(CO)_3$ incorporated in bicosomes and dissolved in DMSO. (A) $C_{12}Re(CO)_3$ distribution (A_1 band) included in bicosomes, (B) $C_{12}Re(CO)_3$ distribution (E band) included in bicosomes, (C) $C_{12}Re(CO)_3$ distribution (A_1 band) dissolved in DMSO and (D) $C_{12}Re(CO)_3$ distribution (E band) dissolved in DMSO. The $C_{12}Re(CO)_3$ scale goes to blue from red, indicating no amount in blue colour and high amount in red colour. The concentration of $C_{12}Re(CO)_3$ is 1% (w/v) in both vehicles.

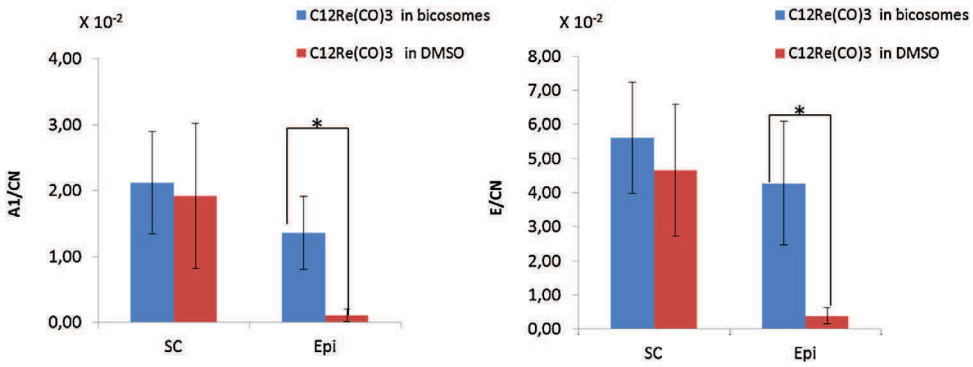

Fig. 5. Mean values and standard deviation (SD) of $AUC_{C_{12}Re(CO)_3,\ A_1}/AUC_{Amide\ II}$ ratio (A) and $AUC_{C_{12}Re(CO)_3,\ E}/AUC_{Amide\ II}$ ratio (B) as a function of penetration depth through the skin (SC and Epi) for $C_{12}Re(CO)_3$ incorporated in bicosomes or dissolved in DMSO ($N = 9$).

in the skin by the bicosomes was approximately twice the amount dissolved in DMSO.

The $AUC_{C_{12}Re(CO)_3,\ A_1}/AUC_{Amide\ II}$ ratios obtained in SC were similar for skin samples treated with the lipophilic molecule incor porated in the bicosomes and dissolved in DMSO (Fig. 5A, SC). In the Epi (Fig. 5A, Epi), the ratio calculated for the skin samples treated with bicosomes was higher that the treated with DMSO. This differ ence was statistically significant. From the values plotted in Fig. 5A, $C_{12}Re(CO)_3$ is incorporated in the bicosomes, 61% of this lipophilic molecule was retained in the SC and 39% reached the Epi. However, when $C_{12}Re(CO)_3$ was dissolved in DMSO, 95% was retained in the SC and only 5% reached the Epi.

The same trend was observed for the $AUC_{C_{12}Re(CO)_3,\ E}/AUC_{Amide\ II}$ ratios obtained in the SC and the Epi (Fig. 5B). In this case, when $C_{12}Re(CO)_3$ is incorporated in the bicosomes, 57% of this lipophilic molecule was retained in the SC and 43% reached the Epi. When $C_{12}Re(CO)_3$ was dissolved in DMSO, 92% was retained in the SC, and only 8% reached the Epi.

Therefore, we can conclude that only a small amount of the $C_{12}Re(CO)_3$ reached the Epi when it was applied on the skin dis solved in DMSO (approximately 5–8% of the total concentration). However, approximately 40% of this lipophilic molecule reached the Epi when it was applied in the bicosomes. These results are in agreement with the information show in the maps in Fig. 4A, B and clearly indicate the penetration capacity of the lipid system compared with the DMSO solution.

4. Discussion

Although skin has a large surface area, delivery of molecules into this tissue is difficult because the skin acts as a formidable barrier [22]. One of the investigated strategies to enhance drug delivery through skin is the introduction of structural alterations within the skin via the addition of chemical enhancers, such as DMSO, surfac tants, fatty acids, alcohols, peptides and other molecules [23–26]. However, the use of chemical enhancers is restricted because these molecules can produce skin irritation and alter skin properties [23].

Liposomes and micellar systems have often been used for skin treatment [5]. Nevertheless, the large size of liposomes (with diameters ranging from 25 nm to several micrometres) as well as the inappropriate composition and elasticity of vesicles make the incorporation of molecules inside the skin using these lipids systems difficult [27]. In addition, the presence of surfactants in micelles usually promotes skin irritation [28].

Bicosomes exhibits a more complex structural variability than liposomes and micelles. In bicosomes, vesicles and free and encap sulated discoidal structures coexist. Spherical vesicles, with a size of approximately 200 nm, would not be able to penetrate through the SC, remaining on the skin surface, in a similar way as described for other lipid vesicles [29]. When in contact with the skin, the bilayer of the external vesicle of the bicosomes bursts, and the encapsu lated disks release from the inside. Previous works have published the penetration mechanism of these discoidal structures, called bicelles, through the narrow interlamellar spaces of the SC [7,8]. Due to their small size and thickness, bicelles are able to penetrate into skin. Once incorporated into the SC, they have the ability to increase in size due to a dilution effect inside the SC mixing with SC lipids [7,8]. This increase involves a transition from bicelles to vesi cles [4] and promotes the retention of the bicelle components in the skin [7]. This mechanism of penetration retention would explain the presence of the $C_{12}Re(CO)_3$ in the skin when it was applied in bicosomes. These facts show that bicosome systems are promis ing vehicles for the incorporation of different molecules inside the skin, including bioactive derivatives [4]. The use of bicosomes facil itates the penetration and retention of bioactive molecules inside the skin. Moreover, the application of this lipid system on skin does not produce any harmful effects on the tissue [5–7]. In this way, these nanoaggregates can be useful carriers for the incorporation of different active compounds inside this tissue to reinforce the skin barrier or treat the tissue.

When $C_{12}Re(CO)_3$ was dissolved in DMSO, this molecule did not penetrate through the spaces of the SC and remained on the skin surface. DMSO is a known enhancer that interacts with skin proteins and lipids to facilitate the transport of hydrophilic and lipophilic molecules [21,23]. The effects of DMSO are concentration dependent. Concentrations of approximately 60% (v/v) are required in the formulation to achieve significant skin penetration enhance ment [23]. In our work pure DMSO was used; thus, an enhanced effect of this solvent on the skin should be expected. However, the penetration of $C_{12}Re(CO)_3$ in DMSO was very weak. The incorpora tion of molecules in the skin depends on their molecular weights and shapes [30]. DMSO has demonstrated its ability to facilitate the penetration of many drugs, such as steroids or antibiotics among others [31–35]. All of them had weights below the molecular weight of $C_{12}Re(CO)_3$ (620 g/mol). This difference in molecular weight could be responsible for the poor penetration of this lipophilic molecule in our skin samples when dissolved in DMSO. In contrast, the differences in our experimental conditions (temperature, pH, application time, type of skin) with respect to the conditions used in other studies could also be responsible for the low penetration of $C_{12}Re(CO)_3$ inside the skin [31–35]. Under these experimental conditions, this lipophilic molecule penetrates at higher concen trations when incorporated in bicosomes than dissolved in DMSO. Therefore, it is important to emphasize the increasing penetration capacity of this lipid system, which is more effective than a typical enhancer molecule, such as DMSO.

5. Conclusions

This work reports the monitoring of the penetration of a model lipophilic molecule into skin in solution and in bicosomes using FTIR. $C_{12}Re(CO)_3$ is a good tag for use in skin because it can be differentiated from the skin vibrations. This fact makes the use of this derivative interesting for skin applications.

The penetration of this lipophilic molecule into the skin is more efficient when incorporated into bicosomes than dissolved in DMSO. The specific interactions between the bicosomes and the skin seem to be responsible for this effect.

The results of the incorporation of $C_{12}Re(CO)_3$ into bicosomes are promising. We suggest the use of bicosomes to promote the penetration of other molecules with similar physicochemical char acteristics into skin.

We can conclude that bicosomes are promising vehicles for the incorporation of lipophilic molecules inside skin.

Acknowledgements

The authors wish to thank the Veterinary Faculty of the Univer sidad Autónoma de Barcelona which was the provider of the pig skin. This work has supported by funds from CTQ 2013 44998 P.

References

[1] P.W. Wertz, Adv. Drug Deliv. Rev. 18 (1996) 283.
[2] P. Desai, R.R. Patlolla, M. Sinngh, Mol. Membr. Biol. 27 (2010) 247.
[3] Z.E. Suntre, J. Toxicol. 2011 (2011) 152474.
[4] G. Rodriguez, G. Soria, E. Coll, L. Rubio, L. Barbosa Barros, C. Lopez Iglesias, A.M. Planas, J. Estelrich, A. de la Maza, O. Lopez, Biophys. J. 99 (2010) 480.
[5] B. Maherani, E. Arab Tehrany, M.R. Mozafari, C. Gaiani, M. Linder, Curr. Nanosci. 7 (2011) 436.
[6] L. Rubio, G. Rodríguez, C. Alonso, C. López Iglesias, M. Cócera, L. Coderch, A. de la Maza, J.L. Parra, O. López, Soft Matter 78 (2011) 8488.
[7] G. Rodríguez, L. Barbosa Barros, L. Rubio, M. Cócera, C. López Iglesias, A. de la Maza, O. López, Colloids Surf. B: Biointerfaces 84 (2011) 390.
[8] G. Rodríguez, M. Cócera, L. Rubio, C. Alonso, R. Pons, C. Sandt, P. Dumas, C. López Iglesias, A. de la Maza, O. López, Phys. Chem. Chem. Phys. 17 (2012) 14523.
[9] M. Cotte, P. Dumas, M. Besnard, P. Tchoreloff, P. Walter, J. Control. Release 97 (2004) 269.
[10] S. Clède, C. Policar, Chem. Eur. J. 21 (2015) 942.
[11] K.V. Kong, W. Chew, L.H.K. Lim, W.Y. Fan, W.K. Leong, Bioconjug. Chem. 18 (2007) 1370.
[12] K. Meister, J. Niesel, U. Schatzschneider, N. Metzler Nolte, D.A. Schmidt, Angew. Chem. Int. Ed. 49 (2010) 3310.
[13] S. Clède, F. Lambert, R. Saint Fort, M.A. Plamont, H. Bertrand, A. Vessières, C. Policar, Chem. Eur. J. 20 (2014) 8714.
[14] C. Policar, J.B. Waern, M.A. Plamont, S. Clède, C. Mayet, R. Prazeres, J.M. Ortega, A. Vessières, A. Dazzi, Angew. Chem. Int. Ed. 50 (2011) 860.
[15] S. Clède, F. Lambert, C. Sandt, S. Kascakova, M. Unger, E. Harté, M. A. Plamont, R. Saint Fort, A. Deniset Besseau, Z. Gueroui, C.J. Hirschmugl, A. Vessières, C. Policar, Analyst 138 (2013) 5627.
[16] S. Clède, N. Delsuc, C. Laugel, F. Lambert, C. Sandt, A. Baillet Guffroy, C. Policar, Chem. Commun. 51 (2015) 2687.
[17] S. Clède, C. Policar, C. Sandt, Appl. Spectrosc. 68 (2014) 113.
[18] S. Clède, F. Lambert, C. Sandt, Z. Gueroui, M. Réfrégiers, M.A. Plamont, P. Dumas, A. Vessières, C. Policar, Chem. Commun. 48 (2012) 7729.
[19] H.C. Bertrand, S. Clède, R. Guillot, F. Lambert, C. Policar, Inorg. Chem. 53 (2014) 6204.
[20] K.S. Schmitz, An Introduction to Dynamic Light Scattering by Macromolecules, Academic Press, San Diego, CA, 1990.
[21] Z. Yu, P.J. Quinn, Mol. Membr. Biol. 15 (15) (1998) 59.
[22] K.C. Madison, J. Invest. Dermatol. 121 (2003) 231.
[23] A.C. Williams, B.W. Barry, Adv. Drug Deliv. Rev. 56 (2004) 603.
[24] L.B. Lopes, E. Furnish, P. Komalavilas, B.L. Seal, A. Panitch, M.V.L. Bentley, C.M. Brophy, Eur. J. Pharm. Biopharm. 68 (2008) 441.
[25] S. Wang, D. Zeng, J. Niu, H. Wang, L. Wang, Q. Li, C. Li, H. Song, J. Chang, L. Zhang, J. Mater. Chem. B 2 (2014) 877.
[26] J.B. Rothbard, S. Garlington, Q. Lin, T. Kirschberg, E. Kreider, L.P. McGrane, P.A. Wender, P.A. Khavari, Nat. Med. 6 (2000) 1253.
[27] G.M. El Maghraby, A.C. Williams, B.W. Barry, J. Pharm. Pharmacol. 58 (2006) 415.
[28] E. Berardesca, G.P. Vignoli, F. Distante, P. Brizzi, G. Rabbiosi, Contact Dermat. 32 (1995) 83.
[29] R.H. Muller, R.D. Petersen, A. Hommos, J. Pardeike, Adv. Drug Deliv. Rev. 59 (2007) 522.
[30] D. Cobb, J. Orthomol. Med. 25 (2010) 214.
[31] R.B. Stoughton, Arch. Dermatol. 91 (1965) 657.
[32] S.G. Elfbaum, K. Laden, J. Soc. Cosmet. Chem. 19 (1967) 119.
[33] B.M. Tashtoush, S.A. Al Safi, K.J. Al Fanek, Pharmazie 59 (2004) 143.
[34] L.H. Reddy, B. Ghosh, Indian J. Exp. Biol. 39 (2001) 47.
[35] B. Kumar, S.K. Jain, S.K. Prajapati, Int. J. Drug Deliv. 3 (2011) 83.

Appendix C

Résumé

Introduction

Au cours des dernières années, l'imagerie a pris une importance croissante dans l'étude des processus biologiques. C'est pourquoi de nombreux outils moléculaires (sondes, etc.) et techniques (fluorescence : FRET, FRAP, FLIM, etc.), visant à détecter et localiser les biomolécules et à mettre en évidence leurs interactions, ont été concomitamment développés.

Les protéines auto-fluorescentes telles que la GFP (Green Fluorescent Protein) sont parmi les sondes les plus utilisées en biologie cellulaire. Leur utilisation a permis d'élucider de nombreux mécanismes biologiques. Cependant, du fait de leur taille (environ 30 kDa), ces sondes peuvent altérer certaines propriétés de la protéine marquée : elles peuvent par exemple perturber son interaction avec d'autres protéines ou encore sa mobilité au sein du milieu cellulaire [212, 213]. Pour pallier ces problèmes, des méthodes pour lier spécifiquement des sondes chimiques de petite taille à une protéine ont été développées [157,158,161–163,192,214]. Plusieurs stratégies ont émergé, parmi lesquelles : (i) la reconnaissance d'une séquence peptidique spécifique (tag), insérée génétiquement dans la séquence de la protéine d'intérêt, par la sonde fonctionnalisée de manière adaptée; (ii) le greffage de la sonde à un ligand de la protéine; (iii) l'introduction enzymatique d'une fonction 'bio-orthogonale' sur la protéine; et (iv) l'incorporation lors de la synthèse protéique d'acides aminés non naturels (portant directement la sonde ou une fonction bio-orthogonale réagissant spécifiquement avec la sonde).

D'autre part, si la technique la plus employée en imagerie biologique reste la microscopie de fluorescence, des techniques complémentaires telles que les spectroscopies infrarouge (IR) et Raman commencent également à être utilisées [67, 68, 215]. L'absorption IR présente notamment les avantages (i) d'être spécifique d'une fonction chimique donnée, limitant ainsi le bruit de fond, (ii) d'exciter des niveaux vibrationnels, donc de ne pas induire de photoblanchiment, contrairement à l'imagerie de fluorescence, et (iii) d'impliquer

des énergies faibles, ce qui permet de limiter la nocivité pour les cellules.

La combinaison de plusieurs modalités d'imagerie sur une même molécule sonde permettrait en théorie de tirer parti des avantages de chaque type d'imagerie, pour une meilleure compréhension globale du système étudié. Il serait de plus souhaitable que ces modalités soient combinées sur un même coeur moléculaire, afin de limiter la taille de la sonde et donc les perturbations éventuelles sur l'objet d'étude. Du fait de la versatilité de leurs propriétés, les complexes métalliques constituent des outils de choix pour atteindre ce but. Les complexes Re(I) tricarbonyl, en particulier, ont suscité l'intérêt pour le marquage de biomolécules et pour leurs propriétés spectroscopiques. En effet, les complexes de type métal-carbonyle ($[M(CO)_n]$) présentent un signal infrarouge intense vers 1800–2200 cm^{-1}, dans une région où la cellule n'absorbe pas en infra-rouge. C'est pourquoi de tels dérivés ont été utilisés comme marqueurs biologiques, pour l'immunodosage par exemple [5, 58], et dans quelques exemples de cartographie cellulaire [2, 63, 65, 70, 71, 215]. D'autre part, ces complexes peuvent être rendus luminescents par coordination d'un ligand d'orbitale π^* basse en énergie (par exemple un ligand de type α-diimine ou dipicolylamine). Ils présentent alors une bande d'absorption de type MLCT, liée à la promotion d'un électron depuis une orbitale dπ métal-centrée à une orbitale π^* centrée sur le ligand. L'excitation de cette bande à 320–360 nm conduit a une émission autour de 500–550 nm, selon le type de ligand présent autour du rhénium.

Le groupe de C. Policar a utilisé de tels complexes comme sondes multimodales pour le marquage et l'imagerie de biomolécules (Figure C.1) [1, 3, 4, 33, 64, 90, 91]. Le groupe a pu réaliser dans un premier temps l'imagerie sub-cellulaire d'un SCoMPI modèle dans des cellules MDA-MB-231, par microscopie de fluorescence et micropectroscopie infrarouge [4]. En outre, il a été démontré lors d'une autre étude que les propriétés infrarouge de ces complexes peuvent être utilisées pour quantifier l'internalisation du SCoMPI sur une population de cellules [90]. Un dérivé du mestranol a été marqué par un SCoMPI et imagé à l'échelle sub-cellulaire par microscopie de fluorescence et par diverses microspectroscopies vibrationnelles (notamment infrarouge) [3]. Plus récemment, l'imagerie corrélative (fluorescence et infrarouge) d'un peptide vecteur a été réalisée dans des échantillons de peau [1].

Jusqu'à présent, les molécules marquées par des SCoMPIs et étudiées par imagerie sont des molécules exogènes. Nous nous sommes intéressés à la possibilité de marquer des molécules endogènes avec des SCoMPIs (notamment les protéines), et de les détecter à l'échelle cellulaire par microscopie de fluorescence et infrarouge. Pour atteindre cet objectif, nous avons procédé par étapes de difficulté croissante pour ce qui concerne le marquage par des SCoMPIs et leur détection. Nous avons tout d'abord souhaité étudier l'internalisation cellulaire de peptides vecteurs ou CPPs (Cell-Penetrating Peptides) marqués par des SCoMPIs (Chapitre 1). Ceci nous a conduit dans un premier temps à étudier les propriétés spectroscopiques de différents SCoMPIs en solution ou en présence de membranes modèles ou cellulaires, puis l'influence du cycle cellulaire sur l'internalisation des CPP-SCoMPI. Dans

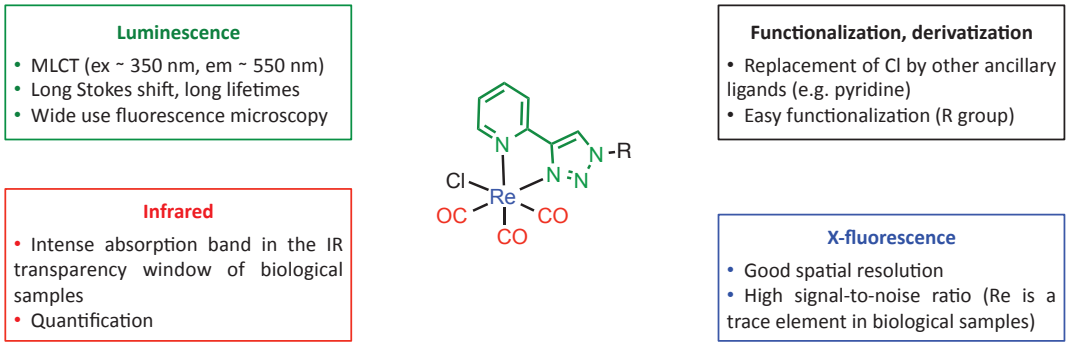

(a) Structure et propriétés des SCoMPIs

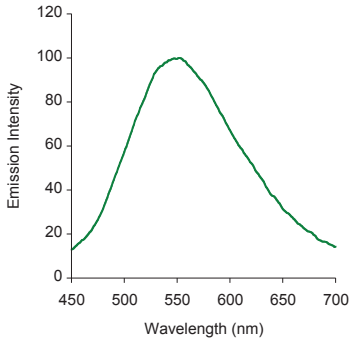

(b) Spectre d'émission d'un SCoMPI ($\lambda_{ex} = 350$ nm)

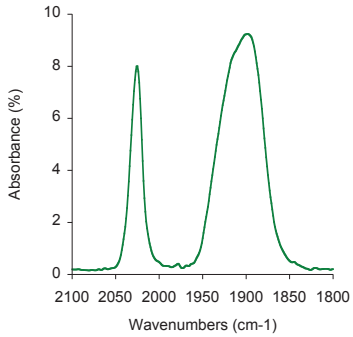

(c) Signal IR d'un SCoMPI

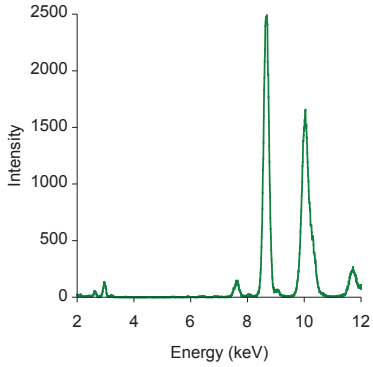

(d) Signal de Fluorescence X d'un SCoMPI

Figure C.1: Structure et propriétés générales des SCoMPIs (*S*ingle *Co*re Multimodal *P*robes for *I*maging)

un second temps, nous avons synthétisé un SCoMPI adapté au marquage *in vitro* de protéines contenant des cystéines via un couplage thiol-maléimide. Notre objectif étant de réaliser l'imagerie de protéines dans un contexte cellulaire, nous avons choisi, en collaboration avec O. Lequin et S. Sagan, de marquer l'homéodomaine d'*Engrailed-2*, qui est internalisé dans les cellules (Chapitre 2). Enfin, nous avons testé la possibilité de marquer et d'imager des protéines endogènes par des SCoMPIs. Nous avons pour cela ciblé les Anhydrases carboniques IX et XII, deux protéines membranaires surexprimées dans certaines tumeurs solides (Chapitre 3).

Outre leurs modalités de luminescence et infrarouge, les SCoMPIs peuvent également être détectés par microspectroscopie de fluorescence X du fait de la présence du centre Re. Notre groupe s'est récemment intéressé à leur utilisation comme sondes pour ce type d'imagerie. Le rhénium possède une abondance naturelle très faible, il serait donc possible de détecter des molécules marquées avec des SCoMPIs avec une bonne sensibilité et un bon rapport signal-sur-bruit. De plus, la microspectroscopie de fluorescence X présente une résolution adaptée aux échelles des échantillons biologiques ($\sim$ nm – μm). Nous avons donc testé le potentiel des SCoMPIs en tant que sonde de fluorescence X pour l'imagerie de protéines. Ces résultats préliminaires seront discutés dans les chapitres 2 et 3.

C.1 Marquage et imagerie multimodale de CPPs.

Les CPPs (Cell-Penetrating Peptides, ou peptides vecteurs) sont de petits peptides contenant généralement 8 à 30 acides aminés et qui sont internalisés efficacement dans les cellules. Ils ont de plus la capacité de faire pénétrer avec eux des molécules qui leur sont associées (aussi appelées "cargaisons"), ce qui en fait des outils thérapeutiques ou diagnostiques potentiels.

Afin de pouvoir addresser efficacement des molécules d'intérêt biologique en utilisant des CPPs, il est essentiel de bien comprendre leur(s) mécanisme(s) d'internalisation. Différents mécanismes ont été identifiés, notamment la translocation directe et différents mécanismes d'endocytose. Ces mécanismes peuvent co-exister ou l'un d'eux peut être privilégié, selon le type de CPP, de cellules, et plus généralement les conditions expérimentales. La détermination exacte du mécanisme d'internalisation d'un CPP est donc parfois difficile, voire controversée.

De nombreuses méthodes physico-chimiques, biophysiques et biologiques peuvent être mises en œoeuvre pour étudier ces mécanismes. L'utilisation de modèles membranaires (vésicules lipidiques de type Large Unilamellar Vesicles : LUV ou Giant Unilamellar Vesicles : GUV) permet par exemple d'étudier les mécanismes de translocation directe. Des études sur cellules ont également été réalisées, utilisant fréquemment la microscopie de fluorescence. Toutefois, si la microscopie de fluorescence permet d'obtenir des informations sur la localisation du composé dans la cellule, il est souvent difficile de déterminer la quantité

de peptide internalisé. D'autres méthodes, permettant la détermination de la quantité de peptide internalisé de manière fiable, ont toutefois été développées. Burlina *et al.* ont notamment mis au point un protocole rigoureux de quantification de l'internalisation, fondé sur la spectrométrie de masse MALDI-TOF.

Dans ce contexte, il nous a paru intéressant d'utiliser la multimodalité des SCoMPIs pour étudier l'internalisation des CPPs. En effet, les propriétés de luminescence des SCoMPIs permettent de détecter les peptides marqués par microscopie de fluorescence avec une bonne résolution spatiale, tandis que leurs propriétés infrarouge permettraient de déterminer la quantité de peptide internalisé.

D'autre part, notre laboratoire s'intéresse à l'amélioration des propriétés spectroscopiques des SCoMPIs, notamment leur rendement quantique, en modifiant la sphère de coordination du rhénium (ligands bidentate ou ancillaire). Nous nous sommes ici intéressés à l'effet du ligand ancillaire (chlorure ou pyridine) sur les propriétés de luminescence des SCoMPIs. Une étude récente réalisée par l'équipe de S. Lavielle au Laboratoire des Biomolécules a montré que, lorsque des CPPs marqués avec des sondes fluorescentes (comme la rhodamine ou la fluorescéine) étaient accumulés localement, les sondes pouvaient subir un phénomène de *quenching* (ou extinction de fluorescence). Ce phénomène peut ainsi introduire des biais dans l'interprétation des clichés de microscopie de fluorescence, les zones "sombres" pouvant à la fois traduire une absence ou une concentration élevée de peptide marqué. Nous avons donc souhaité tester les propriétés spectroscopiques des CPPs marqués avec des SCoMPIs en solution et en présence de membranes lipidiques et cellulaires.

Nous avons donc synthétisé deux SCoMPIs fonctionnalisés avec un acide carboxylique pour le marquage de peptides à leur extrêmité *N*-terminale. Ces deux SCoMPIs diffèrent par leur ligand ancillaire (Cl ou Pyridine). La synthèse des complexes peut se décomposer en trois grandes parties (Figure C.2): (i) synthèse du ligand pyridine-1,2,3-triazole commun, sous forme d'ester méthylique; (ii) Complexation du centre rhénium tricarbonyl halogéné puis échange éventuel de ligand; (iii) déprotection (saponification) du complexe et couplage au peptide en solution. Dans le cadre de cette étude, nous avons marqué deux CPP riches en arginine, R9 et R6W3.

Tableau C.1: Propriétés spectroscopiques des complexes $[Re(CO)_3(X)(PytaCOOMe)]$

	$\epsilon_0^{350}(M^{-1} \cdot cm^{-1})$	$\lambda_{em}^{ex350}(nm)$	$\Phi^a(\%)$
X = Cl SCoMPI-Cl	1.8×10^3	550	0.044 ± 0.004
X = Py SCoMPI-Py	2.0×10^3	495	0.96 ± 0.05
Cl-R9	1.8×10^3	550	0.17 ± 0.02
Cl-R6W3	1.8×10^3	550	0.13 ± 0.01
Py-R9	2.0×10^3	495	0.69 ± 0.05
Py-R6W3	2.0×10^3	495	0.14 ± 0.02

[a] Les rendements quantiques ont été mesurés par N.Delsuc dans l'eau (2% DMSO) pour les complexes SCoMPI-Cl et SCoMPI-Py, et dans l'HEPES pour les peptides.

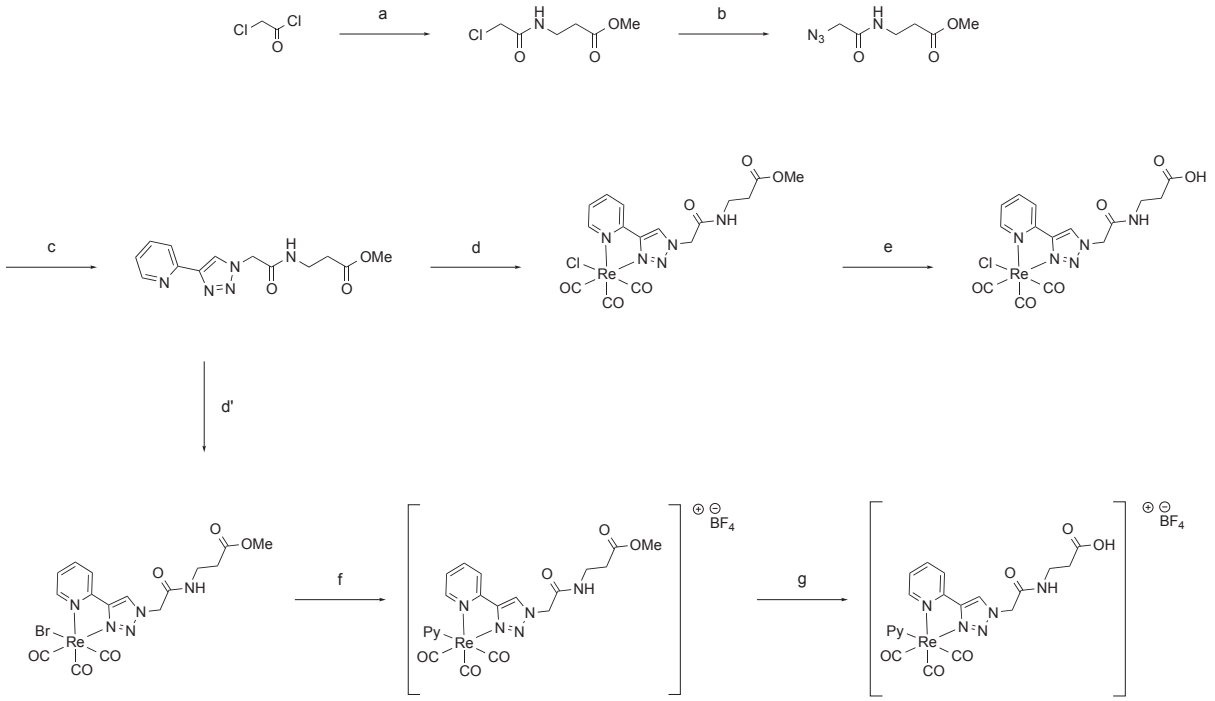

Schéma C.1: Synthèse des dérivés SCoMPI pour le marquage *N*-terminal de peptides
Conditions de réaction: (a) β-alanine methyl ester hydrochloride salt, DIEA, dry DCM, 1h, 0 °C to RT, 66%, (b) NaN_3, NaI, acetone:water (3:1 v:v), 16h, 35 °C, 79%, (c) 2-ethynylpyridine, $CuSO_4$, sodium ascorbate, acetone:water (2:1 v:v), 2h, RT, 70%, (d) $Re(CO)_5Cl$, toluene, 6h, reflux, 100%, (d') $Re(CO)_5Br$, toluene, 6h, reflux, 100%, (e) $LiOH \cdot H_2O$, THF:water (2:1 v:v), 45 min, RT, 80%, (f) $AgBF_4$, acetonitrile, 5h, reflux, Ar; pyridine, THF, 20h, reflux, 79%, (g) $LiOH \cdot H_2O$, THF:water (2:1 v:v), 1h, RT, 87 %.

Nous avons ensuite étudié les propriétés de luminescence des complexes parents (forme ester methylique) et des peptides marqués en solution. En solution, le complexe SCoMPI-Py présentant un ligand pyridine possède un rendement quantique environ vingt fois supérieur à celui du complexe portant un ligand chlorure (Tableau C.1), ce qui le rend potentiellement intéressant pour la détection de biomolécules par imagerie de fluorescence. Il faut également noter que l'émission du complexe portant un ligand chlorure est à 550 nm, contre 495 nm pour le complexe portant un ligand pyridine. La conjugaison au peptide ne modifie pas la longueur d'onde d'émission. En revanche, les rendements quantiques des peptides marqués diffèrent de ceux de leur complexe parent. Dans le cas des sondes SCoMPI-Cl, la conjugaison au peptide a tendance à augmenter le rendement quantique de la sonde. Au contraire, les peptides marqués avec la sonde SCoMPI-Py ont un rendement quantique inférieur à celui du complexe parent. Par ailleurs, le rendement quantique des peptides R9 est supérieur à celui des peptides R6W3 correspondants.

Nous avons également étudié l'influence que pouvait avoir un environnement lipidique sur les propriétés spectroscopiques de la sonde. Pour cela, une concentration donnée de chaque peptide conjugué a été mise en présence de concentrations croissantes de vésicules unilamellaires (Large Unilamellar Vesicle, LUV), et le spectre d'émission enregistré pour une excitation à 350 nm. Nous avons pu constater que les deux sondes présentaient des com-

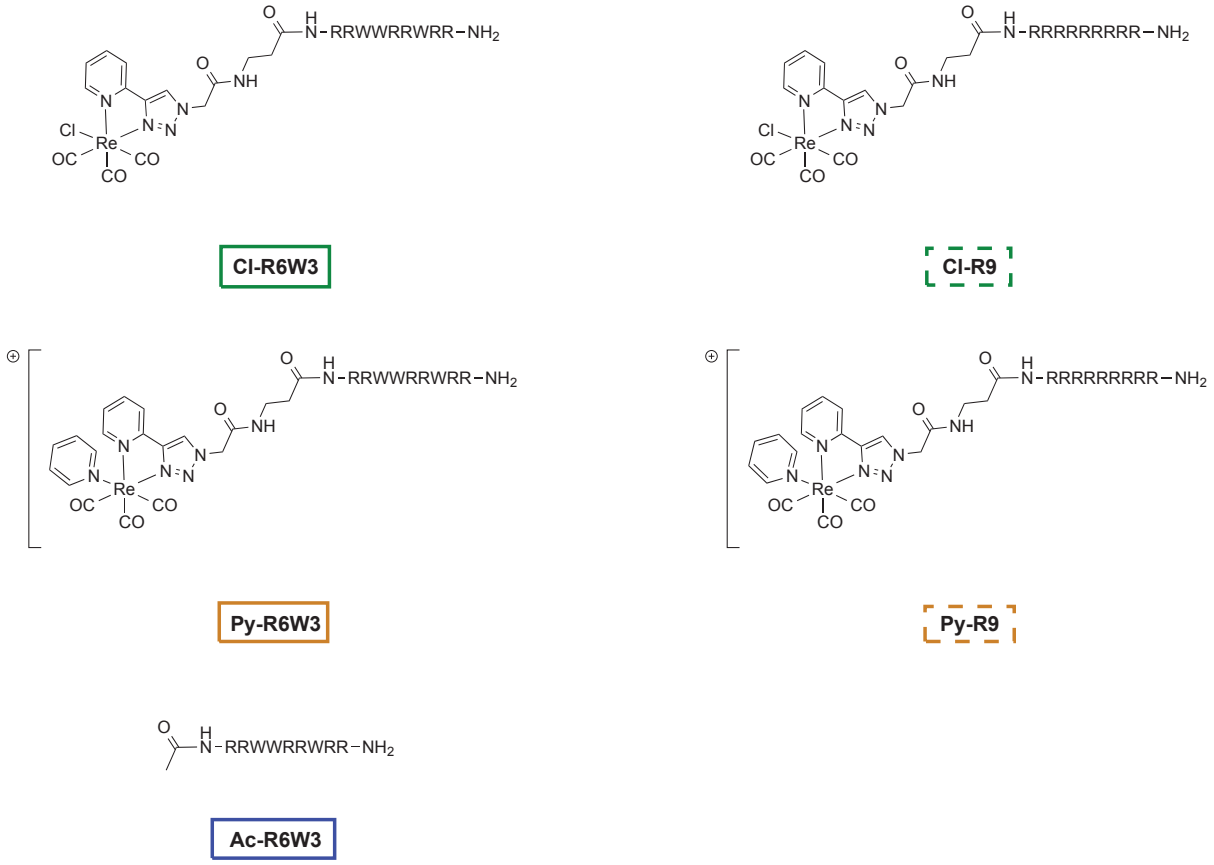

Figure C.2: Structure des peptides marqués avec les complexes SCoMPI-Cl et SCoMPI-Py

portements très différents en présence de membranes modèles: les peptides marqués avec la sonde SCoMPI-Cl montraient une forte augmentation de luminescence, contrairement aux peptides marqués avec la sonde SCoMPI-Py dont l'intensité d'émission en présence de LUV restait au mieux constante, voire diminuait (Figure C.3).

Nous avons souhaité confirmer ces résultats dans l'environnement membranaire complexe que représentent les cellules. Des cellules CHO (Chinese Hamster Ovarian cells, cellules d'ovaire de hamster chinois) ont été cultivées sur lames de CaF_2 (utilisables en microscopies infrarouge et de fluorescence) et incubées avec les peptides Py-R9 et Cl-R9. Nous avons pu observer par microscopie de fluorescence que les cellules incubées avec Cl-R9 montraient des intensités de luminescence plus deux fois supérieures à celles des cellules incubées avec Py-R9. Afin de vérifier que cette différence n'était pas due à une différence de concentration des deux peptides dans les cellules, nous avons comparé les signaux infrarouge des SCoMPIs dans les deux échantillons. En effet, il a été montré lors de précédents travaux que l'aire des signaux infrarouge des SCoMPIs était peu dépendante de leur environnement et pouvait être utilisée pour quantifier la concentration locale en SCoMPI [3]. L'imagerie infrarouge a montré que le peptide Py-R9 était certes moins internalisé que le peptide Cl-R9, mais que cette différence était minime par rapport à celle obtenue par microscopie de fluorescence. Le comportement des deux sondes observé sur membranes modèles a donc

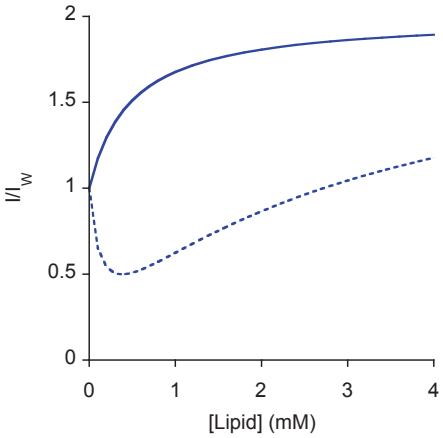

(a) Modèles de partition entre les LUVs et le tampon: partition simple (trait plein) ou "*self-quenching*" (trait pointillé)

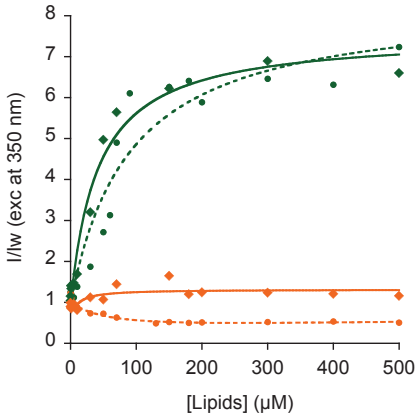

(b) Luminescence des CPP-SCoMPI en présence de LUVs (λ_{ex} = 350 nm; $\lambda_{em} \sim$ 550 nm (Cl-R9 et Cl-R6W3) or $\lambda_{em} \sim$ 495 nm (Py-R9 et Py-R6W3))

Figure C.3: Évolution de l'intensité maximale des SCoMPIs en fonction de la concentration en lipides

Titrage d'une solution de peptide marqué par un SCoMPI (1 µM) par des vésicules de DOPG: Cl-R9 (cercles verts, trait pointillé), Py-R9 (cercles oranges, trait pointillé), Cl-R6W3 (losanges verts, trait plein), Py-R6W3 (losanges oranges, trait plein) and Ac-R6W3 (losanges bleus, trait plein)

été confirmé en milieu cellulaire. Bien que présentant un meilleur rendement en solution, la sonde SCoMPI portant un ligand pyridine semble donc moins adaptée que son homologue chloré pour l'imagerie de fluorescence dans le cas d'une localisation membranaire.

Par ailleurs, nous nous sommes intéressés au suivi de l'internalisation des CPP-SCoMPI en fonction du cycle cellulaire. En effet, des études préliminaires sur kératinocytes (cellules HaCaT) ont montré une inhomogénéité de l'internalisation de Cl-R9 dans ces cellules, qui semblait être corrélée au cycle cellulaire. Nous avons souhaité confirmer ces résultats en suivant l'internalisation de Cl-R9 sur cellules HaCaT synchronisées, c'est-à-dire dans la même phase du cycle cellulaire, en fonction du temps. A des temps donnés, les cellules ont été incubées avec Cl-R9, fixées, et observées par microscopie de fluorescence. Il est intéressant de noter qu'à chaque temps, le signal de fluorescence des cellules était globalement plus homogène dans les cellules HaCaT synchronisées que dans les contrôles non synchronisés. De plus, l'intensité moyenne de luminescence restait globalement constante dans les échantillons non synchronisées, mais évoluait en fonction du temps dans les cellules synchronisées. Ainsi, l'intensité de luminescence augmentait jusqu'à atteindre un maximum, pour ensuite re-décroître. Ces résultats, encourageants, restent à confirmer à la fois par d'autres études en microscopie de fluorescence et surtout par imagerie infrarouge. Il serait notamment souhaitable de pouvoir identifier quelle phase du cycle cellulaire permet la meilleure internalisation de Cl-R9, et plus généralement de CPPs analogues.

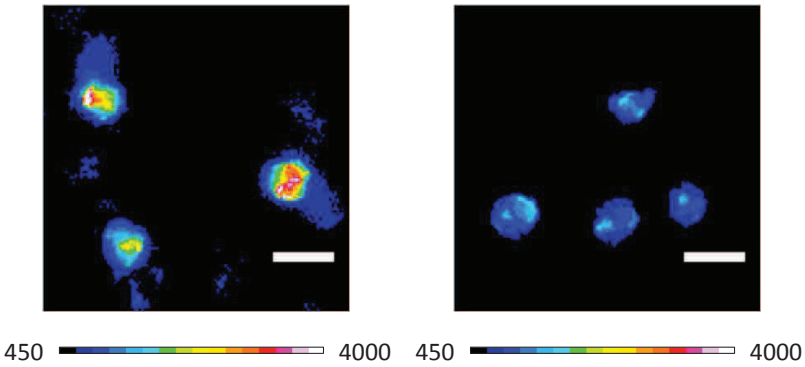

(a) Cellules CHO incubées avec Cl-R9

(b) Cellules CHO incubées avec Py-R9

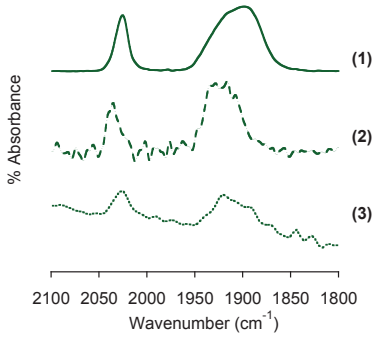

(c) Signal IR de Cl-R9 dans les cellules ou pur

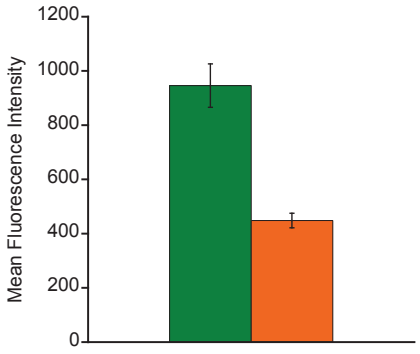

(d) Intensité moyenne de luminescence

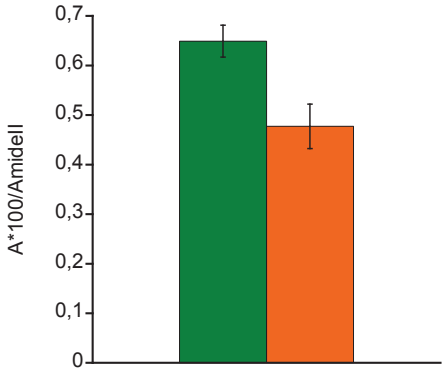

(e) Signal IR moyen

Figure C.4: Comparaison des signaux infrarouge et de luminescence de cellules CHO incubées avec Cl-R9 et Py-R9

(a,b) Cellules CHO incubées 1 h à 37 °C en présence de 10 µM Cl-R9 (a) ou Py-R9 (b). La gamme d'intensité est identique pour les deux images, et varie du noir/bleu (faible intensité) au rouge/blanc (forte intensité). Barre d'échelle = 20 µm. (c) Absorbance IR des SCoMPIs: (1,2) spectre FTIR du composé $[Re(CO)_3(Cl)(PytaCOOMe)]$ pur (1, trait plein) et de Cl-R9 pur (2, tirets longs); (3) Spectre FTIR-MS de cellules CHO incubées avec Cl-R9 (3, pointillés). Les bandes A_1 (2025 cm^{-1}) et E (1940 cm^{-1}) sont représentées.(d) Intensités de luminescence moyennes des régions d'intérêt (ROI, regions of interest) calculées pour des cellules CHO incubées avec Cl-R9 (vert, n=47 ROI) or Py-R9 (orange, n=41 ROI). Les barres d'erreur représentent l'erreur type de la moyenne. (e) Aire moyenne de l'absorbance IR de la bande A_1 du SCoMPI dans des cellules CHO incubées en présence de Cl-R9 (vert, n=33 spectra) ou Py-R9 (orange, n=13 spectra). Pour chaque spectre, cette aire est normalisée par l'aire de l'absorbance IR des Amide II, et la moyenne du rapport est calculée. Les barres d'erreur représentent l'erreur type de la moyenne.

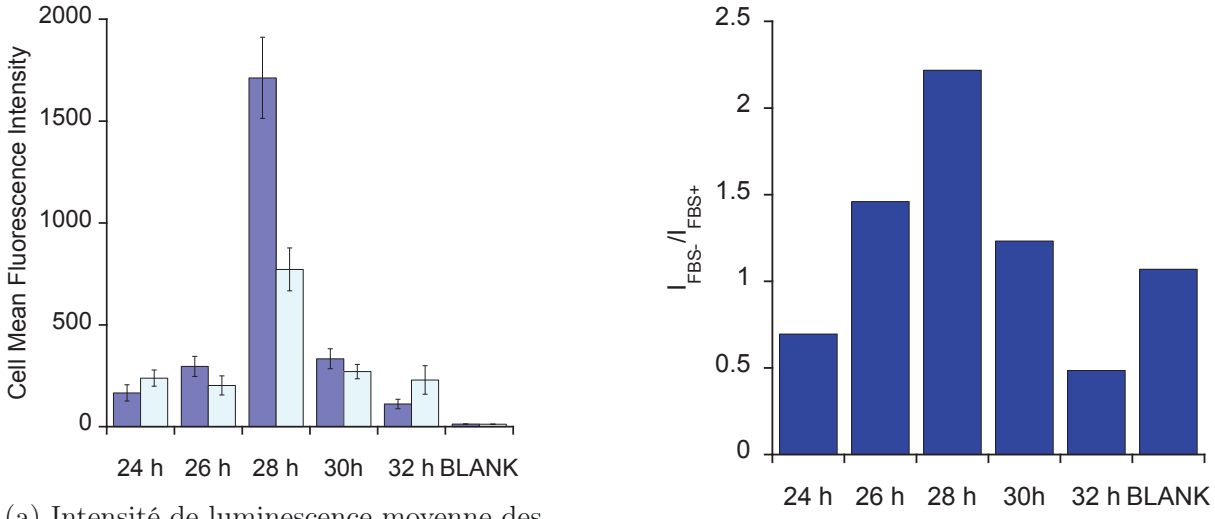

(a) Intensité de luminescence moyenne des cellules HaCaT

(b) Rapports des intensités de luminescence moyennes (FBS-/FBS+)

Figure C.5: Internalisation de Cl-R9 dans des cellules HaCaT synchronisées et non synchronisées

L'intensité de fluorescence moyennée sur toutes les cellules du plan a été mesurée à différents temps pour les cellules synchronisées (FBS-, bleu foncé) et pour les cellules non synchronisées (FBS +, bleu clair) (a). Le rapport des intensités moyennes des échantillons synchronisés (FBS-) sur celles des échantillons non synchronisés (FBS +) a été calculé à chaque temps et représenté sur le graphe (b).

C.2 Marquage et imagerie de l'homéodomaine *Engrailed-2*

Ayant réalisé l'imagerie de fluorescence et infrarouge de peptides marqués par des SCoMPIs, nous avons ensuite voulu tester la possibilité de marquer des protéines avec des SCoMPIs et de les détecter en milieu cellulaire par microscopie de fluorescence, microspectroscopies infrarouge et de fluorescence X. Nous avons choisi de marquer *in vitro* un homéodomaine. Les homéodomaines forment un domaine protéique hautement conservé des homéoprotéines (des facteurs de transcription). Ce domaine, d'environ 60 acides aminés, est constitué de trois hélices et est essentiel à l'interaction des homéoprotéines avec l'ADN. Les homéodomaines ont en outre montré des propriétés de pénétration cellulaire intéressantes, qui ont par la suite inspiré la conception et la découverte de nombreux CPPs. Il est ainsi possible de marquer ces protéines *in vitro* tout en conservant la possibilité d'en réaliser l'imagerie multimodale dans un contexte cellulaire. Nous avons choisi de marquer l'homéodomaine d'*Engrailed-2*, souvent utilisé comme homéodomaine modèle, ainsi qu'une version "étendue" présentant une séquence d'addressage au noyau (NLS, Nuclear Localization Signal). Ces deux homéodomaines, nommés HD et NLSHD par la suite, présentent une cystéine unique et non native, qui permet le marquage par diverses sondes *via* un couplage thiol-maléimide (Figure C.6).

Nous avons effectué la production et la purification de ces deux homéodomaines en col-

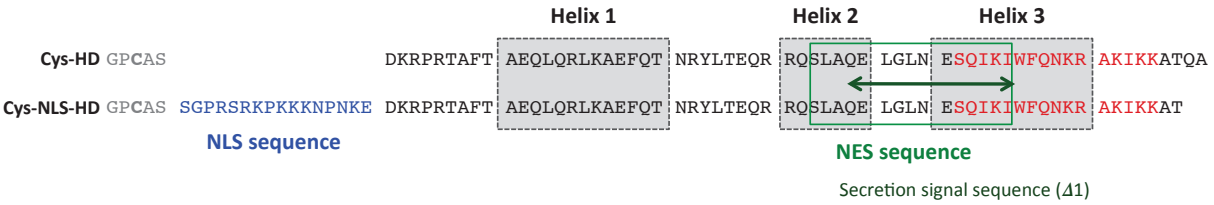

Figure C.6: Séquences de *Engrailed-2*: Cys-HD (haut) et Cys-NLS-HD (bas). Cinq acides aminés (GPCAS, en gris) n'appartiennent pas à la séquence native de l'homéodomaine. Ces acides aminés incluent les acides aminés résiduels du site de clivage de PreScission (G,P) ainsi que la cystéine non native (en gras). La séquence d'addressage au noyau (NLS, Nuclear Localization Signal) est représentée en bleu, la séquence essentielle à l'internalisation cellulaire (CIS, Cell Internalization Signal) en rouge. Le signal d'export du noyau (NES, Nuclear Export Signal) est encadréen vert. Les cadres gris indiquent les séquences des trois hélices de l'homéodomaine d'*Engrailed-2*. Ces domaines ont été attribués à l'aide d'une analyse de séquence (PDB et référence [127]) et des références [129, 133].

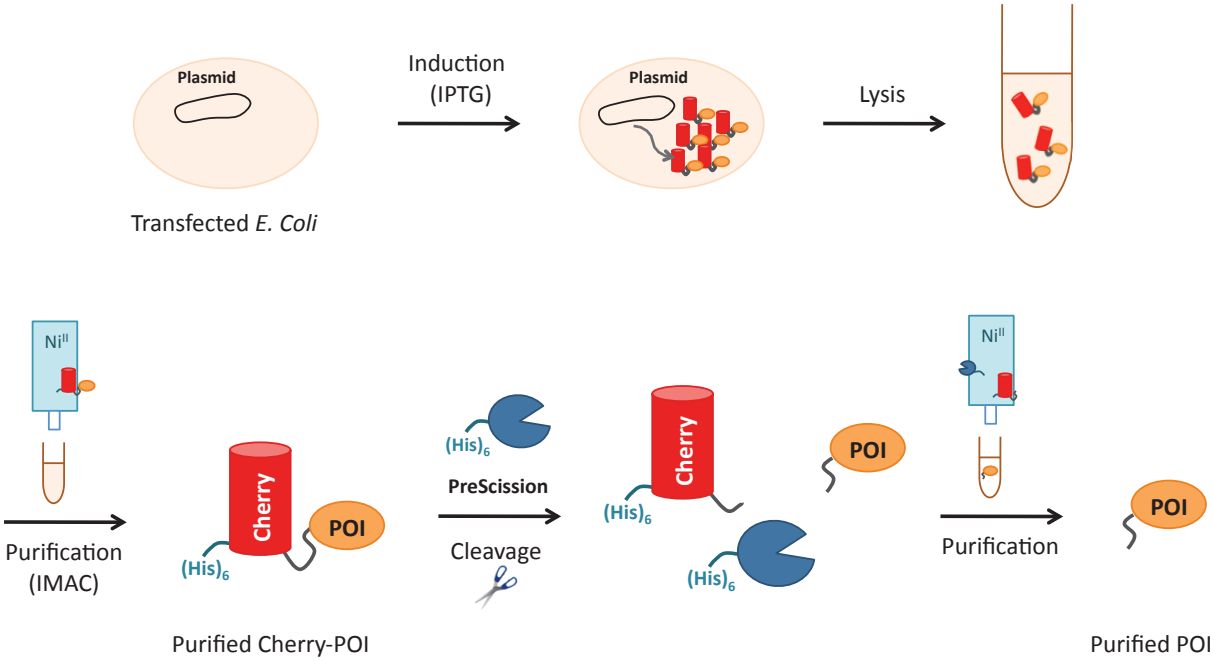

Figure C.7: Principe de la production et de la purification de HD et NLSHD (*Engrailed 2*)

laboration avec le Pr O. Lequin au Laboratoire des Biomolécules (Figure C.7). Chacune des deux protéines a été produite sous forme d'une protéine de fusion avec la protéine "Cherry" (domaine du cytochrome associé à l'hème) dans des bactéries *E. coli* compétentes. Cette construction permet de produire la protéine de fusion de manière efficace, et fournit un contrôle visuel aisé (couleur rouge) à toutes les étapes de la purification. La protéine de fusion porte une étiquette hexahistidine et a donc pu être purifiée par chromatographie d'affinité sur colonne de Ni(II). La protéine de fusion purifiée est ensuite mise en présence de l'enzyme PreScission, qui permet le clivage entre la protéine d'intérêt (ici HD ou NLSHD) et la protéine Cherry. La protéine Cherry, l'enzyme PreScission et la protéine de fusion non clivée portent toutes une étiquette hexahistidine et sont retenues sur colonne de Ni(II), tandis que la protéine d'intérêt purifiée est collectée dans la fraction non retenue.

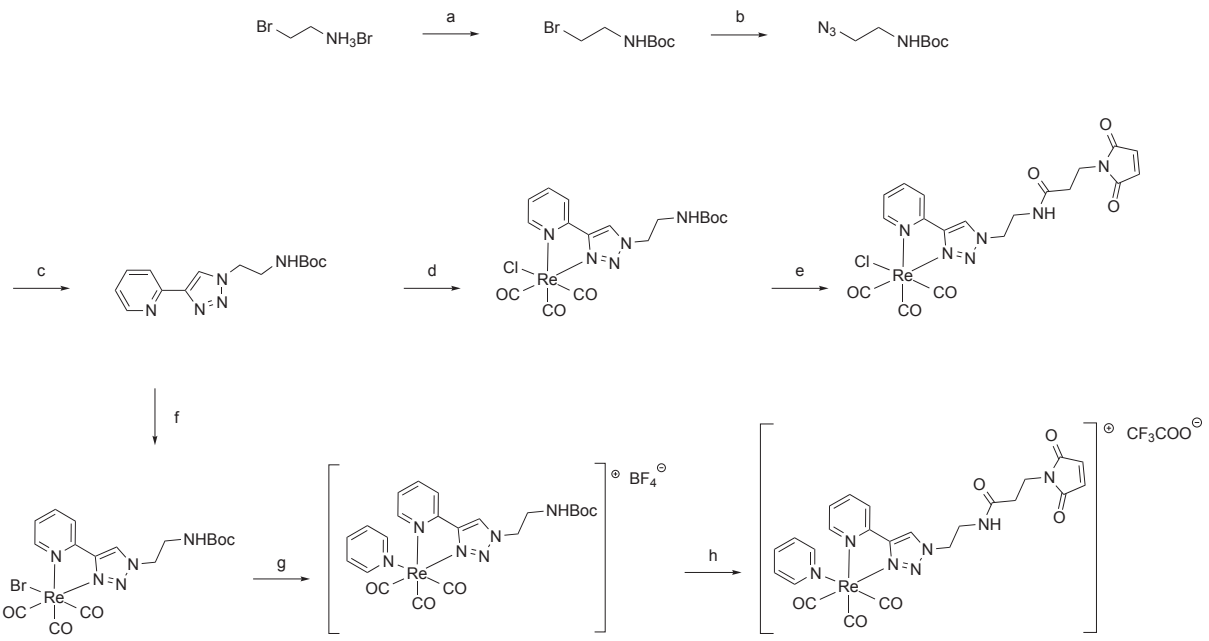

Schéma C.2: Synthèse de SCoMPIs pour le marquage de l'homéodomaine *Engrailed 2*
Reaction conditions: (a) Boc_2O, DIEA, THF, 1h, 0 °C to RT, 99%; (b) NaN_3, NaI, acetone:water (3:1 v:v), 48h, RT, 77%; (c) 2-ethynylpyridine, $CuSO_4$, sodium ascorbate, acetone:water (2:1 v:v), 2h, RT, 78%; (d) $Re(CO)_5Cl$, toluene, 6h, 80 degreeCelsius, 99%; (e) *i.* TFA:DCM (1:1 v:v), 1h, RT, *ii.* 3-maleimidopropionic acid *N*-hydroxysuccinimide ester, DIEA, dry DMF, overnight, RT; (f) $Re(CO)_5Br$, toluene, 6h, 80 degreeCelsius, 94%; (g) $AgBF_4$, acetonitrile, 3 days, 65 °C, Ar; pyridine, THF, 36h, 60 °C, 68%, (h) *i.* TFA:DCM (1:1 v:v), 1h, RT, *ii.* 3-maleimidopropionic acid *N*-hydroxysuccinimide ester, DIEA, dry DMF, overnight, RT, 34%.

Nous avons d'autre part synthétisé les sondes SCoMPI portant soit un ligand chlorure, soit un ligand pyridine, et présentant un groupement maléimide pour le marquage de la cystéine des homéodomaines HD et NLSHD (Schéma C.2). Nous avons pour cela d'abord synthétisé les SCoMPI portant une fonction amine protégée par un groupement Boc. Lors de l'étape finale, les SCoMPIs sont fonctionnalisés avec un groupement maléimide par déprotection de l'amine, suivie d'une réaction avec l'ester activé (N-hydroxysuccinimide) de l'acide 3-maléimidopropanoïque. Cette stratégie permet l'obtention facile de SCoMPIs fonctionalisés avec un maléimide, tout en conservant la possibilité d'autres fonctionalisations de la forme amine des SCoMPIs. La synthèse des sondes SCoMPIs protégéées par un groupement Boc suit une stratégie très similaire à celle développée dans le Chapitre 1: après protection de la 2-bromoethylamine, un groupement azoture est substitué au brome, puis l'azoture formé réagit avec la 2-éthynylpyridine pour former le ligand pyta sous forme d'amine protégée par un Boc. On réalise ensuite la complexation du centre Re(I) par réaction du ligand avec le précurseur $[Re(CO)_5X]$ (X = Cl, Br), éventuellement suivie d'étapes d'échange de ligands. Enfin, comme mentionné précédemment, l'amine est déprotégée et couplée à l'acide 3-maléimidopropanoïque.

La dernière étape consiste à marquer la protéine d'intérêt avec la sonde SCoMPI-maléimide. Cette étape s'effectue sous atmosphère inerte, en solution aqueuse dégazée et en présence de TCEP et de cinq équivalents de SCoMPI par équivalent de protéine. Les

rendements de marquage sont bons, et la protéine marquée conserve des propriétés de luminescence et infrarouge semblables à celles du SCoMPI parent.

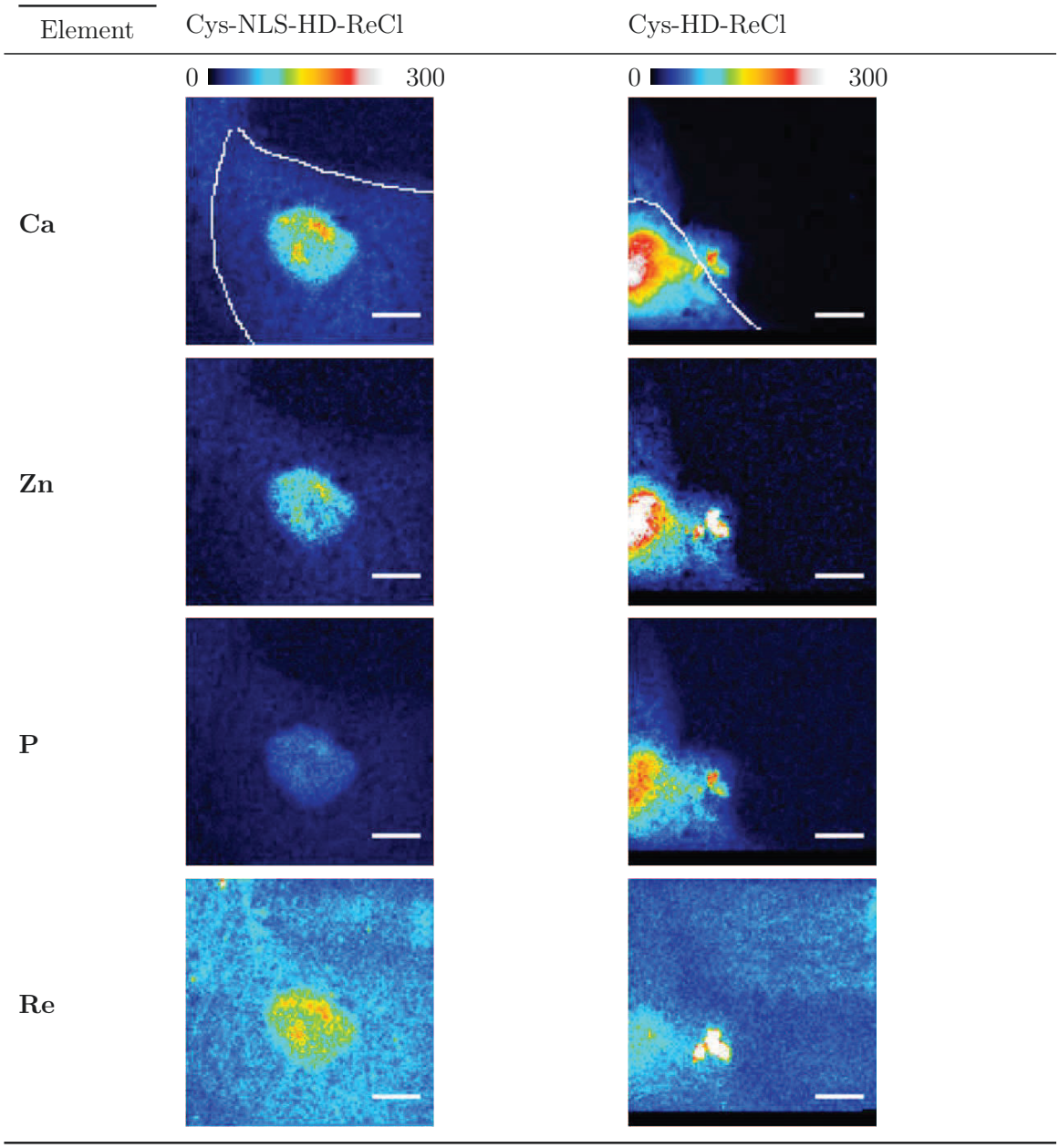

Figure C.8: Cartographie des signaux de Ca, Zn, P et Re par microspectroscopie de fluorescence X sur cellules CHO incubées avec Re(Cl)-NLS-HD and Re(Cl)-HD.

Nous avons ensuite testé la possibilité de détecter ces protéines marquées dans un contexte cellulaire. Nous avons donc incubé des cellules CHO avec chacune des deux protéines (HD et NLSHD) marquée soit avec une sonde SCoMPI-Py, soit avec une sonde SCoMPI-Cl. Les cellules ont dans un premier temps été observée par microscopies de fluorescence et infrarouge. Malheureusement, il n'a été possible de détecter le signal infrarouge et de luminescence des SCoMPIs dans aucun des quatre échantillons. Il est probable que les quantités présentes par cellules soient trop faibles pour être détectées par infrarouge. En

outre, le rendement quantique de ces SCoMPI est probablement trop faible pour pouvoir les détecter par microscopie de fluorescence de manière sensible. Cependant, nous avons également souhaité observer ces échantillons par microspectroscopie de fluorescence X, sur la ligne Nanoscopium du synchrotron SOLEIL. Nous avons alors pu observer le signal du Re(I) dans les cellules incubées avec HD et NLSHD marquées par la sonde SCoMPI-Cl (Cl-HD et Cl-NLSHD, respectivement). En outre, la localisation observée était cohérente avec celle attendue: dans l'échantillon Cl-NLSHD, le signal du Re(I) est localisé, dans une région par ailleurs riche en phosphore et en zinc, éléments souvent considérés comme des "marqueurs" du noyau en fluorescence X. Ceci est cohérent avec la présence d'un signal d'adressage au noyau dans la séquence de la protéine. En revanche, Cl-HD présentait un signal du rhénium plus diffus au sein de la cellules, ce qui peut être expliqué par l'absence du signal NLS de la séquence de l'homéodomaine. Ces résultats, préliminaires, devront être confirmés par des expériences complémentaires. Néanmoins, la microspectroscopie de fluorescence X semble être une méthode suffisamment sensible pour détecter le signal du rhénium, même présent à de faibles quantités. Un brevet sur l'application des SCoMPIs comme sondes de fluorescence X a été déposé.

C.3 Marquage et imagerie des Anhydrases Carboniques

Nous avons ensuite souhaité tester la faisabilité du marquage et de l'imagerie multimodale de protéines endogènes avec des SCoMPIs. Nous avons pour cela choisi de marquer les anhydrases carboniques IX et XII. Ces protéines membranaires sont surexprimées dans certains types de cancers, notamment dans les tumeurs solides. Cette échelle est pertinente notamment pour la modalité infrarouge des SCoMPIs, qui permettrait à terme de quantifier la quantité de protéine dans un tissu. Plusieurs stratégies existent pour le marquage covalent et spécifique de protéines par de petites molécules dans des cellules vivantes. La plupart utilisent une combinaison de méthodes d'ingénierie génétique et de chimie de synthèse: fusion de la protéine d'intérêt à une étiquette protéique ou peptidique qui réagit ensuite avec le marqueur moléculaire souhaité, marquage d'un inhibiteur, etc. Dans le cadre de cette étude, nous avons choisi d'utiliser une des stratégies de marquage par affinité "sans trace" (Traceless Affinity Labelling) développées par le Pr I. Hamachi. Ces stratégies consistent à synthétiser des marqueurs de protéines endogènes constitués (i) d'un ligand de la protéine d'intérêt, permettant la selectivité du marquage; (ii) d'une molécule sonde, permettant la détection selon la modalité choisie (fluorescence, par exemple); (iii) d'un espaceur possédant un groupement modérément réactif en solution, mais qui, une fois que la protéine est liée à la partie 'ligand" du marqueur, va réagir avec l'une des chaines latérales nucléophiles des acides aminés proches du site actif. La partie ligand du marqueur est alors libre de diffuser hors du site actif, tandis que la sonde est liée covalemment à la protéine d'intérêt. En collaboration avec le laboratoire du Pr I. Hamachi, nous avons choisi d'adopter la stratégie

LDAI (Ligand-Directed Acyl Imidazole chemistry), utilisant un groupement "clivable" de type acyl-imidazole.

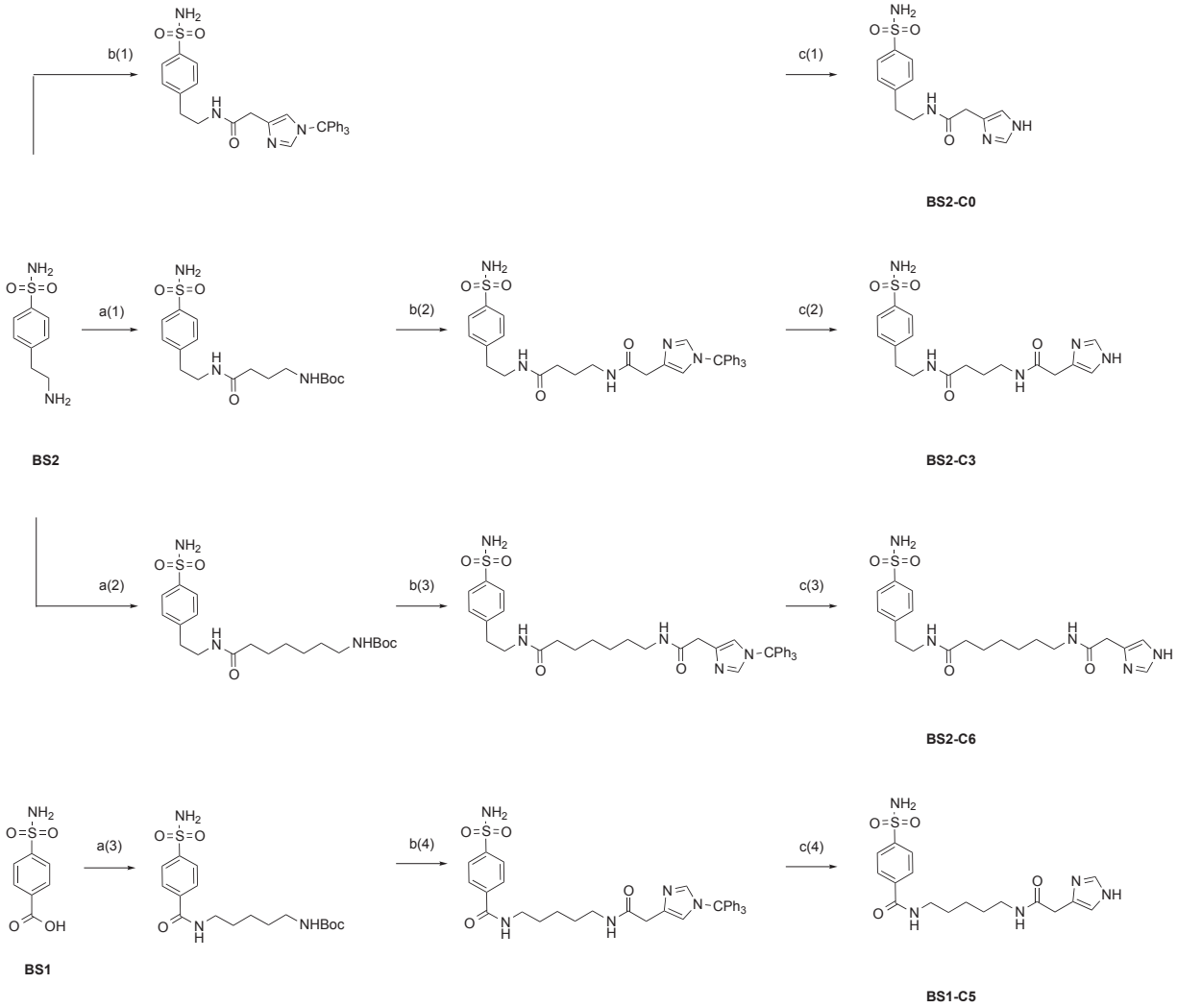

Schéma C.3: Synthèse des réactifs LDAI-SCoMPI: synthèse des ligand-imidazoles
(a1) *N*-Boc-4-aminobutyric acid, EDC, HOBt, DIEA, dry DMF, Ar, overnight, 68%; (a2) *N*-Boc-7-aminoheptanoic acid, EDC, HOBt, DIEA, dry DMF, Ar, overnight, 67%; (a3) *N*-Boc-1,5-diaminopentane, EDC, HOBt, DIEA, dry DMF, Ar, overnight, 74%; (b1) 1-trityl-1*H*-imidazole-4-acetic acid, EDC, HOBt, DIEA, dry DMF, Ar, overnight, 40%; (b2) *i.* TFA:DCM 50:50, 1h, RT, *ii.* same conditions as (b2), 54%; (b3) same conditions as (b2), 42%; (b4) same conditions as (b2), 34%; (c1) TFA:DCM 20:80, TIS, 1h, RT, 93%; (c2) voir conditions (c1), 85%; (c3) voir conditions (c1), 88%; (c4) voir conditions (c1), 90%.

La synthèse, convergente, consiste en la synthèse d'une part de la partie ligand-imidazole du réactif LDAI (Schéma C.3), et d'autre part de la partie sonde sous forme de "carbonate activé" (Schéma C.4). Il avait été montré, lors de précédents travaux du laboratoire du Pr Hamachi, que les réactifs LDAI de type BS1-C5-Sonde marquent efficacement les anhydrases carboniques IX et XII sur cellules. Afin d'essayer d'améliorer l'efficacité et surtout la sélectivité du marquage pour l'anhydrase carbonique IX, nous avons également synthétisé une série de réactifs LDAI-SCoMPI présentant un ligand légèrement différent (BS2) et possédant une meilleure affinité pour l'anhydrase carbonique IX. La longueur de l'espaceur entre le ligand et la partie imidazole varie de manière à "explorer" l'espace proche du site

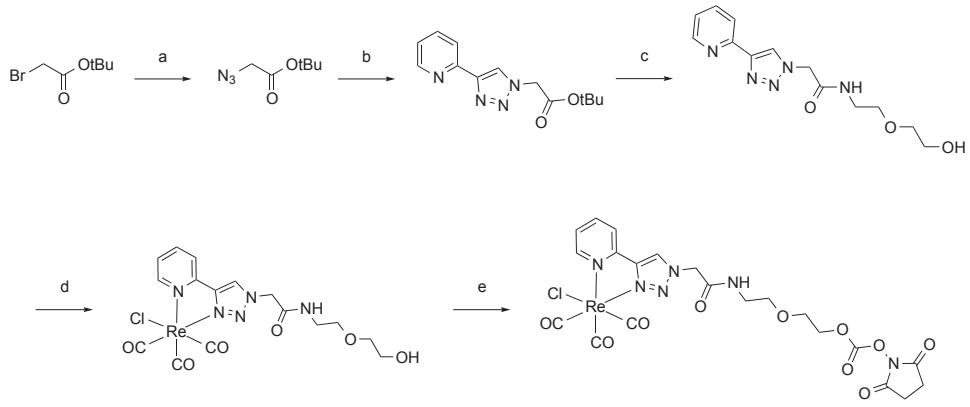

Schéma C.4: Synthèse des réactifs LDAI-SCoMPI: synthèse du "carbonate activé" de la sonde SCoMPI

(a) NaN_3, acetone:water (3:2 v:v), reflux, 20h, 97%; (b) 2-ethynylpyridine, $Cu(OAc)_2$, sodium ascorbate, *t*-BuOH : H_2O (1:1 v:v), 1h30, RT, 93%; (c) *i.* TFA:DCM 50:50, 2h, RT, *ii.* EDC, 2-(2-aminoethoxy)-ethanol, DIEA, 40%; (d) $Re(CO)_5Cl$, MeOH, reflux, overnight, 99%; (e) DSC, triethylamine, dry DMF, 6h, RT.

actif et atteindre une chaîne latérale nucléophile. La synthèse des imidazoles procède en quatre (trois pour le cas de l'imidazole C0). Le ligand souhaité (BS1 ou BS2) est couplé à l'espaceur C3, C5 ou C6 protégé par un groupement Boc. L'amine de l'espaceur est ensuite déprotégée et couplée à l'imidazole. Pour une plus grande facilité de synthèse et de purification, l'imidazole a été protégé par un groupement trityl. Dans le cas de l'imidazole "C0", le ligand est directement couplé à l'imidazole protégé. L'imidazole est enfin déprotégé avant réaction avec le "carbonate activé" de la sonde. D'autre part, la sonde SCoMPI est synthétisée de manière similaire à celle décrite dans les précédents chapitres. On forme dans un premier temps le ligand pyta sous forme d'ester *tert*-butylique, auquel on couple par la suite un espaceur hydrophile pour obtenir un ligand pyta fonctionnalisé par un alcool. Le ligand complexe ensuite le centre rhénium tricarbonyl chlorure à partir du précurseur $Re(CO)_5Cl$, puis on forme le "carbonate activé" par réaction du complexe avec le DSC (disuccinimidyl carbonate, carbonate de disuccinimide). Enfin, les réactifs LDAI-SCoMPI sont formés par réaction des différents imidazoles avec le "carbonate activé" du SCoMPI (Schéma C.5).

Nous avons ensuite testé *in vitro* l'efficacité de marquage des différents réactifs LDAI-SCoMPI sur l'anhydrase carbonique I, une isoforme soluble des anhydrases carboniques IX et XII (Figure C.9). Cette efficacité a été mesurée par spectrométrie de mass (MALDI-TOF) et par fluorescence sur gel. L'anhydrase carbonique I a été incubée dans un premier temps en présence de deux équivalents de chacun des LDAI-SCoMPI, et le marquage a été suivi par MALDI-TOF toutes les deux heures pendant six heures. Le réactif C0-SCoMPI présentait l'efficacité la moindre, avec seulement 10% de protéine marquée après six heures d'incubation à 37 °C. Les réactifs C3-SCoMPI, C5-SCoMPI et C6-SCoMPI, en revanche, présentaient des efficacités de marquage plus élevées, autour de 40–45 % après six heures. Ces valeurs sont inférieures à celles obtenues pour d'autres sondes (biotine,

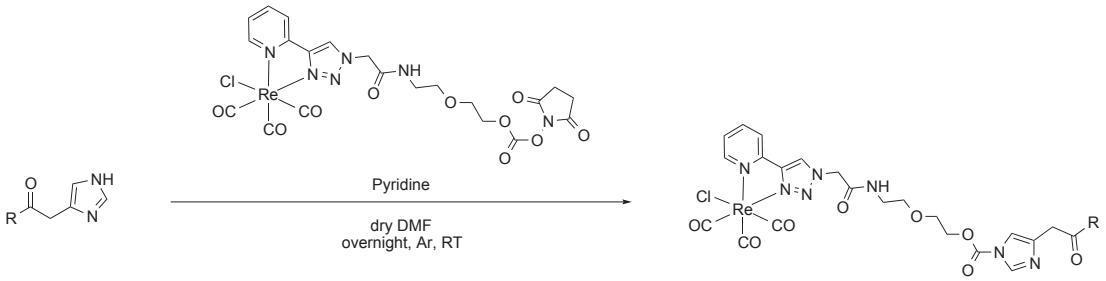

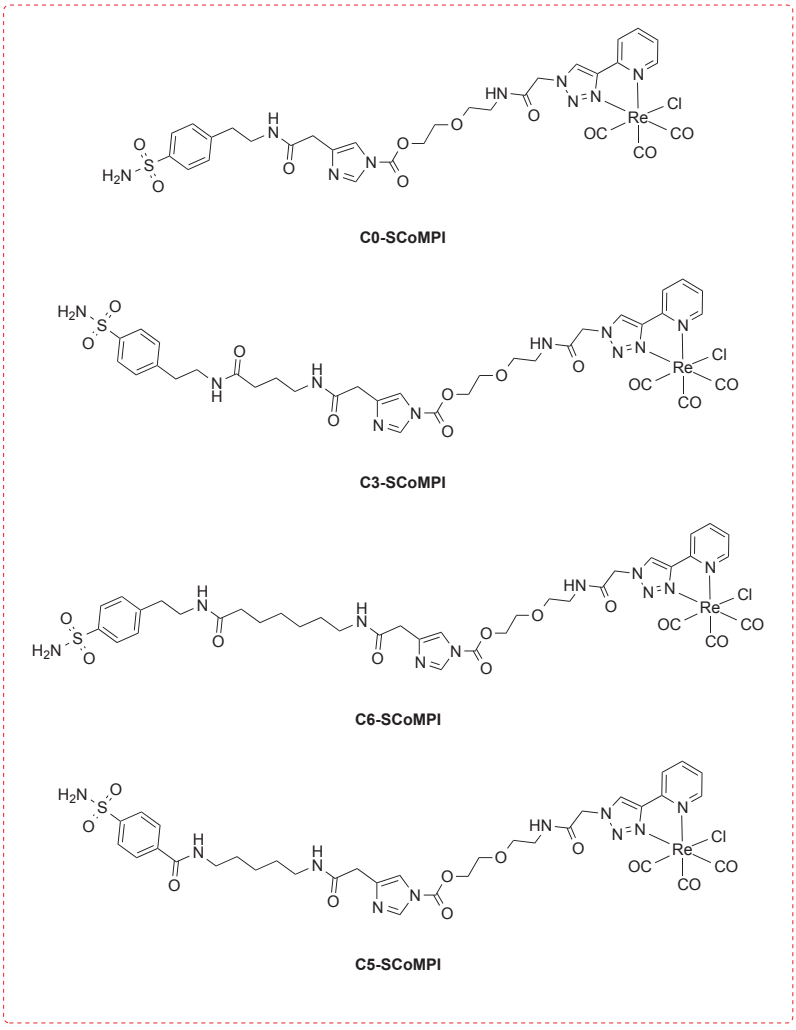

Schéma C.5: Synthèse des réactifs LDAI-SCoMPI: formation des réactifs Acyl-Imidazole

dérivé de coumarine, etc). Cette dépendance de l'efficacité de marquage en fonction de la sonde est l'une des caractéristiques de ce type de marquage d'affinité "sans trace". Par ailleurs, aucun marquage de la protéine n'a pu être observé dans l'échantillon témoin, dans lequel la protéine est incubée en présence du LDAI-SCoMPI et d'un inhibiteur comppétitif de l'anhydrase carbonique, l'ethoxzolamide (EZA). Ceci montre la nécessité du ligand et donc de l'interaction avec la protéine pour un marquage efficace de celle-ci. Nous avons ensuite cherché à améliorer l'efficacité de marquage en augmentant le nombre d'équivalents lors de l'incubation, dans le cas des trois réactifs C3-SCoMPI, C5-SCoMPI et C6-SCoMPI. Par MALDI comme par fluorescence sur gel, nous avons pu observer que l'efficacité de marquage des trois réactifs atteignaitÒ un plateau autour de 80% de marquage, dès deux heures d'incubation. Il était donc difficile de "départager" ces trois réactifs sur la base de ces expériences *in vitro*, et nous avons donc choisi de tester ces trois réactifs pour le marquage d'anhydrases carboniques IX et XII endogènes.

Les anhydrases carboniques IX et XII sont surexprimées dans certains types de cancers, mais peuvent également être surexprimées en plaçant les cellules en hypoxie. Des cellules A549 (cellules d'adénocarcinome) ont donc été placées en conditions hypoxiques pendant 24h, puis incubées avec les différents réactifs LDAI-SCoMPI. Nous avons souhaité tester plusieurs conditions d'incubations, menant en principe à des localisations cellulaires différentes. En effet, il a été montré que les cellules incubées en présence de LDAI présentent dans un premier temps un marquage membranaire (0–3 h, marquage des anhydrases membranaires) puis que des endosomes "marqués" apparaissent (> 3 h, internalisation des anhydrases carboniques marquées membranaires pour dégradation). Nous avons ensuite observé ces échantillons par microscopie de fluorescence et microspectroscopie infrarouge. Toutefois, nous n'avons pu détecter le signal des SCoMPIs dans aucun de ces échantillons par ces deux types d'imagerie. Comme dans le cas de l'anhydrase carbonique, les raisons en sont probablement (i) un manque de sensibilité de la technique dans le cas de l'infrarouge, ne permettant pas la détection à l'échelle cellulaire, et (ii) un rendement quantique de luminescence trop modeste pour détecter des petites quantités de protéines par microscopie de fluorescence.

Nous avons toutefois tenté de de détecter les anhydrases carboniques marquées par les SCoMPIs par microspectroscopie de fluorescence X. Nous avons alors pu observer le signal du rhénium sur les cellules incubées avec C5-SCoMPI (Figure C.10). Ce signal, bien que faible, montre la grande sensibilité de la fluorescence X et l'efficacité des complexes de rhénium comme sondes pour ce type d'imagerie. S'il n'a pas été possible, au moment des expériences, de cartographier le signal du rhénium au sein d'une cellule, nous espérons que des améliorations techniques futures (augmentation du flux, etc) le permettront.

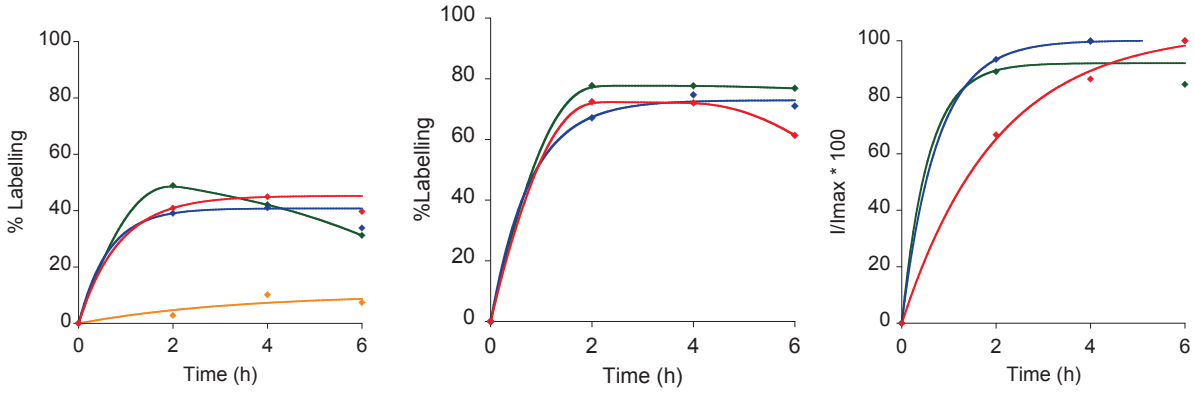

(a) MALDI-TOF, 2 equivalents

(b) MALDI-TOF, 20 equivalents

(c) Gel Imaging, 20 equivalents

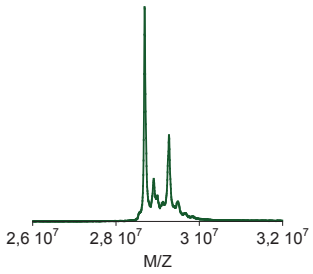

(d)

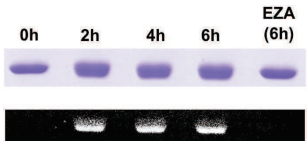

(e)

Figure C.9: Quantification du marquage *in vitro* de l'anhydrase carbonique I par les différents réactifs LDAI-SCoMPI

(a) MALDI-TOF MS: Suivi par MALDI-TOF du marquage de l'anhydrase carbonique I (SI10 in 50 mM HEPES buffer pH 7.2) incubée à 37 °C en présence de 2 équivalents de C0-SCoMPI (orange), C3-SCoMPI (bleu), C6-SCoMPI (rouge), C5-SCoMPI (vert). Le pourcentage de marquage est le rapport de l'aire sous le pic de la protéine marquée sur la somme des aires des pics de la protéine marquée et non marquée; *(b) MALDI-TOF MS:* Suivi par MALDI-TOF du marquage de l'anhydrase carbonique I (SI10 in 50 mM HEPES buffer pH 7.2) incubée à 37 °C en présence de 20 équivalents de C3-SCoMPI (bleu), C6-SCoMPI (rouge), C5-SCoMPI (vert); *(c) Fluorescence sur gel:* Suivi par fluorescence sur gel du marquage de l'anhydrase carbonique I (SI10 in 50 mM HEPES buffer pH 7.2) incubée à 37 °C en présence de 20 équivalents de C3-SCoMPI (bleu), C6-SCoMPI (rouge), C5-SCoMPI (vert). Les intensités moyennes ont été mesurées avec le logiciel ImageJ, et le rapport de l'intensité sur l'intensité maximale a été représenté ici. *(d)* Exemple de spectre MALDI-TOF d'un échantillon d'anhydrase carbonique I (10 µM) incubées en présence de C5-SCoMPI. *(e)* Exemple de suivi par fluorescence sur gel SDS-PAGE du marquage de l'anhydrase carbonique I en présence de 20 équivalents de C5-SCoMPI (haut: marquage au Bleu de Coomassie, bas: imagerie de fluorescence).

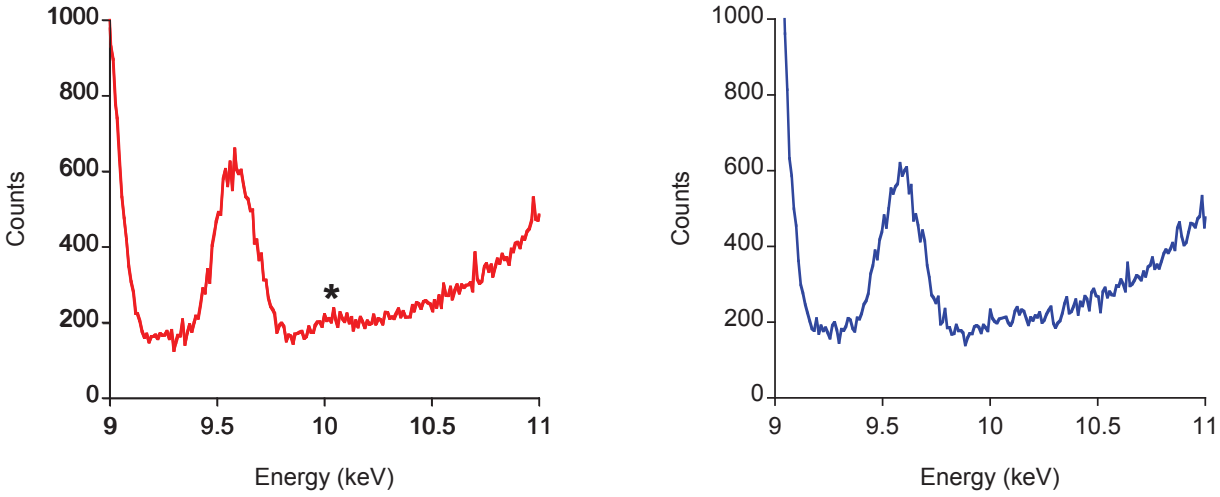

(a) C5-SCoMPI (b) Control

Figure C.10: Spectres de fluorescence X enregistrés sur cellules A549 incubées avec 10 µM C5-SCoMPI (gauche) et sur cellules témoins (droite)

Le temps d'acquisition des spectres est de 1000 s. Un agrandissement du spectre dans la région 9-11 keV est représentée ici pour chque échantillon. On peut observer à 9.6 keV une des bandes K du Zn, d'intensité comparable dans les deux échantillons. À environ 10 keV, l'une des bandes L du Re est présente pour l'échantillon incubé avec C5-SCoMPI.

Conclusions and perspectives

Dans le présent travail de thèse, des SCoMPIs adaptés au marquage de biomolécules *in vitro* et sur cellules ont été développés. Nous avons pu fonctionnaliser ces complexes Re(I) tricarbonyl avec des groupements variés, *via* le ligand pyta, notamment: (i) un groupement acide carboxylique, pour le marquage de peptides en position N-terminale; (ii) un groupement amine, utilisé ici pour permettre ensuite l'introduction d'un groupement réagissant avec les thiols; (iii) un groupement maléimide, pour le marquage spécifique de protéines *in vitro*par réaction avec le groupement thiol d'une cystéine; (iv) une fonction alcool, comme précurseur pour la formation d'un carbonate ou d'un carbamate. Nous avons pu marquer *in vitro* des CPPs (peptides vecteurs) et des protéines pouvant être internalisées dans les cellules (homéodomaines), ainsi que l'Anhydrase Carbonique I. Nous avons pu constater, dans la plupart des cas, que les peptides et protéines marqués conservaient les propriétés infrarouge et de luminescence de leur complexe parent.

Tableau C.2: Bilan: Imagerie multimodale de peptides et protéines en utilisant des SCoMPIs

	Quantité par cellule (mol)	Ref	Fluorescence	Infrared	X fluorescence
CPP (R9, R6W3)					
membranaire	$\sim 500 \times 10^{-18}$	[107]	✓	✓	Likely
internalisé	$\sim 10 \times 10^{-18}$	[107]			
CysHD *internalisé*	$\sim 2 \times 10^{-18}$	*	✗	✗	✓
CA-IX, CA-XII	$\sim 0.3 \times 10^{-18}$	[198]	✗	✗	✓

* Non publié

Nous avons ensuite étudié la possibilité de détecter et de réaliser l'imagerie multimodale de peptides et de protéines à l'échelle de la cellule unique. Nous avons pu détecter facilement les CPPs marqués par des SCoMPIs par microscopie de fluorescence et infrarouge. La modalité de luminescence du SCoMPI permet de visualiser rapidement la localisation des peptides par microscopie de fluorescence, ainsi qu'une estimation qualitative de l'internalisation de ces peptides dans certaines cas. Toutefois, nous avons montré dans le Chapitre 1 que l'intensité de luminescence de ces complexes pouvait présenter des variations importantes en fonction de leur environnement. En revanche, la modalité infrarouge de la sonde a pu être utilisée pour quantifier de manière plus fiable la concentration locale en SCoMPI, et donc en peptide.

Bien que les peptides marqués par des SCoMPIs aient été facilement détectables par microscopies de fluorescence et infrarouge, il n'a été possible de détecter ni des protéines exogènes (homéodomaines) ni des protéines endogènes (anhydrases carboniques) par ces deux modes d'imagerie, du moins à l'échelle cellulaire. Les concentrations présentes dans ces deux derniers cas sont inférieures à celles présentes pour des CPPs, ce qui peut expliquer ce manque de succès: la sensibilité de l'imagerie infrarouge est probablement insuffisante,

et le rendement quantique de luminescence des SCoMPI trop modeste, pour détecter ces quantités. Cependant, il a été possible de cartographier par microspectroscopie de fluorescence X le signal du Re dans des cellules incubées avec les homéodomaines HD et NLSHD marqués par des SCoMPI. Nous avons également pu détecter - bien que difficilement - le signal du Re lié aux anhydrases carboniques endogènes. L'utilisation des SCoMPIs comme sondes pour la fluorescence X est donc prometteuse et fait l'objet d'un dépôt de brevet.

Ces résultats montrent tout d'abord qu'il est souhaitable d'améliorer les propriétés de luminescence des SCoMPIs, et notamment leur rendement quantique, afin d'être capable de détecter de manière plus sensible des biomolécules par microscopie de fluorescence. Cela est possible notamment en modifiant la structure du ligand diimine du SCoMPI. Notre groupe a par exemple montré que les complexes portant un ligand pyridine triazole "inversé" (tapy, A-(2-pyridyl)-1,2,3-triazole) présentaient des rendements quantiques supérieurs à leurs analogues portant un ligand pyta classique. Ces complexes "tapy" pourraient ainsi être utilisés pour une meilleure détection des SCoMPI en milieu biologique par microscopie de fluorescence.

Parce qu'elle fournit le spectre IR complet de l'achantillon en un point donné, la microspectroscopie infrarouge permet d'obtenir des informations sur l'environnement local du SCoMPI. Il est ainsi possible de suivre certains processus biologiques en même temps qu'on détecte le signal (et la quantité) de SCoMPI. Par exemple, la signature IR d'une cellule évolue en fonction du cycle cellulaire. Il est en principe possible de caractériser par IR chacune des étapes du cycle cellulaire et de suivre l'internalisation des CPPs marqués avec des SCoMPIs lors de ces différentes étapes. Par ailleurs, il n'a pas été possible de détecter des protéines à l'échelle cellulaire par cette technique d'imagerie. On peut toutefois imaginer marquer ces protéines avec plusieurs SCoMPI (dimère, trimère de SCoMPI), bien que l'encombrement de la sonde puisse interférer avec les propriétés de la molécule marquée, notamment ses interactions avec son environnement. Il est également envisageable d'utiliser la modalité IR des SCoMPIs pour déterminer la quantité de biomolécule marquée sur une population de cellules ou un tissu. L'imagerie IR est bien adaptée à l'imagerie tissulaire, du fait de la bonne pénétration des rayonnements IR dans ces tissus. Il serait notamment intéressant de détecter les anhydrases carboniques à l'échelle tissulaire, puisque ces protéines sont surexprimées dans les tumeurs solides.

Enfin, la microspectroscopie de fluorescence X et l'utilisation des SCoMPIs comme sondes pour cette imagerie peuvent être développés. La tomographie de fluorescence X est une méthode qui commence à être développée, et l'imagerie en trois dimensions de biomolécules marquées par des compelxes de Re est envisageable. En outre, comme pour l'infrarouge, changer le rhénium pour un autre métal changerait la signature du complexe en fluorescence, ce qui rendrait possible une imagerie multicolore par fluorescence X.

Les SCoMPIs sont donc des outils prometteurs pour la détection et l'imagerie multimodale de biomolécules, qui bénéfécieront de l'amélioration de leurs propriétés spectro-

scopiques et des futurs développements de techniques d'imagerie alternative comme l'infrarouge et la fluorescence X.

List of Figures

List of Schemes

List of Tables

List of Abbreviations

$\Delta 1$	Secretion signal
K_P	Apparent partition coefficient between a lipid membrane and aqueous buffer
ACN	acetonitrile
ACP	Acyl-Carrier Protein
AFM	Atomic Force Microscopy
AFMIR	Atomic Force Microscope based Infrared spectroscopy
AGD	Affinity-Guided DMAP chemistry
aTf	apo-Transferrin
B16-F1	Mouse melanoma cells
B_2R	Bradykinin B_2 receptor
BCN	(*1R,8S,9S*)-bicyclo[6.1.0]non-4-yn-9-ylmethanol
bpm	bis(phenanthridinylmethyl)amine
Boc	*tert*-Butoxycarbonyl
bpy	2,2'-bipyridine
BSA	Bovine Serum Albumine
CA	Carbonic Anhydrase
CA-IX	Carbonic Anhydrase IX
CA-XII	Carbonic Anhydrase XII
CHO	Chinese Hamster Ovarian cells
CMIA	Carbonyl Metallo-ImmunoAssay

CORM	CO-Releasing Molecule
COS-7	Fibroblast cell line
CPP	Cell-Penetrating Peptide
CuAAC	Cu-catalyzed azide alkyne cycloaddition
DCC	dicyclohexylcarbodiimide
DCM	dichloromethane
DIBO	Dibenzocyclooctyne
DIEA	N, N'-diisopropylethylamine
DMAP	4-dimethylaminopyridine
DMF	Dimethylformamide
dmp	4,7-dimethyl-1,10-phenanthroline
DMSO	Dimethyl sulfoxide
DOPG	1,2-Dioleoyl-*sn*-glycero-3-phosho-*rac*-(1-glycerol)
DTT	Dithiothreitol
EDC	N-(3-Dimethylaminopropyl)-N'-ethylcarbodiimide hydrochloride
EDTA	Ethylenediaminetetracetic acid
EGFR	epidermal growth factor receptor
EZA	Ethoxzolamide
FBS	Fetal Bovine Serum
FKBP12	FK506 Binding Protein 12
FlAsH	**Fl**uorescein **As**enic **H**airpin Binder
FLIP	Fluorescence Loss in Photobleaching
Fmoc	Fluorenylmethyloxycarbonyl
FP	Fluorescent Protein
FPR	Formyl Peptide Receptor

FRAP	Fluorescence Recovery After Photobleaching
FTIR	Fourier Transform Infrared
GRP	Gastrin releasing peptide
GUV	Giant Unilamellar Vesicle
HaCaT	Keratinocyte
HBTU	N,N,N',N'-Tetramethyl-O-(1H-benzotriazol-1-yl)uronium hexafluorophosphate
hCA-I	human Carbonic Anhydrase I
HD	Homeodomain
HeLa	Cervical cancer cells
HIV	Human Immunodeficience Virus
HIV-Tat	Human immunodeficiency virus - trans-activator of transcription
HOBt	1-hydroxybenzotriazole
HP	Homeoprotein
HSA	Human Serum Albumin
HT-29	Colon cancer cells
IgG	Immunoglobulin G
IMAC	Immobilized Metal ion Affinity Chromatography
IPTG	isopropyl-β-D-thiogalactoside
IR	Infrared
KN1	Knotted-1
LDAI	Ligand-Directed Acyl Imidazole (chemistry)
LDBB	Ligand-Directed diBromoBenzoate (chemistry)
LDT	Ligand-Directed Tosyl (chemistry)
LSC	Local Single Electron Transfer Chemistry
LUV	Large Unilamellar Vesicle

MALDI-TOF-MS	Matrix-assisted laser desorption/ionization-time-of-flight- mass spectroscopy
MCF-7	Human breast carcinoma cells expressing nuclear estrogen receptors
MDA-MB-231	Human breast carcinoma cells not expressing nuclear estrogen receptors
MLCT	Metal-to-Ligand Charge Transfer
MoAL	Modular method for Affinity Labelling
NES	Nuclear Export Signal
NHS	N-hydroxy succinimide
NLS	Nuclear Localization Signal
NMP	1-Methyl-2-pyrrolidinone
OSCC	Oral squamous carcinoma cells
PBS	Phosphate Buffer Saline
PC-3	Human prostate adenocarcinoma
PDT	Photo-Dynamic Therapy
phen	1,10-phenanthroline
PNA	Peptide Nucleic Acid
POI	Protein of Interest
PPTase	Phosphopantetheinyl transerases
PTIR	Photothermal Induced Resonance
pyta	4-(2-pyridyl)-1,2,3-triazole
SAAC	Single Amino-Acid Chelate
SCoMPI	*S*ingle *Co*re *M*ultimodal *P*robe for *I*maging
SERS	Surface-Enhanced Raman Spectroscopy
SH2	Src Homology domain 2
SLP	Self-Labelling Proteins
SR-FTIR-MS	Synchrotron Radiation FTIR Microspectroscopy

SR-UV-MS	Synchrotron Radiation UV Microspectroscopy
TCEP	tris(2-carboxyethyl)phosphine
TFA	Trifluoroacetic acid
THF	Tetrahydrofuran
TIS	Triisopropylsilane
TMRE	tetramethylrhodamine ethyl ester
TRIR	Time-Resolved Infrared
Trityl,Tr	triphenylmethyl

Bibliography

[1] Clède, S., Delsuc, N., Laugel, C., Lambert, F., Sandt, C., Baillet-Guffroy, A., and Policar, C., An easy-to-detect nona-arginine peptide for epidermal targeting, *Chem. Commun.* **2015**, *51*(13), 2687–2689.

[2] Clède, S. and Policar, C., Metal–Carbonyl Units for Vibrational and Luminescence Imaging: Towards Multimodality, *Chem.–Eur. J.* **2015**, *21*(3), 942–958.

[3] Clède, S., Lambert, F., Sandt, C., Kascakova, S., Unger, M., Harté, E., Plamont, M.A., Saint-Fort, R., Deniset-Besseau, A., Gueroui, Z., Hirschmugl, C., Lecomte, S., Dazzi, A., Vessières, A., and Policar, C., Detection of an estrogen derivative in two breast cancer cell lines using a single core multimodal probe for imaging (SCoMPI) imaged by a panel of luminescent and vibrational techniques, *Analyst* **2013**, *138*(19), 5627–5638.

[4] Clède, S., Lambert, F., Sandt, C., Gueroui, Z., Réfrégiers, M., Plamont, M.A., Dumas, P., Vessières, A., and Policar, C., A rhenium tris-carbonyl derivative as a single core multimodal probe for imaging (SCoMPI) combining infrared and luminescent properties, *Chem. Commun.* **2012**, *48*(62), 7729–7731.

[5] Salmain, M. and Vessières, A., Organometallic Complexes as Tracers in Non-isotopic Immunoassay, in G. Jaouen, editor, *Bioorganometallics*, pages 263–302, Wiley-VCH Verlag GmbH & Co. KGaA **2005**.

[6] Salmain, M., Labeling of Proteins with Organometallic Complexes: Strategies and Applications, in G. Jaouen, editor, *Bioorganometallics*, pages 181–213, Wiley-VCH Verlag GmbH & Co. KGaA **2005**.

[7] Patra, M. and Gasser, G., Organometallic Compounds: An Opportunity for Chemical Biology?, *ChemBioChem* **2012**, *13*(9), 1232–1252.

[8] Lo, K.K.W., Zhang, K.Y., and Li, S.P.Y., Recent Exploitation of Luminescent Rhenium(I) Tricarbonyl Polypyridine Complexes as Biomolecular and Cellular Probes, *Eur. J. Inorg. Chem.* **2011**, *2011*(24), 3551–3568.

[9] Lo, K.K.W., Tsang, K.H.K., Sze, K.S., Chung, C.K., Lee, T.K.M., Zhang, K.Y., Hui, W.K., Li, C.K., Lau, J.S.Y., Ng, D.C.M., and Zhu, N., Non-covalent binding of luminescent transition metal polypyridine complexes to avidin, indole-binding proteins and estrogen receptors, *Coord. Chem. Rev.* **2007**, *251*(17–20), 2292–2310.

[10] Lo, K.K.W., Choi, A.W.T., and Law, W.H.T., Applications of luminescent inorganic and organometallic transition metal complexes as biomolecular and cellular probes, *Dalton Trans.* **2012**, *41*(20), 6021.

[11] Coogan, M.P., Doyle, R.P., Valliant, J.F., Babich, J.W., and Zubieta, J., Single amino acid chelate complexes of the $M(CO)_3^+$ core for correlating fluorescence and radioimaging studies (M=^{99m}Tc or Re), *J. Labelled Compd. Radiopharm.* **2014**, *57*(4), 255–261.

[12] Amoroso, A.J., Coogan, M.P., Dunne, J.E., Fernández-Moreira, V., Hess, J.B., Hayes, A.J., Lloyd, D., Millet, C., Pope, S.J.A., and Williams, C., Rhenium fac tricarbonyl bisimine complexes: biologically useful fluorochromes for cell imaging applications, *Chem. Commun.* **2007**, *2007*(29), 3066–3068.

[13] Thorp-Greenwood, F.L., Balasingham, R.G., and Coogan, M.P., Organometallic complexes of transition metals in luminescent cell imaging applications, *J. Organomet. Chem.* **2012**, *714*, 12–21.

[14] Balasingham, R.G., Coogan, M.P., and Thorp-Greenwood, F.L., Complexes in context: Attempting to control the cellular uptake and localisation of rhenium *fac*-tricarbonyl polypyridyl complexes, *Dalton Trans.* **2011**, *40*(44), 11663–11674.

[15] Fernández-Moreira, V., Thorp-Greenwood, F.L., and Coogan, M.P., Application of d^6 transition metal complexes in fluorescence cell imaging, *Chem. Commun.* **2009**, *46*(2), 186–202.

[16] Kumar, A., Sun, S.S., and Lees, A.J., Photophysics and Photochemistry of Organometallic Rhenium Diimine Complexes, in A.J. Lees, editor, *Photophysics of Organometallics*, volume 29, pages 37–71, Springer Berlin Heidelberg, Berlin, Heidelberg **2009**.

[17] Bhuvaneswari, J., Mareeswaran, P.M., Shanmugasundaram, S., and Rajagopal, S., Protein binding studies of luminescent rhenium(I) diimine complexes, *Inorg. Chim. Acta* **2011**, *375*(1), 205–212.

[18] Choi, A.W.T., Liu, H.W., and Lo, K.K.W., Rhenium(I) polypyridine dibenzocyclooctyne complexes as phosphorescent bioorthogonal probes: Synthesis, characterization, emissive behavior, and biolabeling properties, *J. Inorg. Biochem.* **2015**, *148*, 2–10.

[19] Lo, K.K.W., Hui, W.K., Chung, C.K., Tsang, K.H.K., Ng, D.C.M., Zhu, N., and Cheung, K.K., Biological labelling reagents and probes derived from luminescent transition metal polypyridine complexes, *Coord. Chem. Rev.* **2005**, *249*(13-14), 1434–1450.

[20] Lo, K.K.W., Louie, M.W., and Zhang, K.Y., Design of luminescent iridium(III) and rhenium(I) polypyridine complexes as in vitro and in vivo ion, molecular and biological probes, *Coord. Chem. Rev.* **2010**, *254*(21–22), 2603–2622.

[21] Lo, K.K.W., Ng, D.C.M., Hui, W.K., and Cheung, K.K., Luminescent rhenium(I) polypyridine complexes with an isothiocyanate moiety–versatile labelling reagents for biomolecules, *J. Chem. Soc., Dalton Trans.* **2001**, (18), 2634–2640.

[22] Lo, K.K.W., Luminescent Rhenium(I) and Iridium(III) Polypyridine Complexes as Biological Probes, Imaging Reagents, and Photocytotoxic Agents, *Acc. Chem. Res.* **2015**.

[23] Lo, K.K.W., Hui, W.K., Ng, D.C.M., and Cheung, K.K., Synthesis, Characterization, Photophysical Properties, and Biological Labeling Studies of a Series of Luminescent Rhenium(I) Polypyridine Maleimide Complexes, *Inorg. Chem.* **2002**, *41*(1), 40–46.

[24] Lo, K.K.W., Tsang, K.H.K., Hui, W.K., and Zhu, N., Synthesis, Characterization, Crystal Structure, and Electrochemical, Photophysical, and Protein-Binding Properties of Luminescent Rhenium(I) Diimine Indole Complexes, *Inorg. Chem.* **2005**, *44*(17), 6100–6110.

[25] Louie, M.W., Ho-Chuen Lam, M., and Kam-Wing Lo, K., Luminescent Polypyridinerhenium(I) Bis-Biotin Complexes as Crosslinkers for Avidin, *Eur. J. Inorg. Chem.* **2009**, *2009*(28), 4265–4273.

[26] Louie, M.W., Choi, A.W.T., Liu, H.W., Chan, B.T.N., and Lo, K.K.W., Synthesis, Emission Characteristics, Cellular Studies, and Bioconjugation Properties of Luminescent Rhenium(I) Polypyridine Complexes with a Fluorous Pendant, *Organometallics* **2012**, *31*(16), 5844–5855.

[27] Amoroso, A.J., Arthur, R.J., Coogan, M.P., Court, J.B., Fernández-Moreira, V., Hayes, A.J., Lloyd, D., Millet, C., and Pope, S.J.A., 3-Chloromethylpyridyl bipyridine *fac*-tricarbonyl rhenium: a thiol-reactive luminophore for fluorescence microscopy accumulates in mitochondria, *New J. Chem.* **2008**, *32*, 1097.

[28] Fernández-Moreira, V., Thorp-Greenwood, F.L., Amoroso, A.J., Cable, J., Court, J.B., Gray, V., Hayes, A.J., Jenkins, R.L., Kariuki, B.M., Lloyd, D., Millet,

C.O., Williams, C.F., and Coogan, M.P., Uptake and localisation of rhenium *fac*-tricarbonyl polypyridyls in fluorescent cell imaging experiments, *Org. Biomol. Chem.* **2010**, *8*(17), 3888.

[29] Stephenson, K.A., Banerjee, S.R., Besanger, T., Sogbein, O.O., Levadala, M.K., McFarlane, N., Lemon, J.A., Boreham, D.R., Maresca, K.P., Brennan, J.D., Babich, J.W., Zubieta, J., and Valliant, J.F., Bridging the Gap between in Vitro and in Vivo Imaging: Isostructural Re and ^{99m}Tc Complexes for Correlating Fluorescence and Radioimaging Studies, *J. Am. Chem. Soc.* **2004**, *126*(28), 8598–8599.

[30] Raszeja, L., Maghnouj, A., Hahn, S., and Metzler-Nolte, N., A Novel Organometallic ReI Complex with Favourable Properties for Bioimaging and Applicability in Solid-Phase Peptide Synthesis, *ChemBioChem* **2011**, *12*(3), 371–376.

[31] Bartholomä, M., Valliant, J., Maresca, K.P., Babich, J., and Zubieta, J., Single amino acid chelates (SAAC): a strategy for the design of technetium and rhenium radiopharmaceuticals, *Chem. Commun.* **2009**, pages 493–512.

[32] Obata, M., Kitamura, A., Mori, A., Kameyama, C., Czaplewska, J.A., Tanaka, R., Kinoshita, I., Kusumoto, T., Hashimoto, H., Harada, M., Mikata, Y., Funabiki, T., and Yano, S., Syntheses, structural characterization and photophysical properties of 4-(2-pyridyl)-1,2,3-triazole rhenium(I) complexes, *Dalton Trans.* **2008**, (25), 3292–3300.

[33] Bertrand, H.C., Clède, S., Guillot, R., Lambert, F., and Policar, C., Luminescence Modulations of Rhenium Tricarbonyl Complexes Induced by Structural Variations, *Inorg. Chem.* **2014**, *53*(12), 6204–6223.

[34] van der Peet, P.L., Connell, T.U., Gunawan, C., White, J.M., Donnelly, P.S., and Williams, S.J., A Click Chemistry Approach to 5,5-Disubstituted-3,3-Bisisoxazoles from Dichloroglyoxime and Alkynes: Luminescent Organometallic Iridium and Rhenium Bisisoxazole Complexes, *J. Org. Chem.* **2013**, *78*(14), 7298–7304.

[35] Viola-Villegas, N., Rabideau, A.E., Bartholomä, M., Zubieta, J., and Doyle, R.P., Targeting the Cubilin Receptor through the Vitamin B12 Uptake Pathway: Cytotoxicity and Mechanistic Insight through Fluorescent Re(I) Delivery, *J. Med. Chem.* **2009**, *52*(16), 5253–5261.

[36] Bartholomä, M.D., Vortherms, A.R., Hillier, S., Joyal, J., Babich, J., Doyle, R.P., and Zubieta, J., Synthesis, cytotoxicity and cellular uptake studies of N3 functionalized Re(CO)3 thymidine complexes, *Dalton Trans.* **2011**, *40*(23), 6216–6225.

[37] Huang, R., Langille, G., Gill, R.K., Li, C.M.J., Mikata, Y., Wong, M.Q., Yapp, D.T., and Storr, T., Synthesis, characterization, and biological studies of emissive rhenium–glutamine conjugates, *JBIC, J. Biol. Inorg. Chem.* **2013**, *18*(7), 831–844.

[38] Esteves, T., Xavier, C., Gama, S., Mendes, F., Raposinho, P.D., Marques, F., Paulo, A., Pessoa, J.C., Rino, J., Viola, G., and Santos, I., Tricarbonyl M(I) (M = Re, 99mTc) complexes bearing acridine fluorophores: synthesis, characterization, DNA interaction studies and nuclear targeting, *Org. Biomol. Chem.* **2010**, *8*(18), 4104–4116.

[39] Agorastos, N., Borsig, L., Renard, A., Antoni, P., Viola, G., Spingler, B., Kurz, P., and Alberto, R., Cell-Specific and Nuclear Targeting with [M(CO)3]+ (M=99mTc, Re)-Based Complexes Conjugated to Acridine Orange and Bombesin, *Chem.–Eur. J.* **2007**, *13*(14), 3842–3852.

[40] Reece, S.Y. and Nocera, D.G., Direct Tyrosine Oxidation Using the MLCT Excited States of Rhenium Polypyridyl Complexes, *J. Am. Chem. Soc.* **2005**, *127*(26), 9448–9458.

[41] Fernández-Moreira, V., Ortego, M.L., Williams, C.F., Coogan, M.P., Villacampa, M.D., and Gimeno, M.C., Bioconjugated Rhenium(I) Complexes with Amino Acid Derivatives: Synthesis, Photophysical Properties, and Cell Imaging Studies, *Organometallics* **2012**, *31*(16), 5950–5957.

[42] Viola-Villegas, N., Rabideau, A., Cesnavicious, J., Zubieta, J., and Doyle, R., Targeting the Folate Receptor (FR): Imaging and Cytotoxicity of ReI Conjugates in FR-Overexpressing Cancer Cells, *ChemMedChem* **2008**, *3*(9), 1387–1394.

[43] Stephenson, K.A., Zubieta, J., Banerjee, S.R., Levadala, M.K., Taggart, L., Ryan, L., McFarlane, N., Boreham, D.R., Maresca, K.P., Babich, J.W., and Valliant, J.F., A New Strategy for the Preparation of Peptide-Targeted Radiopharmaceuticals Based on an Fmoc-Lysine-Derived Single Amino Acid Chelate (SAAC). Automated Solid-Phase Synthesis, NMR Characterization, and in Vitro Screening of fMLF(SAAC)G and fMLF([SAACRe$(CO)_3$]$^+$)G, *Bioconjugate Chem.* **2004**, *15*(1), 128–136.

[44] Leonidova, A., Pierroz, V., Rubbiani, R., Heier, J., Ferrari, S., and Gasser, G., Towards cancer cell-specific phototoxic organometallic rhenium(I) complexes, *Dalton Trans.* **2014**, *43*(11), 4287–4294.

[45] Leonidova, A., Pierroz, V., Adams, L.A., Barlow, N., Ferrari, S., Graham, B., and Gasser, G., Enhanced Cytotoxicity through Conjugation of a "Clickable" Luminescent Re(I) Complex to a Cell-Penetrating Lipopeptide, *ACS Med. Chem. Lett.* **2014**, *5*(7), 809–814.

[46] DeRosa, M.C. and Crutchley, R.J., Photosensitized singlet oxygen and its applications, *Coord. Chem. Rev.* **2002**, *233–234*, 351–371.

[47] Ragone, F., Saavedra, H.H.M., Gara, P.M.D., Ruiz, G.T., and Wolcan, E., Photosensitized Generation of Singlet Oxygen from Re(I) Complexes: A Photophysical Study Using LIOAS and Luminescence Techniques, *J. Phys. Chem. A* **2013**, *117*(21), 4428–4435.

[48] Spada, R.M., Cepeda-Plaza, M., Gómez, M.L., Günther, G., Jaque, P., Pizarro, N., Palacios, R.E., and Vega, A., Clean Singlet Oxygen Production by a ReI Complex Embedded in a Flexible Self-Standing Polymeric Silsesquioxane Film, *J. Phys. Chem. C* **2015**, *119*(18), 10148–10159.

[49] Guo, X.Q., Castellano, F.N., Li, L., Szmacinski, H., Lakowicz, J.R., and Sipior, J., A Long-Lived, Highly Luminescent Re(I) Metal–Ligand Complex as a Biomolecular Probe, *Anal. Biochem.* **1997**, *254*(2), 179–186.

[50] Guo, X.Q., Castellano, F.N., Li, and Lakowicz, J.R., Use of a Long-Lifetime Re(I) Complex in Fluorescence Polarization Immunoassays of High-Molecular-Weight Analytes, *Anal. Chem.* **1998**, *70*(3), 632–637.

[51] Dattelbaum, J.D., Abugo, O.O., and Lakowicz, J.R., Synthesis and Characterization of a Sulfhydryl-Reactive Rhenium MetalLigand Complex, *Bioconjugate Chem.* **2000**, *11*(4), 533–536.

[52] Dwaraknath, S., Tran, N.H., Dao, T., Colbert, A., Mullen, S., Nguyen, A., Cortez, A., and Cheruzel, L., A facile and versatile methodology for cysteine specific labeling of proteins with octahedral polypyridyl d^6 metal complexes, *J. Inorg. Biochem.* **2014**, *136*, 154–160.

[53] Choi, A.W.T., Tso, K.K.S., Yim, V.M.W., Liu, H.W., and Lo, K.K.W., Modification of 1,2,4,5-tetrazine with cationic rhenium(I) polypyridine units to afford phosphorogenic bioorthogonal probes with enhanced reaction kinetics, *Chem. Commun.* **2015**, *51*(16), 3442–3445.

[54] Blanco-Rodríguez, A.M., Busby, M., Grădinaru, C., Crane, B.R., Di Bilio, A.J., Matousek, P., Towrie, M., Leigh, B.S., Richards, J.H., Vlček, A., and Gray, H.B., Excited-State Dynamics of Structurally Characterized $[Re^{I}(CO)_3(phen)(HisX)]^+$ (X = 83, 109) Pseudomonas aeruginosa Azurins in Aqueous Solution, *J. Am. Chem. Soc.* **2006**, *128*(13), 4365–4370.

[55] Shih, C., Museth, A.K., Abrahamsson, M., Blanco-Rodriguez, A.M., Bilio, A.J.D., Sudhamsu, J., Crane, B.R., Ronayne, K.L., Towrie, M., Jr., A.V., Richards, J.H.,

Winkler, J.R., and Gray, H.B., Tryptophan-Accelerated Electron Flow through Proteins, *Science* **2008**, *320*(5884), 1760–1762.

[56] Blanco-Rodríguez, A.M., Busby, M., Ronayne, K., Towrie, M., Grădinaru, C., Sudhamsu, J., Sýkora, J., Hof, M., Záliš, S., Bilio, A.J.D., Crane, B.R., Gray, H.B., and Vlček, A., Relaxation Dynamics of Pseudomonas aeruginosa $Re^{I}(CO)_3(\alpha-diimine)(HisX)^+$ (X = 83, 107, 109, 124, 126)CuII Azurins, *J. Am. Chem. Soc.* **2009**, *131*(33), 11788–11800.

[57] Tavaré, R., Williams, J., Howland, K., Blower, P.J., and Mullen, G.E.D., $[Re(CO)_3]^+$ labelling of a novel cysteine/hexahistidine tag: Insights into binding mode by liquid chromatography-mass spectrometry, *J. Inorg. Biochem.* **2012**, *114*, 24–27.

[58] Salmain, M., Vessières, A., Varenne, A., Brossier, P., and Jaouen, G., A new application of bioorganometallics: the first simultaneous triple assay by the carbonylmetalloimmunoassay (CMIA) method, *J. Organomet. Chem.* **1999**, *589*(1), 92–97.

[59] Salmain, M., Gunn, M., Gorfti, A., Top, S., and Jaouen, G., Labeling of proteins by organometallic complexes of rhenium(I). Synthesis and biological activity of the conjugates, *Bioconjugate Chem.* **1993**, *4*(6), 425–433.

[60] Salmain, M., Malisza, K.L., Top, S., Jaouen, G., Senechal-Tocquer, M.C., Senechal, D., and Caro, B., [η^5-Cyclopentadienyl]metal Tricarbonyl Pyrylium Salts: Novel Reagents for the Specific Conjugation of Proteins with Transition Organometallic Labels, *Bioconjugate Chem.* **1994**, *5*(6), 655–659.

[61] Woys, A.M., Mukherjee, S.S., Skoff, D.R., Moran, S.D., and Zanni, M.T., A Strongly Absorbing Class of Non-Natural Labels for Probing Protein Electrostatics and Solvation with FTIR and 2D IR Spectroscopies, *J. Phys. Chem. B* **2013**, *117*(17), 5009–5018.

[62] Kim, H. and Cho, M., Infrared Probes for Studying the Structure and Dynamics of Biomolecules, *Chem. Rev.* **2013**, *113*(8), 5817–5847.

[63] Kong, K.V., Chew, W., Lim, L.H.K., Fan, W.Y., and Leong, W.K., Bioimaging in the Mid-Infrared Using an Organometallic Carbonyl Tag, *Bioconjugate Chem.* **2007**, *18*, 1370–1374.

[64] Clède, S., Lambert, F., Sandt, C., Gueroui, Z., Delsuc, N., Dumas, P., Vessières, A., and Policar, C., Synchrotron radiation FTIR detection of a metal-carbonyl tamoxifen analog. Correlation with luminescence microscopy to study its subcellular distribution, *Biotechnol. Adv.* **2013**, *31*(3), 393–395.

[65] Meister, K., Niesel, J., Schatzschneider, U., Metzler-Nolte, N., Schmidt, D., and Havenith, M., Label-Free Imaging of Metal–Carbonyl Complexes in Live Cells by Raman Microspectroscopy, *Angew. Chem. Int. Edit.* **2010**, *49*(19), 3310–3312.

[66] Kopf, I., Peindy N'Dongo, H.W., Ballout, F., Schatzschneider, U., Bründermann, E., and Havenith, M., Introducing cymantrene labels into scattering scanning near-field infrared microscopy, *Analyst* **2012**, *137*(21), 4995.

[67] Miller, L.M. and Dumas, P., Chemical imaging of biological tissue with synchrotron infrared light, *BBA - Biomembranes* **2006**, *1758*(7), 846–857.

[68] Jamin, N., Dumas, P., Moncuit, J., Fridman, W.H., Teillaud, J.L., Carr, G.L., and Williams, G.P., Highly resolved chemical imaging of living cells by using synchrotron infrared microspectrometry, *Proc. Natl. Acad. Sci. U. S. A.* **1998**, *95*(9), 4837–4840.

[69] Kong, K.V., Lam, Z., Goh, W.D., Leong, W.K., and Olivo, M., Metal Carbonyl–Gold Nanoparticle Conjugates for Live-Cell SERS Imaging, *Angew. Chem. Int. Edit.* **2012**, *51*(39), 9796–9799.

[70] Kong, K.V., Lam, Z., Lau, W.K.O., Leong, W.K., and Olivo, M., A Transition Metal Carbonyl Probe for Use in a Highly Specific and Sensitive SERS-Based Assay for Glucose, *J. Am. Chem. Soc.* **2013**, *135*(48), 18028–18031.

[71] Policar, C., Waern, J.B., Plamont, M.A., Clède, S., Mayet, C., Prazeres, R., Ortega, J.M., Vessières, A., and Dazzi, A., Subcellular IR Imaging of a Metal-Carbonyl Moiety Using Photothermally Induced Resonance, *Angew. Chem. Int. Edit.* **2011**, *50*, 860–864.

[72] Martin, M.C., Dabat-Blondeau, C., Unger, M., Sedlmair, J., Parkinson, D.Y., Bechtel, H.A., Illman, B., Castro, J.M., Keiluweit, M., Buschke, D., Ogle, B., Nasse, M.J., and Hirschmugl, C.J., 3D spectral imaging with synchrotron Fourier transform infrared spectro-microtomography, *Nat. Methods* **2013**, *10*(9), 861–864.

[73] Quaroni, L., Obst, M., Nowak, M., and Zobi, F., Three-Dimensional Mid-Infrared Tomographic Imaging of Endogenous and Exogenous Molecules in a Single Intact Cell with Subcellular Resolution, *Angew. Chem. Int. Edit.* **2015**, *54*(1), 318–322.

[74] Lu, G., Hillier, S.M., Maresca, K.P., Zimmerman, C.N., Eckelman, W.C., Joyal, J.L., and Babich, J.W., Synthesis and SAR of Novel Re/ 99m Tc-Labeled Benzenesulfonamide Carbonic Anhydrase IX Inhibitors for Molecular Imaging of Tumor Hypoxia, *J. Med. Chem.* **2013**, *56*(2), 510–520.

[75] Morais, M., Paulo, A., Gano, L., Santos, I., and Correia, J.D.G., Target-specific $Tc(CO)_3$-complexes for in vivo imaging, *J. Organomet. Chem.* **2013**, *744*, 125–139.

[76] Alberto, R., Radiopharmaceuticals, in G. Jaouen, editor, *Bioorganometallics*, pages 97–124, Wiley-VCH Verlag GmbH & Co. KGaA **2005**.

[77] Kluba, C. and Mindt, T., Click-to-Chelate: Development of Technetium and Rhenium-Tricarbonyl Labeled Radiopharmaceuticals, *Molecules* **2013**, *18*(3), 3206–3226.

[78] Alberto, R., Ortner, K., Wheatley, N., Schibli, R., and Schubiger, A.P., Synthesis and Properties of Boranocarbonate: A Convenient in Situ CO Source for the Aqueous Preparation of $[^{99m}Tc(OH_2)_3(CO)_3]^+$, *J. Am. Chem. Soc.* **2001**, *123*(13), 3135–3136.

[79] Piccinonna, S., Denora, N., Margiotta, N., Laquintana, V., Trapani, G., and Natile, G., Synthesis, Characterization, and Binding to the Translocator Protein (18 kDa, TSPO) of a New Rhenium Complex as a Model of Radiopharmaceutical Agents, *Z. Anorg. Allg. Chem.* **2013**, *639*(8-9), 1606–1612.

[80] Lecina, J., Palacios, Ò., Atrian, S., Capdevila, M., and Suades, J., Rhenium and technetium tricarbonyl, $\{M(CO)_3\}^+$ (M = Tc, Re), binding to mammalian metallothioneins: new insights into chemical and radiopharmaceutical implications, *JBIC, J. Biol. Inorg. Chem.* **2014**, *20*(3), 465–474.

[81] Burai, R., Ramesh, C., Nayak, T.K., Dennis, M.K., Bryant, B.K., Prossnitz, E.R., and Arterburn, J.B., Synthesis and Characterization of Tricarbonyl-Re/Tc(I) Chelate Probes Targeting the G Protein-Coupled Estrogen Receptor GPER/GPR30, *PLoS ONE* **2012**, *7*(10).

[82] Kothari, K., Prasad, S., Korde, A., Mukherjee, A., Mathur, A., Jaggi, M., Venkatesh, M., Pillai, A.M.R., Mukherjee, R., and Ramamoorthy, N., $^{99m}Tc(CO)_3$-VIP analogues: Preparation and evaluation as tumor imaging agent, *Appl. Radiat. Isot.* **2007**, *65*(4), 382–386.

[83] Schaffer, P., Gleave, J.A., Lemon, J.A., Reid, L.C., Pacey, L.K.K., Farncombe, T.H., Boreham, D.R., Zubieta, J., Babich, J.W., Doering, L.C., and Valliant, J.F., Isostructural fluorescent and radioactive probes for monitoring neural stem and progenitor cell transplants, *Nucl. Med. Biol.* **2008**, *35*(2), 159–169.

[84] Hickey, J.L., Simpson, E.J., Hou, J., and Luyt, L.G., An Integrated Imaging Probe Design: The Synthesis of ^{99m}Tc/Re-Containing Macrocyclic Peptide Scaffolds, *Chem.–Eur. J.* **2015**, *21*(2), 568–578.

[85] Yazdani, A., Janzen, N., Banevicius, L., Czorny, S., and Valliant, J.F., Imidazole-Based [2 + 1] Re(I)/^{99m}Tc(I) Complexes as Isostructural Nuclear and Optical Probes, *Inorg. Chem.* **2015**, *54*(4), 1728–1736.

[86] Anderson, C.B., Elliott, A.B.S., McAdam, C.J., Gordon, K.C., and Crowley, J.D., fac-Re(CO)3Cl Complexes of [2-(4-R-1H-1,2,3-Triazol-1-yl)methyl]pyridine Inverse "Click" Ligands: A Systematic Synthetic, Spectroscopic, and Computational Study, *Organometallics* **2013**, *32*(3), 788–797.

[87] Anderson, C.B., Elliott, A.B.S., Lewis, J.E.M., McAdam, C.J., Gordon, K.C., and Crowley, J.D., fac-Re(CO)3 complexes of 2,6-bis(4-substituted-1,2,3-triazol-1-ylmethyl)pyridine "click" ligands: synthesis, characterisation and photophysical properties, *Dalton Trans.* **2012**, *41*(48), 14625–14632.

[88] Kim, T.Y., Elliott, A.B.S., Shaffer, K.J., John McAdam, C., Gordon, K.C., and Crowley, J.D., Rhenium(I) complexes of readily functionalized bidentate pyridyl-1,2,3-triazole "click" ligands: A systematic synthetic, spectroscopic and computational study, *Polyhedron* **2013**, *52*, 1391–1398.

[89] Lo, W.K.C., Huff, G.S., Cubanski, J.R., Kennedy, A.D.W., McAdam, C.J., McMorran, D.A., Gordon, K.C., and Crowley, J.D., Comparison of Inverse and Regular 2-Pyridyl-1,2,3-triazole "Click" Complexes: Structures, Stability, Electrochemical, and Photophysical Properties, *Inorg. Chem.* **2015**, page 150123104629006.

[90] Clède, S., Lambert, F., Saint-Fort, R., Plamont, M.A., Bertrand, H., Vessières, A., and Policar, C., Influence of the Side-Chain Length on the Cellular Uptake and the Cytotoxicity of Rhenium Triscarbonyl Derivatives: A Bimodal Infrared and Luminescence Quantitative Study, *Chem.–Eur. J.* **2014**, *20*(28), 8714–8722.

[91] Fernández, E., Rodríguez, G., Hostachy, S., Clède, S., Cócera, M., Sandt, C., Lambert, F., de la Maza, A., Policar, C., and López, O., A rhenium tris-carbonyl derivative as a model molecule for incorporation into phospholipid assemblies for skin applications, *Colloids Surf. B* **2015**, *131*, 102–107.

[92] Hummer, A.A. and Rompel, A., The use of X-ray absorption and synchrotron based micro-X-ray fluorescence spectroscopy to investigate anti-cancer metal compounds in vivo and in vitro, *Metallomics* **2013**, *5*(6), 597–614.

[93] Ortega, R., Chemical elements distribution in cells, *Nucl. Instrum. Methods Phys. Res. B* **2005**, *231*(1–4), 218–223.

[94] Ortega, R., Direct speciation analysis of inorganic elements in single cells using X-ray absorption spectroscopy, *J. Anal. At. Spectrom.* **2010**, *26*(1), 23–29.

[95] Majumdar, S., Peralta-Videa, J.R., Castillo-Michel, H., Hong, J., Rico, C.M., and Gardea-Torresdey, J.L., Applications of synchrotron -XRF to study the distribution of biologically important elements in different environmental matrices: A review, *Anal. Chim. Acta* **2012**, *755*, 1–16.

[96] Copolovici, D.M., Langel, K., Eriste, E., and Langel, Ü., Cell-Penetrating Peptides: Design, Synthesis, and Applications, *ACS Nano* **2014**, *8*(3), 1972–1994.

[97] Milletti, F., Cell-penetrating peptides: classes, origin, and current landscape, *Drug Discov. Today* **2012**, *17*(15-16), 850–860.

[98] Heitz, F., Morris, M.C., and Divita, G., Twenty years of cell-penetrating peptides: from molecular mechanisms to therapeutics, *Br. J. Pharmacol.* **2009**, *157*(2), 195–206.

[99] Brock, R., The Uptake of Arginine-Rich Cell-Penetrating Peptides: Putting the Puzzle Together, *Bioconjugate Chem.* **2014**, *25*(5), 863–868.

[100] Derossi, D., Chassaing, G., and Prochiantz, A., Trojan peptides: the penetratin system for intracellular delivery, *Trends Cell Biol.* **1998**, *8*(2), 84–87.

[101] Aussedat, B., Dupont, E., Sagan, S., Joliot, A., Lavielle, S., Chassaing, G., and Burlina, F., Modifications in the chemical structure of Trojan carriers: impact on cargo delivery, *Chem. Commun.* **2008**, page 1398.

[102] Koren, E. and Torchilin, V.P., Cell-penetrating peptides: breaking through to the other side, *Trends Mol. Med.* **2012**, *18*(7), 385–393.

[103] Bechara, C. and Sagan, S., Cell-penetrating peptides: 20 years later, where do we stand?, *FEBS Lett.* **2013**, *587*(12), 1693–1702.

[104] Swiecicki, J.M., Bartsch, A., Tailhades, J., Di Pisa, M., Heller, B., Chassaing, G., Mansuy, C., Burlina, F., and Lavielle, S., The Efficacies of Cell-Penetrating Peptides in Accumulating in Large Unilamellar Vesicles Depend on their Ability To Form Inverted Micelles, *ChemBioChem* **2014**, *15*(6), 884–891.

[105] Persson, D., Thorén, P.E.G., Lincoln, P., and Nordén, B., Vesicle Membrane Interactions of Penetratin Analogues †, *Biochemistry* **2004**, *43*(34), 11045–11055.

[106] Henriques, S.T. and Castanho, M.A.R.B., Environmental factors that enhance the action of the cell penetrating peptide pep-1: A spectroscopic study using lipidic vesicles, *BBA - Biomembranes* **2005**, *1669*(2), 75–86.

[107] Walrant, A., Correia, I., Jiao, C.Y., Lequin, O., Bent, E.H., Goasdoué, N., Lacombe, C., Chassaing, G., Sagan, S., and Alves, I.D., Different membrane behaviour and cellular uptake of three basic arginine-rich peptides, *BBA - Biomembranes* **2011**, *1808*(1), 382–393.

[108] Jobin, M.L., Blanchet, M., Henry, S., Chaignepain, S., Manigand, C., Castano, S., Lecomte, S., Burlina, F., Sagan, S., and Alves, I.D., The role of tryptophans on the cellular uptake and membrane interaction of arginine-rich cell penetrating peptides, *BBA - Biomembranes* **2015**, *1848*(2), 593–602.

[109] Di Pisa, M., Chassaing, G., and Swiecicki, J.M., Translocation Mechanism(s) of Cell-Penetrating Peptides: Biophysical Studies Using Artificial Membrane Bilayers, *Biochemistry* **2015**, *54*(2), 194–207.

[110] Melikov, K. and Chernomordik, L.V., Arginine-rich cell penetrating peptides: from endosomal uptake to nuclear delivery, *Cell. Mol. Life. S.* **2005**, *62*(23), 2739–2749.

[111] Richard, J.P., Melikov, K., Vives, E., Ramos, C., Verbeure, B., Gait, M.J., Chernomordik, L.V., and Lebleu, B., Cell-penetrating Peptides A REEVALUATION OF THE MECHANISM OF CELLULAR UPTAKE, *J. Biol. Chem.* **2003**, *278*(1), 585–590.

[112] Drin, G., Cottin, S., Blanc, E., Rees, A.R., and Temsamani, J., Studies on the Internalization Mechanism of Cationic Cell-penetrating Peptides, *J. Biol. Chem.* **2003**, *278*(33), 31192–31201.

[113] Burlina, F., Sagan, S., Bolbach, G., and Chassaing, G., A direct approach to quantification of the cellular uptake of cell-penetrating peptides using MALDI-TOF mass spectrometry, *Nat. Protoc.* **2006**, *1*(1), 200–205.

[114] Wolff, M., Munoz, L., François, A., Carrayon, C., Seridi, A., Saffon, N., Picard, C., Machura, B., and Benoist, E., Tricarbonylrhenium complexes from 2-pyridyl-1,2,3-triazole ligands bearing a 4-substituted phenyl arm: a combined experimental and theoretical study, *Dalton Trans.* **2013**, *42*(19), 7019–7031.

[115] Seridi, A., Wolff, M., Boulay, A., Saffon, N., Coulais, Y., Picard, C., Machura, B., and Benoist, E., Rhenium(I) and technetium(I) complexes of a novel pyridyltriazole-based ligand containing an arylpiperazine pharmacophore: Synthesis, crystal structures, computational studies and radiochemistry, *Inorg. Chem. Commun.* **2011**, *14*(1), 238–242.

[116] Connell, T.U., Hayne, D.J., Ackermann, U., Tochon-Danguy, H.J., White, J.M., and Donnelly, P.S., Rhenium and technetium tricarbonyl complexes of 1,4-Substituted pyridyl-1,2,3-triazole bidentate 'click' ligands conjugated to a targeting RGD peptide, *J. Labelled Compd. Radiopharm.* **2014**, *57*(4), 262–269.

[117] Boulay, A., Seridi, A., Zedde, C., Ladeira, S., Picard, C., Maron, L., and Benoist, E., Tricarbonyl ReI Complexes from Functionalised Pyridine–Triazole Derivatives:

From Mononuclear to Unexpected Dimeric Complexes, *Eur. J. Inorg. Chem.* **2010**, *2010*(32), 5058–5062.

[118] Doose, S., Neuweiler, H., and Sauer, M., Fluorescence Quenching by Photoinduced Electron Transfer: A Reporter for Conformational Dynamics of Macromolecules, *ChemPhysChem* **2009**, *10*(9-10), 1389–1398.

[119] Blanco-Rodríguez, A.M., Towrie, M., Sýkora, J., Záliš, S., and Vlček, A., Photoinduced Intramolecular Tryptophan Oxidation and Excited-State Behavior of [Re(L-AA)(CO) 3 (-diimine)] + (L = Pyridine or Imidazole, AA = Tryptophan, Tyrosine, Phenylalanine), *Inorg. Chem.* **2011**, *50*(13), 6122–6134.

[120] Santos, N.C., Prieto, M., and Castanho, M.A.R.B., Quantifying molecular partition into model systems of biomembranes: an emphasis on optical spectroscopic methods, *BBA - Biomembranes* **2003**, *1612*(2), 123–135.

[121] Melo, M.N. and Castanho, M.A.R.B., Omiganan interaction with bacterial membranes and cell wall models. Assigning a biological role to saturation, *BBA - Biomembranes* **2007**, *1768*(5), 1277–1290.

[122] Pan, J., Heberle, F.A., Tristram-Nagle, S., Szymanski, M., Koepfinger, M., Katsaras, J., and Kucerka, N., Molecular structures of fluid phase phosphatidylglycerol bilayers as determined by small angle neutron and X-ray scattering, *Biochim. Biophys. Acta* **2012**, *1818*(9), 2135–2148.

[123] Christiaens, B., Symoens, S., Vanderheyden, S., Engelborghs, Y., Joliot, A., Prochiantz, A., Vandekerckhove, J., Rosseneu, M., and Vanloo, B., Tryptophan fluorescence study of the interaction of penetratin peptides with model membranes, *Eur. J. Biochem.* **2002**, *269*(12), 2918–2926.

[124] Cooper, G.M., The Eukaryotic Cell Cycle, in *The cell: a molecular approach*, Sunderland (MA): Sinauer Associates, 2nd edition **2000**.

[125] Pena-Diaz, J., Hegre, S.A., Anderssen, E., Aas, P.A., Mjelle, R., Gilfillan, G.D., Lyle, R., Drablos, F., Krokan, H.E., and Saetrom, P., Transcription profiling during the cell cycle shows that a subset of Polycomb-targeted genes is upregulated during DNA replication, *Nucleic Acids Res.* **2013**, *41*(5), 2846–2856.

[126] Sardet, C., Vidal, M., Cobrinik, D., Geng, Y., Onufryk, C., Chen, A., and Weinberg, R.A., E2F-4 and E2F-5, two members of the E2F family, are expressed in the early phases of the cell cycle, *Proc. Natl. Acad. Sci. U. S. A.* **1995**, *92*(6), 2403–2407.

[127] Carlier, L., Balayssac, S., Cantrelle, F.X., Khemtémourian, L., Chassaing, G., Joliot, A., and Lequin, O., Investigation of Homeodomain Membrane Translocation Properties: Insights from the Structure Determination of Engrailed-2 Homeodomain in Aqueous and Membrane-Mimetic Environments, *Biophys. J.* **2013**, *105*(3), 667–678.

[128] Fraenkel, E., Rould, M.A., Chambers, K.A., and Pabo, C.O., Engrailed homeodomain-DNA complex at 2.2 Å resolution: a detailed view of the interface and comparison with other engrailed structures1, *J. Mol. Biol.* **1998**, *284*(2), 351–361.

[129] Spatazza, J., Lullo, E.D., Joliot, A., Dupont, E., Moya, K.L., and Prochiantz, A., Homeoprotein Signaling in Development, Health, and Disease: A Shaking of Dogmas Offers Challenges and Promises from Bench to Bed, *Pharmacol. Rev.* **2013**, *65*(1), 90–104.

[130] Fuchs, J., Stettler, O., Alvarez-Fischer, D., Prochiantz, A., Moya, K.L., and Joshi, R.L., Engrailed signaling in axon guidance and neuron survival, *Eur. J. Neurosci.* **2012**, *35*(12), 1837–1845.

[131] Joliot, A., Pernelle, C., Deagostini-Bazin, H., and Prochiantz, A., Antennapedia homeobox peptide regulates neural morphogenesis, *Proc. Natl. Acad. Sci. U. S. A.* **1991**, *88*(5), 1864–1868.

[132] Frankel, A.D. and Pabo, C.O., Cellular uptake of the tat protein from human immunodeficiency virus, *Cell* **1988**, *55*(6), 1189–1193.

[133] Prochiantz, A., Messenger proteins: homeoproteins, TAT and others, *Curr. Opin. Cell Biol.* **2000**, *12*(4), 400–406.

[134] Berlose, J.P., Convert, O., Derossi, D., Brunissen, A., and Chassaing, G., Conformational and Associative Behaviours of the Third Helix of Antennapedia Homeodomain in Membrane-Mimetic Environments, *Eur. J. Biochem.* **1996**, *242*(2), 372–386.

[135] Roux, I.L., Joliot, A.H., Bloch-Gallego, E., Prochiantz, A., and Volovitch, M., Neurotrophic activity of the Antennapedia homeodomain depends on its specific DNA-binding properties, *Proc. Natl. Acad. Sci. U. S. A.* **1993**, *90*(19), 9120–9124.

[136] Derossi, D., Joliot, A.H., Chassaing, G., and Prochiantz, A., The third helix of the Antennapedia homeodomain translocates through biological membranes., *J. Biol. Chem.* **1994**, *269*(14), 10444–10450.

[137] Prochiantz, A., Getting hydrophilic compounds into cells: lessons from homeopeptides, *Curr. Opin. Neurobiol.* **1996**, *6*(5), 629–634.

[138] Prochiantz, A., Homeodomain-Derived Peptides: In and Out of the Cells, *Ann. N. Y. Acad. Sci.* **1999**, *886*(1), 172–179.

[139] Derossi, D., Calvet, S., Trembleau, A., Brunissen, A., Chassaing, G., and Prochiantz, A., Cell Internalization of the Third Helix of the Antennapedia Homeodomain Is Receptor-independent, *J. Biol. Chem.* **1996**, *271*(30), 18188–18193.

[140] Joliot, A. and Prochiantz, A., Peptides transducteurs: La face utile d'un nouveau mode de signalisation, *Med. Sci. (Paris)* **2005**, *21*(3), 309–314.

[141] Jiao, C.Y., Delaroche, D., Burlina, F., Alves, I.D., Chassaing, G., and Sagan, S., Translocation and Endocytosis for Cell-penetrating Peptide Internalization, *J. Biol. Chem.* **2009**, *284*(49), 33957–33965.

[142] Lensink, M.F., Christiaens, B., Vandekerckhove, J., Prochiantz, A., and Rosseneu, M., Penetratin-Membrane Association: W48/R52/W56 Shield the Peptide from the Aqueous Phase, *Biophys. J.* **2005**, *88*(2), 939–952.

[143] Joliot, A., Maizel, A., Rosenberg, D., Trembleau, A., Dupas, S., Volovitch, M., and Prochiantz, A., Identification of a signal sequence necessary for the unconventional secretion of Engrailed homeoprotein, *Curr. Biol.* **1998**, *8*(15), 856–863.

[144] Maizel, A., Bensaude, O., Prochiantz, A., and Joliot, A., A short region of its homeodomain is necessary for engrailed nuclear export and secretion, *Development* **1999**, *126*(14), 3183–3190.

[145] Dupont, E., Prochiantz, A., and Joliot, A., Identification of a Signal Peptide for Unconventional Secretion, *J. Biol. Chem.* **2007**, *282*(12), 8994–9000.

[146] Joliot, A., Trembleau, A., Raposo, G., Calvet, S., Volovitch, M., and Prochiantz, A., Association of Engrailed homeoproteins with vesicles presenting caveolae-like properties, *Development* **1997**, *124*(10), 1865–1875.

[147] Getz, E.B., Xiao, M., Chakrabarty, T., Cooke, R., and Selvin, P.R., A comparison between the sulfhydryl reductants tris (2-carboxyethyl) phosphine and dithiothreitol for use in protein biochemistry, *Anal. Biochem.* **1999**, *273*(1), 73–80.

[148] Shafer, D.E., Inman, J.K., and Lees, A., Reaction of Tris(2-carboxyethyl)phosphine (TCEP) with Maleimide and -Haloacyl Groups: Anomalous Elution of TCEP by Gel Filtration, *Anal. Biochem.* **2000**, *282*(1), 161–164.

[149] Nguyen, T. and Francis, M.B., Practical Synthetic Route to Functionalized Rhodamine Dyes, *Org. Lett.* **2003**, *5*(18), 3245–3248.

[150] Krishnamurthy, V.M., Kaufman, G.K., Urbach, A.R., Gitlin, I., Gudiksen, K.L., Weibel, D.B., and Whitesides, G.M., Carbonic Anhydrase as a Model for Biophysical and Physical-Organic Studies of Proteins and ProteinLigand Binding, *Chem. Rev.* **2008**, *108*, 946–1051.

[151] Supuran, C.T., Briganti, F., Tilli, S., Chegwidden, W.R., and Scozzafava, A., Carbonic anhydrase inhibitors: sulfonamides as antitumor agents?, *Bioorg. Med. Chem.* **2001**, *9*(3), 703–714.

[152] Supuran, C.T. and Scozzafava, A., Carbonic anhydrases as targets for medicinal chemistry, *Bioorg. Med. Chem.* **2007**, *15*(13), 4336–4350.

[153] Winum, J.Y., Rami, M., Scozzafava, A., Montero, J.L., and Supuran, C., Carbonic anhydrase IX: A new druggable target for the design of antitumor agents, *Med. Res. Rev.* **2008**, *28*(3), 445–463.

[154] Švastová, E., Hulıková, A., Rafajová, M., Zat'ovičová, M., Gibadulinová, A., Casini, A., Cecchi, A., Scozzafava, A., Supuran, C.T., Pastorek, J., and Pastoreková, S., Hypoxia activates the capacity of tumor-associated carbonic anhydrase IX to acidify extracellular pH, *FEBS Lett.* **2004**, *577*(3), 439–445.

[155] Lau, J., Pan, J., Zhang, Z., Hundal-Jabal, N., Liu, Z., Bénard, F., and Lin, K.S., Synthesis and evaluation of 18F-labeled tertiary benzenesulfonamides for imaging carbonic anhydrase IX expression in tumours with positron emission tomography, *Bioorg. Med. Chem. Lett.* **2014**, *24*(14), 3064–3068.

[156] Thiry, A., Dogné, J.M., Masereel, B., and Supuran, C.T., Targeting tumor-associated carbonic anhydrase IX in cancer therapy, *Trends Pharmacol. Sci.* **2006**, *27*(11), 566–573.

[157] Hayashi, T. and Hamachi, I., Traceless Affinity Labeling of Endogenous Proteins for Functional Analysis in Living Cells, *Acc. Chem. Res.* **2012**, *45*(9), 1460–1469.

[158] Hinner, M.J. and Johnsson, K., How to obtain labeled proteins and what to do with them, *Curr. Opin. Biotechnol.* **2010**, *21*, 766–776.

[159] Zhang, J., Campbell, R.E., Ting, A.Y., and Tsien, R.Y., Creating new fluorescent probes for cell biology, *Nat. Rev. Mol. Cell Biol.* **2002**, *3*(12), 906–918.

[160] Tamura, T. and Hamachi, I., Recent Progress in Design of Protein-Based Fluorescent Biosensors and Their Cellular Applications, *ACS Chem. Biol.* **2014**, *9*(12), 2708–2717.

[161] Uchinomiya, S., Ojida, A., and Hamachi, I., Peptide Tag/Probe Pairs Based on the Coordination Chemistry for Protein Labeling, *Inorg. Chem.* **2013**.

[162] Lang, K. and Chin, J.W., Bioorthogonal Reactions for Labeling Proteins, *ACS Chem. Biol.* **2014**, *9*(1), 16–20.

[163] Lang, K. and Chin, J.W., Cellular Incorporation of Unnatural Amino Acids and Bioorthogonal Labeling of Proteins, *Chem. Rev.* **2014**, *114*(9), 4764–4806.

[164] Bertozzi, C.R., A Decade of Bioorthogonal Chemistry, *Acc. Chem. Res.* **2011**, *44*(9), 651–653.

[165] Tsien, R.Y., The Green Fluorescent Protein, *Annu. Rev. Biochem.* **1998**, *67*(1), 509–544.

[166] Tsukiji, S., Wang, H., Miyagawa, M., Tamura, T., Takaoka, Y., and Hamachi, I., Quenched Ligand-Directed Tosylate Reagents for One-Step Construction of Turn-On Fluorescent Biosensors, *J. Am. Chem. Soc.* **2009**, *131*, 9046–9054.

[167] Prifti, E., Reymond, L., Umebayashi, M., Hovius, R., Riezman, H., and Johnsson, K., A Fluorogenic Probe for SNAP-Tagged Plasma Membrane Proteins Based on the Solvatochromic Molecule Nile Red, *ACS Chem. Biol.* **2014**, *9*(3), 606–612.

[168] Daughtry, K.D., Martin, L.J., Sarraju, A., Imperiali, B., and Allen, K.N., Tailoring Encodable Lanthanide-Binding Tags as MRI Contrast Agents, *ChemBioChem* **2012**, *13*(17), 2567–2574.

[169] Allen, K.N. and Imperiali, B., Lanthanide-tagged proteins—an illuminating partnership, *Curr. Opin. Chem. Biol.* **2010**, *14*(2), 247–254.

[170] Mizukami, S., Watanabe, S., Akimoto, Y., and Kikuchi, K., No-Wash Protein Labeling with Designed Fluorogenic Probes and Application to Real-Time Pulse-Chase Analysis, *J. Am. Chem. Soc.* **2012**, *134*(3), 1623–1629.

[171] Mizukami, S., Yamamoto, T., Yoshimura, A., Watanabe, S., and Kikuchi, K., Covalent Protein Labeling with a Lanthanide Complex and Its Application to Photoluminescence Lifetime-Based Multicolor Bioimaging, *Angew. Chem. Int. Edit.* **2011**, *50*(37), 8750–8752.

[172] Mizukami, S., Watanabe, S., Hori, Y., and Kikuchi, K., Covalent Protein Labeling Based on Noncatalytic -Lactamase and a Designed FRET Substrate, *J. Am. Chem. Soc.* **2009**, *131*(14), 5016–5017.

[173] Sletten, E.M. and Bertozzi, C.R., From Mechanism to Mouse: A Tale of Two Bioorthogonal Reactions, *Acc. Chem. Res.* **2011**, *44*(9), 666–676.

[174] Zhou, Z., Koglin, A., Wang, Y., McMahon, A.P., and Walsh, C.T., An Eight Residue Fragment of an Acyl Carrier Protein Suffices for Post-Translational Introduction of Fluorescent Pantetheinyl Arms in Protein Modification in vitro and in vivo, *J. Am. Chem. Soc.* **2008**, *130*(30), 9925–9930.

[175] Chen, I., Howarth, M., Lin, W., and Ting, A.Y., Site-specific labeling of cell surface proteins with biophysical probes using biotin ligase, *Nat. Methods* **2005**, *2*(2), 99–104.

[176] Hauke, S., Best, M., Schmidt, T.T., Baalmann, M., Krause, A., and Wombacher, R., Two-Step Protein Labeling Utilizing Lipoic Acid Ligase and Sonogashira Cross-Coupling, *Bioconjugate Chem.* **2014**, *25*(9), 1632–1637.

[177] Fernández-Suárez, M., Baruah, H., Martínez-Hernández, L., Xie, K.T., Baskin, J.M., Bertozzi, C.R., and Ting, A.Y., Redirecting lipoic acid ligase for cell surface protein labeling with small-molecule probes, *Nat. Biotechnol.* **2007**, *25*, 1483–1487.

[178] Jakobs, S., Andresen, M., and Wurm, C.A., "FlAsH" Protein Labeling, in L.W. Miller, editor, *Probes and Tags to Study Biomolecular Function*, pages 73–88, Wiley-VCH Verlag GmbH & Co. KGaA, Weinheim, Germany **2008**.

[179] Halo, T.L., Appelbaum, J., Hobert, E.M., Balkin, D.M., and Schepartz, A., Selective recognition of protein tetraserine motifs with a cell-permeable, pro-fluorescent bis-boronic acid, *J. Am. Chem. Soc.* **2009**, *131*(2), 438–439.

[180] Kiefer, H., Lindstrom, J., Lennox, E.S., and Singer, S.J., Photo-affinity labeling of specific acetylcholine-binding sites on membranes, *Proc. Natl. Acad. Sci. U. S. A.* **1970**, *67*(4), 1688–1694.

[181] Wofsy, L., Metzger, H., and Singer, S.J., Affinity Labeling—a General Method for Labeling the Active Sites of Antibody and Enzyme Molecules*, *Biochemistry* **1962**, *1*(6), 1031–1039.

[182] Koshi, Y., Nakata, E., Miyagawa, M., Tsukiji, S., Ogawa, T., and Hamachi, I., Target-Specific Chemical Acylation of Lectins by Ligand-Tethered DMAP Catalysts, *J. Am. Chem. Soc.* **2008**, *130*, 245–251.

[183] Hayashi, T., Sun, Y., Tamura, T., Kuwata, K., Song, Z., Takaoka, Y., and Hamachi, I., Semisynthetic Lectin-4-Dimethylaminopyridine Conjugates for Labeling and Profiling Glycoproteins on Live Cell Surfaces., *J. Am. Chem. Soc.* **2013**, *135*(33), 12252–12258.

[184] Wang, H., Koshi, Y., Minato, D., Nonaka, H., Kiyonaka, S., Mori, Y., Tsukiji, S., and Hamachi, I., Chemical Cell-Surface Receptor Engineering Using Affinity-Guided, Multivalent Organocatalysts, *J. Am. Chem. Soc.* **2011**, *133*, 12220–12228.

[185] Hayashi, T., Yasueda, Y., Tamura, T., Takaoka, Y., and Hamachi, I., Analysis of Cell-Surface Receptor Dynamics through Covalent Labeling by Catalyst-Tethered Antibody, *J. Am. Chem. Soc.* **2015**, *137*(16), 5372–5380.

[186] Song, Z., Takaoka, Y., Kioi, Y., Komatsu, K., Tamura, T., Miki, T., and Hamachi, I., Extended Affinity-guided DMAP Chemistry with a Finely Tuned Acyl Donor for Intracellular FKBP12 Labeling, *Chem. Lett.* **2015**, *44*(3), 333–335.

[187] Kunishima, M., Nakanishi, S., Nishida, J., Tanaka, H., Morisaki, D., Hioki, K., and Nomoto, H., Convenient modular method for affinity labeling (MoAL method) based on a catalytic amidation, *Chem. Commun.* **2009**, (37), 5597–5599.

[188] Sato, S. and Nakamura, H., Ligand-Directed Selective Protein Modification Based on Local Single-Electron-Transfer Catalysis, *Angew. Chem. Int. Edit.* **2013**, *52*(33), 8681–8684.

[189] Tsukiji, S., Miyagawa, M., Takaoka, Y., Tamura, T., and Hamachi, I., Ligand-directed tosyl chemistry for protein labeling in vivo, *Nat. Chem. Biol.* **2009**, *5*, 341–343.

[190] Tamura, T., Tsukiji, S., and Hamachi, I., Native FKBP12 Engineering by Ligand-Directed Tosyl Chemistry: Labeling Properties and Application to Photo-Cross-Linking of Protein Complexes in Vitro and in Living Cells, *J. Am. Chem. Soc.* **2012**, *134*(4), 2216–2226.

[191] Tamura, T., Kioi, Y., Miki, T., Tsukiji, S., and Hamachi, I., Fluorophore Labeling of Native FKBP12 by Ligand-Directed Tosyl Chemistry Allows Detection of Its Molecular Interactions in Vitro and in Living Cells, *J. Am. Chem. Soc.* **2013**, *135*(18), 6782–6785.

[192] Tsukiji, S. and Hamachi, I., Ligand-directed tosyl chemistry for in situ native protein labeling and engineering in living systems: from basic properties to applications, *Curr. Opin. Chem. Biol.* **2014**, *21*, 136–143.

[193] Takaoka, Y., Sun, Y., Tsukiji, S., and Hamachi, I., Mechanisms of chemical protein 19F-labeling and NMR-based biosensor construction in vitro and in cells using self-assembling ligand-directed tosylate compounds, *Chem. Sci.* **2011**, *2*(3), 511–520.

[194] Yamaura, K., Kuwata, K., Tamura, T., Kioi, Y., Takaoka, Y., Kiyonaka, S., and Hamachi, I., Live cell off-target identification of lapatinib using ligand-directed tosyl chemistry, *Chem. Commun.* **2014**, *50*(91), 14097–14100.

[195] Takaoka, Y., Nishikawa, Y., Hashimoto, Y., Sasaki, K., and Hamachi, I., Ligand-directed dibromophenyl benzoate chemistry for rapid and selective acylation of intracellular natural proteins, *Chem. Sci.* **2015**, *6*(5), 3217–3224.

[196] Tanaka, K., Kitadani, M., Tsutsui, A., Pradipta, A.R., Imamaki, R., Kitazume, S., Taniguchi, N., and Fukase, K., A cascading reaction sequence involving ligand-directed azaelectrocyclization and autooxidation-induced fluorescence recovery enables visualization of target proteins on the surfaces of live cells, *Org. Biomol. Chem.* **2014**, *12*(9), 1412–1418.

[197] Fujishima, S., Yasui, R., Miki, T., Ojida, A., and Hamachi, I., Ligand-directed acyl imidazole chemistry for labeling of membrane-bound proteins on live cells, *J. Am. Chem. Soc.* **2012**, *134*(9), 3961–3964.

[198] Miki, T., Fujishima, S.h., Komatsu, K., Kuwata, K., Kiyonaka, S., and Hamachi, I., LDAI-Based Chemical Labeling of Intact Membrane Proteins and Its Pulse-Chase Analysis under Live Cell Conditions, *Chem. Biol.* **2014**, *21*(8), 1013–1022.

[199] Matsuo, K., Kioi, Y., Yasui, R., Takaoka, Y., Miki, T., Fujishima, S.h., and Hamachi, I., One-step construction of caged carbonic anhydrase I using a ligand-directed acyl imidazole-based protein labeling method, *Chem. Sci.* **2013**, *4*(6), 2573.

[200] Hughes, C.C., Yang, Y.L., Liu, W.T., Dorrestein, P.C., Clair, J.J.L., and Fenical, W., Marinopyrrole A Target Elucidation by Acyl Dye Transfer, *J. Am. Chem. Soc.* **2009**, *131*(34), 12094–12096.

[201] Asano, K. and Matsubara, S., Effects of a Flexible Alkyl Chain on a Ligand for CuAAC Reaction, *Org. Lett.* **2010**, *12*(21), 4988–4991.

[202] Bedolla, D.E., Kenig, S., Mitri, E., Ferraris, P., Marcello, A., Grenci, G., and Vaccari, L., Determination of cell cycle phases in live B16 melanoma cells using IRMS, *Analyst* **2013**, *138*(14), 4015.

[203] Jimenez-Hernandez, M., Hughes, C., Bassan, P., Ball, F., Brown, M.D., Clarke, N.W., and Gardner, P., Exploring the spectroscopic differences of Caki-2 cells progressing through the cell cycle while proliferating in vitro, *Analyst* **2013**, *138*(14), 3957.

[204] Jimenez-Hernandez, M., Brown, M.D., Hughes, C., Clarke, N.W., and Gardner, P., Characterising cytotoxic agent action as a function of the cell cycle using fourier transform infrared microspectroscopy, *Analyst* **2015**, *140*(13), 4453–4464.

[205] de Jonge, M.D. and Vogt, S., Hard X-ray fluorescence tomography — an emerging tool for structural visualization, *Curr. Opin. Struc. Biol.* **2010**, *20*(5), 606–614.

[206] Fulmer, G.R., Miller, A.J.M., Sherden, N.H., Gottlieb, H.E., Nudelman, A., Stoltz, B.M., Bercaw, J.E., and Goldberg, K.I., NMR Chemical Shifts of Trace Impurities:

Common Laboratory Solvents, Organics, and Gases in Deuterated Solvents Relevant to the Organometallic Chemist, *Organometallics* **2010**, *29*(9), 2176–2179.

[207] Fabbrizzi, P., Menchi, G., Raspanti, S., Guarna, A., and Trabocchi, A., Role of Side-Chain Bioisosteres in Determining the Binding Affinity of Click Chemistry Derived RGD Peptidomimetics to v3 Integrin, *Eur. J. Org. Chem.* **2014**, *2014*(34), 7595–7604.

[208] Bonnard, V., Azoulay, S., Giorgio, A.D., and Patino, N., Polyamide amino acids: a new class of RNAligands, *Chem. Commun.* **2009**, (17), 2302–2304.

[209] van Dijk, M., van Nostrum, C.F., Hennink, W.E., Rijkers, D.T.S., and Liskamp, R.M.J., Synthesis and Characterization of Enzymatically Biodegradable PEG and Peptide-Based Hydrogels Prepared by Click Chemistry, *Biomacromolecules* **2010**, *11*(6), 1608–1614.

[210] Crosby, G.A. and Demas, J.N., Measurement of photoluminescence quantum yields. Review, *J. Phys. Chem.* **1971**, *75*(8), 991–1024.

[211] Olmsted, J., Calorimetric determinations of absolute fluorescence quantum yields, *J. Phys. Chem.* **1979**, *83*(20), 2581–2584.

[212] Das, S.C., Panda, D., Nayak, D., and Pattnaik, A.K., Biarsenical Labeling of Vesicular Stomatitis Virus Encoding Tetracysteine-Tagged M Protein Allows Dynamic Imaging of M Protein and Virus Uncoating in Infected Cells, *J. Virol.* **2009**, *83*, 2611–2622.

[213] Andresen, M., Schmitz-Salue, R., and Jakobs, S., Short tetracysteine tags to β-tubulin demonstrate the significance of small labels for live cell imaging, *Mol. Biol. Cell* **2004**, *15*(12), 5616–5622.

[214] Dieterich, D.C., Chemical reporters for the illumination of protein and cell dynamics, *Curr. Opin. Neurobiol.* **2010**, *20*, 623–630.

[215] Hildebrandt, P., A Spectral Window to the Cell, *Angew. Chem. Int. Edit.* **2010**, *49*(27), 4540–4541.